UNIVERSITY OF LIVERPOOL

Fabricating Multiscale Quasiperiodic Architectures: Artificial Spin-Ice and Molecular Thin Films

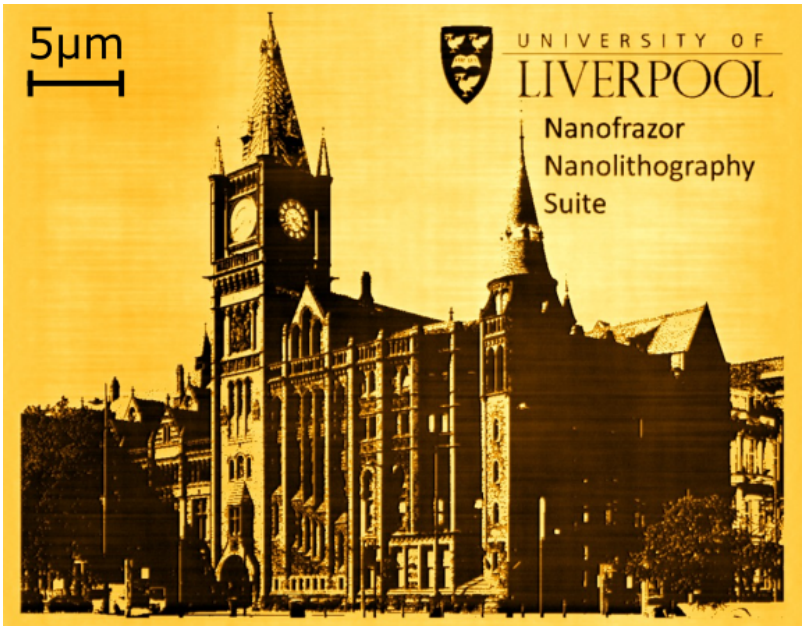

Thesis submitted in accordance with the requirements of the University of Liverpool for the degree of Doctor in Philosophy by

Liam Chandler

July 2025

If I have seen further it is by standing on the shoulders of Giants

- Sir Isaac Newton

For my father and mother, thank you

Abstract

This thesis addresses the challenge of studying quasicrystal surfaces for potential applications by fabricating atomic- and nanoscale quasiperiodic (QP) architectures. Measuring the surfaces of natural quasicrystals presents significant experimental barriers, including scarcity, ultra-high vacuum requirements, and extensive surface preparation. There is therefore a need to fabricate quasiperiodic architectures that physically model quasicrystal surfaces, enabling access to fundamental properties and the exploration of potential applications.

Fabrication of multiscale QP architectures is achieved with nanolithography of nanomagnetic arrays and molecular deposition on real quasicrystal surfaces. These investigations reveal interesting properties such as forced excitation and anisotropic adsorption.

An important advance is the establishment of a protocol for fabricating nano-scale QP tilings with thermal-scanning probe lithography (t-SPL), a nanolithography technique, for new researchers to the field. By optimising the design, chemical, and physical challenges, reproducibly high quality and complex QP tilings are fabricated.

Next, the nanomagnetic properties of nano-lithograped 8-fold Ammann-Beenker (ABT) and 4-fold Square Fibonacci (SFT) artificial spin-ice tilings are investigated with micromagnetic modelling, magnetic force microscopy (MFM), and X-ray magnetic circular dichroism - photoemission electron microscopy (XMCD-PEEM). Investigations reveal forced excitations within ground state domains of the ABT, and pinned high-energy states stabilised by quasiperiodic structure within the SFT. These phenomena have the potential to be applied to neuromorphic computing architectures.

Finally, by depositing molecular C_{60} on the surface of the annealed 2-fold Al-Ni-Co quasicrystal surface, the first demonstration of anisotropic chains of C_{60} with quasiperiodic separations are formed, as measured with scanning tunneling microscopy. This result advances the potential for molecular electronics of functional endofullerines on quasicrystal surfaces.

This work demonstrates how fabricating multiscale quasiperiodic architectures enables the crucial investigation of fundamental physics and advances potential applications.

Declaration

I hereby confirm this work is my own, except where other works are referenced. This work has not previously been submitted to any institute, including this one. This thesis does not exceed the relevant word count.

Liam Chandler

Acknowledgements

I first began studying at the University of Liverpool in 2017, where I found the university, my peers, and the city to be welcoming, supportive, and an excellent home for the next eight years of my life. Without these influences, I would not be where I am today. I want to thank Dr. Hem Raj Sharma, Prof. Ronan McGrath, and Dr. Liam O'Brien, who welcomed me into their research groups, and allowed me to pursue research in my own direction with their guidance and expert knowledge.

I had the great fortune of collaborating with many exceptional scientists, who helped me to grow as a scientist. I want to thank Dr. Sam Coates, whose unassuming support was continuously available and indispensable. Next, I also thank Prof. Ron Lifshitz, and Prof. Philip Moriarty, who gave their time, resources, and advice to support the work undertaken in this thesis. I especially thank Dr. Tyler James and Connor Fields, who on several occasions (including overnight sessions at beamlines) gave their time and full attention to my research. Thanks also to Dr. Alex Wright, Dr. Andrea Vezzoli, Dr. Chongguang Liu, Oliver Barker, Armaan Mohammadi-Motlagh, and Nich Cook, who collaborated and trained me in nanolithography and metal deposition techniques. I thank Dr. Sam Haq, Dr. Oscar Shedwick, Dr. Matthew Bilton, Dr. Sahil Tippireddy, and Dr. Gavin Stenning who trained me on surface experimental techniques. Additionally, thanks go to the beamline staff at Diamond, especially Dr. Larissa Ishibe-Veiga, Dr. Brice Sarpi, and Dr. Francesco Maccherozzi, without whom high-quality synchrotron data could not have been collected.

Thanks go to the Engineering and Physical Sciences Research Council, International Union of Crystallography, and EC-MetAC, for funding my research, training schools, and presentations at conferences.

On a personal level, I want to thank my friends and family, without whom I could never have achieved such happiness. My friends Rob, Molly, Lizzie, and Rian, who influenced me to stay in Liverpool past undergrad, had a huge positive impact on my life over the last eight years. I also thank everyone in the surface science tearoom, who were a constant source of support and fun. Special thanks go to Ellie and Ahowd, who were interesting and sapient neighbours. I thank my Dad, Mum, and sister Rebecca, who were always able to whisk me away from university life. I also thank my new colleagues at Kore Technology,

who have welcomed me into the next stage of my life. Finally, to my girlfriend Louisa, who showed patience, kindness, unwavering belief in me, and the warmth that made even my hardest days feel lighter - thank you.

Contents

Abstract **v**

Acknowledgements **vii**

1 Introduction **1**

2 Theory **3**

2.1 Nanomagnetism . . . 3

2.1.1 Types of Magnetism . . . 3

2.1.2 Magnetic Domains and Domain Walls . . . 5

2.1.3 Geometric Frustration . . . 7

2.1.4 Artificial Spin-Ice . . . 7

2.2 Fundamental Crystallography . . . 9

2.3 Introduction to Quasiperiodic Systems . . . 10

2.4 Generating 2-Dimensional Quasiperiodic Tilings . . . 13

2.4.1 Substitution Method . . . 14

2.4.2 Generalised Dual-Grid Method . . . 16

2.4.3 Cut-and-Project Method . . . 17

2.5 3-Dimensional Decagonal Quasicrystals . . . 17

2.5.1 Structure of Decagonal Quasicrystals . . . 18

2.5.2 Decagonal Al-Ni-Co . . . 20

2.6 Thin Film Growth on Crystalline Surfaces . . . 24

2.6.1 Surface Energy and Stress . . . 25

2.6.2 Structural Models of Solid Interfaces . . . 25

3 Literature Review **27**

3.1 Artificial Spin Ice . . . 27

3.1.1 Periodic Artificial Spin Ice . . . 27

3.1.2 Quasiperiodic Artificial Spin Ice . . . 37

3.2 Nanolithographic Fabrication of QP Tilings . . . 40

3.2.1 Scanning Probe Lithography . . . 40

3.2.2 Electron Beam Lithography . . . 41
3.2.3 Photolithography . . . 44
3.3 The 8-fold Ammann-Beenker Tiling . . . 44
3.4 Growth of Thin Films on Quasicrystals . . . 49
3.4.1 Rotational Epitaxy . . . 49
3.4.2 Quasiperiodic Modulation . . . 50
3.4.3 Templated Growth . . . 51

4 Experimental Methods 58
4.1 Introduction . . . 58
4.2 Achieving and Measuring Ultra-High Vacuum . . . 58
4.2.1 Vacuum Pressure and Flow Types . . . 58
4.2.2 Vacuum Pumps . . . 60
4.2.3 Vacuum Gauges . . . 63
4.3 Thermal-Scanning Probe Lithography . . . 64
4.3.1 Chemical Method . . . 64
4.3.2 Principle of t-SPL . . . 69
4.4 Electron Beam Evaporation . . . 72
4.5 Scanning Electron Microscopy . . . 73
4.6 Quasicrystal Surface Analysis Techniques . . . 75
4.6.1 Surface Preparation and Molecular Evaporation . . . 75
4.6.2 Scanning Tunnelling Microscopy . . . 78
4.6.3 Low Energy Electron Diffraction . . . 80
4.7 Magnetic Measurement Techniques . . . 82
4.7.1 Magnetic Force Microscopy . . . 82
4.7.2 Superconducting Quantum Interference Device - Vibrating Sample Magnetometer . . . 84
4.7.3 X-Ray Magnetic Dichroism Photoemission Electron Microscopy . . . 85
4.7.4 Quasiperiodic Micromagnetic Simulations with MuMax3 . . . 89

5 Fabricating Quasiperiodic Tilings with Thermal-Scanning Probe Lithography 95
5.1 Introduction . . . 95
5.2 Results and Discussion . . . 98
5.2.1 Designing, Coding, and Resolution Optimisations . . . 98
5.2.2 Optimising the Chemical Process . . . 103
5.2.3 t-SPL Optimisation . . . 113
5.2.4 Fabrication Results . . . 123
5.3 Conclusion and Outlook . . . 129

6 Magnetic Ordering and Frustration in Ammann-Beenker Artificial Spin-Ice 130
6.1 Introduction . . . 130
6.2 Experimental and Modelling Details . . . 132
6.3 Results and Discussion . . . 133
6.3.1 Square Artificial Spin-Ice . . . 133
6.4 Ammann-Beenker Tiling Artificial Spin-Ice . . . 137
6.4.1 Magnetic Imaging . . . 137
6.4.2 MuMax3 Micromagnetic Simulation Results . . . 137
6.4.3 Vertices-Only Model . . . 143
6.4.4 The Skeleton Model . . . 146
6.4.5 The Correlation Model . . . 151
6.5 Summary of Model Regimes Analysis . . . 155
6.6 Magnetometry and XMCD-PEEM . . . 156
6.6.1 Experimental Techniques . . . 156
6.6.2 Results and Discussion . . . 157
6.7 Summary of Anneal Studies . . . 163
6.8 Conclusion . . . 163

7 Magnetic Ordering and Frustration in Square-Fibonacci Artificial Spin-Ice 164
7.1 Introduction . . . 164
7.2 Experimental and Modelling Techniques . . . 165
7.2.1 Experimental Techniques . . . 165
7.2.2 Modelling Techniques . . . 165
7.3 Results and Discussion . . . 166
7.3.1 Micromagnetic Modelling Results . . . 166
7.3.2 XMCD-PEEM Results . . . 170
7.4 Conclusion . . . 172

8 Quasiperiodic Arrays of C_{60} Molecular Chains Induced by Anisotropic Growth 173
8.1 Introduction . . . 173
8.2 Experimental Details . . . 174
8.3 Results and Discussion . . . 175
8.3.1 Model Atomic Structure . . . 175
8.3.2 Clean Surface . . . 178
8.3.3 C_{60} Adsorption . . . 184
8.3.4 C_{60} Height Difference . . . 192

8.3.5 Finite-Chain Observations and Analysis 195
8.4 Conclusions 201

9 Conclusions and Future Work **202**

Bibliography **205**

Appendices **229**

A MuMax3 Simulation Code **229**
A.1 Introduction 229
A.2 Example Script for 3i Total Energy 229

B Publications **232**

Chapter 1

Introduction

The city of Petra, delicately carved into the cliffs of Jordan, and the Great Wall of China, meticulously built over centuries, demonstrate how simple elements can be carefully fabricated into beautiful multiscale architectures. Similarly, nature fabricates intricate structures through quasiperiodic order. Quasicrystalline materials have no translational symmetry yet exhibit perfect long-range order [1]. They are typically associated with rotational symmetries such as 5-, 8-, and 10-fold that are incompatible with periodicity. Quasicrystalline order has been observed in various materials, such as inter-metallic alloys [1], colloids [2, 3], soft-matter [4, 5], and perovskites [6, 7]. Since their discovery, a major research effort has been undertaken to understand properties related to their structure [8,9]. Characterising the physical properties of atomic-scale quasicrystals poses several challenges, primarily due to the quasiperiodic arrangement of atoms, which complicates structure determination and requires advanced measurement techniques [10]. In particular, the repertoire of quasicrystals available is limited to certain structures, such as icosahedral and decagonal systems.

While nature can construct quasicrystals, the controlled fabrication and characterisation of such architectures at the nanoscale remains limited. This thesis addresses this gap through two complementary approaches: nano-lithographed artificial spin-ice (ASI) systems, and atomic-scale molecular deposition atop a real quasicrystal surface. This work establishes a new nanofabrication technique, thermal-scanning probe lithography (t-SPL), as an accessible nanofabrication platform for quasiperiodic tilings - which model the surface of quasicrystals. Optimised protocols enable new researchers to replicate these architectures. ASI are single-domain nanomagnets precisely positioned along tiling edges, and their interactions may be characterised using magnetic microscopy and micromagnetic simulations. Studies of quasiperiodic ASI reveal emergent magnetic phenomena in the first experimental realisations of 8-fold Ammann-Beenker (ABT) and 4-fold Square Fibonacci (SFT) ASI tilings. Finally, the first experimental realisation of anisotropically ordered C_{60} monolayers grown on the surface of the 2-fold *d*-Al-Ni-Co is presented, increasing

understanding of templated molecular adsorption unique to quasicrystals.

The thesis is structured as follows. Chapter 2 establishes the theoretical framework for understanding fundamental crystallography and quasiperiodic systems, decagonal quasicrystals, thin film growth, and nanomagnetism. Four distinct literature reviews are provided in Chapter 3, detailing nanolithography of quasiperiodic tilings, early and relevant ASI results, recent investigations of the 8-fold Ammann-Beenker tiling, and growth of thin films on the surfaces of quasicrystals. The experimental methods are given in Chapter 4, covering vacuum systems, the full t-SPL method, electron-beam evaporation of metals for t-SPL, scanning electron microscopy, scanning tunneling microscopy (STM) and low energy electron diffraction, and finally the magnetic measurement techniques utilised and the simulation method.

The results chapters for this thesis start with Chapter 5 which describes the optimisations of the t-SPL process for fabricating quasiperiodic ASI tilings. Next, Chapter 6 investigates the 8-fold Ammann-Beenker tiling ASI with magnetic force microscopy (MFM) and micromagnetic simulations, revealing unique and interesting magnetic phenomena due to geometric frustration. The last part of Chapter 6 covers an anneal study performed on the ABT ASI with magnetometry and X-ray circular magnetic dichroism - photoelectron emission microscopy (XMCD-PEEM). In Chapter 7, micromagnetic simulations and XMCD-PEEM is further performed on the thermalised SFT, identifying instrinsic topologically excited vortex states not present in the periodic square ASI analogue. Finally, in Chapter 8, the first anisotropic molecular arrangement on the surface of a quasicrystal was demonstrated with STM, by depositing C_{60} atop the 2-fold surface of the decagonal Al-Ni-Co quasicrystal.

A conclusion bringing together all results is given in Chapter 9, with potential future work directions discussed.

Chapter 2

Theory

This chapter will cover all necessary theory for the literature reviews (Chapter 3), methods (Chapter 4), and results (Chapters 5-8) of this thesis. It begins with an introduction to nanomagnetism, fundamental crystallography and quasiperiodicity, 2- and 3- Dimensional quasicrystalline systems, and finally thin film growth mechanics.

2.1 Nanomagnetism

In this section, the theory required for investigating magnetic properties of fabricated QP tilings in Chapter 8 will be covered. To begin, types of magnetism and domain walls are defined, including the influence of temperature on systems. Lastly, an introduction to geometric frustration and artificial spin-ice is given.

2.1.1 Types of Magnetism

Magnetism has been a subject of scientific inquiry since antiquity, with the attraction between lodestone and iron documented by ancient Greek scholars [11]. Today, magnetic phenomena are fundamental to numerous ubiquitous technologies, though their operation often remains unseen. Core functionalities in modern devices, such as data storage in computers and smartphones, depend critically on principles derived from our understanding of magnetism. At the quantum level, magnetism originates from intrinsic electron properties: spin and orbital magnetic moments. Macroscopic magnetic behaviour emerges from distinct collective spin ordering regimes, categorised as paramagnetism, ferromagnetism, antiferromagnetism, and ferrimagnetism. These foundational classifications form the basis for discussion in subsequent sections.

Paramagnetism

Paramagnetic materials contain atoms with unpaired electrons in incomplete sub-shells, resulting in a permanent atomic magnetic moment. Consequently, these materials can develop a net magnetisation upon application of an external magnetic field. In the absence of such a field, thermal fluctuations cause the atomic moments to remain randomly oriented, yielding zero net magnetisation. Even under an applied field, paramagnets exhibit only partial alignment of moments. For ideal paramagnetic systems where inter-moment interactions are negligible, the magnetisation M relates to the applied field H according to the Curie law:

$$M = \chi H = \frac{CH}{T} \tag{2.1.1}$$

Here χ defines the magnetic susceptibility, C is the material specific Curie constant, and T is the absolute temperature. Equation 2.1.1 demonstrates that the induced magnetisation increases as temperature decreases. This occurs because reduced thermal energy less effectively disrupts the alignment of moments with the applied field.

Ferromagnetism

Ferromagnetism describes materials capable of exhibiting spontaneous magnetisation, with the ability to form permanent magnets. This behaviour originates from the exchange interaction between electron spins, which energetically favours parallel alignment. The Heisenberg model quantifies this interaction in ferromagnets as [12]:

$$U_{ij} = -2J_{i,j}S_i \cdot S_j \tag{2.1.2}$$

Here, $J_{i,j}$ denotes the exchange integral; a positive $J_{i,j}$ signifies ferromagnetic coupling. The spins S_i and S_j typically interact significantly only between nearest neighbours. Upon applying an external magnetic field, spins align parallel to the field direction. Crucially, this parallel alignment persists upon field removal due to the energy minimisation inherent in the exchange interaction. However, ferromagnetic order is thermodynamically stable only below a critical temperature, the Curie temperature (T_C). Above T_C, the material becomes paramagnetic, with susceptibility χ following the Curie-Weiss law: $\chi = \frac{H}{T-T_C}$. This relation predicts the divergence of χ at $T = T_C$ [13]. Notably, only a few pure elements exhibit ferromagnetism, primarily the transition metals Fe, Ni, and Co. Their approximate T_C are 1043 K, 627 K, and 1388 K, respectively [13]. Ferromagnetic behaviour also occurs in certain alloys, particularly those based on these elements or rare-earth metals.

Domain theory is fundamental to understanding ferromagnetic behaviour. A magnetic

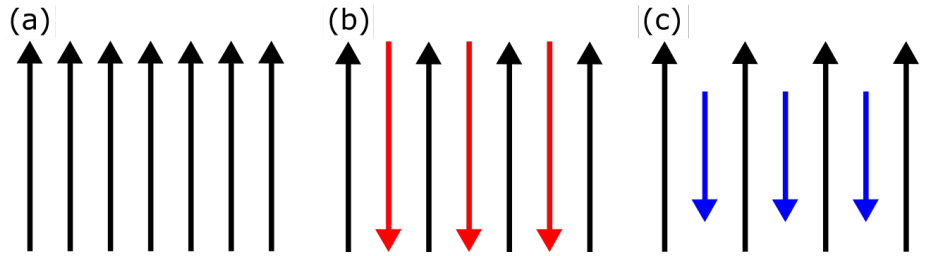

Figure 2.1: Graphic with arrows representing magnetic moments describing: (a) Ferromagnetism, (b) Antiferromagnetism, and (c) Ferrimagnetism.

domain is a region within a material where the magnetisation is uniform, meaning all atomic magnetic moments are aligned parallel. Macroscopic ferromagnetic specimens typically comprise multiple domains. This multidomain structure minimises the system's free energy, although domain boundaries introduce exchange energy penalties between misaligned spins at interfaces, they significantly reduce the magnetostatic energy (energy stored in a static magnetic field). The transition region separating adjacent domains is termed a domain wall, across which the magnetisation direction rotates gradually. Detailed descriptions of domain structures follow later in this section.

Antiferromagnetism and Ferrimagnetism

In contrast to ferromagnetic materials where neighbouring spins energetically favour parallel alignment, antiferromagnetic systems exhibit preferential antiparallel spin orientation. This distinction is captured in the Heisenberg model shown in Equation 2.1.2 by a negative exchange integral $J_{i,j}$. The defining characteristic of an antiferromagnet is zero net magnetisation, resulting from exact cancellation between antiparallel spins of equal magnitude. Ferrimagnets, while also exhibiting antiparallel alignment, possess inequivalent magnetic sublattices. This sublattice imbalance yields a non-zero net moment. Figure 2.1 illustrates the characteristic spin arrangements in ferromagnetic, antiferromagnetic, and ferrimagnetic systems. Common antiferromagnets include transition-metal compounds such as FeMn and NiO, whereas YFeO, ferrites, and other magnetic garnets exemplify ferrimagnetic materials.

2.1.2 Magnetic Domains and Domain Walls

Magnetic domains constitute regions of uniform magnetisation where all atomic magnetic moments are aligned. While exchange interactions favour single-domain configurations in sufficiently small nanoparticles, larger ferromagnetic specimens develop multiple domains to minimise magnetostatic energy. This multidomain structure reduces the demagnetising field by confining flux closure within the material. The principle of magnetostatic energy reduction through domain formation is illustrated schematically in Figure 2.2. The

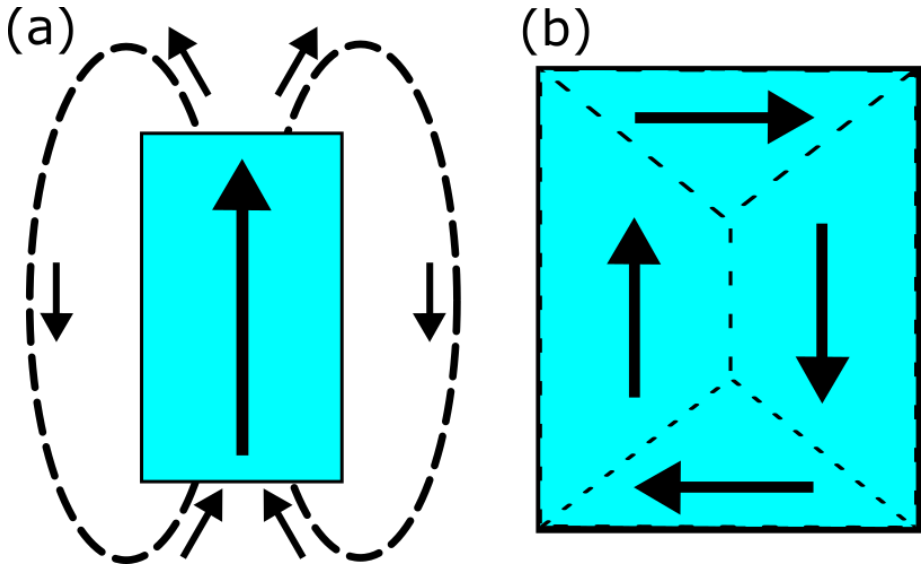

Figure 2.2: Graphic showing how multidomain structures reduce magnetostatic energy. (a) A single domain ferromagnet, with stray field indicated with dashed black lines and small black arrows. (b) A multidomain structure with a flux closure loop and removed stray field

interface separating adjacent magnetic domains is termed a domain wall, depicted schematically by dotted lines in Figure 2.2. Within these transition regions, magnetisation rotates between the orientations of neighbouring domains. Domain walls are principally classified into two types: Bloch walls and Néel walls, distinguished by their characteristic spin rotation geometries relative to the wall plane [12].

The Bloch wall, predominantly occurs in bulk magnetic materials. The Bloch wall's defining characteristic is magnetisation rotation within a plane perpendicular to the material's easy axis. In contrast, the Néel wall is stabilised in thin films, where magnetisation rotates within the film plane. Néel walls typically remain stable in films up to bulk thickness. These walls are further classified into: transverse walls (magnetisation at the center of the wall directed transverse to the strip axis), and vortex walls (magnetisation forms a vortex at the center of the wall) [14]. The stability of these domain wall types within nanostructures is governed by the nanostructure's cross-sectional area. For instance, in permalloy ($Ni_{80}Fe_{20}$) strips, vortex walls become energetically favourable at larger bulk-like cross-sections exceeding around 1000 nm^2, while transverse walls dominate in thinner and less wide strips [15].

Superparamagnetism

As particle size increases beyond a critical threshold, ferromagnetic materials transition from single-domain to multidomain configurations to minimise magnetostatic energy. Conversely, sufficiently small single-domain particles exhibit superparamagnetic behaviour. In this regime, thermal fluctuations drive stochastic transitions between magnetisation orien-

tations, overcoming the diminished energy barrier separating stable states. The Néel relaxation time τ_n quantifies the average interval between spontaneous magnetisation reversals, governed by the Néel-Arrhenius relation, with attempt time τ_0, magnetic anisotropy energy density K, and volume V [16]:

$$\tau_n = \tau_0 \; exp\left(\frac{KV}{k_B T}\right) \tag{2.1.3}$$

Blocking Temperature

The observation of superparamagnetic behaviour depends critically on the measurement timescale τ_m relative to τ_n. When τ_m is greater than τ_n, stochastic magnetisation reversals occur frequently during measurement, exhibiting characteristic superparamagnetic fluctuations. Conversely, if τ_m is less than τ_n, reversals are thermally inaccessible within the experimental timeframe, resulting in a magnetically 'blocked' state where moments remain fixed. Near $\tau_m = \tau_n$, intermittent switching becomes detectable. This timescale dependence motivates defining a characteristic blocking temperature T_B marking the transition between superparamagnetic and blocked regimes for experimentally accessible τ_m. This temperature is derived from Equation 2.1.3 as:

$$T_B = \frac{KV}{k_B \; ln\left(\frac{\tau_m}{\tau_0}\right)} \tag{2.1.4}$$

2.1.3 Geometric Frustration

Geometric frustration occurs when a system's spatial arrangement prevents simultaneous minimisation of all pairwise interactions [17]. This is exemplified by Ising spins coupled antiferromagnetically at the vertices of structures in Figure 2.3. For example, in Figure 2.3(a), when the first two spins adopt antiparallel alignment, the third spin (indicated with an '?') cannot minimise its interaction energy with both neighbours concurrently. The system energy remains degenerate with respect to the third spin's orientation (± 1), resulting in multiple ground states with identical energy. Similar degeneracy is observed with pentagonal and centred square geometries in Figures 2.3(b) and (c), respectively. This degeneracy directly stems from the lattice geometry's incompatibility with perfect antiferromagnetic ordering.

2.1.4 Artificial Spin-Ice

An artificial spin-ice (ASI) is an engineered system built of interacting single-domain nanomagnets decorated on specific sites of different lattices. They are so-called for their analogous behaviour to spins in crystal lattices such as rare-earth titanate pyrochlores, which have Ising anisotropy, for example $Ho_2Ti_2O_7$ [17]. Ising anisotropy is when a system of

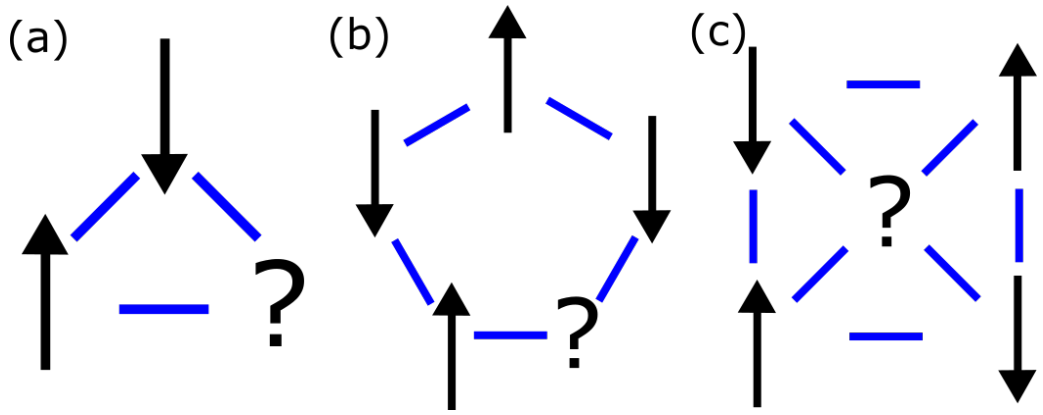

Figure 2.3: A graphic demonstrating basic geometric frustration of Ising spins represented by arrows, with increasingly complex geometry: (a) triangle, (b) pentagon, (c) centred square. The '?' represents degenerately frustrated spins.

interactions are strongly directional, and that spins preferentially align along an easy axis. For example in a tetrahedral pyrochlore spin-ice, spins occupy the vertices, and either point 'in' or 'out' towards the centre. The ground state has neighbouring spins with two 'in' and two 'out' moments. This results in a geometrically frustrated ground state, arising from the presence of dominant ferromagnetic interactions and axial single-spin anisotropy.

With the advent of nanolithography techniques [18], fabricated systems of nanomagnets with tailor-made geometries allowed for artificial spin-ice mimicking pyrochlores to be materialised. With nanolithography techniques, elongated-island shaped masks on the substrate, which follow the desired lattice geometry, can be etched. This is followed by metal deposition with physical vapour deposition, where particles condense to form the desired ASI lattice pattern [19, 20]. Ferromagnetic materials are typically investigated, as they exhibit clustered magnetic dipole moments of domains with anisotropic orientations. These domains are created as the most energetically favourable orientation [21, 22]. Permalloy is typically chosen for ASI systems due to its well-understood ferromagnetic properties, such as saturation magnesation $M_S = 8.6 \times 10^5 Am^{-1}$ and exchange stiffness constant $A_{ex} = 1.3 \times 10^{-11} Jm^{-1}$ [23]. This easily allows for micromagnetic calculations alongside experimental work with simulators such as OOMPH and MuMax3 [24, 25].

By restricting ferromagnetic material to a narrow width (< 200 nm) along the hard axis (also termed nanoisland width), single-domain nanoislands can be fabricated. As nanoislands are single-domain, they exhibit a single macrospin or moment, which can be observed with magnetic microscopy techniques. These moments can display geometric frustration when thermally annealed then cooled, leading to configurations above the ground state [26–31].

2.2 Fundamental Crystallography

A basic lattice description of periodic crystals is essential before developing into describing QP crystals. The textbook *Introduction to solid state physics* by Kittel and McEuen is used throughout this section as a reference [13].

Periodic crystals are built by the infinite repetition of identical groups of atoms described as the basis. The crystal lattice is the set of mathematical points the basis attaches to. These mathematical points can belong to any number of dimensions $\mathbf{n}$, such that they can be mapped by translation vectors:

$$\mathbf{R_n} = a_1\mathbf{n}_1 + a_2\mathbf{n}_2 + a_3\mathbf{n}_3 + \dots \tag{2.2.1}$$

where a_m represents the integer lattice constant in a given direction. Figure 2.4(a) shows an example for a 3D crystal, which can be translated across with $\mathbf{n} = 3$ a_m vectors. One of the most important characteristics of periodic crystals is the unit cell; defined as the smallest repeating structure which completely captures the symmetry and structure of the crystal lattice. For the 3D crystal in Figure 2.4(a), the unit cell is the parallelepiped formed by $a_1 \times a_2 \times a_3$. The allowed set of periodic 2D and 3D crystal lattices with unit cells are described by the Bravais Lattice groups, the 2D set shown in Figure 2.4(b). As these lattices are made up of well-defined infinitely repeating unit cells, they produce periodic crystals. There are five distinct Bravais Lattices in 2D, and fourteen in 3D. Additionally, there are special points on the faces and vertices of these groups that are strictly limited to having 2-, 3-, 4, and 6-fold rotational symmetry.

The faces or planes of any $\mathbf{n}$ dimensional crystals are described by an index system, known as Miller indices. Figure 2.4(c) shows how the Miller indices for an arbitrary plane are assigned. The cell size is cubic with $a_1 = a_2 = a_3 = 5$. The first step is to determine the intercept of the plane on each of the axis, coloured 3, 4, and 5. These intercepts are then divided by their respective lattice vector a_m, for example $\frac{4}{a_3} = 0.8$. Finally, to obtain the Miller indices for the plane, the reciprocal is applied to each as shown in Figure 2.4(c). This gives a plane of (1.66, 1, 1.25) or ($\frac{5}{3}$, 1, $\frac{5}{4}$). These are then multiplied so that fractions are eliminated ($\frac{5}{3}$, 1, $\frac{5}{4}$) $\rightarrow$ (20, 12, 15). This process can be applied to any $\mathbf{n}$ dimensional crystal, by adding an a_m for each new translational vector. Figure 2.4(d) shows two further examples of common planes (1, 0, 0) and (1, 0, 1). If there is no axis intercept the index is undefined and reduces to 0.

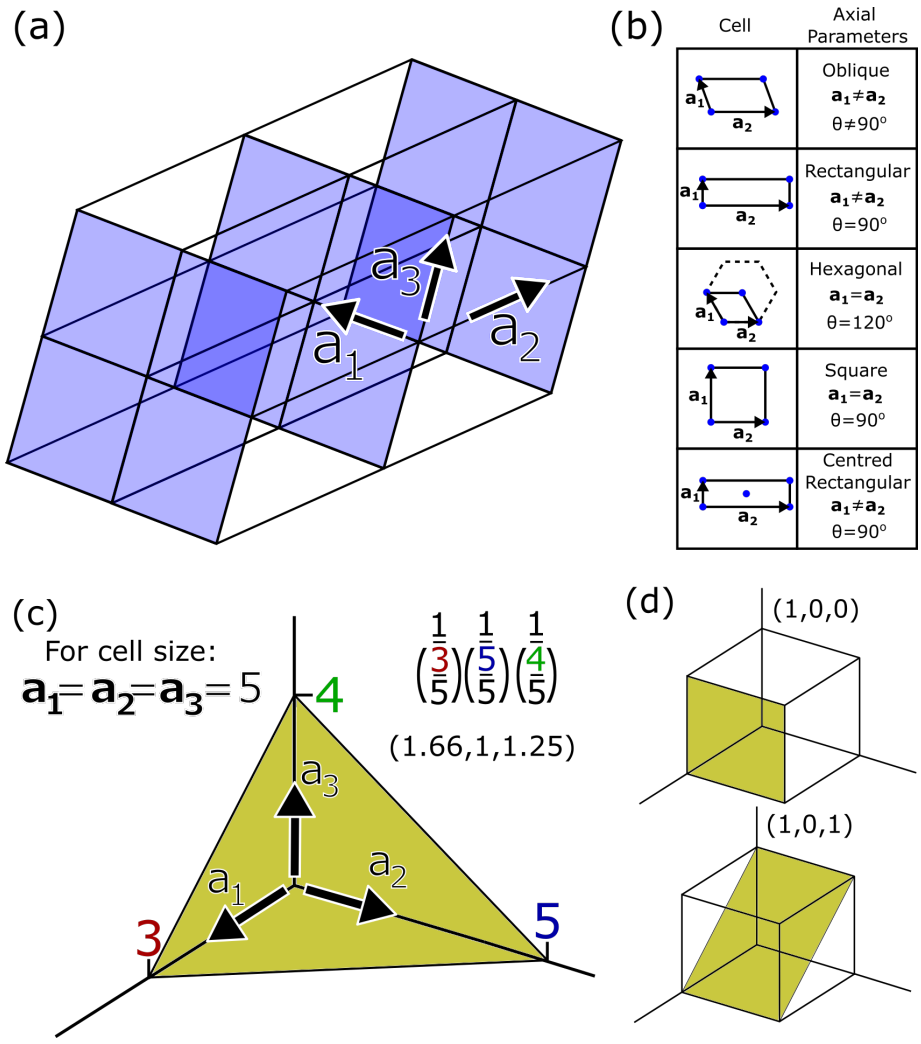

Figure 2.4: (a) a 3D crystal with a_1, a_2, and a_3 lattice vectors. (b) The 2D Bravais Lattice groups, where θ is the angle between a_1 and a_2. (c) An illustrative diagram for determining Miller indices of an arbitrary plane. (d) Miller indices for common periodic crystal planes.

2.3 Introduction to Quasiperiodic Systems

Before the groundbreaking discovery of quasicrystals in the early 1980s [1, 32], the world of crystallography was governed by the simple elegance of periodic order and the Bravais lattices. Repetition of unit cells defined periodicity, and crystallographic understanding at the time. It was believed that only certain building blocks were allowed to be placed to achieve crystallographic order. For 2D crystal systems, allowed rotational symmetries included 1-, 2-, 3-, 4-, and 6-fold systems, built from repeating 3-, 4-, and 6-sided polygons such as those shown in Figure 2.5(a). For example, a square can be built to produce a 4-fold system, whereas a hexagon may produce a 6-fold system. Note periodic systems of 5-fold symmetry cannot be constructed with pentagons, as these leave gaps in the structure, seen in Figure 2.5(b). Due to the well-defined repetition, periodic systems produce discrete

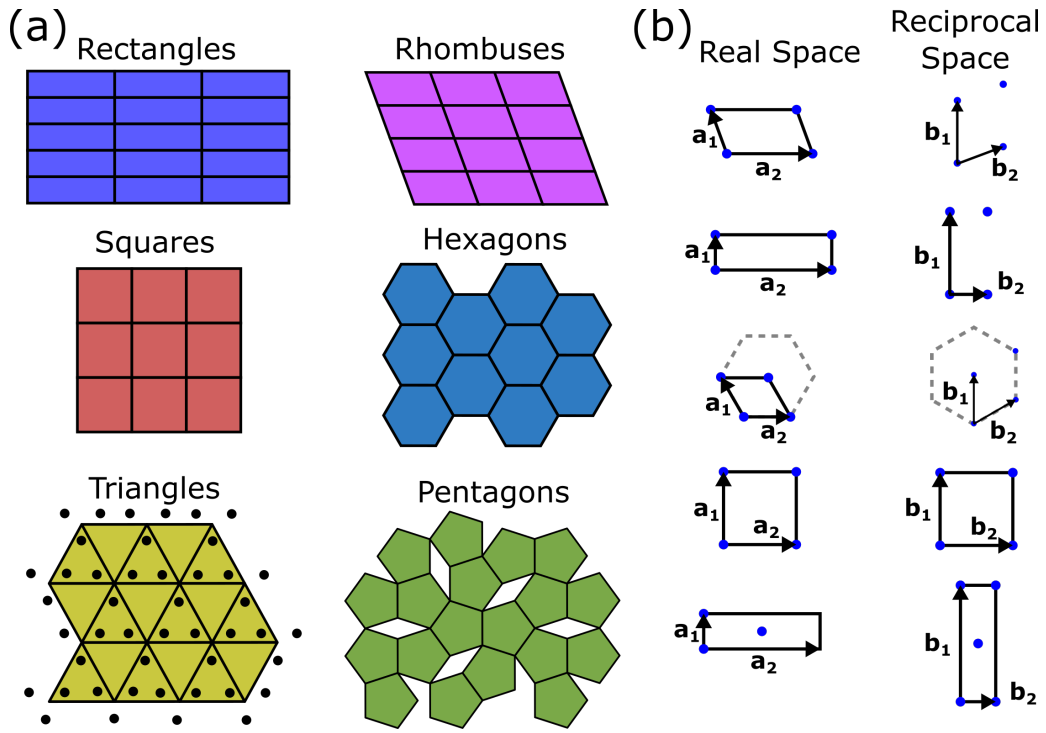

Figure 2.5: (a) A selection of 3, 4, and 6 sided polygons produce allowed rotational symmetries. Triangles are decorated with a motif at lattice points to produce a 3-fold but not a 6-fold rotational symmetry lattice. A 5 sided polygon (pentagon) does not effectively fill space and therefore cannot produce a 5-fold rotationally symmetric crystal lattice. (b) Real space Bravais lattices projected onto reciprocal space.

diffraction patterns in reciprocal space, with peaks indicative of the rotational order. Figure 2.5(b) shows the reciprocal space lattices of each of the 2D Bravais lattice.

The 3-, 4-, and 6-sided polygon paradigm was the backbone of crystallography until the discovery by Daniel Shechtman in the 1980's of a Al-Mn alloy that demonstrated diffraction peaks (reciprocal space lattice points) with icosahedral (10-fold) symmetry [32]. The higher rotational symmetry lattice crystals were eventually termed quasicrystals. The existance of quasicrystals forced classical concepts of Bravais lattices to be better defined as part of a Kuhnian revolution, shifting the old crystallographic paradigm into the new. The old crystallographic paradigm determined over a century ago that crystal order and periodicity were synergetic in nature, when Bragg performed the X-ray diffraction in crystals experiment [33]. Seventy years later the challenge to this notion by Shechtman, that alloys existed with no such periodicity but still exhibiting observable Bragg (diffraction) peaks, shook the crystallographic community at the core. There was significant opposition and hesitancy from the scientific community, with Linus Pauling quoted as proclaiming *'There is no such thing as quasi-crystals, only quasi-scientists'* [34]. Pauling described apparent aperiodicity as 'twinning' of cubic crystals which would cause similar Bragg peaks - in essence five intersecting cubic crystal planes rotated 72° to one another would appear

Fibonacci sequence	S	L	Total
S	1	0	1
L	0	1	1
LS	1	1	2
LSL	1	2	3
LSLLS	2	3	5
LSLLSLSL	3	5	8
LSLLSLSLLSLLS	5	8	13
LSLLSLSLLSLLSLSLLSLSL	8	13	21

Table 2.1: The Fibonacci sequence of long L and short S lengths, with substitution rules S = L and L = LS. The total of L and S following a Fibonacci sequence, and ratio of L and S tending towards $\frac{L}{S} = \tau$, the golden ratio and characteristic quasicrystalline feature.

to have icosahedral symmetry [35]. This argument however falls flat when forbidden symmetry found in quasicrystals is isotropic and ubiquitous, but twinning only causes such symmetry at grain boundaries, describing an incommensurate crystal. Quasicrystals then must then have order without periodicity. However, this order, much alike periodic crystals, presents as indistinguishability - when transformations are applied, the new lattice appears indistinguishable to the original to an observer [36–39]. Pauling never accepted the existence of quasicrystals, but the International Union of crystallography changed the definition of a crystal in 1992 to *'any solid having an essentially discrete diffraction diagram'*. Daniel Shechtman won the Nobel Prize for Chemistry in 2011 for the discovery.

The most basic expression of quasicrystalline order can be seen through a 1D Fibonacci sequence. This sequence is also surprisingly prevalent in higher dimensional quasicrystalline systems. A Fibonacci sequence is made by starting with two initial numbers, and then generating each subsequent number by adding the two numbers that come immediately before it. Mathematically this is expressed as $F_n = F_{n-1} + F_{n-2}$. For example, with starting values $F_{(0)} = 0$ and $F_{(1)} = 1$ one would obtain a sequence 0, 1, 1, 2, 3, 5, 8, 13, ... Another way of describing this sequence is with a series of long (L) and short (S) segments. By applying substitution rules $S \to L$ and $L \to LS$, a Fibonacci sequence of L and S is generated. The first seven iterations of L and S substitutions in a sequence starting from S is shown in Table 2.1. One important note is as the sequence increases by n iterations, the ratio of $\frac{L}{S}$ tends towards 1.618.... This number is a characteristic value of quasicrystalline materials known as the golden ratio $\tau = \frac{(1+\sqrt{5})}{2} = 1.618...$. The Fibonacci sequence is therefore an example of a 1D QP chain. Additionally, the sequence can be inflated or deflated, as long as the ratio $\frac{L}{S}$ is preserved, for example by considering larger tiles of $S = LSL, L = LSLSL$, and vice versa. One consequence of these substitution rules are no perfect Fibonacci sequence may have an 'SS' or 'LLL' in order. τ is a fundamental value

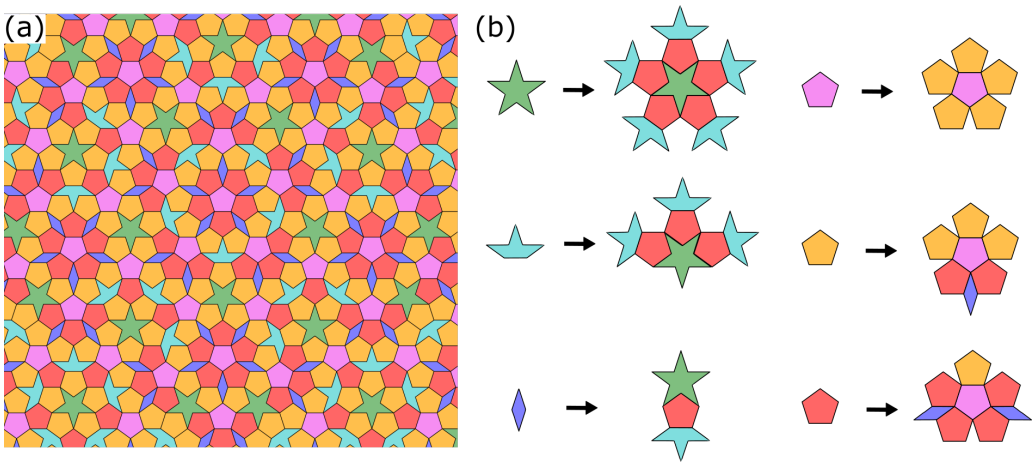

Figure 2.6: (a) A section of the P1 Penrose tiling. (b) Substitution rules with star, boat, rhombus, and pentagonal tiles iteratively replaced.

determining the structure of quasicrystalline structures, such as in decagonal-quasicrystals with lattice spacing related by τ seen in Chapter 8.

2.4 Generating 2-Dimensional Quasiperiodic Tilings

QP tilings are 2D mathematical models of quasicrystals and their surfaces, defined by their long-range crystallographic order with no repeating unit cell. Long-range crystallographic order is evidenced through diffraction patterns with reciprocal lattices showing Bragg peaks related by irrational (such as τ) scaling and no periodic unit cell. QP tilings often exhibit classically forbidden rotational symmetries such as 5-, 8-, and 10-fold, requiring a higher dimensional (n $>$ 3) set of vectors to fully translate between lattice points. QP tilings are however not limited to exotic forbidden symmetries, with 2-, 3-, 4-, and 6-fold quasiperiodicity easily achieved with irrational scaling and quasi-unit cells. Quasi-unit cells are the set of non-periodically repeating blocks which effectively fill space with specific long-range order. Previously in Figure 2.5(a) it was shown that pentagons could not fill space without overlapping, but with a combination of pentagons, rhombuses, and specific rules on where to place them - the space can be effectively covered. The most famous QP tilings, Penrose tilings, filled space with pentagons and subsets of rhombuses, the first (P1) shown in Figure 2.6(a) [40, 41]. The basis of employing more than one tile shape, reflection, or rotation of a shape, be it L and S in 1D, or pentagons and rhumbuses in 2D, is fundamental to producing quasiperiodicity and QP tilings.

In this section, three methods for generating QP tilings are discussed: substitution, generalised dual-grid, and the cut-and-project method. Throughout this section the online Tilings Encyclopedia is used as a reference [42].

2.4.1 Substitution Method

The P1 Penrose tiling can be creating from substitution rules, with prototiles (quasi-unit cells) substituting into further tilings, as shown in Figure 2.6(b). Substitution rules for QP tilings are generally derived by exploiting the self-similarity inherent in these structures. Researchers begin by identifying the basic prototiles of the tiling and then determine an appropriate scaling factor, such as the golden ratio in the case of Penrose tilings. By applying this scaling factor, one 'inflates' a tile, and the key step is to decompose this enlarged version into a collection of smaller tiles that are congruent (rotations or reflections) to the original set of prototiles. This decomposition directly leads to the substitution rule, which can be applied recursively to generate the entire QP pattern. The Penrose tiling generated via this method is presented in some fabricated tilings in Chapter 5.

In results Chapters 5 and 6, the 8-fold Ammann-Beenker tiling (ABT) is used throughout as a design for fabricating and magnetic Investigations. The ABT was first discovered by Ammann in 1977, and formally described algebraically in 1982 by Beenker following the lines of de Bruijn [43–45]. While the golden mean is used for Penrose tilings, the ABT scales by the silver mean $\delta = 1 + \sqrt{2}$. The silver ratio is found by considering a unit hexagon with sides = 1, the width from face to face is then $= 1 + 2 \times \sqrt{1} = 1 + \sqrt{2}$, as shown in Figure 2.7(a). In the next section, recent literature which investigates the ABT is reviewed. Here, the substitution rules for generating the ABT are shown. Prototiles are iteratively substituted for $\mathbf{n}$ generations to effectively cover space. An $\mathbf{n} = 4$ iteration ABT is shown in Figure 2.7(a), generated from starting with eight rhombuses in a central star. The final design is centred with 8-fold rotational symmetry - this is a unique high symmetry point for the tiling. The substitution rules are shown in Figure 2.7(b). One rhombus substitutes into three rhombuses and four squares, and one square substitutes into four rhombuses and five squares.

It is also possible to generate a 2D QP tiling based on the Fibonacci sequence of L and S discussed in the previous section. The tiling is produced by taking a chain of L and S generated from substitution rules, with lengths $L = S \times \tau$, and plotting chains orthogonal to one another. The tiling was introduced by Lifshitz in 2002, with the full tiling and substitution rules shown in Figure 2.8 [46]. The sequence of L and S can be transfered tiles whose lengths are proportional to S = 1 and L = τ. Other ways of generating this tiling would be to superimpose two Fibonacci grids, and with a cut-and-project method from 4-dimensional space, among other methods [47–49]. For completeness, the cut-and-project and dual-grid methods will be shown in the next sections. The Square Fibonacci tiling generated via the substitution method was used for the artificial spin-ice work in Chapter 6.

Overall, while trivial, the substitution method has some drawbacks. Firstly the computing time exponentially rises for higher iterations. Secondly, choosing the same initial

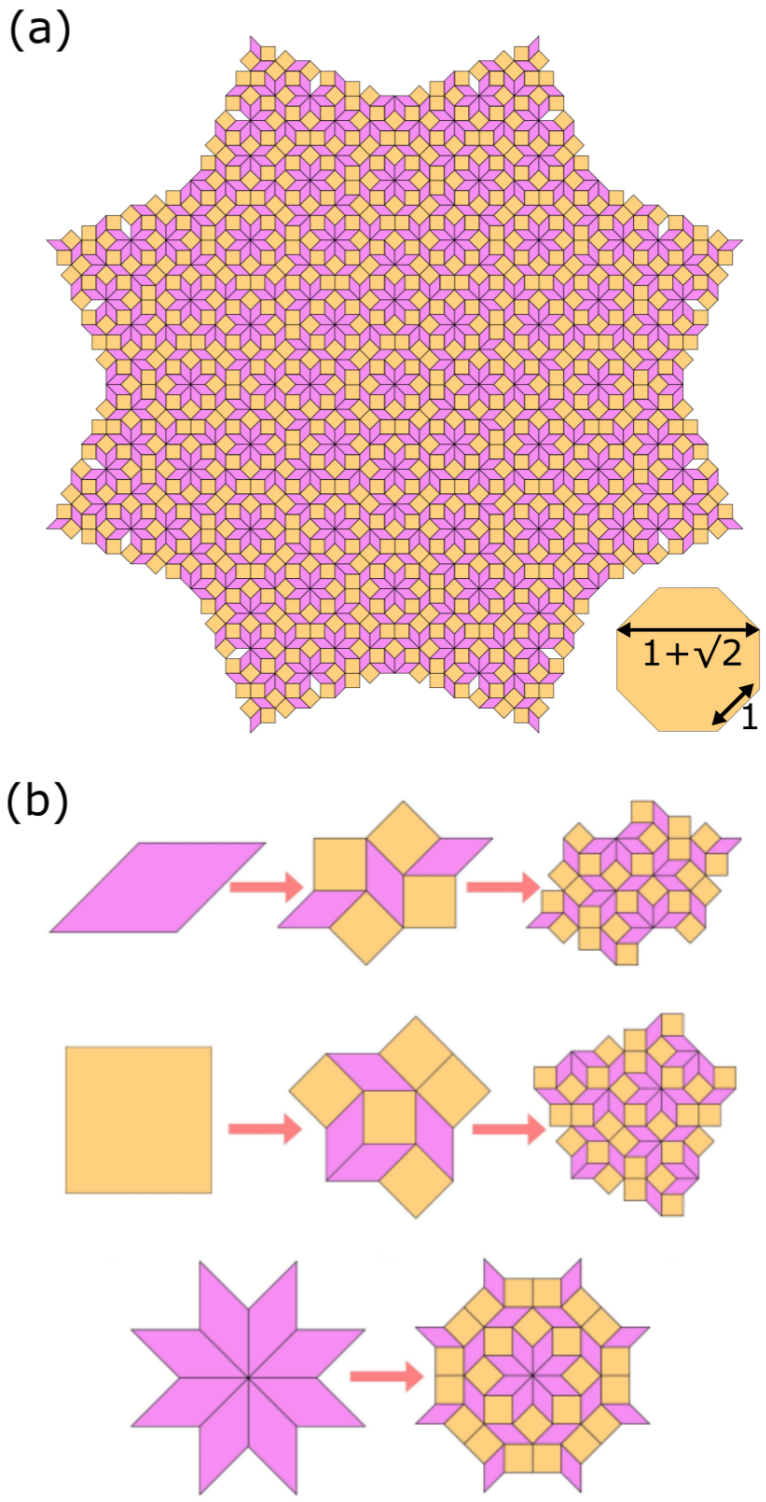

Figure 2.7: (a) A large section of the 8-fold ABT produced with substitution rules, alongside an octagonal cluster with the irrational scale factor $1 + \sqrt{2}$. (b) Substitution rules for the ABT with rhombus and square prototiles iteratively replaced to generate larger tilings. The 8-point rhombic star set as the initial tiling for producing (a) is also shown.

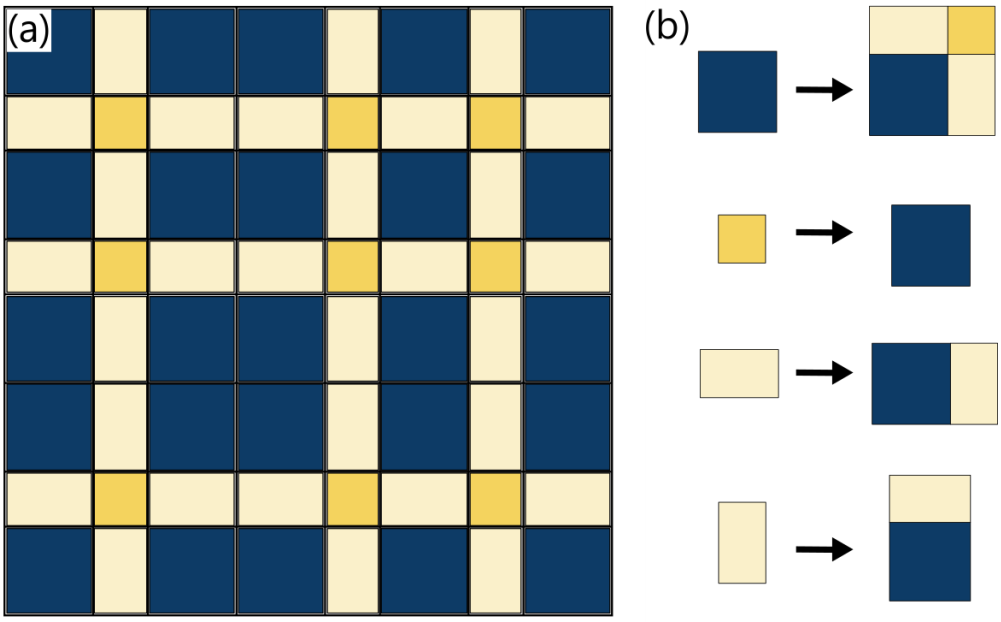

Figure 2.8: (a) A small section of the 4-fold Square Fibonacci tiling with three distinguishable prototiles: blue L x L, cream L x S (and S x L), and yellow S x S. (b) Substitution rules for each blue, cream, and yellow prototiles, for producing the Square Fibonacci tiling

tile at $\mathbf{n} = 1$ iterations leads to identical structures; if the goal is to generate indistinguishable tilings of n-fold symmetry then this method is insufficient. One way to overcome such bias would be to generate a tiling with many iterations, then zoom in and arbitrarily move a window onto the structure, producing indistinguishable tilings.

2.4.2 Generalised Dual-Grid Method

The next method for generating QP tilings is the generalised dual grid method. This method for generating QP tilings was introduced by N. de Bruijn (1981) [44] with ordinary grids superimposed, then generalised by J. Socolar and colleagues (1985) [50]. Figure 2.9(a) shows seven coloured grids superimposed to create a pattern with 7-fold rotational symmetry. The tiling is generated by placing a rhombus tile where two grid lines intersect, with characteristic angles the same as the overlapping lines. An off-centre tiling may be created by trivially shifting grids away from intersecting at the centre. The rotational order $\mathbf{g}$ of the generated tiling is increased by increasing the number of grids rotated by $\frac{360}{\mathbf{g}}\circ$. Tilings generated by this method are termed regular dual grids if no more than two lines intersect at any point, or otherwise termed singular dual grids [51]. Regular tilings result in parallelogram prototiles such as squares and rhombuses, as seen in Figure 2.9(b). Singular tilings where more than two lines intersect result in tilings which contain prototiles with more than four edges.

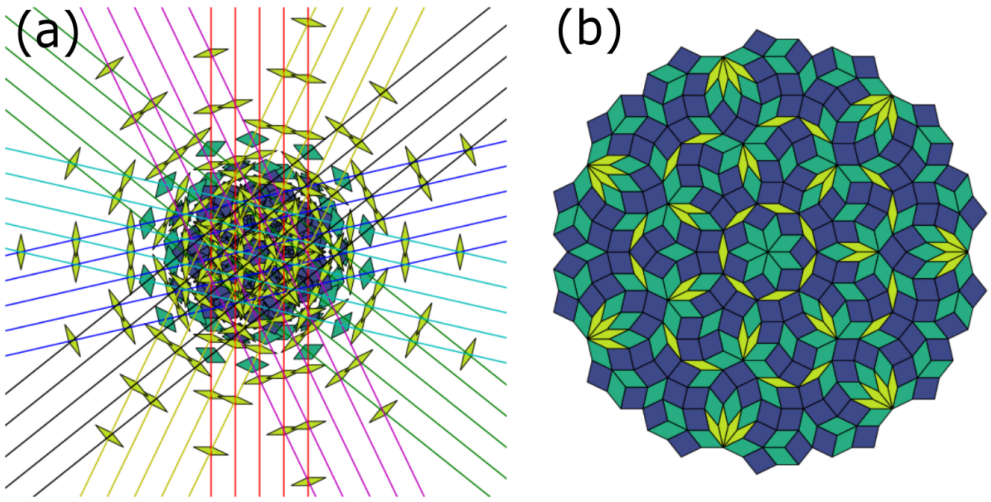

Figure 2.9: (a) Procedure for generating QC by the generalised dual-grid method with seven superimposed grids with tiles placed on two overlapping lines. (b) The constructed 7-fold tiling.

2.4.3 Cut-and-Project Method

The cut-and-project method defines a periodic lattice along a plane, which then intersects with a lower dimensional plane that is being projected to. The simplest way to demonstrate this method is by projecting a 2D periodic crystal lattice, and cutting to produce a 1D QP Fibonacci sequence, as shown in Figure 2.10. A periodic crystal with two orthogonal axis $E_\perp$ and $E_\parallel$ in complementary space are cut by a 1D section which is rotated about X by an irrational angle α. Here Δ represents an acceptance window, $\Delta = a(Cos(\alpha)+Sin(\alpha))$ with lattice constant a. In Figure 2.10(a), points within an acceptance window are projected onto $E_\parallel$, described by $L = aCos(\alpha)$ and $S = aSin(\alpha)$. A finite section of an infinite Fibonacci sequence of L and S is formed $= \ldots LSLSLSLLSLS \ldots$. In Figure 2.10(b), a similar method instead draws a Δ acceptance window parallel to $E_\perp$ at each of the periodic lattice points. Due to having a slightly different value of Δ, a different finite section of the Fibonacci sequence is formed $= \ldots LSLLSLSLLSL \ldots$. The cut-and-project method can be extended to create lattice points of a quasiperiodic tiling by projecting from a higher dimensional lattice [51].

2.5 3-Dimensional Decagonal Quasicrystals

Inter-metallic alloy quasicrystals (QC) can be divided into two families: icosahedral (i) and decagonal (d). i-QC are isotropically quasiperiodic, exhibiting quasicrystalline order in all three dimensions. In contrast, d-QC feature a structure characterised by a stacking of quasicrystalline planes perpendicular to the 10-fold axis, indicated with a green arrow in Figures 2.11(a) (labelled for Al-Ni-Co). In chapter 8, molecules of C_{60} are adsorbed atop

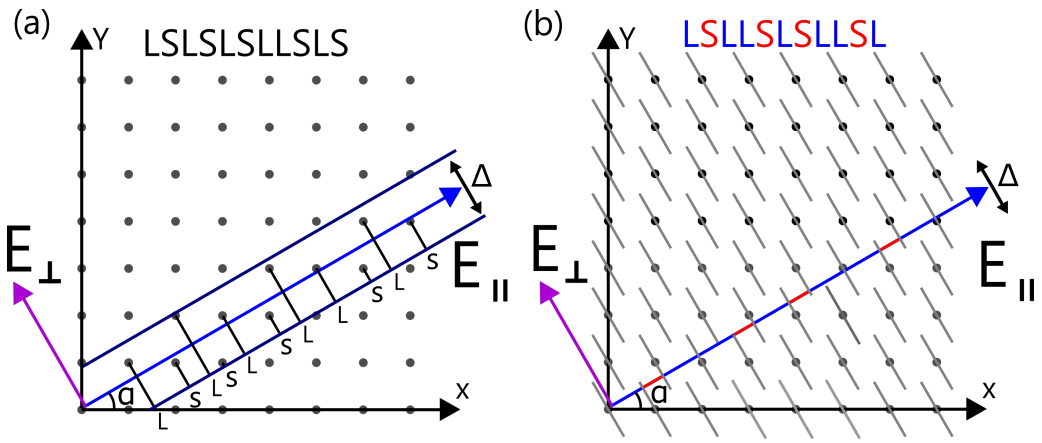

Figure 2.10: Generation of a 1-dimensional Fibonacci sequence from a 2-dimensional hypercubic lattice using (a) the strip-projection method and (b) the section method.

one of the 2-fold surfaces of the *d*-QC Al-Ni-Co. This section describes the required theory for discussing *d*-QC including the clean surface, structure, and atomic models, focusing in particular on Al-Ni-Co.

2.5.1 Structure of Decagonal Quasicrystals

Of the ≈ 100 stable QC known, Al-based alloys are the most commonly available [10, 52]. *d*-QC are interesting because their geometry forms surfaces with orthogonal periodic and QP directions, providing a unique opportunity to simultaneously investigate the influence of quasiperiodically and periodically ordered adsorption sites. The first stable *d*-QC systems discovered in 1988 were Al-Co-Cu [53, 54] and Al-Ni-Co [55], measured with electron microscopy techniques. Structure determination began as a result of growing single *d*-QC large enough for X-ray diffraction. The physical structure of the Al-Ni-Co *d*-QC is shown in Figure 2.11(a) with an electron micrograph taken by A. P. Tsai [56]. Binary and ternary alloy *d*-QC phases are known to exist, Figure 2.11(b) shows the ternary phase stability pyramid of known *d*-QC [52]. As with other QC types, Al-based *d*-QC are the majority of available systems, followed by Zn-based *d*-QC. The classification of *d*-QC is based on their periodic stacking along the 10-fold direction, quantified by n (the number of repeated two-layer atomic stacks). Stable phases exist for n = 1, 2, 3, and 4 [52].

A macroscopic view of a *d*-QC crystal is shown in Figure 2.11(c) and (d), showing 2-fold and 10-fold facets. The periodic (green arrow head) and quasiperiodic (yellow and black arrow head) directions are indicated. Orthogonal to the periodic direction, 5-fold planes are alternately rotated in-plane and stacked, creating decagonal columnar clusters with an overall 10-fold symmetry in the periodic direction. The interplanar distance along the periodic axis is 0.2 nm. The resulting 10-fold quasiperiodic facet (blue outline) is shown in Figure 2.11(c) and (d). Another result of alternating 5-fold planes are two in-

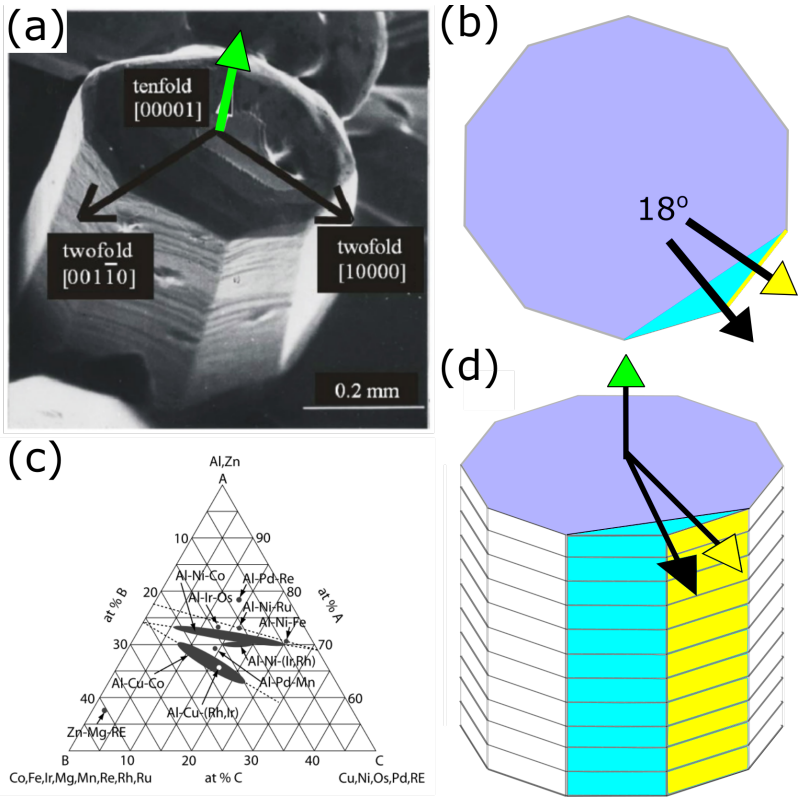

Figure 2.11: (a) An SEM micrograph of *d*-Al-Ni-Co showing a decagonal crystal, reproduced and modified from [56]. (b) Ternary phase diagram of stable *d*-QC, reproduced from [52]. (c) Major periodic (green) and quasiperiodic (yellow), (black) directions are overlaid on the decagonal surface (blue). The black arrow direction bisects the edge of two decagonal facets to form the first 2-fold facet. The yellow arrow direction produces the second facet on each face of the decagon. Therefore, there are ten equivalent 2-fold facets for each direction. (c) Shows a 2D view of the 10-fold surface, with the two corresponding 2-fold surfaces which may be produced.

equivalent 2-fold axes, indicated with yellow and cyan planes in Figure 2.11(c) and (d), which exist alternately at 18° perpendicular to the tenfold axis. The stacking of structural units in the periodic direction leads to 0.4 and 0.8 (Al-Co/Ni, Al-Co-Cu/Ni/Pd, Al-Fe-Ni), 1.2 (Al-Mn, Al-Mn-Pd), and 1.6 nm (Al-Pd/Fe, Al-Fe/Os/Mn/Mg/Ru-Pd, Al-Ni-Ru) periodicity [57]. Sample composition (rich in one species) and preparation (annealing and cooling rates) influence stabilising specific periodicities. Additionally, for metastable binary and ternary *d*-QC that are stable at higher temperatures, rapid solidification can trap the quasicrystalline phase.

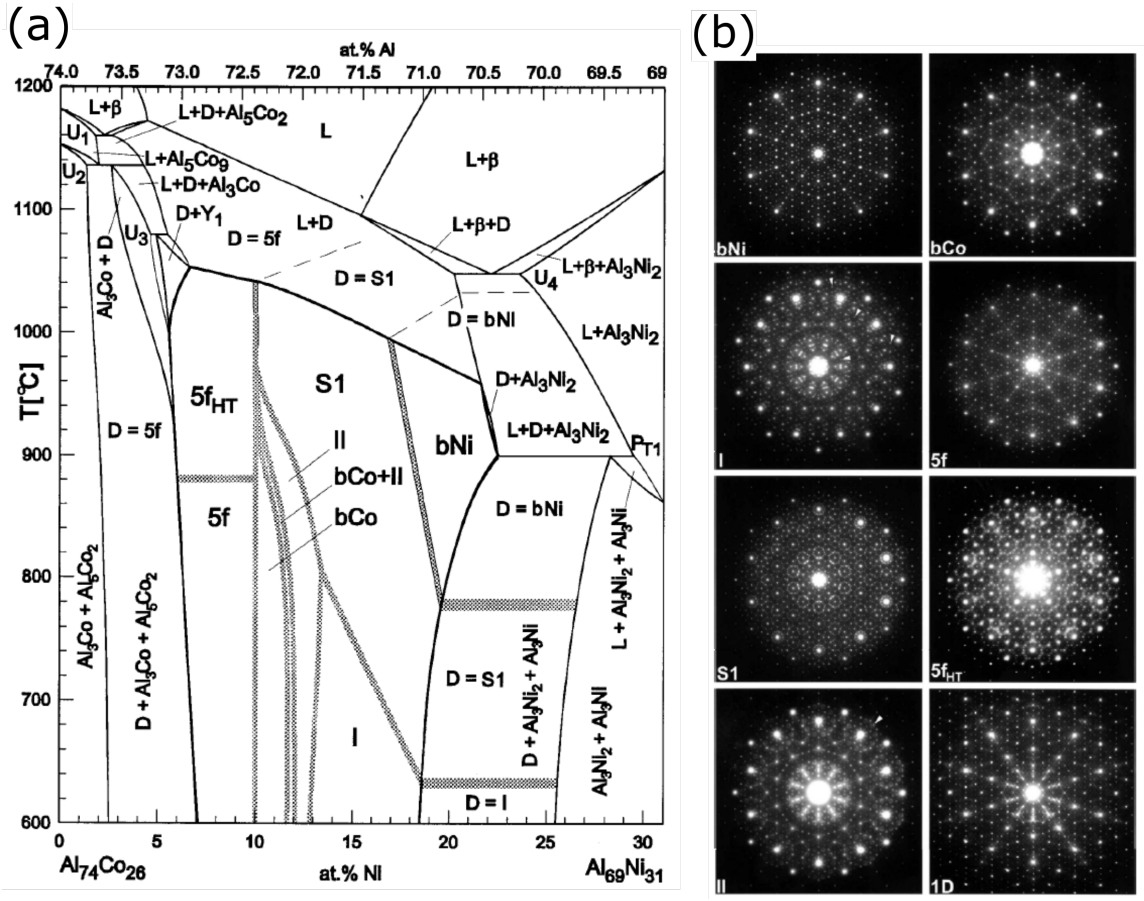

Figure 2.12: Reproduced and modified from [58]. (a) The phase diagram for *d*-Al-Ni-Co. QC phase abbreviations are given in the text, additionally D refers to decagonal phase, and L refers to liquid phase. (b) Electron diffraction patterns perpendicular to the periodic axis (10-fold surface) of different *d*-Al-Ni-Co phases.

2.5.2 Decagonal Al-Ni-Co

Phases

d-Al-Ni-Co alloys are especially interesting due to a wide composition of different quasicrystalline and approximant (periodically repeated quasi-unit cells) phases. There are at least eight quasicrystalline phases, namely: basic Ni-rich (bNi), type I superstructure (I), S1 superstructure (S1), type II superstructure (II), basic Co-rich (bCo), one dimensional quasicrystal (1D), pentagonal (5f), and pentagonal with superstructure ($5f_{HT}$) [59, 60]. Figure 2.12(a) shows the phase diagram for *d*-Al-Ni-Co, where a given phase is found by plotting a straight line between the composition of Al to Ni within the sample, as a function of temperature, or the temperature before rapid solidification quenching [58]. To experimentally determine each structure, samples were heated in a furnace under reduced Ar pressure, and measured with transmission electron microscopy and magnetothermal analysis [58]. Each quasicrystalline phase can be distinguished with slightly different tiling

decorations: pentagonal (bNi, S1, II, bCo, 1D, 5f), or rhombic (I, II, 1D, 5f$_{HT}$) [59]. As well as periodicity along the 10-fold axis, composition and thermal treatment, phases may additionally be distinguished by their superstructure reflections, ordering of atom clusters, tiling decoration, and ordering [61]. Superstructure reflections are weaker intensity compared to the main reflection, but are not indexable with integer indices with respect to the basis vectors [59]. Tiling decorations are made by connecting decagonal atom clusters separated by 0.1978 nm, which act as vertices of 5-fold Penrose tilings [61]. For example, the surface of the bNi phase is decorated ny the pentagonal Penrose tiling previously shown in Figure 2.6(a), with decagonal atom clusters at vertices. As a result of different tiling decorations the structure surfaces, and by extension electron diffraction patterns, of each phase are unique and may be categorised. Figure 2.12(b) shows the electron diffraction patterns of the eight phases discussed [58].

Indexing

As with periodic crystals, indexing involves identifying the minimum number of basis vectors required to translate between main reflections of a reciprocal lattice. For *d*-QC, five basis vectors are required, four in-plane of the 10-fold surface, and one out-of-plane to translate between stacks, as described with 2.5.1 [59]:

$$\mathbf{R_n} = \sum_{j=1}^{5} h_j \mathbf{a_j} \tag{2.5.1}$$

Here, $\mathbf{R_n}$ is the total translation vector, h_j are integer Miller indices, $\mathbf{a_j} = a(cos\frac{2\pi j}{5}, sin\frac{2\pi j}{5}, 0)$, and $\mathbf{a_5} = (0, 0, 1)$, in cartesian coordinates. Each $\mathbf{a_j}$ is shown in Figure 2.13(a), four in-plane $\mathbf{a_1} - \mathbf{a_4}$, and one out-of-plane $\mathbf{a_5}$. Five in-plane vectors are not required as the negative sum of the first four vectors can translate to the fifth vector, as shown in Figure 2.13(a). The five basis vectors are written as Miller indices in the form (h_1, h_2, h_3, h_4, h_5), and as such are used for identifying planes within *d*-QC reciprocal space, as shown in Figure 2.13(b). Given the distance to the first main reflections in Figure 2.13 is $\mathbf{a_j}$ for j = 0-4, the distance to the second main reflection is $\mathbf{a}\tau$, following irrational scaling typical of QC systems. In real space, the 10-fold (00001) plane is orthogonal to the [00001] direction, previously indicated with a green arrow head in Figure 2.11(c), where each plane is periodically stacked to produce decagonal clusters.

Atomic Structure and Surfaces

The *d*-Al-Ni-Co sample measured in Chapter 8 corresponds to the type I superstructure determined by previous experiments [62], and so in this section the model proposed by Yamamoto and colleagues is introduced, which also supports decagonal clusters separated

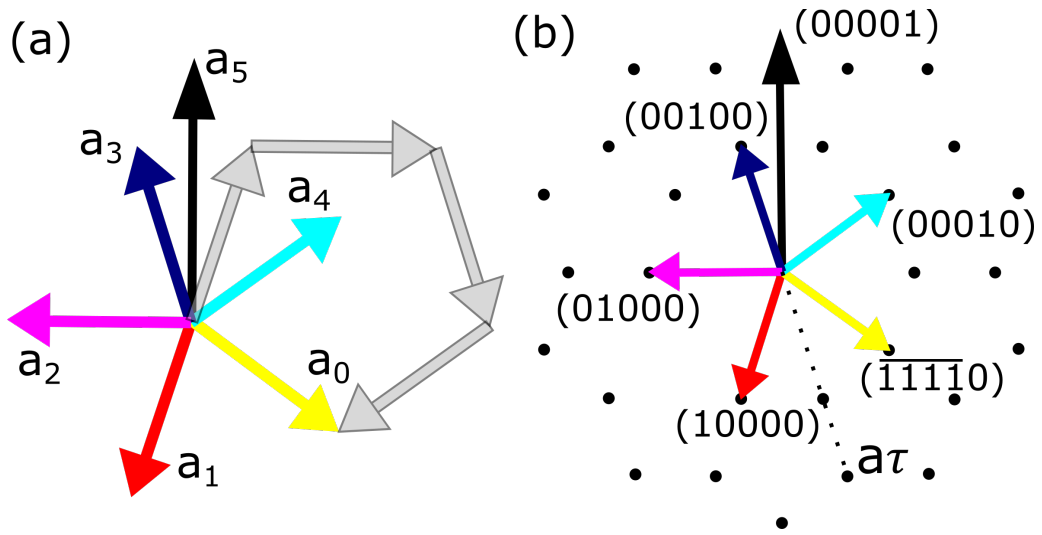

Figure 2.13: Reciprocal lattice indexing of d-QC: (a) Coloured $\mathbf{a_0}$ - $\mathbf{a_4}$ are shown in-plane, with $\mathbf{a_0}$ able to be described by the sum of the four other in-plane vectors $\mathbf{a_5}$ is shown out-of-plane. (b) Indexed first order diffraction peaks according to (h_1, h_2, h_3, h_4, h_5), with the second order $\mathbf{a}\tau$ separated main reflection indicated.

by 1.978 nm [63, 64]. Like many quasicrystals, the d-Al-Ni-Co crystal has short reciprocal lattice vectors in infinite directions, suggesting a large range of possible facet formations. However, many vectors do not exhibit densely packed atomic planes, and thus no morphologically stable surface can exist. Strong Bragg reflections helped to identify high-density atomic planes such as along the 2-fold [001$\bar{1}$0] and [10000] directions [61]. d-Al-Ni-Co therefore has three surface terminations: the 10-fold (00001), 2-fold (10000), and 2-fold (001$\bar{1}$0) surfaces.

Figure 2.14(a) shows a section of the model 10-fold d-Al-Ni-Co surface, with high density rows along the [001$\bar{1}$0] indicated with black lines. Indicated densely packed atomic planes in the model exhibit strong Bragg reflections and best support morphologically stable surface terminations [61]. 5-fold equivalence of the [001$\bar{1}$0] direction is observed in high density rows at 36° to one another as seen in Figure 2.14(a). This 5-fold equivalence of high density rows leads to ten equivalent (10000) and a different ten equivalent (001$\bar{1}$0) surfaces, rotated at 18° to one another with respect to the [00001] direction, as seen in Figure 2.11(b) and (c). In figure 2.14(a), perpendicular spacing between high density rows along [001$\bar{1}$0] are related by L = S×τ, with L = 0.75 nm and S = 0.47 nm, producing a section of a perfect Fibonacci sequence. High-density rows are determined with a similar procedure to the literature [61], identifying slices parallel to [001$\bar{1}$0] with a high concentration of atoms. Additionally, Al atoms at the centre of high-density slices also form a Fibonacci sequence of L and S, shown closer later. The yellow line corresponds to the (10000) surface outlined in yellow in Figure 2.14(b). Finally, the separation between high-symmetry decagonal cluster centres in the 10-fold (00001) plane is 1.978 nm.

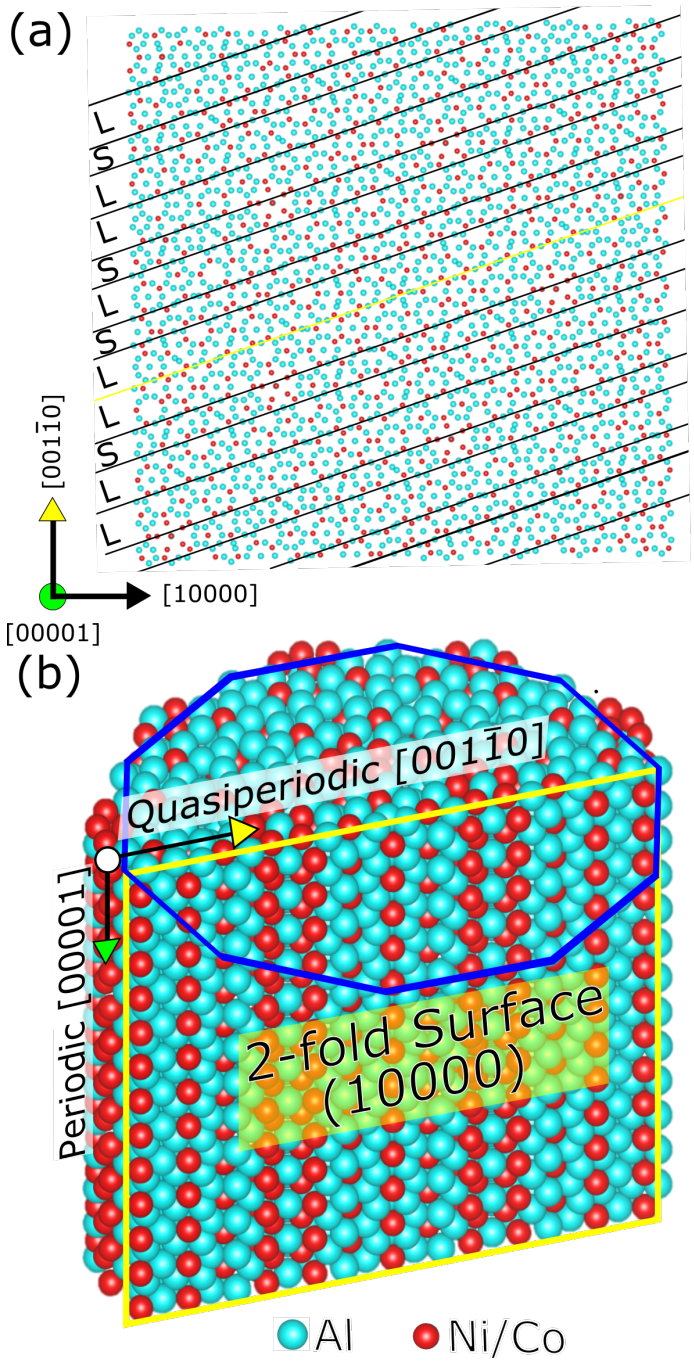

Figure 2.14: The bulk structure model of the *d*-Al-Ni-Co, with Al atoms in blue and Ni/Co atoms in red. (a) The 10-fold (00001) surface, with high density atomic rows along one set of ten equivalent [001$\bar{1}$0] rows are indicated with black lines. The 2-fold (10000) surface terminates at these high density atomic rows, separated with terrace step heights related by L and S Fibonacci segments. The yellow indicated plane indicates the corresponding surface in (b). The three major directions are shown in the bottom left. (b) The bulk truncated 10-fold (00001) (marked by a blue decagon) and 2-fold (10000) (marked by a yellow rectangle) planes. Periodic [00001] and quasiperiodic [001$\bar{1}$0] directions are indicated with arrows.

Extensive experimental work has established the structure of the 10-fold (00001) surface [65]. This surface can be prepared to high quality, as demonstrated by sensitive He atom scattering, low-energy electron diffraction, low energy ion scattering, and ion scattering spectroscopy [60, 62, 66, 67]. These scattering and diffraction techniques rely on atomically flat surfaces, and reveal patterns of closely-spaced spots consistent with the symmetry anticipated from the underlying bulk structure. Crucially, all observed diffraction spots can be indexed using the surface-projected basis vectors of the bulk material. This indicates that the surface structure corresponds to a simple termination of the bulk lattice, with no evidence of reconstruction. Scanning tunnelling microscopy (STM) has been employed to investigate the atomic structure of the surface, which has revealed flat-terrace planes with pentagonal features separated by terrace heights of 0.2 nm [62, 66–68]. Comparing STM images with atomic resolution to the atomic structure of a bulk-truncated surface indicate that the brightest topographic features predominantly correspond to Al atom sites. This observation aligns with *ab initio* calculations performed on a surface model derived from the W-Al-Ni-Co approximant phase structure [69]. Overall, results conclude that the tunnelling current is dominated by contributions from Al *s-p* electrons, thereby explaining the association of enhanced STM contrast with Al positions.

Experimental work has also established the structure of the 2-fold surfaces, whose planes have orthogonal periodic (in the [00001] direction) and quasiperiodic separations, as seen in Figure 2.14(b). As with the (00001) surface, bulk truncations of the 2-fold surfaces through the centre of high-density planes are established via He and electron diffraction [60, 66, 70]. Atomic resolution STM images support that these surfaces consist of both Al and Ni/Co atoms, separated by step-terraces with step heights of L and S segments. The (10000) surface, shown in Figure 2.14(b) has L = 0.78 ± 0.03 nm and S = 0.47 ± 0.03 nm [68,71,72]. The columns of Al atoms in the model are separated by long (L = 0.759 nm) and short (S = 0.469 nm) distances [64]. The $(001\bar{1}0)$ surface has shorter L = 0.220 ± 0.007 nm and S = 0.374 ± 0.002 nm step heights, with atomic columns separated by a Fibonacci sequence of L' = 1.48 ± 0.01 nm and L'S' = 2.24 ± 0.13 [71].

2.6 Thin Film Growth on Crystalline Surfaces

This section provides the theoretical background for thin film growth, covering surface energy and growth modes of thin films. Thin films can be braodly categorised as the layers, or islands, of atoms or molecules which adhere to and cover a surface, from sub monolayer (ML) to several overlayers thick. Chapter 3 contains a literature review of thin film growth on QC. These themes are relevant for this thesis as in Chapters 6 and 8, a metallic alloy was fabricated on a Si substrate, while in Chapter 7, C_{60} molecules were grown on a *d*-Al-Ni-Co substrate.

2.6.1 Surface Energy and Stress

A surface may be described in terms of its morphology or structure. Morphology denotes the macroscopic shape of solids, while structure refers to the precise spatial arrangement of atoms (microscopic). The observed morphology depends on the property studied and the resolution of the characterisation technique. Atomic structure often significantly influences or determines macroscopic morphology; for instance, interatomic forces dictate whether metal deposition on a semiconductor proceeds layer-by-layer or via island formation. Hence, understanding interfaces requires consideration of both morphology and structure from macroscopic and atomistic perspectives. Next, thermodynamics helps us understand surface and interface formation in solids. The surface free energy of a crystal is associated surface stress, which relates to the equilibrium macroscopic shape of the surface. Upon surface creation, the electronic charge distribution near the interface adjusts to the absence of adjacent atoms, altering chemical bonding details compared to the bulk. Consequently, forces on atoms within the topmost layers differ from those in the bulk. The surface stress is induced by a change in the force per unit length relative to the bulk. Equation 2.6.1 describes how surface stress τ_s changes as a function of the spatial variation of stress along the z axis $\tau(z)$, and the bulk stress $\tau(bulk)$. A positive surface stress ($\tau_s > 0$) causes contraction as work required to stretch the surface elastically (tensile stress). In contrast, a negative surface stress ($\tau_s < 0$) is compressive.

$$\tau_s = \int_{-\infty}^{\infty} \tau(z) - \tau(bulk)\, dz \tag{2.6.1}$$

2.6.2 Structural Models of Solid Interfaces

Surface creation breaks interatomic bonds, reducing coordination of surface atoms versus bulk. This yields surface free energy requiring minimisation for stability. The terrace-step-kink model [73,74] shown in Figure 2.15(a), treats atoms as cubes in a simple cubic lattice, where face-sharing atoms form single bonds [75]. A surface atom's energy depends on its bond count, while atomic transition energies derive from bonds broken/formed between initial and final states. Energy minimisation maximises bonds formed. Though simplified, this model correctly predicts experimentally observed surface sites and defects [76, 77].

Thin film growth is primarily determined by the sticking coefficient **s**, the ratio of adsorbate atoms which stick to the surface as a fraction of the total number of atoms. The coefficient is a function of the available adsorption sites, the bonding strength between the adsorbate and surface, and the rate of diffusion between the surface and bulk [78]. There are three thin film growth modes, as shown in Figure 2.15(b) [77], which can be generally separated based on whether they are dominated by layer-by-layer, island growth, or a mixture of the two. Firstly, Frank van der Merwe, or layer-by-layer growth, is where

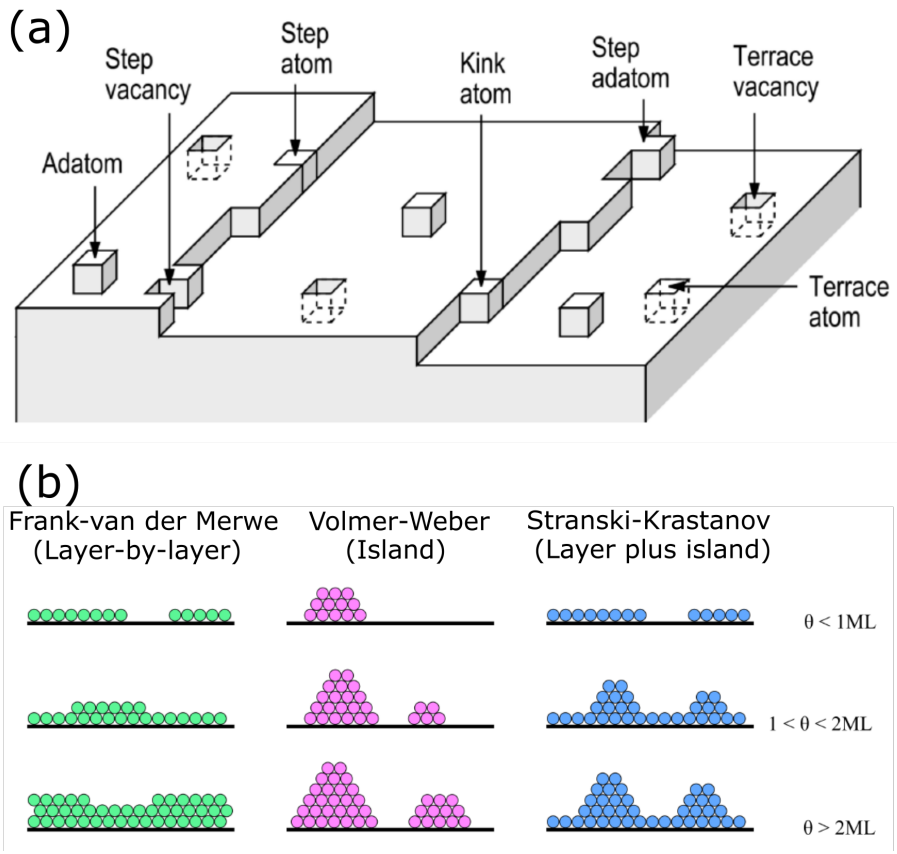

Figure 2.15: (a) The terrace-step-kink model [73,74], with labelled adatoms and vacancies. Repoduced from [75]. (b) Thin film growth modes, which depend on adsorbant - substrate interactions. Reproduced and modified from [75,77].

each new adsorbed atom grows successively until a layer is filled. This is because adsorbed atoms are more attracted to the surface than they are to other adsorbed atoms. Next Volmer-Weber, or island growth, occurs when atoms are attracted to other adsorbed atoms adsorbed on the substrate, forming island clusters on the surface. Island formation may be caused by an increase in strain, such as when the adsorbate is incommensurate with the surface [76,77]. Finally, Stranski-Krastanov, or layer plus island growth, occurs when atoms are initially strongly attracted to the substrate in forming the first monolayer, but subsequently are more attracted to other adsorbed atoms rather than the surface. The result is monolayer coverage with island growth [75,78]. These growth modes are typical for crystalline surfaces, special cases for growth on QC surfaces including rotational epitaxy, quasiperiodic modulation, and templated growth, will be discussed in the literature review in section 3.4.

Chapter 3

Literature Review

This chapter contains literature reviews which provide the necessary background reading for Chapters 5-8 of this thesis. These reviews cover several research topics across fields of, artificial spin-ice, nanolithography, the 8-fold Ammann-Beenker tiling, and thin film deposition on quasicrystalline substrates.

3.1 Artificial Spin Ice

An artificial spin-ice (ASI) is an engineered system built of interacting single-domain nanomagnets arranged on a lattice. This section aims to review the evolution of anneal protocols for bringing an ASI from an excited as-grown state, to a minimised energy state, or ground state. This will include the chosen structure, main results, and technical theory where needed. The first section covers periodic systems and their derivatives, which is the main bulk of the literature, and the second section will explore QP ASI results. Review papers of ASI already exist which cover results beyond the scope of this thesis - for our review of ASI, reviews by Heyderman [27] and Nisoli [26] for work up to 2013, and Skjærvø for later ASI work [79] will be referred to.

3.1.1 Periodic Artificial Spin Ice

Simple (periodic) ASI systems have been well-investigated in the literature, including Square [29, 80–91] and Kagome systems [29, 82, 85, 86, 92, 93]. In this section, a summary of the early works is shown in table 3.1.

AC Demagnetisation

Wang (group led by Schiffer and Crespi) [80] introduced the first experimental realisation of an artificial spin ice system in 2006, a landmark achievement in the study of geometric frustration. A two-dimensional lattice of single-domain ferromagnetic permalloy islands

was fabricated using electron-beam lithography. These elongated islands ($80 \times 220 \times 25$ nm^3) were arranged in a square lattice with alternating vertical and horizontal orientations, as shown in Figure 3.1(a) (expanding field-of-view provided by Nisoli [81]). Islands are ellipsoidal, with a long 'easy' axis of spins that ferromagnetically align into mesoscopic domains. Island width is kept narrow to avoid multi-domain effects. By varying the lattice spacing (320-880 nm), the team tuned the strength of dipolar interactions between islands, enabling systematic exploration of frustration effects. Magnetic force microscopy (MFM) and atomic force microscopy (AFM) were employed to directly visualise the magnetic moments of individual islands, confirming their single-domain behaviour. Single-domain moments are observed with MFM due to their dense flux concentration at tips of islands, which either attract or repel the potential from a magnetised tip. The shape anisotropy of the islands forced moments to align along their long axes, effectively creating an Ising-like system. To prepare low-energy configurations, the samples were subjected to a demagnetisation protocol involving rotation in a descending magnetic field with alternating polarity. For small lattice spacings (320 nm), where dipolar interactions were strongest, over 70% of lattice vertices exhibited the 'two-in/two-out' spin configuration characteristic of ice rules. This fraction decreased monotonically with increasing lattice spacing, approaching the 37.5% expected for random configurations at larger spacings (880 nm), where interactions became negligible. The authors separated vertices by their frustration, with least frustrated (alternating in-out) labelled Type I, up to the most frustrated (all-out or all-in) labelled Type IV. A short-range correlation model dominated the system, particularly between nearest-neighbor (NN) and transverse (T) island pairs, while long-range order was conspicuously absent, described as a hallmark of frustrated systems [17, 95, 96]. This behaviour is attributed to the near-degeneracy of low-energy states, allowing seamless domain

Author	Year	H (ΔH) (Oe)	Dwell (s)	Ramp (Oe/s)
Wang [80]	2006	1300		
Wang [83]	2007	1300 (16.3)	1	24 000
Nisoli [81]	2007	1300 (16.3)	1	24 000
Ke [84]	2008	1280 (1.6)	5	11 200
Mengotti [93]	2008	850 (5 mTs^{-1})	Continuous	
Nisoli [82]	2010	2000 (1.6)	5	11 200
Li [85]	2010	1280 (1.6)	5	11 200
Lammert [90]	2010	1280 (1.6)	5	11 200
Rougemaille [92]	2011	Sinusoidal (0.11)	1	
Budrikis [94]	2012	2000 (22)		

Table 3.1: A list of early work investigating ASI, which all focused on AC-demagnetisation as anneal protocol. Technical details are discussed in the text.

boundaries between ice-rule-compliant regions (vertex types I and II) without introducing high-energy defects. The tunability of interactions via lattice spacing and the ability to engineer frustration through lithography opened new avenues for studying exotic magnetic states. Potential technological applications are high-density magnetic storage, where near-degenerate states might suppress unwanted magnetisation reversals. This seminal paper established artificial spin ice as a versatile platform for probing frustration physics, combining design flexibility with experimental accessibility.

Wang then addressed their demagnetisation protocols with a study emphasizing the critical role of field alternation [83]. Protocol 1 involved stepping the field down in magnitude while alternating its polarity, achieving minimal remanent magnetisation $m_{tot} \approx 0.05 - 0.15$ (1 is fully magnetised). The protocol is shown in Figure 3.1(b) [84]. Protocol 1 far outperformed linear (protocol 2) or non-alternating stepwise (protocol 3) protocols, which left significant residual magnetisation $m_{tot} = 0.5$. The efficacy of protocol 1 arises from nonmonotonic field variations near the coercive field ($H_c \approx 770$ Oe), which disrupt collective alignment while avoiding history dependence (49% of islands retain orientation across cycles). MFM imaging and Fourier analysis confirmed that protocol 1 minimises m_{tot}, as seen in weak central peaks in Fourier transforms. The results further show how varying lattice spacing varies the interaction strength: arrays with smaller spacings (320 nm) exhibit stronger dipolar coupling, enhancing frustration and reducing m_{tot}, while larger spacings (880 nm) approach independent dipole behaviour. The study demonstrated the necessity of alternating polarity to mitigate coherent interactions and access low-energy disordered states.

Next, Nisoli [81] investigated the disordered states of square ASI generated via rotational demagnetisation. While the system's unique antiferromagnetic ground state was never reached, the demagnetisation protocol of alternating the magnetic field's polarity while reducing its magnitude produced a static, disordered configuration with extensive degeneracy. A 'vertex-gas' model was used to analyze the populations of the four vertex types (I-IV). A vertex-gas model approximates the system as a gas of independent vertices, instead of modeling the full spin system (including long-range interactions). Experimental data revealed that for small lattice spacings (320 nm), the specific vertex energy was minimised. At larger spacings (> 600 nm), where dipolar interactions weaken, vertex populations approach random distributions. Key to this behaviour is the system's athermal nature: energy barriers from shape anisotropy suppress thermal fluctuations, yet the demagnetisation process mimics thermodynamic equilibration. By maximising an effective entropy derived from defect multiplicity, the model predicted vertex populations with no free parameters, matching experimental results. Multiplicity is the number of microstates corresponding to a particular macrostate [97]. The effective degeneracy mirrors natural spin ice, suggesting that frustration-induced near-degeneracy, rather than thermal disorder,

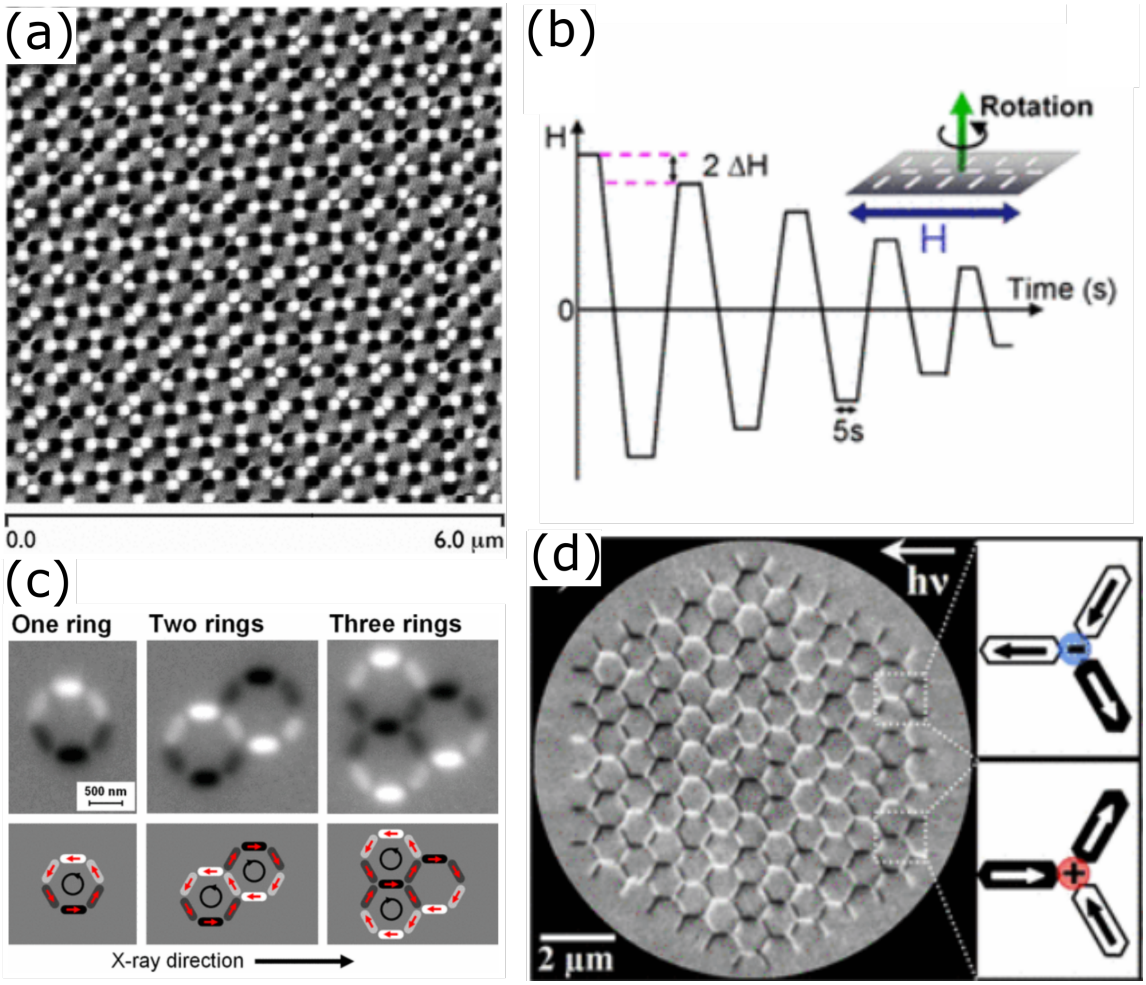

Figure 3.1: (a) An MFM image of the square ASI, with north (white) and south (black) representing out-of-plane field contrast. Reproduced and modified from [81]. (b) A schematic of an AC demagnetisation protocol. Reproduced and modified from [84]. (c) XMCD-PEEM contrast images of increasingly complex rings of the Kagome ASI, from one ring to three rings. Reproduced and modified from [93]. (d) (left) XMCD-PEEM image of a Kagome ASI, with X-ray vector hv indicated. (right) The associated geometrically frustration 'monopole' excitations at each vertex type. Reproduced and modified from [92].

led to the system's disordered state.

Building on AC demagnetisation protocols, Ke [84] explored how the step size ΔH influenced the energy landscape of square ASI. For $\Delta < 12.8$ Oe (near inter-island field strength), net magnetisation tends $m_{tot} \to 0$, but as energy continues to decrease with finer ΔH, it never reaches the ground state. Short-range correlation (diagonal and transverse) pairs strengthen with smaller ΔH, while longitudinal pairs exhibit competing interactions due to frustration. Monte Carlo simulations revealed that the disordered state can be described by a maximum-entropy ensemble constrained solely by nearest-neighbor correlations, despite the absence of thermal anneal protocol. The results found that AC

demagnetisation traps the system in a manifold of near-degenerate states, characteristic of frustrated systems, rather than driving it toward the global energy minimum.

Around the same time, Mengotti [93] fabricated a Kagome ASI system, as shown in Figure 3.1(c), inspired by previous theoretical work on Kagome systems [98–100]. Note Kagome ASI are typically constructed by placing moments on the vertices, giving it a hexagonal appearance, unless otherwise stated. Mengotti studied one-, two-, and three-ring basic building blocks of hexagonal arrays with X-Ray Magnetic Dichroism (XMCD), and dipolar energy calculations, to characterise their magnetic configurations. For single-ring structures, demagnetisation protocols efficiently populate the vortex ground state (94%), as the system lacks intrinsic frustration. However, introducing additional rings increases frustration at three-island vertices, reducing the probability of accessing low-energy states: two- and three-ring structures achieve their respective ground state (double-vortex or flux-closure configurations) with only 48% and 31% efficiency. Extrapolating these results, the ground state becomes inaccessible in infinite Kagome systems. Notably, all vertices obey the 'two-in/one-out' or 'one-in/two-out' ice rule, even at weak dipolar coupling. At low coupling strengths, the final magnetic configurations are biased by the applied field direction, favouring states aligned with the last field orientation before freezing. Rougemaille [92] also focused on the Kagome system with XMCD, as shown in Figure 3.1(d), stating the necessity of dipolar spin ice (DSI) models over short-range spin ice models. A short-range spin ice model assumes ice rules, in essence a '2-in 1-out' vertex, and considers only nearest neighbour interactions, predicting a macroscopically degenerate ground state (many equivalent low-energy configurations) due to frustration. This method however ignores any longer-range magnetostatic interactions. The DSI model instead computes a Hamiltonian with Monte Carlo simulations, which accounts for long-range dipolar interactions between nanomagnets, and lifts the ground-state degeneracy by introducing subtle energy differences between configurations.

Despite evidence for AC demagnetisation protocols never being able to access a systems ground state, further work was done to improve the method, and with new geometries. Firstly, Nisoli [82], introduced effective temperature to describe the statistical properties of square and hexagonal ASI. By alternating field polarity while reducing step size ΔH, the system's vertex populations followed a distribution close to thermal equilibrium. Square vertex types I-IV followed a vertex-gas model, where the effective temperature scales with ΔH. For the hexagonal lattice, ground-state compliance (type-I vertices) dominated at small ΔH, with the effective temperature similarly controlled by the protocol. The work showed that despite being athermal, ASI exhibited thermodynamic-like behaviour, with effective temperature serving as a control parameter for disorder. Li [85] compared square, brickwork (symmetry-broken hexagonal), and hexagonal lattices, focusing on the role of local symmetry in frustration accommodation. The hexagonal lattice achieved the low-

est energy states, determining that the local symmetry of interactions in these frustrated magnets is more important than the topology of the interacting moments in determining how the system accommodates frustration. Smaller ΔH demagnetisation and reducing lattice spacing improves correlations, but the square and brickwork lattices remain kinetically jammed, unlike hexagonal lattices. Lammert [90] calculated entropy densities and applied them to ASI , showing that nearest-neighbour correlations drive longer-range ones. Finally, simulation and experimental work by Budrikis [88,89,94] investigated the competition between frustration, disorder, and field protocols in square ASI. Field-driven quenched disorder disrupts ideal ordering pathways but enables equilibration when combined with randomised field sequences. Also, vertex-based models and network analysis demonstrate the importance of edge effects and long-range interactions. While field protocols alone struggle to achieve ground state order, controlled disorder, whether intrinsic (fabrication variations) or extrinsic (randomised fields), facilitates exploration of low-energy states. Overall, AC demagnetisation is not a perfect tool for accessing the true ground state of ASI. While it is highly effective for reducing residual magnetisation and probing low-energy states, several limitations prevent it from reliably reaching the ground state, as evidenced by the studies discussed.

Thermal Annealing

In this section a second method is introduced for minimising m_{tot} and achieving a long-range ordered ground state, by thermally annealing (heating) arrays [101]. Morgan [102] in 2011 experimentally realised thermal annealing during thin-film deposition. They observed a near-ground-state configuration in the as-fabricated sample using MFM. Figure 3.2(a) shows a schematic of the ground state ordering with chiral flux closure loops (left), and ordering superimposed on an MFM image (right). Ordering was attributed to thermalisation effects during the early stages of material growth, when the magnetic layer is ultrathin (≈ 1 nm). At this stage, the Néel-Arrhenius law [103,104] (explained next) allows moments to explore low-energy states via thermal fluctuations, followed by kinetic freezing as the film thickens. Residual defects in the ordered lattice, identified as monopole- and string-like excitations, exhibit a Boltzmann-distributed abundance, consistent with equilibration at an effective temperature during deposition. The defect energetics and spatial distribution further suggest monopole interactions during thermalisation, favouring closed-loop excitations over extended strings. This work demonstrated that controlled fabrication conditions can intrinsically anneal artificial spin ice, bypassing post-growth field protocols and providing insights into the role of thermodynamics in nanomagnetic self-organisation.

The Néel-Arrhenius law describes the thermal reversal rate of magnetic moments in single-domain nanoparticles, given by $f = f_0 exp(\frac{-\Delta K_u V}{k_B T})$, where f_0 is the attempt frequency prefactor ($\tau = \frac{1}{f_0}$), f is the reversal rate, K_u is the uniaxial anisotropy energy

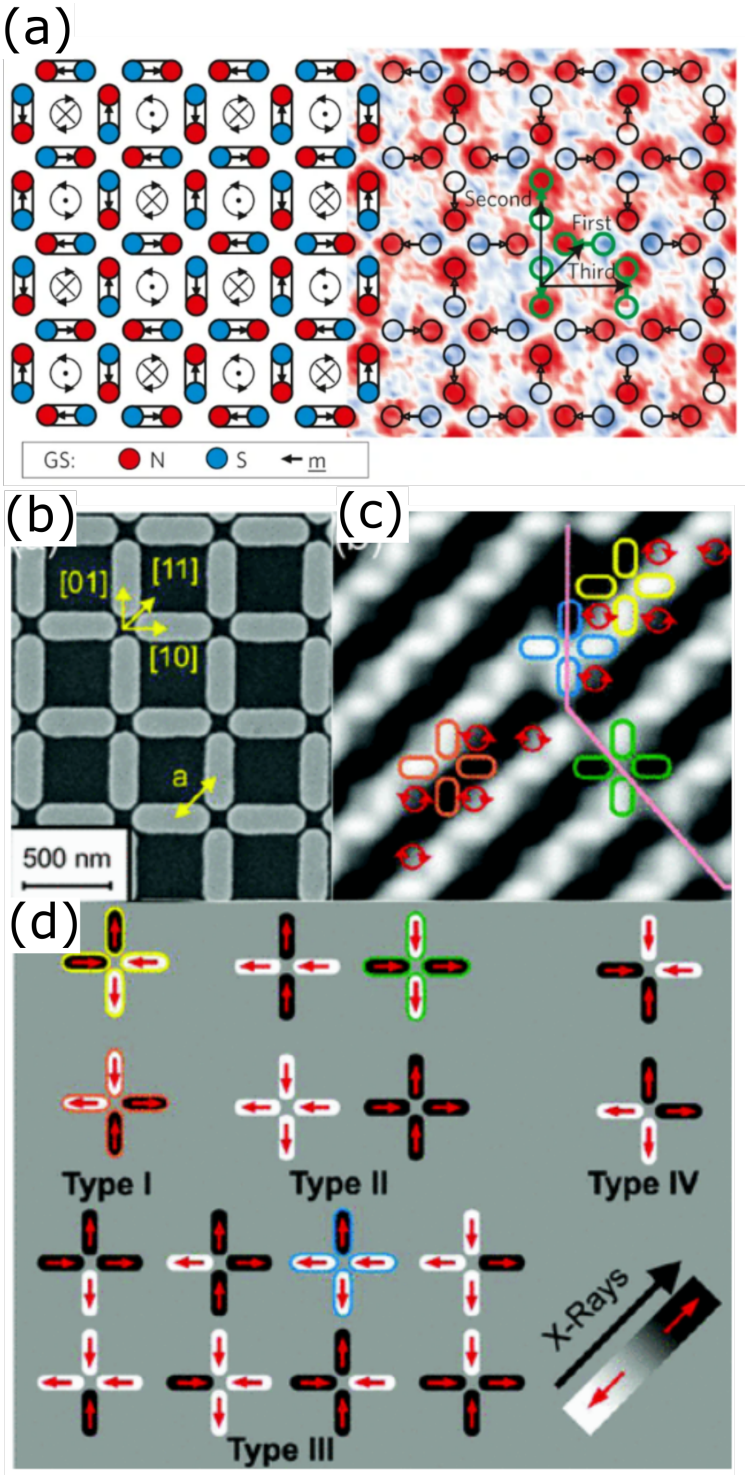

Figure 3.2: (a) (left) The model ground state ordering with chirally alternating flux closure loops. (Right) The model is superimposed on an MFM image. North (red) and south (blue) poles represent out-of-plane field contrast. Reproduced from [102]. (b) SEM of a square ASI, with labelled vector indices [xy], and lattice constant a. (c) An XMCD-PEEM image of an annealed array of the square ASI, exhibiting predominantly type I ground state vertices. (d) Each vertex type I - IV is shown with the expected magnetic contrast, alongside the x-ray vector. Reproduced and modified from [87].

density, and volume V [103–105]. The prefactor is determined by intrinsic material parameters such as K_u and damping [106]. The Néel-Arrhenius law follows that to approach zero remanence (thermal equilibrium) a sufficient number of magnetic moments must be reversed by thermal activation over the energy barrier K_uV [107, 108]. The energy barrier for reversal in permalloy ASI will also be referred to interchangeably in the literature as K_uV and KV. K_u is strictly the energy density required to rotate the magnetisation of a material away from its easy axis, whereas K is a general term for total anisotropy energy density. In ASI, as shape anisotropy dominates, $K_u \approx K$.

Thermal annealing protocols popularly overtook AC demagnetisation protocols due to the system's ability to more readily access near-ground-state configurations [29, 86, 87, 102, 109–111]. Farhan [87, 110] investigated thermally active square and kagome ASI, which relax from high energy to low energy states close to room temperature. This is possible by reducing the energy barrier K_uV to promote switching into an equilibrium state, by either selecting a material with a lower K_u than permalloy, or reducing V in terms of the thickness of nanoislands. Note that there are two temperature thresholds of interest in ferromagnetic thin films: the Blocking Temperature (T_B), and the Curie Temperature (T_C - discussed later). The T_B is the threshold where ASI 'melt', undergoing a transition from a ferromagnetic to superparamagnetic regime [109]. Superparamagnetism is a phenomenom where ferromagnetic domains flip with a time-averaged magnetisation of zero, leading to paramagnetic appearance. The superparamagnetism regime in ASI is where, although individual moments may flip artbitrarily, over time, dipolar and magnetostatic interactions with reduced local energy barriers create an energy equilibrium landscape, which favours flips that contribute to collective ground state configurations. The T_B for transition into the superparamagnetic regime within a timeframe t_m is given by $T_B = \frac{KV}{k_B ln(t_m/t_0)}$. Morgan demonstrated that during the initial stage of growth the thickness, and therefore volume of the nanoislands, was small enough such that the shape anisotropy energy barrier KV was comparable to the thermal energy $E_{th} = k_BT$ at the deposition temperature, allowing favoured flipping [102, 109].

Farhan also investigated lowering V using a wedge sample with ASI thickness ranging from 3 to 20 nm, measuring the magnetic state with XMCD-PEEM, and compared with Monte Carlo simulations of a simplified dipolar Hamiltonian [87]. An array of type II vertices was created after application of a saturating magnetic field (35 mT) along the negative [11] direction, and image acquisition was begun immediately after the magnetic field was switched off. The square ASI structure is shown in Figure 3.2(b), XMCD-PEEM image in Figure 3.2(c), and assigned vertex types I - IV arranged energetically in Figure 3.2(d). The system transitioned from an energetically excited state (saturated type II vertex configuration) to the ground state (type I vertices) through two distinct regimes: a string regime and a domain regime. In the string regime, thermal fluctuations nucleate

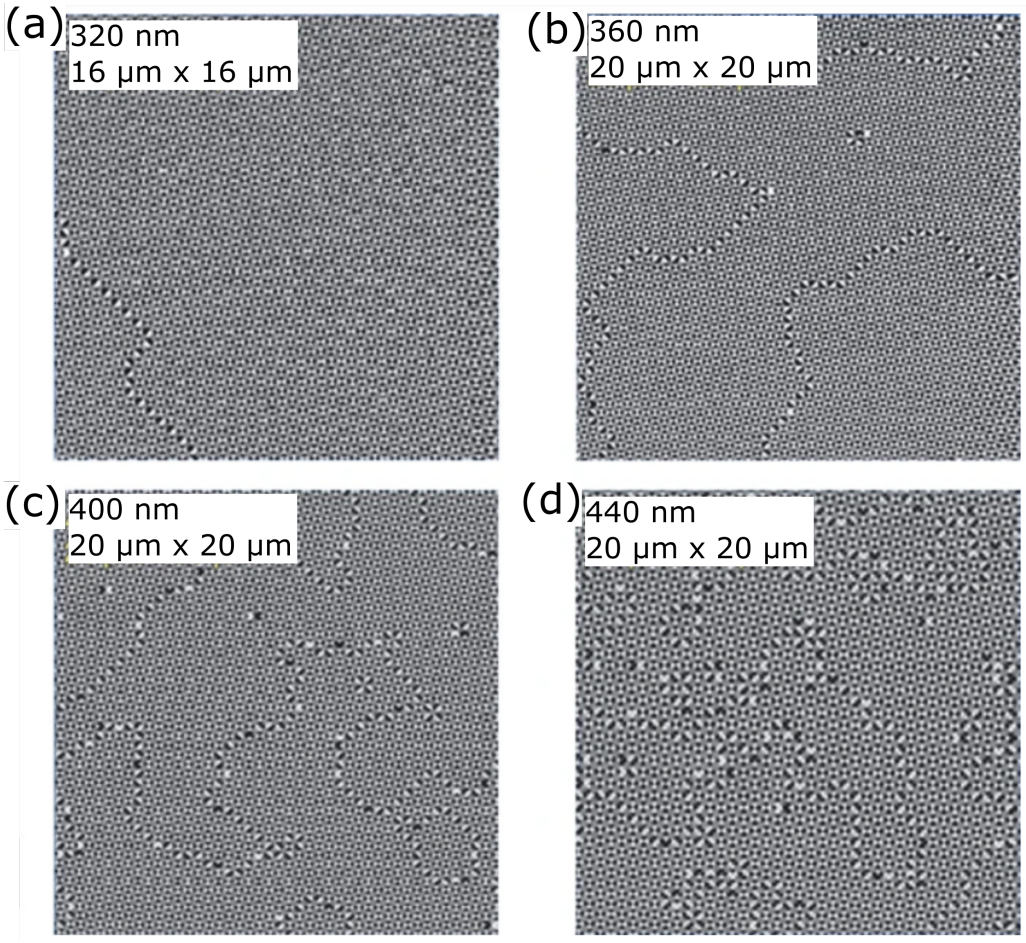

Figure 3.3: MFM images of a square ASI with varying inter-nanoisland tip separation, which influenced domain-wall propagation of excited vertices and ground state formation. Inter-nanoisland separations are: (a) 320 nm, (b) 360, (c) 400 nm, (d) 440 nm. Reproduced and modified from [29].

pairs of type III vertex excitations. These excitations propagate apart, creating chains of energetically favorable type I vertices between them. The separation is driven by a linear decrease in energy as the distance between the type III pair increases, effectively lowering the system's energy. In the domain regime, As chains merge, distinct domains of type I vertices form, separated by boundaries composed of type II and residual type III vertices. These boundaries act as domain walls, which evolve as type III vertices migrate along them, enabling larger domains to expand at the expense of smaller ones. This coarsening continues until the system reaches a uniform ground state dominated by type I vertices. Thermal fluctuations in a Kagome system were also observed with the same method, revealing frustration-induced degeneracy which governed transitions between low-energy states [110].

Once a thermal anneal was realised during deposition and thermally active moments were observed, a third approach was to grow thicker nanoislands (that produce a better

magnetic signal), anneal through the T_C, then slowly cool back to room temperature for measuring [29, 30, 101]. Annealing provides moments with thermal energy through joule heating; when thermal energy is applied to moments ordered in ferromagnetic domains, the competition between interatomic exchange interactions and thermal fluctuations causes net magnetisation to disappear at a well-defined threshold temperature, the T_C [112]. One method of determining T_C is with magnetometry (VSM-SQUID), by measuring the total magnetic moment (emu) of a continuous thin film, and varying temperature until a base emu of non-ferromagnetic behaviour is reached on an emu vs T graph. Normalising with respect to the volume in cm gives the magnetisation (emu cm^{-3}), and the magnetic saturation M_S with an applied saturating field. Once the T_C is reached, nanoislands no longer contain ferromagnetic domains and atomic moments behave paramagnetically. Upon slow cooling (to avoid quenching) back through T_C, nanoisland moments rearrange into energetically favoured ferromagnetic domains via Heisenberg exchange interactions. On the micron scale, nearest neighbour nanoisland interactions simultaneously arrange themselves into a low energy state via magnetostatic and dipolar interactions. Zhang [29] used magnetometry to find the T_C of a 25 nm thick permalloy film to be $\approx$ 542 °C, close to the bulk value of 580 °C. Following the annealing procedure, only a handful of moments located on isolated domain walls were not in the ground state, indicating the thermal anneal procedure to be even more effective than in thermally active arrays. Figure 3.3(a)-(d) shows MFM images which dislay how varying the distance between the tips of nearest nanoislands influences ground state and domain wall formations of excited vertices. Gilbert [30, 31] investigated the shakti and tetris lattices with the same anneal method, observing a ground state which followed a model of ground state vertices and forced excited vertex defects. Later, Farhan [28] applied a similar heating protocol but instead annealing through the T_B, investigating topological height defect offsets between islands, finding evidence that defects act as a plasma of Coulomb-type magnetic charge. Finally, Saccone [113] grew 2.7 nm thick permalloy nanoislands arranged collinearly, with an estimated T_B of 190-240 K, and annealed the samples up to 350 K. Trends towards short-range order as randomness increased was evidenced, but did not show typical spin-ice behaviour. Random behaviour can be explained by the T_B being so low that the KV barrier to random flips for moments was too accessible, with too much energy for the system to reach equilibrium.

The final approach employed for thermal anneal protocols is to use a different material than permalloy, to reduce the anisotropic energy density contribution term, and therefore the energy barrier to switching, in the Néel-Arrhenius equation. Porro [109] grew doped $Ni_{87}Fe_{13}$, reducing T_C by 100 K compared to permalloy. Kapaklis [86] grew δ-doped Pd(Fe) (40 nm Pd, 1.4 monolayer (ML) Fe, 2 nm Pd), finding the energy landscape can be altered through design of lattice geometry and island material, defining thermal behaviour.

Finally, Drisko [111] grew $FePd_3$, finding smaller lattice constants produce larger domains of ground state charge order.

In conclusion, the study of ASI has evolved from foundational explorations of square and kagome lattices to sophisticated investigations of frustration, degeneracy, and thermalisation. Early work by Wang [80,83] established ASI as a tunable platform for probing geometric frustration, demonstrating how demagnetisation protocols and lattice spacing govern residual magnetisation and vertex populations. Subsequent studies revealed the limitations of field-driven methods in accessing true ground state [81,82,84,85,90,92,93,103], prompting a shift toward thermal annealing [101]. By considering the Néel-Arrhenius law, researchers achieved near-ground-state configurations through controlled material growth [102], thickness modulation [87, 110, 113], annealing and cooling through the T_C or T_B [28–31], and tuning material growth to lower T_C [86, 109, 111]. These advances demonstated the exchange between local symmetry, long-range interactions, and effective anneal protocols in ASI. Collectively, these efforts highlight ASI's potential as a playground for frustrated magnetism, and potential applications of novel magnetic technologies, from reconfigurable logic devices to high-density storage systems. Future work will likely focus on integrating dynamic protocols, advanced materials, and unexplored geometries to unlock unprecedented control over spin textures and emergent phenomena.

3.1.2 Quasiperiodic Artificial Spin Ice

The overwhelming amount of ASI work in the literature has focused on simple periodic systems and their derivatives. Shi [114] fabricated an ASI of the 5-fold Penrose tiling, measuring spin states with MFM and supporting this with micromagnetic and Hamiltonian simulations. This is the only work in the literature which decorated separated nanoislands on the edges of a QP tiling to create an ASI, and was the main motivation for work undertaken in this thesis in Chapter 6.

Figure 3.4(a) shows the Penrose tiling design (bottom), with calculated ground state and 1st excited states for each of the seven vertex types of the tiling (top). Micromagnetic simulations were conducted with the object oriented micromagnetic framework (OOMMF), with standard values for permalloy: exchange stiffness $A_{ex} = 1.3 \times 10^{-11}$ Jm^{-1}, crystalline anisotropy $K = 0$, magnetisation $M_S = 8.0 \times 10^5$ Am^{-1}, and damping coefficient $\alpha = 0.5$. The calculated vertex configurations have moments which either point 'in' or 'out' of a vertex, and either fixed (black) moments or a degenerately flippable 'F' (red) moments. F moments occur where flipping the orientation leads to the vertex having the same total energy. Each vertex configuration can also be completely inversed. Level 1 refers to the ground state and level 2 to the 1st excited state. OOMMF calculations are only made for the lowest predicted set of ground states, due to limitations of the software processing time - for this reason complete curves of energy levels with sigmoidal features [93] are not

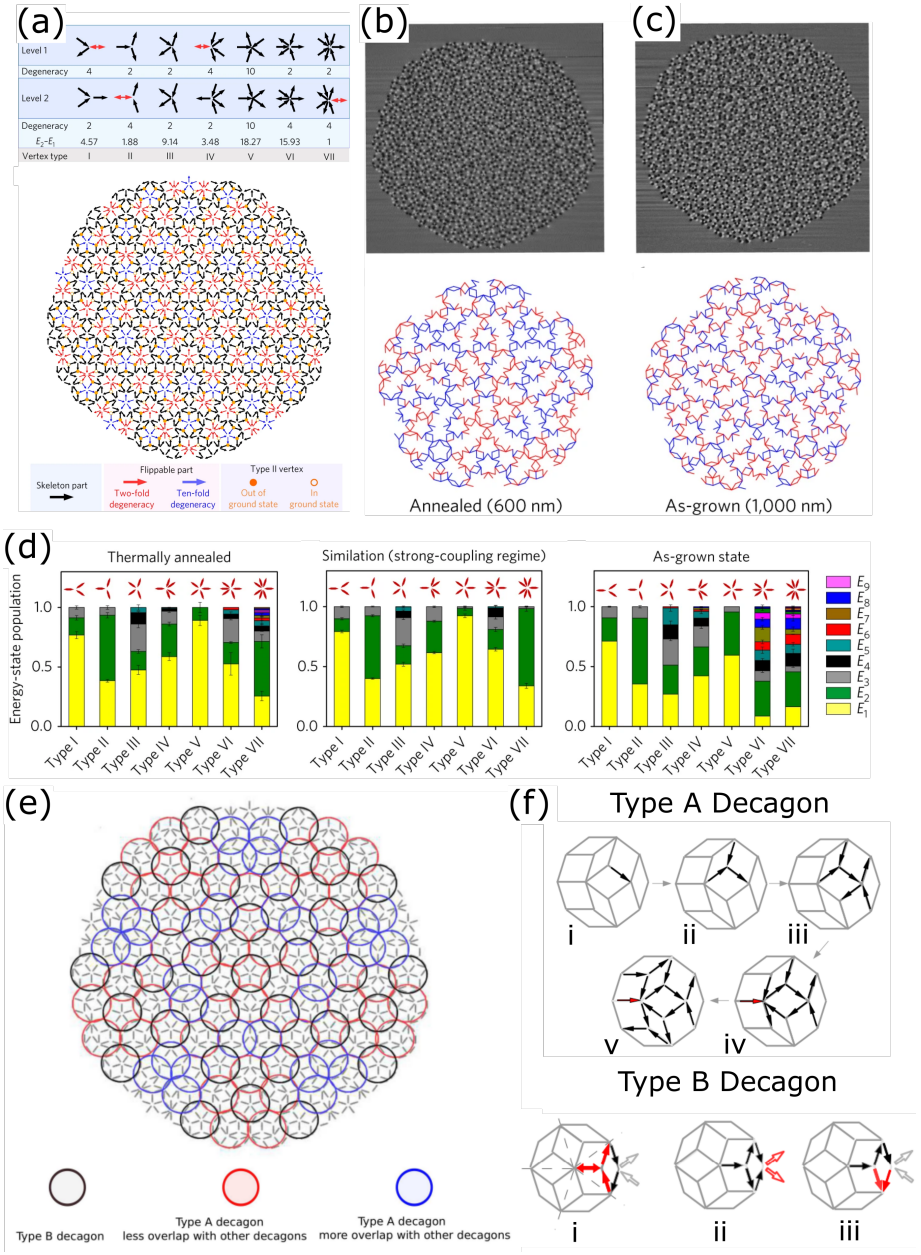

Figure 3.4: The Penrose tiling ASI. (a) (top) OOMMFF calculated ground state (level 1) and 1st excited state (level 2) for each of the seven vertex types. Black moments are fixed, red moments are degenerately flippable. (bottom) The Skeleton Model, with a fixed 'skeleton' of moments in black. Flippable (red) and 10-fold degenerate (blue) moments are indicated, alongside excited ground state vertices (orange dot), and ground state vertices (orange hole). (b) and (c) are MFM images with 600 nm and 1000 nm inter-nanoisland separation, respectively, with the skeleton displayed underneath. The red part and blue part moments align to chirally opposite skeleton directions. (d) Bar charts of the vertex energy distribution for the: (left) thermally annealed moments observed with MFM, (middle) Hamiltonian simulation, and (right) as-grown state. (e) Penrose tiling decorated with decagons of type A and B. (f) The construction of moments in the type A and B decagons, which overlap to produce a skeleton of fixed moments. Reproduced and modified from [114].

shown. Figure 3.4(a) also shows the 'Skeleton Model' of the penrose tiling, which has a fixed skeleton of black moments, alongside F moments with 2-fold and 10-fold degeneracy. With this information, the total number of globally degenerate ground state can be calculated as $W = 2 \times 2^{70} \times 10^{46}$, and the ground state entropy of $S = k_B \ln W = 155\ k_B$. Figures 3.4(b) and (c) shows MFM images with two different inter-nanoisland separations of 600 nm and 1000 nm, respectively. The networks correspond to skeleton macrospin configurations, where red and blue lines represent moments which follow the fixed moments of the skeleton (red) or its inverse (blue). However, this result is not special as skeleton moments are strictly assigned to either red or blue by default.

The ground state vertex population for each vertex type is shown with bar graphs in Figure 3.4(d) for each of the thermally annealed (left), Hamiltonian simulation (middle), and as-grown state (right). The ground state occupancy is shown in yellow, and 1st excited state in green, with other colours shown on the right. In Chapter 3.4, the expected distribution for each isolated vertex type is found with Boltzmann distribution calculations, which show the ground state usually dominates populations, with a small fraction of excited vertices. These distributions will be different when introducing the isolated vertices to a connected tiling, driving up the population of more excited vertices, such as seen in Figure 3.4. Note, the as-grown state chart is especially populated with the highest energy configurations which is not expected for a Boltzmann population - indicating the network has a lot of excited frustration as-grown. The Hamiltonian simulation chart shows a lower fraction of the most excited energy configurations, but nevertheless the fact that there are any of these suggests the system has intense frustration. For example, the Type I and II vertices can only have three combinations, therefore 10 % of the expected vertices have moments with either all 'in' or all 'out'. The thermally annealed chart matches the populations predicted with the Hamiltonian simulations for vertex types I - V, supporting the frustrated nature of the system. However, for types V and VI, there exists a lot of the higher energy configurations, which should not exist with a global ground state. This suggests the vertices with the most moments are susceptible to being trapped in an excited state. Overall, the Penrose ASI observed with MFM has only around 50% of vertices in the ground state, which is a lot lower and more frustrated than the square ASI.

In constructing the Skeleton Model, characteristic QC clusters which overlap to effectively cover the whole tiling were considered, as shown in Figure 3.4(e). For the 5-fold Penrose tilings these are decagons, indicated as either type A, which have type III or IV vertices at the centre, or type B, which have a type V vertex at the centre (giving it local 5-fold rotational symmetry). By minimising the interaction energy of vertex configurations which make up these decagons, the combined decoration is used to build up a minimisation of the complete tiling. Figure 3.4(f) and (g) show the construction of the type A and type B decagon, respectively. A combination of fixed and F moments within decagons can be

combined to decorate the full tiling, leading to the model shown in Figure 3.4(a). This construction is especially relevant for the production of the octagonal clusters in Chapter 6. Overall, the work showed that QC ASI could be fabricated and measured, finding that the Penrose tiling has vertex types which are especially frustrated due to local and global geometry.

3.2 Nanolithographic Fabrication of QP Tilings

In Chapters 5 and 6, thermal-scanning probe nanolithography (t-SPL) is used to fabricate quasiperiodic (QP) tilings. This section will provide a literature review of QP tilings fabricated with nanolithography techniques, starting with a short description of each technique, and identifying any applications. Nanolithography techniques encompass artificial fabrication or manipulation of nanoscale structures to create patterns on a substrate. At the nano- to mesoscopic scale, nanolithography fabrication techniques open new possibilities for precisely engineering the size, shape, and arrangement of nanostructures, thus enabling tailored functionalities [115–119]. Overall, nano-lithographed quasicrystalline nanostructures have demonstrated exceptional properties with enhanced solar efficiency [120, 121], improved catalytic performance [122], and thermoelectric applications [123–125].

Broadly, there are three main nanolithography techniques described in the literature which are used to produce QP tilings: scanning probe lithography (SPL), electron-beam lithography (EBL), and photolithography.

3.2.1 Scanning Probe Lithography

In SPL a direct-write probe manipulates a substrate surface by rearranging, etching, or removing the atoms or molecules, either chemically or physically [115, 126–128]. SPL is an adaption of the atomic force microscope (AFM), modified for a direct-write technique with a probe deliberately interacting with a surface, or resist, to create a pattern. The probe can be used as an integrated AFM to measure surface topology. The probe is direct-write, with no need for high vacuum conditions. Popular techniques include thermal (t-SPL) [128–131], mechanical, and dip-pen. The resolution of SPL techniques is the same scale as probe dimensions, for example the apex of the t-SPL tip. The t-SPL technique used in Chapters 5 and 6 removes surface molecules in a resist layer by thermal sublimation with a heated probe [130]. Resists are materials, typically polymeric, which are designed to break down under certain stimuli to transfer a pattern from a mask or directly onto a substrate. t-SPL is typically used in combination with e-beam deposition, whereby a target material can be patterned onto the substrate. The full experimental details of t-SPL are covered in Chapter 6.

Use of t-SPL to fabricate QP tilings is limited in the literature [18]. Lassaline [132] used

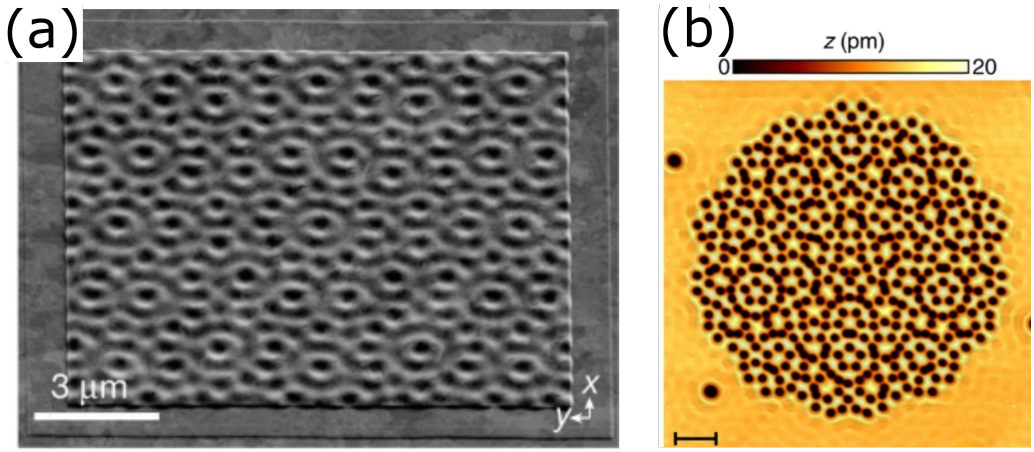

Figure 3.5: (a) A 12-fold optical Fourier surface created by a combination of t-SPL to create a mask, and photolithography. Reproduced and modified from [132]. (b) A QP Penrose tiling made by rearranging 460 CO molecules with SPL, scale bar 5 nm. Reproduced and modified from [133].

t-SPL to etch masks to further fabricate 6- and 12-fold structures with photolithography, as seen in Figure 3.5(a). Photolithography uses photons to transfer energy to surfaces, and so is optically limited, whereas t-SPL probe size is in the order of 10-20 nm, allowing better resolution. The downside of higher resolution of the SPL technique is a lower throughput, and so photolithography is the preferred technique for industrial scaling. Lassaline [132] engineered 6- and 12-fold photonic properties through precise Fourier-spectrum control, for generating photonics devices.

Another SPL technique used to fabricating QP arrays is mechanical SPL, whereby the probe manipulates the position of molecules or atoms on a surface to create a pattern. This same technique was used by IBM to produce the famous 'A Boy and His Atom' [134]. A QP Penrose pattern was created with a similar method by Collins [133], mechanically arranging 460 CO molecules into a rhombic Penrose pattern with an STM tip, to investigate electronic states. The CO molecules Penrose tiling is shown in Figure 3.5(b). Overall, there is no example in the literature of a QP tiling being directly fabricated with an indenting SPL probe, meaning work shown in Chapter 5 is novel in this aspect.

3.2.2 Electron Beam Lithography

EBL is another nanolithography technique used to fabricate QP arrays. The method is similar to SPL but instead of a probe, a high energy e-beam is focused on the surface. The e-beam energy is typically between 50-100 keV [135], and irradiates a resist, often through a mask covering specific areas of the substrate, into the designed pattern. EBL resolution is constrained by the de-Broglie wavelength ($\lambda = \frac{h}{mv}$) of electrons interacting with the resist. EBL is limited by a few issues: high e-beam energy leads to a proximity effect

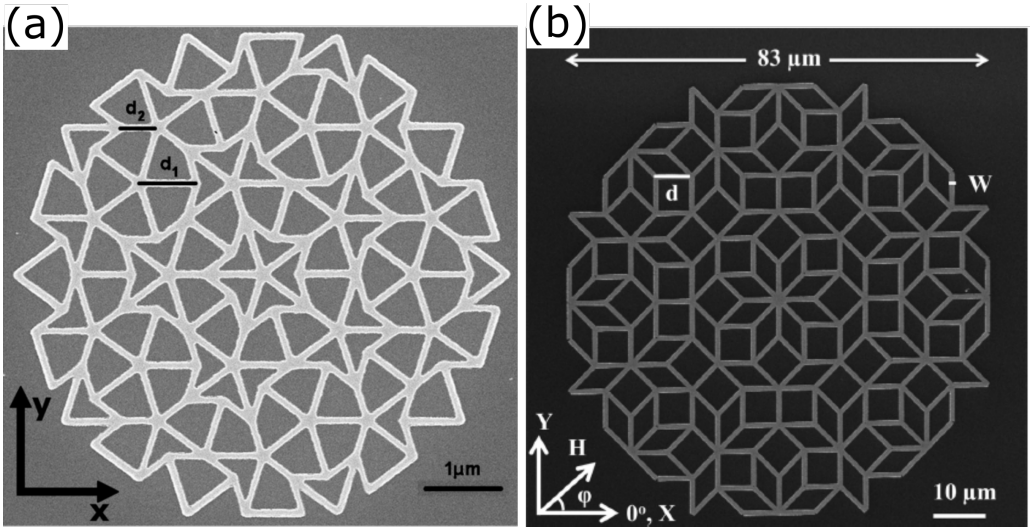

Figure 3.6: Fabricated connected-edge micron-scale QP tilings with EBL. (a) The Penrose tiling, reprinted and modified from [140]. (b) The ABT, reprinted and modified from [141].

caused by scattering into the bulk with increased interaction volume which limits spatial resolution and must be accounted for with a corrective algorithm [136–138]. Interaction depth of the e-beam increases as density (atomic number) decreases due to higher mean free path [139]. EBL must also be performed in a high vacuum system to ensure a large mean free path of incident electrons.

EBL combined with metal deposition is the most popular method for fabricating QP tilings in the literature [114, 140–157]. A significant amount of this research is from the group of Bhat [140–152], who research fabricated permalloy ($Ni_{80}Fe_{20}$) and later $Y_3Fe_5O_{12}$ ferromagnetic Penrose tilings (Figure 3.6(a)) and ABT (Figure 3.6(b)). In those studies it was established that QP structure and high rotational symmetry fundamentally alter static and dynamic magnetic behaviour compared to periodic systems. For example, QP drives non-random magnetisation reversal [140, 143, 144, 148, 152]. Additionally, QP design enables advanced magnonic control (a collective excitation in magnetic order) [140, 148–152]. Finally, the group found with advanced imaging and micromagnetic simulations that short-range exchange interactions enable non-random switching and collective effects. Both exchange and long-range dipolar interactions stabilise ordered ground states with reconfigurable magnonics [143, 146, 149, 150, 152]. These final results are especially relevant for the ferromagnetic ground states explored in Chapter 6.

Next, Shi [114] investigated the ground state of a Penrose artificial spin-ice (ASI) (which motivated our research into the ABT in chapter 6). The edges of the tiling were decorated with elongated permalloy nanoislands, and the separation between vertices was varied to influence dipolar exchange strength. The ground state was realised by thermally annealing islands, to reduce the energy barrier to moment switching - vertex configurations

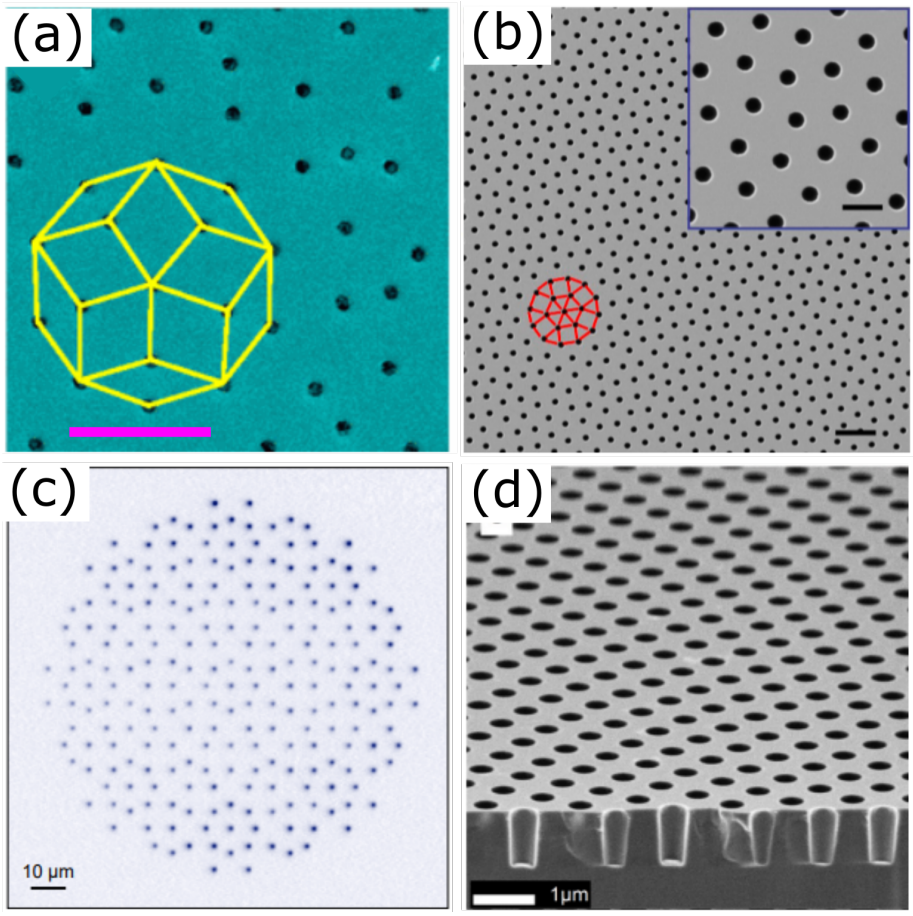

Figure 3.7: Fabricated micron-scale vertices-only QP tilings with EBL. Images are reprinted and modified, with authors decorating a: (a) Penrose tiling with Nb thin film [153], pink scale bar 2 µm. (b) Square-Triangle etched into Si [154]. (c) Trapped Sr atoms patterned into a Penrose tiling [157]. (d) Cross section of air holes in Si with sunflower Fibonacci pattern [120].

then organise into energetically preferred directions. The measurements only covered 10-fold rhombic tilings, which motivated our research to consider other ABT and Fibonacci Square ASI tilings in Chapter 6. A more in-depth review of the magnetic results of the Penrose paper as well as other ASI research is given in a later section.

Fabricating vertices of QP tilings is the most popular route to allow measurement of electronic interactions. Kemmler [153] fabricated Nb superconducting thin films, and determined enhanced critical current (the maximum current density before superconductivity is destroyed) in the Penrose tiling compared to random arrays as shown in Figure 3.7(a). Around the same time, Villegas [158] also investigated QP vortex-lattice dynamics in superconducting Nb thin films, measuring critical temperature of SFT and Penrose tilings. Jia [154] fabricated QP nanohole arrays of Penrose and 12-fold Square-Triangle tilings onto optical fibres - finding high sensitivity for plasmonic sensing applications as shown in

Figure 3.7(b). Kasture [156] also investigated plasmonic quasicrystals, with large area air hole patterns in metal films which showed enhanced transmission for polarised light. Next, Butler [155] fabricated Penrose tilings from carbon nanotubes, and demonstated their function as diffractive elements for optical applications. Holman [157] demonstrated trapping of single atoms in a Penrose pattern with tightly focused beams of light, with applications in many particle quantum systems as shown in Figure 3.7(c). Finally, Mercier [120] etched QP air holes into Si solar cells to minimise reflection, finding a 12-fold pattern reduces reflection to 8.3% compared to 36.4% of bare Si. Mercier determined that increased surface area of air holes lead to greater recombination, but neverless simulated efficiency to improve to 21.1% with a sunflower Fibonacci pattern as shown in Figure 3.7(d) compared to 16.0% of bare Si. Overall, fabricated vertices-only QP structures have demonstrably enhanced performance in a diverse range of fields.

3.2.3 Photolithography

The final nanolithography technique used to fabricate QP tilings is photolithography - a broad term for essentially any photon interaction which transfers a 2D pattern onto a substrate, usually through a mask [119]. Photolithography is an established technique for the semiconductor manufacturing process, with high throughput of pattern transfer, but is optically limited by the diffraction limit of the photon source [119, 162]. With this technique, QP Moiré patterns emerge with multiple interference beams with incommensurately modulated periodicity, spatial frequency, or angles. The resolution is poorer than in SPL or EBL, due to the long wavelength of the photons employed in these techniques. Thus the optical or UV phhotolithography method creates features too large to investigate nanoscale geometric frustration, but can still be useful in creating large thin film QP structures. Optical diffraction limits can be overcome with smaller wavelength photons, which is more standard in the photolithography industry but also more expensive. Langner [159] achieved nanoscale resolution with Cr thermally evaporated into 5- and 8-fold structures, as shown in Figures 3.8(a)-(b), using extreme-UV photons with a lower $\lambda = 13.5nm$. However, the mask used for diffraction was still fabricated with EBL. Mahmood [160](Figures 3.8(c)-(f)) and Lubin [161](Figures 3.8(g)-(h)) also have had success with Moiré lithography, creating up to 22-, and 36-fold structures.

3.3 The 8-fold Ammann-Beenker Tiling

In Chapter 6, the Ammann-Beenker Tiling (ABT) is chosen for studying nanomagnetic artificial spin-ice (ASI) interactions due to the tiling's interesting geometric features. This section will cover the most recent work on the ABT in the literature, to investigate possible motivations for why the ABT may be of interest for ASI research, especially in comparision

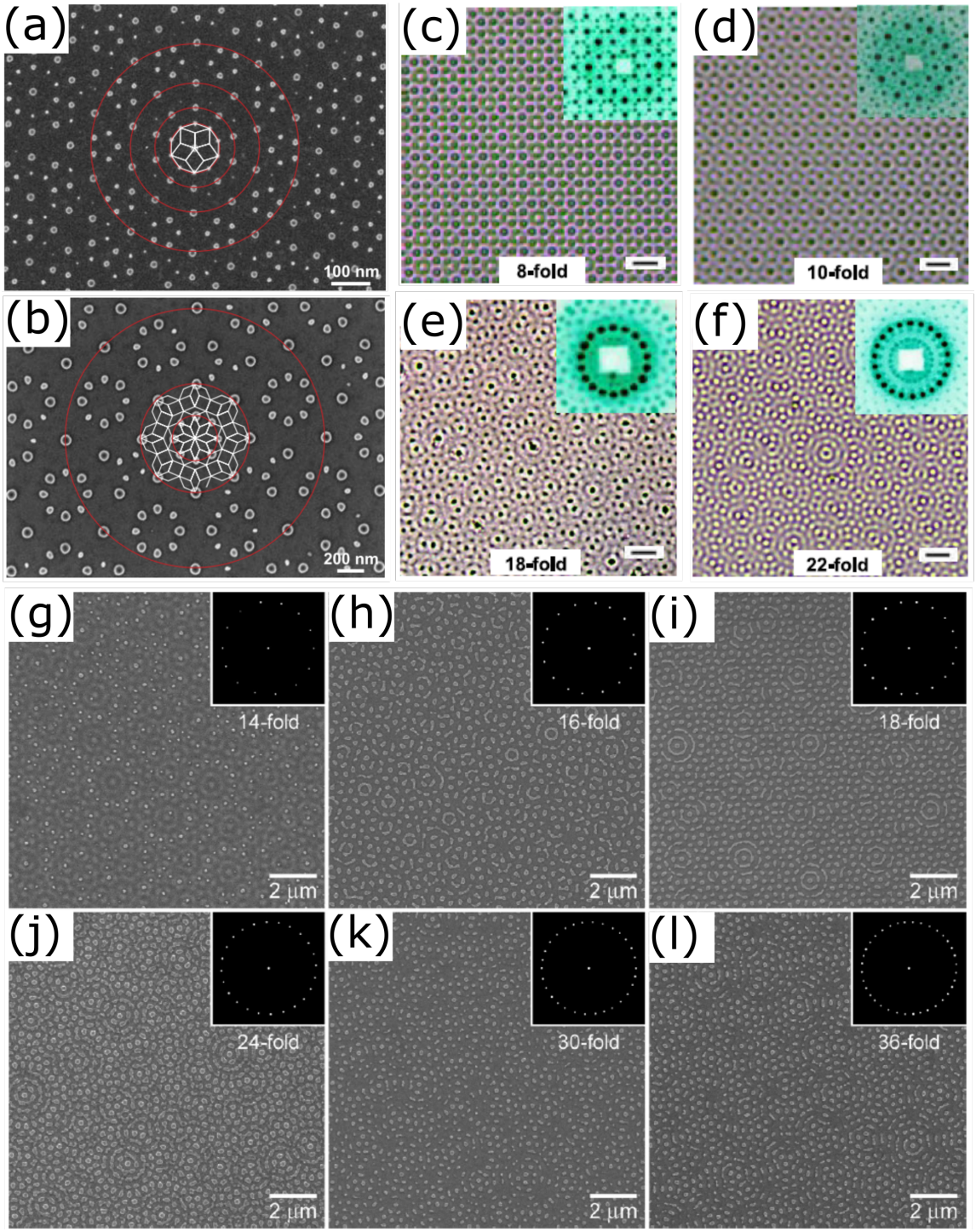

Figure 3.8: A selection of QP tilings fabricated and metallised with a photolithography technique. (a-b) Cr nanodot arrays: (a) 5-fold and (b) 8-fold. Reproduced and modified from [159]. (c-f) Optical microscopy images of Ag arrays: (c) 8-fold, (d) 10-fold, (e) 18-fold, (f) 22-fold. scale bar 10 µm. Reproduced and modified from [160]. (g-i) SEM images of Moiré structures decorated photoresists: (g) 14-fold, (h) 16-fold, (i) 18-fold, (j) 24-fold, (k) 30-fold, and (l) 36-fold. Reproduced and modified from [161].

to the Penrose ASI [114].

Recently, the ABT has been the centre of intense research by the community [163], such as investigating theoretical magnetic long-range order [164–167], electronic models [168–171], topological insulators and photonic quasicrystals [172–174], and geometry and symmetry [18, 175–177]. Some research is motivated by realised 8-fold quasicrystal systems such as ultra-cold atoms [178–180], and known physical crystals [175, 181, 182]. Additionally, the ABT is a good approximant for square systems [173, 177]. The ABT has six distinct local environments with increasing coordination numbers 3 to 8 [167]. Interestingly, the ABT is less frustrated than the Penrose tiling because half of the ABT vertices have even moments that, while degenerate, are not geometrically frustrated. In particular, the highest energy vertex has eight moments which are not geometrically frustrated and are therefore expected to more easily settle into their ASI ground state with high energy barriers to switching once settled. In comparison to the Penrose Tiling, whose highest energy vertices have significant geometric frustration [114], the ABT is interesting because of the potential to support long-range Hamiltonian interactions at these eight moment vertices.

Dimers model diatomic molecules by covering the neighbouring sites on a lattice. The 'Dimer Problem' is about how many ways you can count these dimers without overlaps. Dimers in planar graphs were solved in the 1960s [184–186], providing insight into statistical mechanics and phase transitions. Lloyd [176] recently solved ABT dimers, the tiling shown in Figure 3.9(a), and solved dimers in Figure 3.9(b). The work is interesting because of how the ABT dimer system relates to our ABT ASI, as both systems deal with constrained configurations on the same underlying lattice. In ASI, dimers are effectively replaced with single-domain macrospins. The proof that the ABT allows a perfect dimer covering suggests that the underlying vertex connectivity does not inherently prevent fully constrained states. If dimers can perfectly cover the ABT, then certain spin configurations in the ASI ABT might also be fully constrained and realizable. This result is nontrivial because in the Penrose tiling it is impossible to fully cover all sites with dimers, due to local geometric frustration [183].

Lloyd motives their work saying: 'This tiling has been the topic of much recent attention, with investigations in the context of magnetism [164–166], superconductivity [167], critical eigenstates [187], protected Majorana modes [188], and topological insulators [189]'. One main feature of placing dimers on the ABT is the discrete scale invariance (structure repeats under inflation by the silver ratio $1 + \sqrt{2}$) that the ABT exhibits. These authors prove that unlike Penrose tilings [183], which always force a finite density of monomers due to matching rules, in the thermodynamic limit, the ABT can be perfectly matched. Here, the thermodynamic limit refers to the physical behaviour by a system when its size becomes infinitely large. The discrete scale invariance of the ABT means that under re-

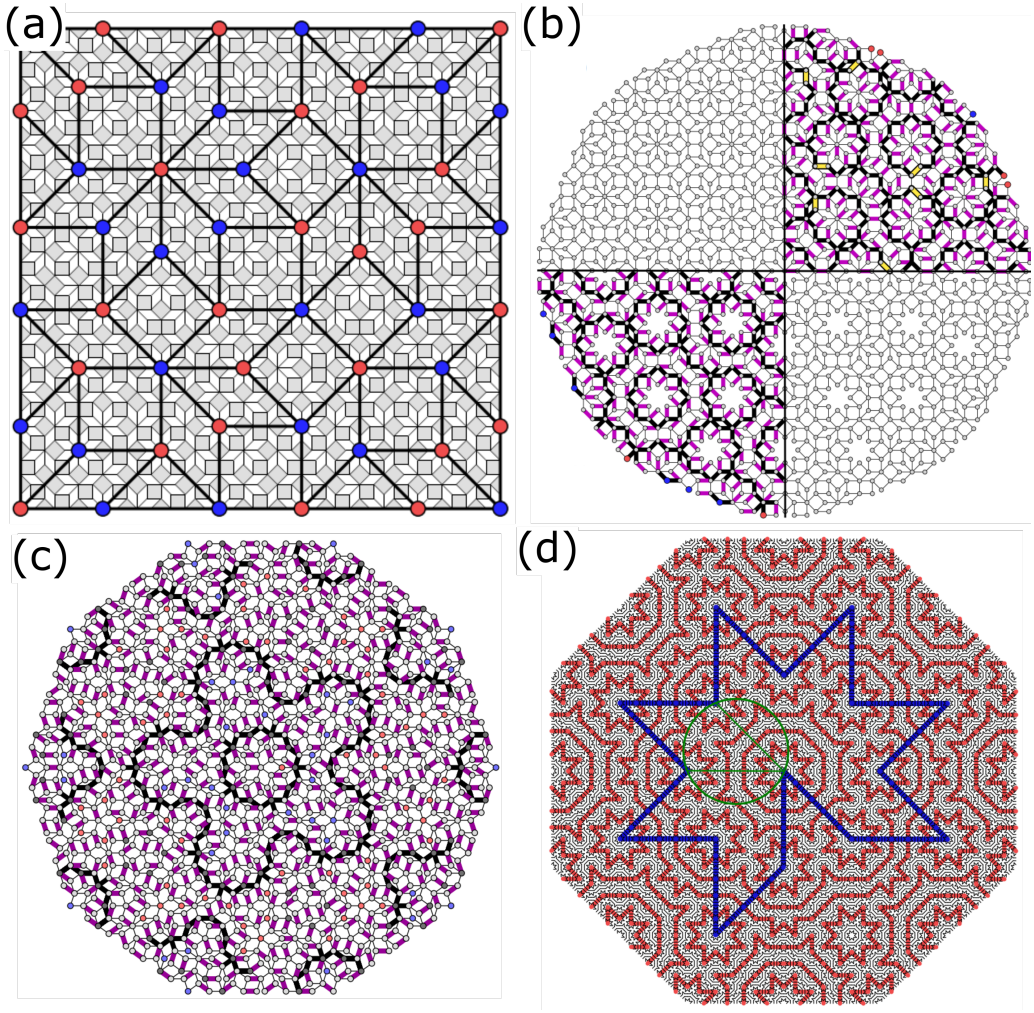

Figure 3.9: Results of studies of the ABT: (a) the inflation scale symmetry of smaller ABT overlaid on an inflated tiling, with lengths increased by $\delta = (1 + \sqrt{2})^2$, connected between vertices of local 8-fold symmetry (alternately coloured red and blue). (b) the solved dimers (purple lines) for ABT (top) and without local 8-fold vertices (bottom). Reproduced and modified from [176]. (c) The Penrose dimer (purple line) and monomer (orange dot) distribution. Reproduced and modified from [183]. (d) The completed Hamiltonian cycle for the ABT which visits every locally 8-fold cluster once without overlap. Black, red, and blue paths indicate Hamiltonian cycles which follow deflated tilings. Reproduced and modified from [175].

peated deflation (or inflation), the tiling maps onto itself but with rescaled lengths. This forms the basis of a hierarchy where effective matching emerges at larger and larger scales.

Flicker [183] attempted to solve the Penrose tiling dimer problem. The main conclusion is that Penrose tilings cannot be perfectly matched, in part, due to their QP structure. As shown in Figure 3.9(c), monomers (orange dots) are shown to be unavoidable with Penrose tiling matching rules. In the thermodynamic limit, in essence with an infinite number of vertices, $\approx 10\%$ of vertices are unpaired. A maximum matchings partition the

tiling into closed fractal regions bounded by loops (black lines) of even-valence vertices (4- or 6-coordinated). These loops act as impermeable barriers to monomer movement. Each region has a net charge (excess of one sublattice's monomers). Adjacent regions have opposite charges, ensuring global neutrality. All maximum matchings are interconnected via local monomer-dimer rearrangements (flipping dimers along alternating paths). This implies ergodicity - where a system is ergodic if, over a sufficiently long time, it visits all possible states consistent with its energy and constraints, within the manifold of defect configurations. Overall, Penrose tilings force dimer models into defect-rich monomer configurations attributed to the tiling's geometric frustration.

The fact that dimers can be perfectly matched on the ABT but not on the Penrose tiling indicates greater connectivity of the ABT. This suggests a fully constrained ground state, with potential to support long-range order between locally degenerate vertex configurations, may be achievable in an ABT ASI. Since the Penrose tiling inherently forces a finite density of geometrically frustrated vertices, ASI built with it may always exhibit a degree of intrinsic frustration. In contrast, the ABT might enable lower frustration and stronger long-range order in the spin configuration. The perfect matching in the dimer model also implies that the hierarchical and scale-invariant structure of the ABT can support long-range correlations. For ASI, this could translate into unusual magnetic ordering phenomena or correlated spin fluctuations that extend to long-range order. In summary, the research by Flicker [176, 183] implies that using the ABT as an ASI could lead to systems with reduced intrinsic disorder, a potentially more ordered ground state, and novel correlation effects that are distinct from those in ASI systems based on Penrose tilings.

Most recently, Flicker [175] investigated Hamiltonian cycles in the ABT, providing a simple algorithm for constructing Hamiltonian graph cycles (visiting every vertex exactly once) on a set of arbitrarily large finite ABT graphs. An example of a Hamiltonian cycle on an ABT graph is shown in Figure 3.9(d). Fractal geometric loop structures are found to include fluctuating domain walls in Ising magnets, similar to how ASI may behave. A special class of loop structures are Hamiltonian cycles as a closed self-avoiding loop that visits every vertex precisely once. Hamiltonian cycles have appeared in protein folding, spin models [190,191], and ice-type models in geometrically frustrated magnetism [192,193]. These results further support the global connectively and decreases frustration of the ABT, compared to the Penrose tiling.

Other recent works theoretically explore the ABT's unique properties across photonic, electronic, and magnetic systems. Zhang [172] and Mao [174] establish real-space topological invariants (Bott index, quadrupole winding), revealing edge or hinge states unattainable in crystals. Damanik [171] and Oktel [170] identify localised eigenfunctions or zero-energy states, with the latter quantifying their symmetry and frequency. Peng [173] demonstrates disorder-induced topology in both quasicrystals and crystals, while Koga [164] links con-

fined states to magnetic order in Hubbard models. Gottlob's [168] configuration-space framework enables thermodynamic analysis of quasicrystalline many-body systems, contrasting with Bloch-based methods for crystals.

3.4 Growth of Thin Films on Quasicrystals

This section provides a literature review of thin film growth on quasicrystal surfaces, covering rotational, QP modulation, and templated growth with atomic and molecular species. Chapter 8 describes the deposition of C_{60} on the 2-fold *d*-Al-Ni-Co surface. For this reason, the most thorough part of this literature is given for molecular growth on quasicrystals at the end of this section.

Local isomorphism of quasicrystals mixed with QP ity leads to an interesting energy landscape for adsorption epitaxy, such as rotational modes, QP modulation, and pseudomorphic growth. Thin film growth on QC surfaces has been a large focus of the QC surface science community in the last decade [194–196]. For periodically arranged substrates, ordered epitaxial growth is facilitated by adsorbates decorating surface unit cells of the substrate. Despite QC not possessing unit cells, periodicity is not a condition of growth - as long as the psuedo-unit cells of the substrate are decorated with the adsorbate, then an ordered super structure can be achieved [197].

3.4.1 Rotational Epitaxy

Local isomorphism of QC allows ordered growth of adsorbates along the main axes of rotational symmetry, where surface and adsorbate energy are minimised [65, 198, 199]. The 5-fold *i*-Al-Pd-Mn and 10-fold *d*-AlNiCo surfaces provide excellent substrates for rotational epitaxy due to their well understood clean surfaces and high order of rotational symmetry. For example, deposition of Au on the 10-fold surface of *d*-AlNiCo resulted in an epitaxial film of 10-fold rotational symmetry, as shown in the reflection high-energy electron diffraction (RHEED) pattern in Figure 3.10(a) [199]. Here, the film of Au was characterised as twinned $AuAl_2$, with (110)-orientated surfaces corresponding to the 10-fold symmetry of the substrate. Figure 3.10(b) shows a model for the interface between the thin film and substrate, with circles representing the thin film and squares representing the substrate. Another example is growth of Al atop the 5-fold *i*-Al-Pd-Mn surface, which exhibit five growth domains where the [111] and [100] Al directions coincide with the 3-fold and 2-fold axes of the substrate, respectively [77, 200]. Rotational epitaxy including 5-fold twinning of periodic crystals was also found for Ag, Bi, Co, Fe, and Ni atop 5-fold *i*-Al-Pd-Mn and Al, Ag, Bi, and Xe atop 10-fold *d*-AlNiCo [77, 201, 202].

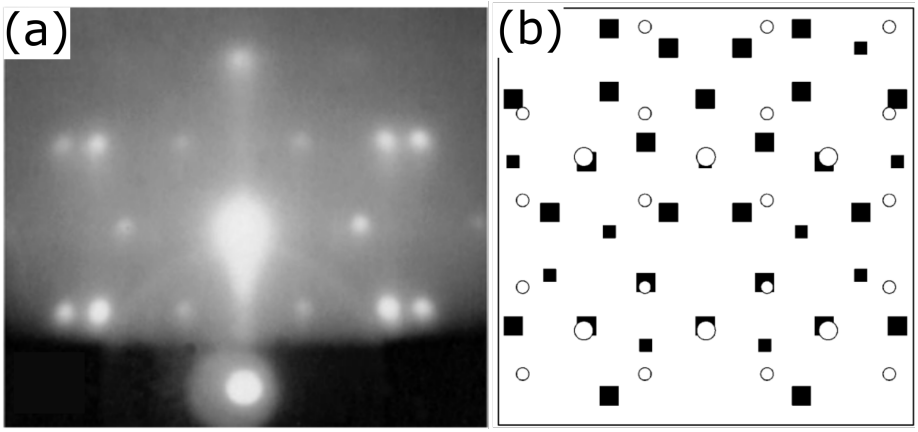

Figure 3.10: Growth of Au atop the 10-fold *d*-Al-Ni-Co surface, which causes epitaxial growth of $AuAl_2$ with 10-fold symmetry. (a) Reflection high-energy electron diffraction (RHEED) pattern. (b) Model for the interface between the thin film and substrate. Circles represent thin film and squares represent the substrate. Reproduced and modified from [199].

3.4.2 Quasiperiodic Modulation

A modified form of rotational epitaxy occurs in quasiperiodically modulated multilayer structures, where the substrate exerts greater influence on the overlayer. Here, adsorbate films exhibit crystalline structure aligned with the substrate's high-symmetry directions. Perpendicular to these directions, however, atomic rows arrange quasiperiodically. This geometry favours coincidence between the high atomic density features of the substrate and adsorbate.

Quasiperiodic modulation is best demonstrated with Cu atop 5-fold *i*-Al-Pd-Mn [203–205]. Figure 3.11(a) shows an of a 70 x 70 nm^2 area STM image with 5.5 ML of Cu (detemined by thresholding successive fractional layer coverages) [203]. Initial adsorption shows no discernible order. However, at coverages between $\approx$ 5 and 25 ML, STM reveals five domains of row structure aligned with the substrate's high-symmetry axes. The row spacings follow a Fibonacci sequence (S = 0.45 nm, L = 0.73 nm, $\frac{L}{S} \approx$), consistent with substrate feature spacings. While STM lacked atomic resolution within rows, low energy electron diffraction (LEED) indicates periodicity. Figure 3.11(b) shows periodically spaced high-intensity streaks (pink) along the five substrate symmetry directions, matching the bulk Cu nearest-neighbour distance [205], with peaks arranged quasiperiodically orthogonal to the streak direction (red L and blue S). The proposed structural model involves a vicinal surface formed by a 13.28° miscut from the (100) direction in a body-centred tetragonal Cu structure, as shown in Figure 3.11(c). This creates a step-terrace structure with terrace separations mirroring the observed Fibonacci sequence, explaining the STM-protruding rows as step edges.

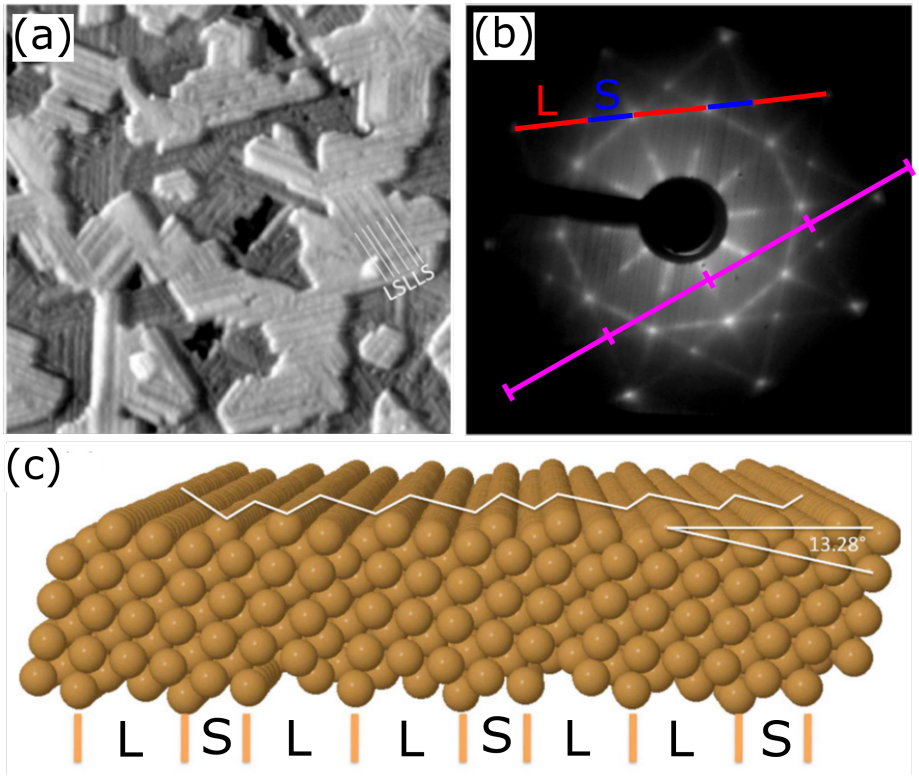

Figure 3.11: A selection of figures showing quasiperiodically modulated Cu deposited atop 5-fold *i*-Al-Pd-Mn. (a) An 70 x 70 nm^2 STM image with 5.5 ML of Cu. Row structure aligned with the substrate's high-symmetry axes follows a Fibonacci sequence (S = 0.45 nm, L = 0.73 nm, $\frac{L}{S} \approx$). Reproduced from [203]. (b) LEED image with indicated periodically spaced high-intensity streaks (pink) along the five substrate symmetry directions. L (red) and S (blue) indicate peaks arranged quasiperiodically orthogonal to the pink streak direction. (c) Structural model, with a vicinal surface formed by a 13.28° miscut from the (100) direction of a body-centred tetragonal Cu structure. The L and S Fibonacci sequence labelled leads to a quasiperiodically modulated step-terrace structure. Reproduced and modified from [205]

3.4.3 Templated Growth

Templated, or pseudomorphic growth, occurs where thin films have quasiperiodically ordered growth on a surface indicative of the substrate chemistry. This is interesting because of the ability to fabricate ordered thin films of species which do not naturally exhibit quasicrystallinity, potentially unlocking new applications. The successful interaction of an adsorbed species reveals a lot about the surface - atomic species may indicate structural features that are difficult to identify on the clean surface, while molecular species can reveal chemical bonding information. Because of this, a large amount of research has been conducted in the last 25 years with several adsorbate species and QC substrates, with a wealth of review articles [201, 202, 206–209]. This section will explore both atomic and molecular templated growth on QC surfaces, which is especially relevant for the C_{60} thin

film growth on *d*-Al-Ni-Co in Chapter 8. For this reason, a summary of relevant results of atomic templated growth is given, with a more in-depth coverage of molecular templated growth.

Atomic Thin Films

Al and Cu adsorbate overlayers exhibit pseudomorphic growth on the 5-fold *i*-Al-Pd-Mn and Al-Cu-Fe surfaces, producing Al and Cu nano-islands observed by STM, as seen for Al/Al-Cu-Fe in Figure 3.12(a) [210, 211]. Nanoislands form as six-atom 'starfish' structures: pentagonally arranged Al atoms with one central atom, as shown in Figure 3.12(b). Nucleation occurs at the substrate's 'dark star' sites, pentagonal arrangements with a central hollow related to truncations of the bulk pseudo-Mackay and Bergman clusters (these clusters describe icosahedral QC). Growth involves trapping an Al atom in this central vacancy, followed by nucleation of five further Al atoms at surrounding bridge sites, forming the starfish. Additional adatoms can nucleate from these centres, forming pentagonal starfish structures where the nucleated adatoms (the starfish legs) sit at bridge sites of substrate pentagons. This mechanism is supported by a measured central depression in experimental data. High coverage Al and Cu show a disordered overlayer structure.

Pseudomorphic growth at monolayer coverage was first reported for Bi and Sb deposition on the 5-fold *i*-Al-Pd-Mn and 10-fold *d*-Al-Ni-Co surfaces [214]. During deposition, the substrates were held at elevated temperatures (373 - 573 K), and coverage was determined by measuring the intensity of a reflected He beam aimed at the sample. LEED and HAS studies confirmed these adsorbate layers exhibited the same symmetries and peak positions as the corresponding clean substrate surfaces. Subsequent STM investigation of Bi atop the 5-fold *i*-Al-Pd-Mn system at room temperature revealed pentagonally arranged Bi clusters at sub-monolayer coverages [212]. These clusters were centred on the pentagonal tiles of the Penrose P1 tiling describing the substrate structure, as indicated with white stars in Figure 3.12(c). Similar pentagonal features were observed for 1 ML Pb on the same surface while annealing to 653 K, as shown in Figure 3.12(d). Here, self-assembled Pb atoms were described by a τ-inflated Penrose P1 tiling, compared to similar structure features of the substrate [213]. Further examples of successful templated growth include Pb on *d*-Al-Ni-Co [215] and Sn on Al-Cu-Fe [216].

The deposition of Pb atop 5-fold *i*-Ag-In-Yb maintains QC structure across several layers, demonstrating multi-layer pseudomorphic growth [217]. The positions of Pb atoms within each adsorbed layer correspond to specific vacant sites of repeating clusters above the surface in the structural model. Investigations using STM, X-ray photoelectron spectroscopy, LEED and density functional theory confirmed the growth of quasicrystalline Pb layers at different heights, exhibiting distinct in-plane structures and adsorption energies [217]. Pb-Pb interlayer distances, close to those in bulk Pb, are considered crucial for

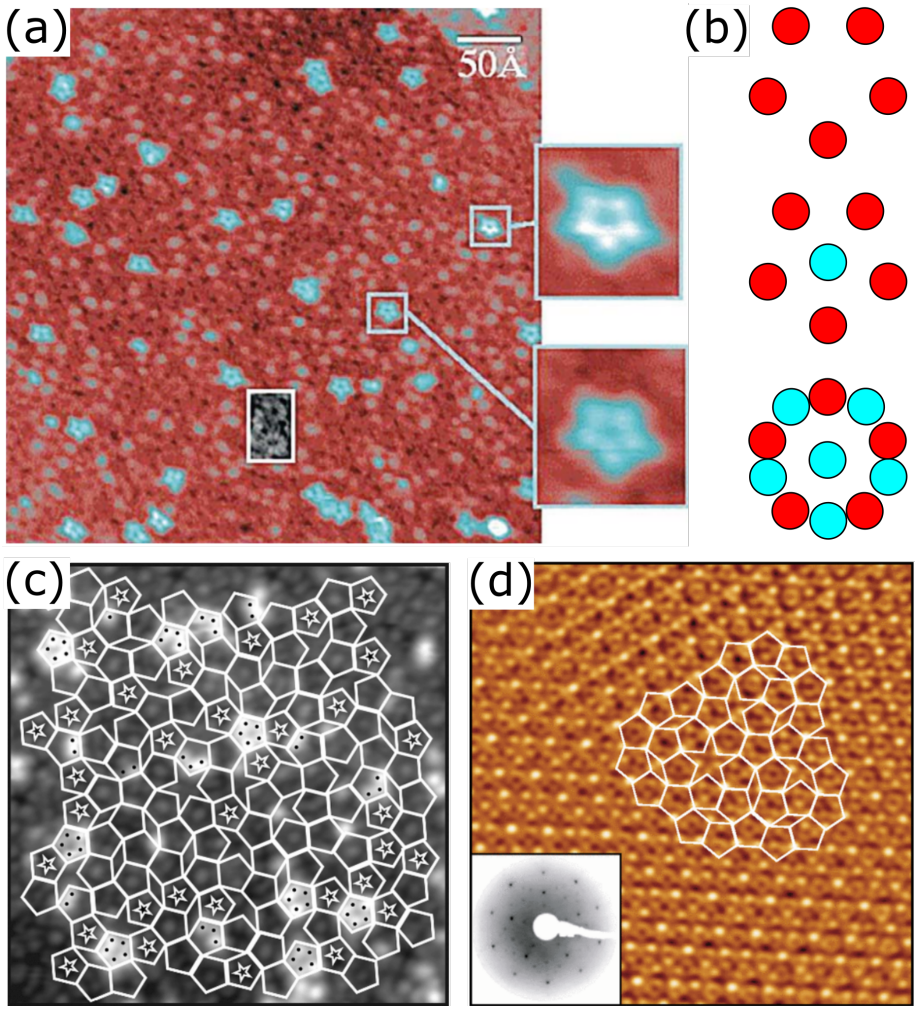

Figure 3.12: A selection of STM images which reveal templated quasicrystalline growth. (a) 0.04 ML coverage of Al atop 5-fold *i*-Al-Cu-Fe, where red colour indicates the substrate and blue is Al. Enlarged images indicate starfish structures discussed in the text. (b) The growth mechanism of Al starfish growth from zero to low coverage. Reproduced and modified from [211] (c) 0.13 ML coverage of Bi atop 5-fold *i*-Al-Pd-Mn, where Bi clusters decorate white stars in pentagonal tiles of the Penrose P1 tiling. Reproduced from [212]. (d) 1 ML of Pb atop 5-fold *i*-Al-Pd-Mn, where self-assembled Pb atoms are described by a τ-inflated Penrose P1 tiling. Reproduced from [213].

stabilising the multi-layer film with a Pb underlayer not observed by STM. Pb atop 5-fold *i*-Ag-In-Yb was therefore the first example of templated 3-dimensional QC growth. The system demonstrates reduced chemical complexity while maintaining quasicrystallinity, being described by the authors as the 'simplest quasicrystal'. This 3-dimensional growth behaviour has also been reported for Bi atop 5-fold *i*-Ag-In-Yb, which also occupies vacant cluster sites [218], and for Pb atop 3-fold *i*-Ag-In-Yb [219].

Molecular Thin Films

Templated growth is extended to molecules, which typically do not form ordered QC thin films when deposited with the substrate held at room temperature. Initial efforts to form such templated molecular overlayers to investigate chemical reactivity, such as benzene on 5-fold *i*-Al-Pd-Mn [220] and ethylene on 10-fold *d*-Al-Ni-Co [221], showed no ordered adsorption. However, as with atomic thin films, successful templating of molecular species was eventually achieved, either by selecting the appropriate molecule or by annealing the substrate during deposition, to enable surface diffusion [65]. The molecule C_{60} (buckminsterfullerene) has been widely chosen due to its isotropic structure and possession of 2-, 3-, and 5-fold symmetry planes, naturally matching *i*-QC structure which has been shown to be significant in molecule - QC substrate interactions.

Early research into the 5-fold *i*-Al-Pd-Mn surface showed a disordered C_{60} thin film is grown deposited with the substrate at room temperature at low to high coverage [223]. However, detailed analysis at 0.065 ML coverages suggested evidence of local τ-scaled Fibonacci order between C_{60} molecules at pentagonal dark star sites. Later, templated quasicrystalline C_{60} thin films were grown on the similarly structured 5-fold *i*-Al-Pd-Mn and *i*-Al-Cu-Fe surfaces [196, 222], and similarly structured 10-fold *d*-Al-Ni-Co and *d*-Al-Cu-Co surfaces [222]. Annealing the substrate during C_{60} deposition was found to facilitate an ordered thin film, by lowering the energy barrier for bonding between C_{60} and the surface or subsurface electron donors, allowing C_{60} diffusion on the surface [195].

In the 5-fold C_{60}/*i*-Al-Cu-Fe and *i*-Al-Pd-Mn systems, two distinct adsorption sites were identified: bright (B) and dark (D), as shown in Figure 3.13(a)-(c). The B molecules bonded to surface Fe atoms, while the D molecules bonded to subsurface Fe atoms, with the latter association suggested involving a slight subsurface reconstruction [196,222]. The subsurface network of Fe is analogous to the dark star network of Mn atoms within the C_{60}/*i*-Al-Pd-Mn [222, 223], and Bi/ Sb/ Pb/ *i*-Al-Pd-Mn systems [212–214]. Charge density difference calculations for C_{60}/Al-Pd-Mn on dark star (D motifs) and white flower (B motifs) sites reveal site-specific bonding mechanisms, as shown in Figure 3.13(d)-(e) [222], respectively. At dark star sites, directional charge accumulation occurs between five lateral C atoms (involved in 6:6 bonds) and five surface Al atoms, while at white flower sites, charge accumulates predominantly between the C pentagonal face and a central subsurface Mn atom, both exhibiting 5-fold symmetry. Projected density of states analysis confirm these interactions; firstly adsorption at dark sites introduces new states at the Fermi level through *s-p* hybridization between C and Al. Secondonly, white flower sites show significant HOMO/LUMO (highest occupied and lowest unoccupied molecular orbitals) shifts, indicating substrate-to-molecule electron transfer and strong *s-p-d* hybridization between C and Mn, suggesting a covalent or iono-covalent bonding character. C_{60} was also shown to selectively adsorb atop Mn on the 2-fold *i*-Al-Pd-Mn surface, forming a square Fibonacci

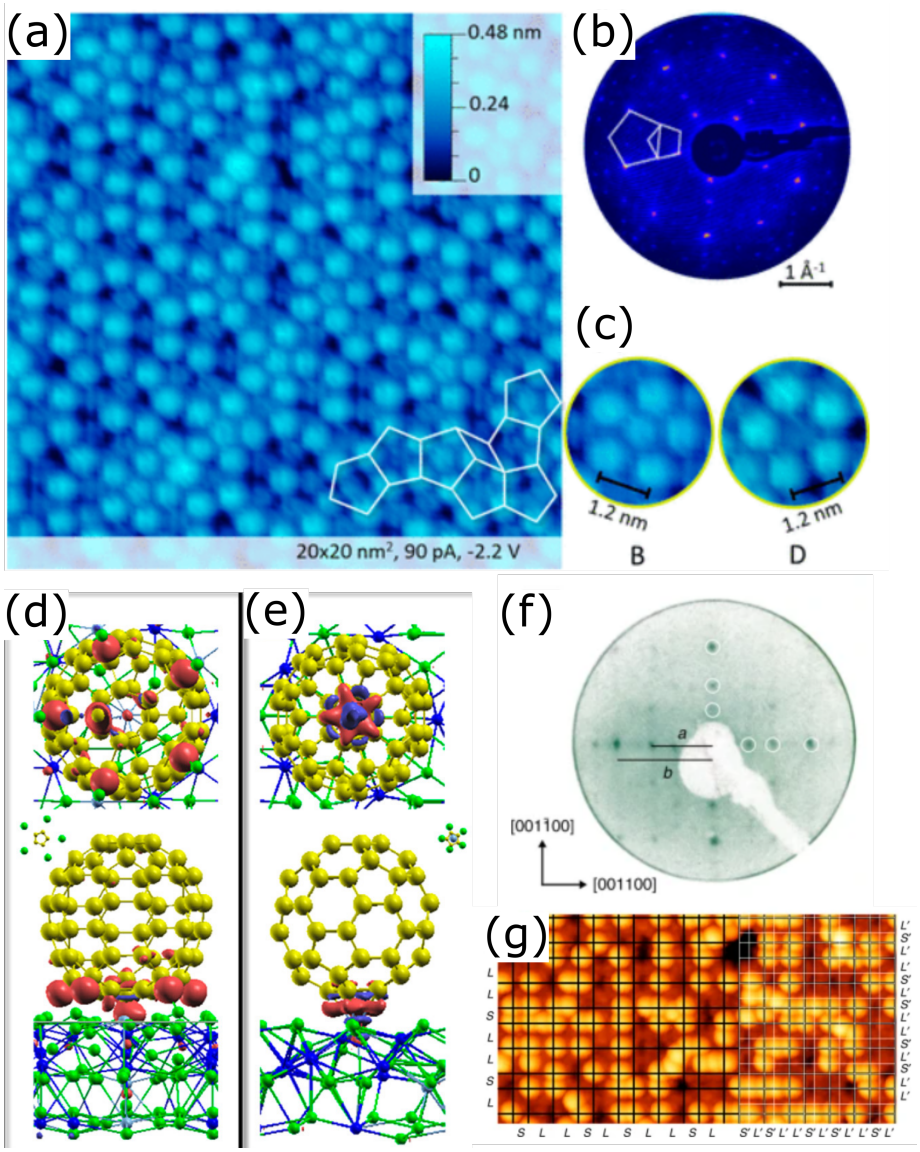

Figure 3.13: (a) STM of 5-fold *i*-Al-Cu-Fe with 1 ML C_{60}, with a Penrose tiling overlaid over a portion, and (b) the corresponding LEED pattern at 43 eV. (c) Local atomic configurations discussed in the text. (d) Isosurfaces of electron density difference between C_{60} and (d) the dark star and (e) white flower site discussed in the text. Reproduced and modified from [222]. (f) LEED pattern of C_{60} deposited atop the 2-fold *i*-Al-Pd-Mn surface, showing τ-scaled a and b. (g) The corresponding STM of (f), showing C_{60} arranged in a square Fibonacci tiling with L, S, and inflated L' and S'. Reproduced and modified from [194].

tiling, as shown in Figure 3.13(f)-(g) [194].

In the 10-fold C_{60}/*d*-Al-Ni-Co and C_{60}/*d*-Al-Cu-Co systems, LEED patterns confirm that the deposited C_{60} monolayer exhibits 10-fold symmetry [222]. STM imaging reveals a compact, QP C_{60} thin film characterised by bright molecules, and a nearest-neighbour distance of 1.01 ± 0.01 nm, consistent with separations of the ideal C_{60} hexagonal close-

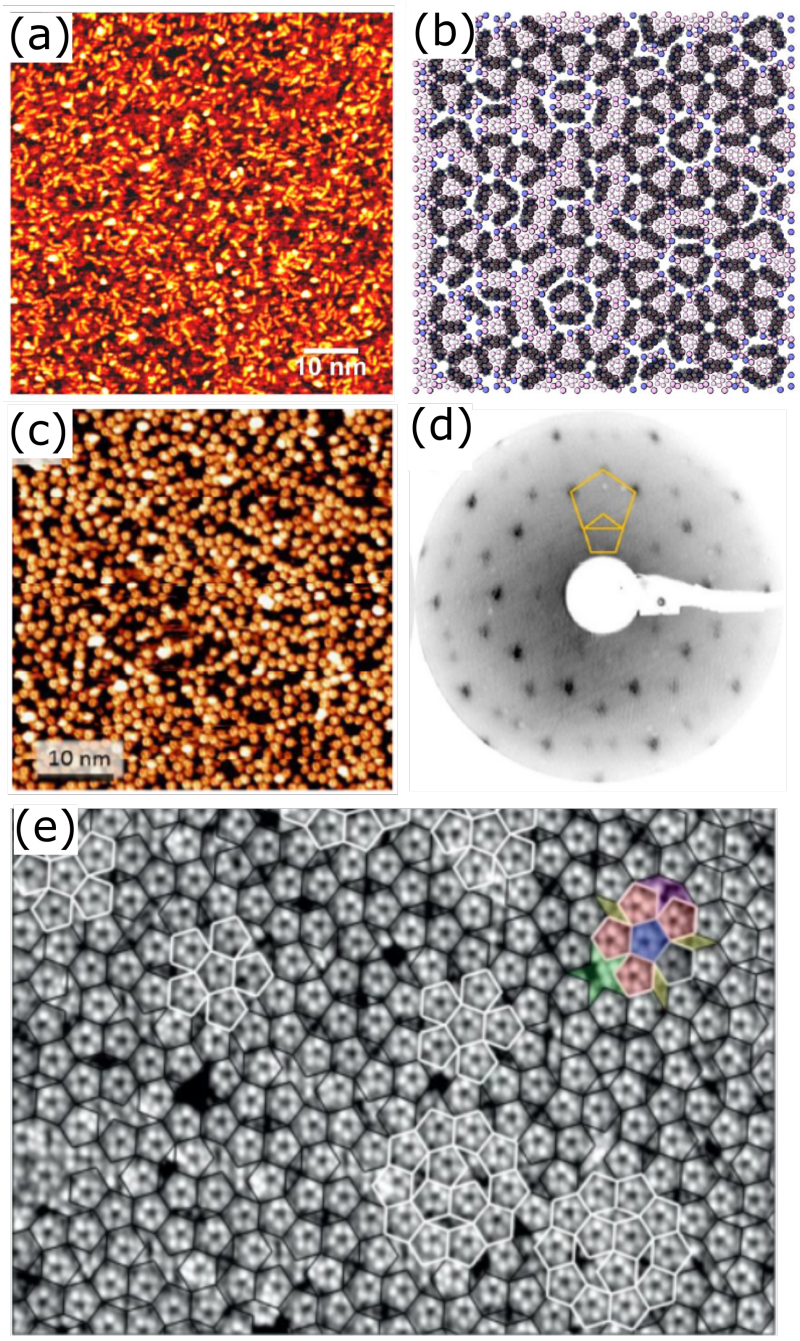

Figure 3.14: (a) STM of pentacene/5-fold *i*-Ag-In-Yb at high coverage and (b) the saturated model of the surface with decorated pentacene, showing pentacene atop 10-fold symmetric points. Reproduced and modified from [196] (c) STM of corannulene/ 5-fold *i*-Ag-In-Yb with 0.85 ML coverage, and grown with substrate held at 473 K. (d) LEED of the same surface as in (c) at 14 eV, showing τ-scaled pentagonal symmetry. Reproduced and modified from [224]. (e) A 40 x 36 nm^2 STM of ferroceneacetic acid deposited atop the periodic Au(111) substrate, which forms a thin film described by the P1 Penrose tiling (overlaid). Reproduced and modified from [225].

packing. The molecular arrangement displays pentagonal tiles with edges of 2.0 ± 0.1 nm, frequently decorated by smaller, centred pentagons (edge 1.2 ± 0.1 nm) rotated by $2\pi/5$, aligning with the substrate's 10-fold symmetry and τ-scaling. This structure matches the underlying decagonal QC's model, where C_{60} molecules adsorb preferentially at cluster centres (nodes of a P1 tiling) and locally 5-fold symmetric sites within 2 nm clusters, reproducing the observed pentagonal motifs. Investigations conclude that without facilitating C_{60} mobility by annealing during deposition, and the chosen molecule having commensurate structure with the substrate, a disordered film is likely to be formed due to C_{60} strongly bonding at the surface [195].

Other molecular adsorbates such as the pentacene ($C_{22}H_{14}$) [196, 208], corannulene ($C_{20}H_{10}$) [224], and coronene ($C_{24}H_{12}$) [226] have also been desposited atop the *i*-Ag-In-Yb and i-Al-Pd-Mn systems, demonstrating templated QC thin film growth. In the pentacene/ 5-fold *i*-Ag-In-Yb system, pentacene is deposited with the substrate at room temperature, found to absorb atop 10-fold symmetric points, as shown in Figure 3.14(a) and (b). At the interface two bonds are formed, each between a pentacene (electron donor) benzene ring and substrate Yb (electron acceptor) atom - as most Yb atoms occur in decagons around clusters, resulting in a 10-fold thin film. Next, pentacene atop the 2- and 3-fold *i*-Ag-In-Yb surfaces was also found to align along the high symmetry directions, resulting in thin films with characteristic QC symmetry of the substrates. Growth of corannulene, which has a similar C pentagonal ring surrounded by five benezene rings as C_{60}, deposited atop the 5-fold *i*-Ag-In-Yb surface, produced a 10-fold QC thin film - as shown with and STM and LEED in Figures 3.14(c) and (d) [224], respectively. Finally, coronene deposited atop 5-fold *i*-Al-Pd-Mn forms a P1 Penrose tiling thin film, indicative of the substrate [226].

Finally, growth of QC thin films has also been achieved on periodic substrates. For example, ferroceneacetic acid (FcCOOH) molecules self-assemble into a thin film with 10-fold symmetry on Au(111), demonstrating QP ordering without influence from a quasicrystalline substrate. The structure comprises cyclic pentamers formed by hydrogen bonding, interconnected by FcCOOH dimers. An overlay of a Penrose P1 tiling confirms the QP arrangement of this molecular network, as shown in Figure 3.14(e) [225].

Chapter 4

Experimental Methods

4.1 Introduction

This chapter will cover the experimental techniques used to prepare and measure fabricated quasiperiodic systems. The methods included in this chapter detail the preparation of multiscale quasiperiodic systems, and the measurement of their properties with various techniques from the atomic to nanoscale. Where applicable, the advantages and limitations of each technique will be discussed in the context of quasiperiodic systems.

4.2 Achieving and Measuring Ultra-High Vacuum

This section will describe pressure regimes from rough to ultra-high vacuum (UHV), vacuum pumps, and vacuum gauges, a full range of which are utilised and measured during the course of this thesis. For this section, the textbooks *A Users Guide to Vacuum Technology* by O'Hanlon [227] and *Fundamentals of Vacuum Technology* by Leybold [228] are referred to throughout as references for gas theory, gauges, and pump function.

4.2.1 Vacuum Pressure and Flow Types

Vacuum pumps reduce gas pressure and density within chambers to higher vacuum pressure regimes. Pressure regimes are important to help describe the type of gas flow behaviour, vacuum pump and gauge ranges, and particle mean free path. The kinetic theory of gases follows from the framework of many Boltzmann distributed distinct particles forming an ideal gas in a fixed volume, between which there are no effective forces. A derivation of the kinetic theory of gases is particle mean free path and collision rates. The mean free path is the average distance covered $\bar{v}t$ by a particle before colliding with another particle, expressed as $\lambda = \frac{\bar{v}t}{V_{Int} \times n}$, where V_{Int} is the volume of interaction and n is the particle number density $n = \frac{N}{V}$ relating to chamber pressure $p = nkT$. The derivation starts by considering two particles of radius r and diameter d=2r in Figure 4.1. The

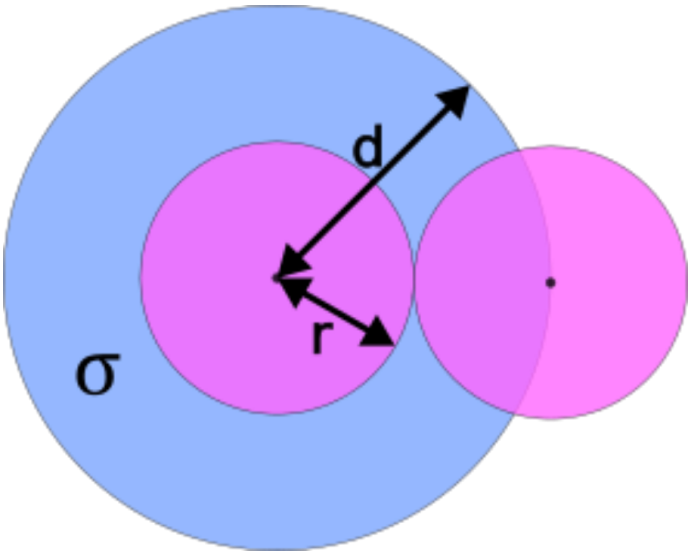

Figure 4.1: Diagram of two atoms (pink circles) of radius r, separated by distance d, interacting with each other over a cross section σ (blue circle).

collision cross-section is $\sigma = \pi \mathrm{d}^2$, and the average directional particle speed following a Boltzmann distribution is $\bar{\mathrm{v}} = \sqrt{\frac{8\mathrm{kT}}{\pi \mathrm{m}}}$. While the distance travelled for one particle is $\bar{\mathrm{v}}\mathrm{t}$, the $\mathrm{V_{Int}}$ must consider relative velocity of two particles moving, which increases volume of interaction by $\bar{\mathrm{v}}_{\mathrm{Rel}} = \bar{\mathrm{v}}\sqrt{2}$. Finally, the mean free path is given with the equation:

$$\lambda = \frac{1}{\sqrt{2}\pi d^2 n} \tag{4.2.1}$$

Gas flow is the directional behaviour of particles, which changes as a function of pressure into three broad categories: viscous flow, Knudsen flow, and molecular flow. The pressure regimes, flow type, and mean free path are shown in Table 4.1. The flow state is characterised by the dimensionless Knudsen's number $\mathrm{K_n} = \frac{\lambda}{\mathrm{D}}$, where D is the diameter of the pipe or chamber. Viscous flow refers to the regime where $\mathrm{K_n} < 0.01$, such that the

Vacuum Type	Pressure (mbar)	Flow Type	λ (m)
Rough: $\mathrm{K_n} < \frac{1}{100}$, $\mathrm{R_n} > 2200$	1000 - 1	Viscous - Turbulent	$10^{-8} - 10^{-5}$
Rough: $\mathrm{K_n} < \frac{1}{100}$, $\mathrm{R_n} < 1200$	1000 - 1	Viscous - Laminar	$10^{-8} - 10^{-5}$
Rough: $\mathrm{K_n} < \frac{1}{100}$, $1200 < \mathrm{R_n} < 2200$	1000 - 1	Viscous - Choked	$10^{-8} - 10^{-5}$
Medium: $0.01 < \mathrm{K_n} < 1$	1 - 10^{-3}	Knudsen	$10^{-5} - 10^{-2}$
High: $\mathrm{K_n} > 1$	$10^{-3} - 10^{-7}$	Molecular	$10^{-2} - 10^{2}$
Ultra-High: $\mathrm{K_n} > 1$	$10^{-7} - 10^{-13}$	Molecular	$10^{2} - 10^{8}$

Table 4.1: Table showing how vacuum type relates to pressure, flow type, and mean free path (λ). $\mathrm{K_n}$ refers to Knudsen's number, and $\mathrm{R_n}$ is Reynold's number, which differentiate flow types.

particle mean free path is much less than the diameter of the pipe, and flow is determined by gas-gas collisions. Depending on the speed distribution (or thermal energy) of particles, viscous flow is further divided into three flow types: Turbulent, Laminar, and Choked. The viscous flow subcategory can be calculated according to the dimensionless Reynold's number: $R_n = \frac{U\rho D}{\nu}$, where U is the stream velocity, ρ is the mass density, and ν is the viscosity. Table 4.1 further shows each R_n value for the viscous flow types. Turbulent flow refers to chaotic vortex motion, laminar flow typically occurs for lower velocity gases which streamlines flow, and choked flow where gas speed is high but through a narrow pipe. Knudsen flow is a superposition of continuum and molecular flow at low to medium vacuum, where gas-gas and gas-wall collisions may occur. Finally, molecular flow is dominant at high to UHV, where no gas-gas collisions occur in a standard sized UHV chamber.

4.2.2 Vacuum Pumps

Many surface analysis techniques, such as electron and tunnelling microscopes, require high and UHV pressure regimes. To reach high pressure regimes, vacuum pumps are needed to remove particles from atmosphere in the chamber, and pressure gauges (Subsection 4.2.3) safely operate the pumps and verify pressure levels. Vacuum pumps are broadly separated into either backing pumps (suitable at operating from rough vacuum) to high vacuum pumps (suitable at operating from high vacuum).

Rotary Vane Pump

The rotary pump is a standard oil-sealed backing pump for UHV chambers and most high-vacuum systems, capable of pumping from atmosphere to roughly 10e-3 mbar. Figure 4.2(a) shows a labelled diagram of a standard rotary pump [227]. Gas enters through the intake (1) and filter into the suction chamber (A), is then compressed (B) by an eccentrically mounted rotor (3) and expelled to atmosphere through the discharge valve (C). An airtight seal is made by spring-loaded vanes and closely spaced sealing surfaces with a low vapour pressure fluid.

Turbomolecular Pump

A standard turbomolecular molecular pump is shown in Figure 4.2(b) [227], which is capable of pumping from rough to high vacuum with the aid of a rotary backing pump. The operating principle is that when gas particles are impacted by a rapidly moving rotor and static stator, there is an impulse which causes a controlled directional flow. The rotor, shown in Figure 4.2(c) [227], operates at speeds in the range of 24,000 - 80,000 rpm, with blade angles increasing in pitch further down into the assembly. Gas particles enter through a large surface area, are directionally but diffusely deflected further down into the

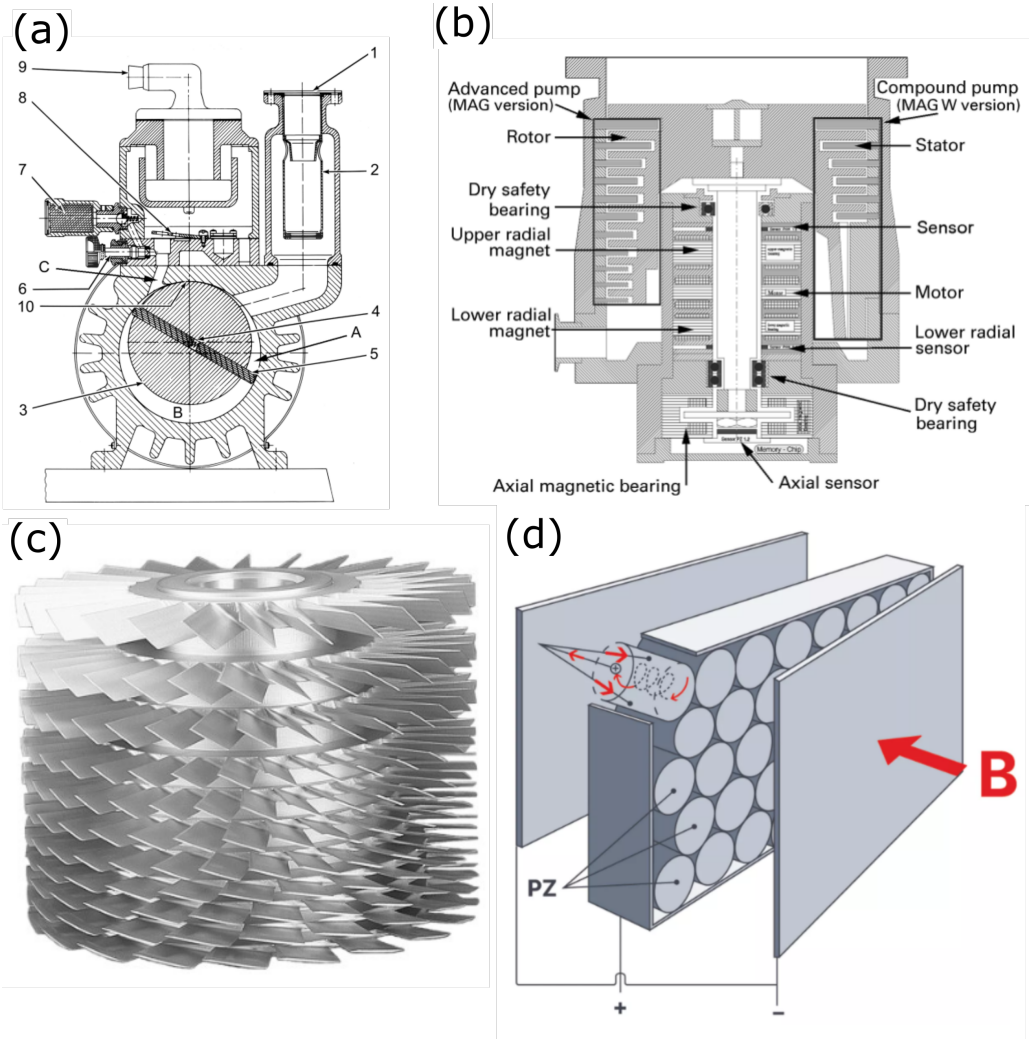

Figure 4.2: (a) Schematic of reotary vane pump: (1) intake, (2) filter, (3) rotor, (4) spring, (5) vane, (6) gas ballast valve, (7) filter, (8) discharge valve, (9) exhaust, (10) sealing surface, (A) suction, (B) compression, and (C) exhaust chamber. (b) Schematic cross-section of turbomolecular pump. (c) Rotor of a turbomolecular pump, showing blades of descreasing pitch from top to bottom. Reproduced from [227]. (d) Schematic of sputter-ion pump, with Penning tubes labelled PZ, high-voltage polarities, and magnetic field B indicated. Helical electron path and straight ion path are drawn. Reproduced from [228].

assembly, where compression increases and the speed of the gas decreases. When operating, the rotor will cause vibration to surrounding components, which may be observable with STM. A common solution is a magnetically levitated axial bearing, which has the added benefit of reducing wear on the assembly without the use of hydrocarbon-based oils (though these may be reintroduced by the rotary pump). Another option is to completely turn off the pump during image acquisition in UHV.

Sputter-Ion Pump

The ion pump is capable of pumping from high to UHV without the use of hydrocarbons or mechanical parts, and exploits embedding of energetic ions in surfaces. The operating principle involves two cathode plates separated by a series of open cylinder anodes, producing electron emission towards the anodes. By applying an axial magnetic field, as shown in Figure 4.2(d) [228] labelled **B**, the electrons become trapped in helical orbit potential well between cathodes, which prevent recombination with the anode. Due to the potential well, the electrons have a much longer path length commensurate with the mean free path, allowing electron ionisation of neutral gas species within the array. Ions formed via electron impact are more massive than electrons, not as easily steered by magnetic fields, and accelerate towards the cathode. In general, ions embed in the surface of the cathode, which is made of Ti, effectively sputtering Ti, secondary electrons, and other surface species back towards the anodes. More specifically - organic vapours, active gases, H, and inert gases, are all pumped with distinct regimes.

Organic vapours are dissociated or fragmented by electron impact and chemisorbed onto the surfaces on the electrodes. Active gases readily react with sputtered Ti, and are either sputtered on anode surfaces, or embedded and chemisorbed in the cathode. H is unique because its low mass prevents it from significantly sputtering the cathode, but can still be embedded and chemisorbed in the cathode. If the residual gas has high concentrations of H, Ti is not effectively sputtered from the surface, and will cause warping of the cathode alongside outgassing when heated. This issue is not really a significant problem because even a small concentration of inert gases will compensate Ti sputtering of the cathode. Inert gases have a comparatively much lower ion pumping efficiency (1-2% of active gases), as they are only embedded and not chemisorbed into the electrodes. This is a problem because the inert gases are more easily re-released from the surface when sputtered. Operation of the turbomolecular pump, or a triode configuration, will relieve this build-up. One important note is that occasionally there is such a significant build-up of compounds in the surface layers that the electrodes under high voltage burp out surface species, increasing chamber pressure. In principle all pumped (absorbed by electrodes) species in surface layers are susceptible to being re-released into the chamber during ion sputtering. Finally, a detector may also be placed near the cathodes to act as an ion gauge.

Titanium Sublimation Pump

The Ti sublimation pump operates with a similar working principle to an ion pump, but a Ti filament is instead heated (approx. 1850 K) to sublimate Ti into the chamber. Ti is deposited onto the chamber walls which readily captures active gases to effectively pump them from the main chamber volume, reducing the pressure.

Cryogenic Pumps

Cryogenic pumping comes in a wide range of forms, where the surface is cooled typically with liquid N- or He-, increasing the sticking coefficient of particles within the chamber. The three main cryopumping mechanisms are cryocondensation, cryosorption, and cryotrapping. Broadly, there are three types of cryopump: bath cryostats, continuous flow cryopumps, and refrigerator cryopumps. Bath cryostats are where the pumping surface is cooled from their back side with a cold trap filled with liquid N (LN2). On a surface cooled with LN2 (77 K), H_20 and CO_2 readily condense, and on a surface cooled with liquid He (LHe) (4 K) all gases except He are capable of condensing. In continuous flow cryopumps the surface acts as a heat exchanger, where LHe is pumped from a reservoir into the evaporator to cool a cold surface, which condenses nearby gas particles. Finally, a refrigerator cryopump is the most common cryopump, where cycles of LHe act as a working fluid between an expander and compressor, cooling the inside of the chamber.

4.2.3 Vacuum Gauges

Penning Cold Cathode Ion Gauge

Cold cathode gauges consist of a cathode and anode with a high voltage applied between the two, which generates electrons at the cathode that travel towards the anode. A permanent magnet surrounds the measurement chamber, creating a magnetic field which causes the electrons to travel in a long helical trajectory, eventually colliding with neutral species to form charge carriers. Positive charge carriers produced by electron impact travel towards the cathode forming a pressure-dependent discharge current which can be measured with a meter. At pressures above 1×10^{-2} mbar the Penning discharge changes to a glow discharge and so the pressure dependent discharge current is overwhelmed and is not suitable for measuring pressure. Ion gauges are therefore suitable to use on UHV chambers. A final note is that the same adsorption mechanism which is beneficial for the ion pump is detrimental for the ion gauge, as species buildup on the electrodes impedes the gauges performance.

Hot Cathode Ion Gauge

The hot cathode gauge is operationally similar to the Penning gauge, but the cathode is heated to produce a much higher yield of electrons, and there is no applied magnetic field. The heated cathodes may be made of W, but oxide-coated Ir (Th_2O_3, Y_2O_3) is more favoured where O is expected to be present in the chamber. The emitted electrons have sufficient energy to ionise residual gas, positive ions are then accelerated towards the anode and collector plate, where their pressure-proportional current can be measured.

Pirani Gauge

The Pirani gauge measures thermal conductivity in the rough vacuum regime. A filament is Joule-heated up to between 100 and 150 °C, which heats gas in the measurement area via radiation and thermal dissipation. If at rough vacuum the mean free path is similar to the filament diameter, heat transfer becomes dependent on the surrounding gas density. The transfer of heat away from the filament therefore increases as pressure increases in rough vacuum, measuring either the resistance (variable temperature) or applied voltage (constant temperature) can therefore give a pressure reading. The Pirani gauge is not suitable for measuring pressure outside of rough vacuum, as heat transfer is no longer a function of pressure. The Pirani gauge is therefore suitable for measuring load-lock pressures during sample mounting into UHV chambers before initialising lower pressure vacuum pumps.

4.3 Thermal-Scanning Probe Lithography

This section describes thermal-scanning probe lithography (t-SPL). The principle of t-SPL is explained, then an overview of the full method is given, before going into detail for each step in the method. Chapter 5 gives a thorough description of t-SPL, and the optimisations that are essential for reproducibly fabricating high-quality nanoscale structures, tailored for the user's needs. Samples measured in Chapters 6 and 7 were fabricated following the methods in this section.

4.3.1 Chemical Method

An overview of the chemical method is shown in Figure 4.3. The substrate is prepared with stacks of resist material, which are designed to break down under a specific stimulus, such as heat or a solvent. The lift-off and thermal resists are sequentially pipetted onto the surface and spin-coated. The first and bottom resist layer, Polydimethyl glutarimide (PMGI), is a standard lift-off resist with a controlled development time, preserving the pattern and chemically removing molecules without leaving residue. PMGI SF2 was used in this research, provided by Kayaku Advanced Materials. The lift-off layer introduces a thermal and physical barrier between the t-SPL tip and the substrate, keeping the tip hot through less heat exchange and avoiding directly scratching the substrate. The thermal resist is pipetted and spin-coated following lift-off resist preparation. Thermal resist polymers are designed to depolymerise under thermal stimuli, sublimating molecules around the heated tip, which do not readily reabsorb onto the surface. For t-SPL, the thermal resist anionically polymerized polyphalaldehyde (PPA) solution is chosen. The PPA used in this research is the AR-P 8100 series provided by AllResist. PPA is distributed as a cooled

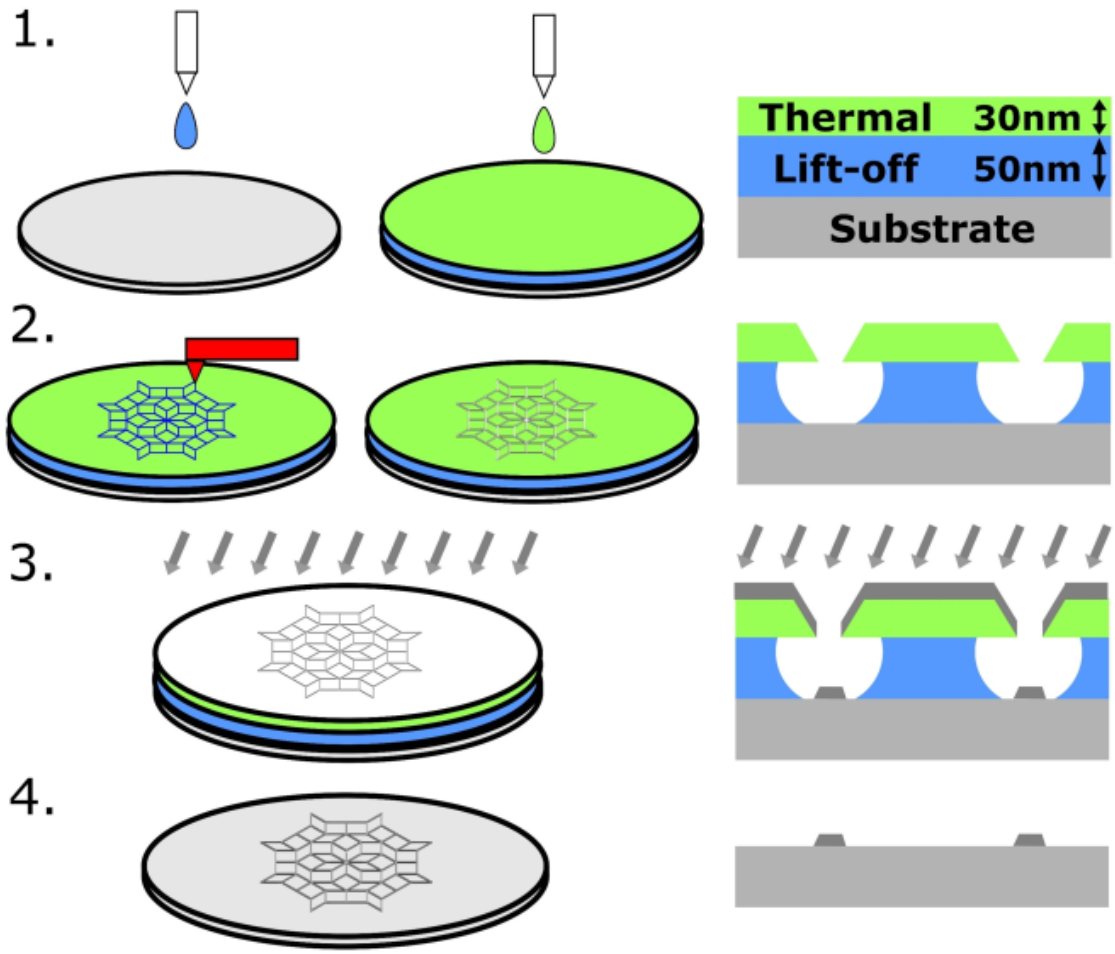

Figure 4.3: A graphic showing the procedure for thermal-scanning probe lithography. Step 1: Lift-off (bottom) and thermal (top) bi-layer polymer resists are deposited and spin-coated sequentially onto a clean atomically flat substrate. Step 2: A heated t-SPL tip sublimates surface molecules into a pattern in the thermal resist, a solvent then chemically etches (resist development) the patterned area which exposes the substrate, creating a mask. Step 3: A user-specified material, chosen for physical properties, is evaporated onto the masked sample. Step 4: The polymer resists are chemically removed in a lift-off process, leaving the desired pattern.

powder, so before coating the substrate the powder must be measured, dissolved in anisole, sonicated, and then filtered before the solution can be pipetted and spin-coated.

In step 2 of Figure 4.3(left), the t-SPL NanoFrazor [229] sublimates patterned structures from greyscale images, patterning pixel-by-pixel whereby darker areas are etched leaving white areas untouched. The result is exposed areas of the bottom lift-off resist following the etched pattern. Greyscale patterns are generated with Inkscape and a Python script for generating quasiperiodic tilings, discussed further in Chapter 5. Greyscale images are uploaded to the NanoFrazor software ready to pattern. In step 2 of Figure 4.3(right) a solution of tetramethylammonium hydroxide (TMAH), an ammonium salt, is mixed

with isopropanol. Exposed areas of the lift-off resist are chemically removed by applying TMAH. Varying the concentration of isopropanol in TMAH influences dissolution rates when applied to the lift-off layer, which develops isotropically, and exposes the substrate. This development creates an 'undercut', whereby the lift-off resist is chemically removed from underneath the thermal resist. The undercut helps to stop sidewall deposition on the lift-off layer during material deposition, which would fuse too easily to the surface and harm the pattern quality.

In Figure 4.3 step 3, controlled material deposition is performed with electron-beam physical vapour deposition. Finally, in Figure 4.3 step 4, the sample is bathed in a dipolar aprotic solvent, such as N-Methyl-2-pyrrolidone (NMP) or Dimethyl Sulfoxide (DMSO), to completely remove the lift-off resist layer, leaving the desired pattern remaining.

Substrate Prep and Spin-Coating

The substrate, typically Si, is delivered in sealed dust-free wafer containers, and when ready to use is washed with acetone and isopropanol before resist coating. The substrate is prepared by pre-baking on a hot plate above 100 °C to evaporate water, and up to 10 s oxygen plasma ashing to remove residue and promote resist adhesion through greater surface energy. Depositing resists with a pipette onto the substrate and then accelerating the spin speed ω through spin-coating allows tailoring of the resist height t_{height} as low as 8 nm as $t_{height} \propto \frac{1}{\sqrt{\omega}}$ [230], with spin-coat tables provided by the resist manufacturers. Post-deposition preparation includes a hot plate bake to reduce the solubility of the resists.

Spin-coating describes the process by which uniform thin films of resist materials are prepared on substrates for nanolithography. In brief, the coating is deposited, then spun such that the centrifugal force moves the coating radially outwards. There are a few factors to consider: deposited volume, angular velocity spin, final film thickness, solution viscosity and concentration, and spin time. The stages of spin-coating are thus:

1. Deposition: The solution (resist) is deposited, then the substrate is accelerated until the resist reaches a critical height as the solution is spread over the substrate.

2. Spin Up: The substrate is accelerated to the desired angular velocity, with velocity tables given in [229]. The target resist height (thickness) is reached in minutes when balanced with the viscous shear drag and angular velocity. The height of the resist after spinning is given by:

$$h(t) = \frac{h_0}{(1 + 4Kth_0^2)^{\frac{1}{2}}} \tag{4.3.1}$$

where $K = \frac{\rho\omega^2}{3n}$, fluid density ρ, angular velocity ω, and absolute viscosity n. Here, fluid viscous forces dominate thinning of the resist.

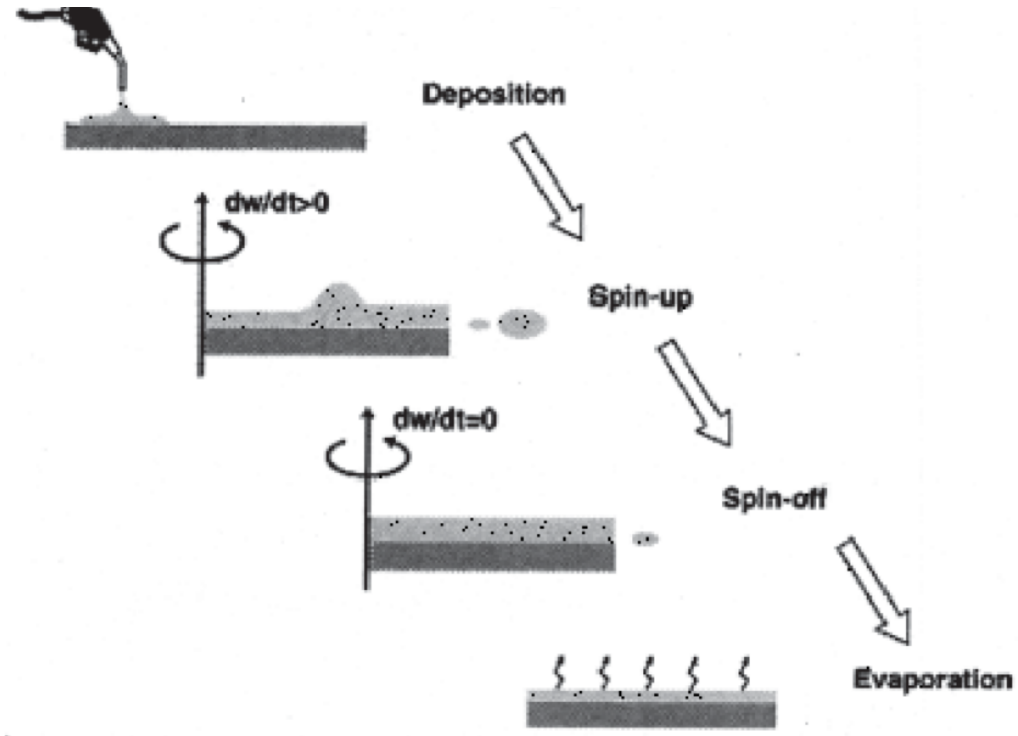

Figure 4.4: Typical stages of the spin-coating process from deposition to evaporation are shown, with the rate of change of angular momentum represented by dw/dt. Reproduced from [231].

3. Spin Down: After the target resist height is reached across the surface, the substrate is decelerated to zero angular velocity, outflow stops, and the substrate is removed from the spin-coater.

4. Evaporation: The resist thin film begins drying immediately. To encourage uniform coverage, the substrate and resist are soft-baked to increase bonding and remove water vapour.

Lift-off Resist (Bottom Layer)

During spin coating, the substrate is accelerated to a specific angular velocity, according to the desired final thickness. Target thickness is calculated for when the viscous shear drag and angular velocity are balanced. Figure 4.5 [232] shows a spin curve of a series of resists for the lift-off resist chosen (SF2). The final thickness of the resist is inversely proportional to angular velocity, so a thinner resist will form with greater spin speeds.

In this experiment PMGI SF2 is chosen to reduce the thin film thickness to a minimum while remaining structurally stable. Before dispensing the resist onto the surface the substrate should be clean and dry. The substrate is washed clean with a solvent such as acetone and then distilled water, and blown dry with Ar before soft-baking on a hot plate

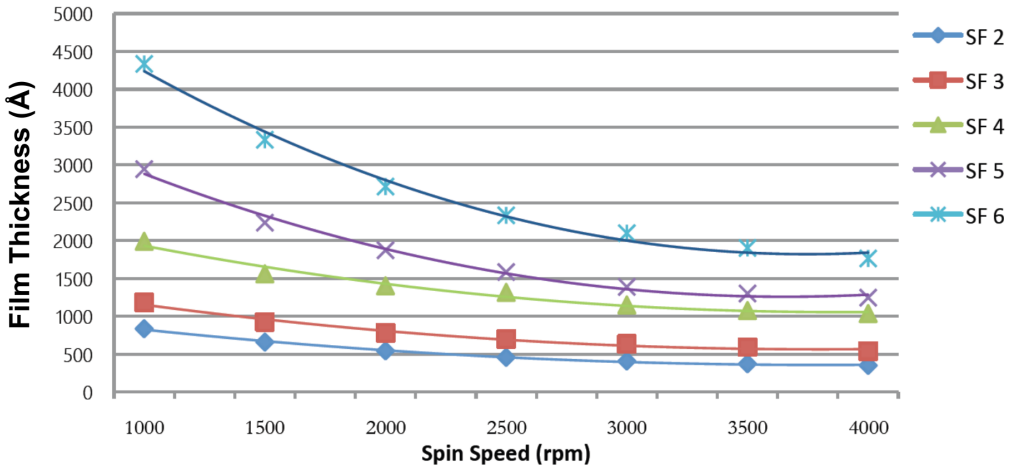

Figure 4.5: Thickness against speed spin for the PMGI SF series of lift-off chemical resists. The SF2 is chosen for this research to reduce thin film thickness to a minimum for high-resolution patterning. Reproduced from [233].

at 200°C for 5 minutes. The soft-bake temperature will influence the adhesion of PMGI to Si, with increasing temperatures leading to a lower dissolution rate [233]. The purpose of the soft-bake is to improve adhesion by dehydrating the surface and increasing surface energy. PMGI easily wets the surface (spreads and adheres well), and dries quickly, so it is important to begin spinning soon after deposition. As thickness is inversely proportion to angular velocity, for SF2 a spin rate of 2000 rpm will be roughly 50 nm thick, whereas 4000 rpm will be roughly 30 nm thick. Thinner resists are more optimum for higher resolution patterns, but SF2 is structurally limited to around 30 nm. Following spin-coating, the substrate is soft-baked to 180°C for 2 minutes to harder the polymer structure.

Thermal-Resist (Top Layer)

Shortly after the lift-off resist has dried onto the substrate, the thermal resist pre-treatment begins. The substrate pre-treatment starts with a soft-bake to dehydrate the surface. The chosen thermal resist for this research is the thermolabile positive resist AR-P 8100, which has the base polymer anionically polymerised polyphaladehyde (PPA), and easily breaks down with heat stimulus such as in t-SPL [234]. Handling of PPA powder must be delicate, as PPA powder has a flash point of 44°C. The PPA is delivered in powder form and must be prepared into a PPA-anisole solution which is insoluble to and easily wets PMGI. Dissolving in anisole increases the flash-point temperature, and is required for resist spin-coating. However, in liquid form the PPA will quickly evaporate in air, and therefore the PPA is stored in powder form in a refrigerator to extend shelf-life. Typical shelf-life of refrigerated PPA powder is of the order of 12 months. The concentration of PPA in anisole is also proportional to the spin-coated resist thickness, as seen in Figure

Concentration	PPA Solutions, Phoenix 8100 film thickness [nm]																																					
wt[%]	6	8	10	12	14	16	18	20	25	30	35	40	45	50	55	60	65	70	75	80	85	90	95	100	110	120	130	140	150	160	170	180	190	200				
0.85		6k	5k		2k																																	
1.3				6k				2k																														
2							6k	4k	2k																														
2.5								6k	5k			2k																										
3										6k				2k																								
5											6k									2k																		
6																			6k	5k		4k		3k		2k												
7.5																					6k							2k										
10																											6k									2k		

Figure 4.6: Spin-coating table of final resist thickness (nm) as a function of the concentration of PPA in anisole. Recommended concentrations are highlighted with a darker blue in the leftmost column. Reproduced from [232].

4.6.

Figure 4.6 shows different concentrations of PPA powder dissolved in anisole, with decreasing spin speeds giving a thicker resist. For example, for a 30nm PPA layer an appropriate mix would be a 2% concentration spun at 2000 rpm or a 2.5% concentration spun at 5000 rpm. It is clear from inspection of this table that small deviations in concentration cause significant deviations in the final film thickness at constant spin speed. Note before mixing, the PPA powder needs to be close to room temperature to avoid moisture condensing into the mixture. The PPA solution preparation protocol for a 14 nm thick resist film is as followed:

1. A 3 mL vial is placed onto an analytical balance and zeroed.

2. Powdered PPA close to room temperature is weighed into the vial. Anisole has a density of 0.995 gmL^{-1}. For a 0.85% PPA concentration in anisole, 0.0255g of PPA powder is added to 2.989 mL of Anisole. Screw on a lid and shake thoroughly.

3. The PPA solution is transferred by a sterile syringe and filtered using a 0.2µm filter into a small clean bottle for storage or directly to spin-coating.

Following the preparation protocol, the solution must be stored in a refrigerator, or directly used for spin-coating. Spin-coating is performed at an angular velocity specified for a given concentration and thickness in Figure 4.6. Following spin-coating, the substrate is finally soft-baked to dehydrate the surface at 110°C for a 1 minute. The substrate and resist stacks are now ready for t-SPL patterning.

4.3.2 Principle of t-SPL

The t-SPL instrument, shown in Figure 4.7(a), and enlarged in (b), is a natural evolution of the atomic force microscope with a potentially heated nanoscale probe, that sublimates surface molecules to etch a pattern into a resist [235]. The probe, indicated 'cantilever' in Figure 4.8(a) is manually mounted onto a piezoelectric cantilever with common, write bias, and read bias applied voltages. These probes feature a cantilever structure with a nanoscale

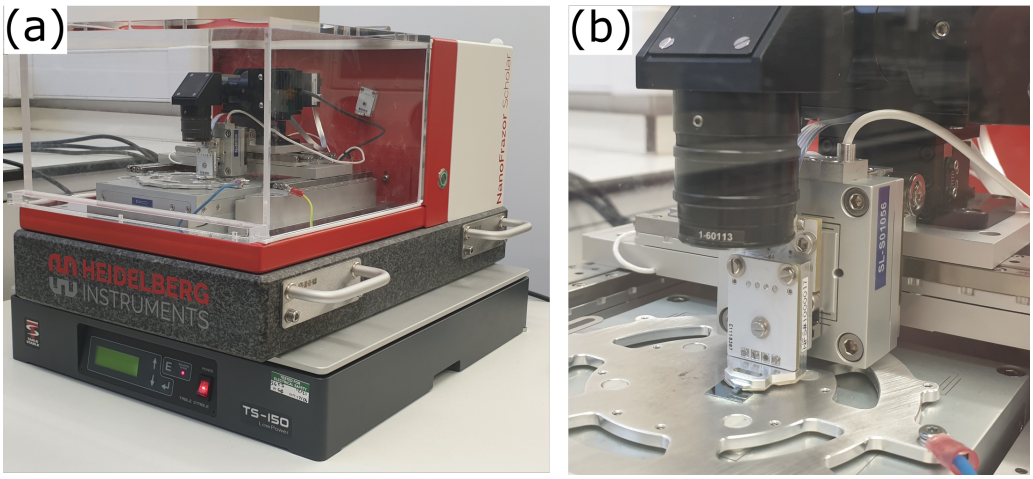

Figure 4.7: Photographs of the NanoFrazor t-SPL instrument. (a) The entire assembly. (b) An enlarged view of the optical camera, cantilever holder, and a square wafer ready for patterning.

tip, shown in Figure 4.8(b) [236]. Early designs relied on laser-assisted heating [237], similar to those in standard scanning probe microscopy systems, but advancements have shifted toward integrated Joule-heated configurations for improved practicality [129]. The representative design, shown in Figure 4.8(b) includes a U-shaped cantilever with a localised heating element in contact at close-proximity to the tip. Joule heating via a write bias generates thermal energy in the region surrounding the tip's apex, creating a nanoscale spot-size corresponding to the tip's curvature. Si-on-insulator techniques combined with oxidation-sharpened tips produce tips with apex radii of 5-20 nm [238]. The legs of the cantilever are composed of heavily doped silicon for conductivity, while the heating zone is lightly doped to enhance resistivity, concentrating heat generation near the tip. Electronically adjustable heater temperatures span from ambient conditions for a programmable heater temperature of $\approx$ 800-1,200°C, with sub-1°C precision and microsecond-scale thermal response times.

In many patterning techniques, the t-SPL probe is moved across the surface while in direct contact to deliver localised heat from the probe to the surface, enabling precise material reactions. Among all process variables, temperature is the most critical factor influencing pattern quality and consistency, necessitating precise regulation [235]. While the write heater temperature (labelled resistive tip heater in Figure 4.8(b)) can be precisely controlled, the actual tip temperature which makes contact with the surface will be lower. To better understand the temperature at the tip and height above the surface, the read sensor temperature is calibrated against the electrical current, or applied voltage, in the cantilever prior to patterning. The read sensor is in close proximity to the heated tip, and therefore forms a feedback loop with respect to the tip to determine tip temperature and height above the surface. The tip is deflected towards the surface with an applied

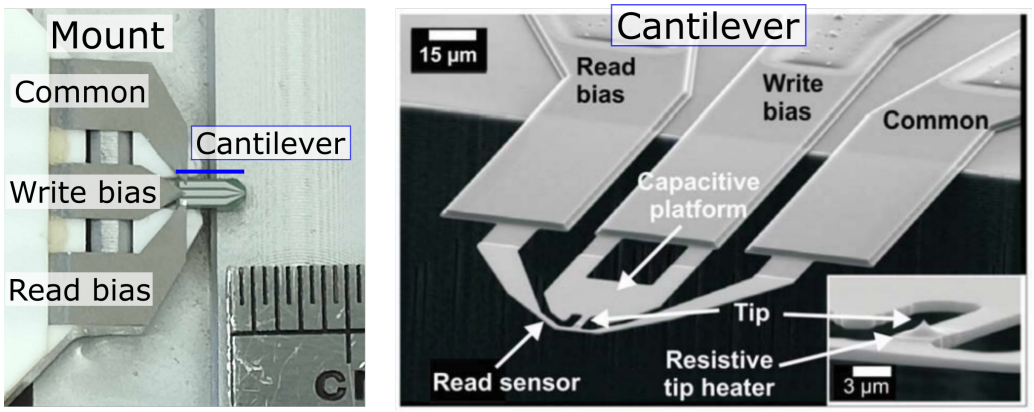

Figure 4.8: The t-SPL mount and cantilever. (a) The cantilever (blue) is shown correctly mounted. The common, write, and read bias junctions of the mount are aligned to the corresponding conductive strips of the cantilever. (b) An SEM micrograph of the cantilever. The tip is heated via the write bias voltage, with a capacitive platform for electrostatic actuation. The read sensor is located separate from the heated tip. A read field is performed by measuring heat exchange of the read sensor with the surface, directly proportional to the air gap between the sensor and surface. A magnified image of the tip and tip heater is shown inset. Reproduced and modified from [236].

voltage to the write bias, while the read sensor is kept at a fixed height and not deflected. As the heated tip deflects away from the read sensor, the temperature of the read sensor decreases. Similarly, as the heated tip is brought closer to the surface, the surface acts as a heat sink and heat is lost from the tip and read sensor. Well above the surface the tip will retain heat better, while in close contact heat is more easily lost, and the read sensor temperature will further drop. During calibration, the cantilever deflection can be monitored, as heating induces mechanical bending. Specialised systems can experimentally measure the heater temperature via Raman or infrared microscopy directly [239]. The Nanofrazor, which lacks such tools, simplified models assume a linear relationship between electrical power dissipation and heater temperature. While less accurate than optical techniques or sophisticated computational models [240], this approach ensures reproducibility in tracking the cantilever's thermoelectric behaviour and operational integrity. The calibration process relies on the unique temperature-dependent resistance of the heater material. At lower temperatures, the heater resistance rises with increasing temperature due to reduced carrier mobility in the semiconducting cantilever. However, beyond approximately 560°C, intrinsic carrier concentration in silicon surges, causing a rapid resistance drop — a phenomenon termed thermal runaway [238]. This sharp transition serves as a reliable calibration reference. For stable operation and prolonged probe durability, temperatures below the thermal runaway threshold are preferred, as they offer better control over thermal conditions. In Chapter 5, the temperature at the interface between the tip, write heater, and surface, is calculated.

A significant benefit of t-SPL over e-beam lithography techniques is producing real-time in-situ images in air of the etched pattern. The same heated tip which writes a pattern by sublimating the thermal resist is again brought into contact with the surface for a read scan, with an offset applying tension between the cantilever and surface. The tip is kept in contact with the surface for any features shallower than the offset depth, set by the user. To avoid damaging the thermal resist polymer during the read scan, a high frequency modulation of the contact force is applied via a dithering technique [236, 241]. With this dithering the tip-sample contact is periodically interrupted, allowing the polymer to relax and preventing the accumulation of excessive shear stress during scanning. The read heater sensor on a separate isolated leg of the cantilever functions as a thermistor with read bias, measuring the heat exchange (thermal conductance) with the heated tip in contact with the surface. The read heater is nominally set to 200 °C by a constant applied voltage, and held at a constant height of 200 nm above the surface. Heat exchange between the read heater and the substrate surface is increased with raised features, causing a drop in the read heater temperature. In this manner, the air between the read heater and surface acts as a heat sink. The read heater temperature and surface topology is therefore directly correlated, 3D maps of the surface are then produced with assistance from piezo approach calibration measurements [130]. A read-field scan can be performed at any time.

4.4 Electron Beam Evaporation

Metal evaporation of $Ni_{80}Fe_{20}$ onto patterned areas of exposured Si is performed for work carried out in Chapters 5 to 7. The chamber used has a load-lock backed rotary and turbomolecular pump, and a main chamber which achieves UHV and is additionally equiped with a cryostat pump. Electron-beam (e-beam) evaporation under UHV is ideal for this project due to its line-of-sight deposition mechanism, minimising contamination risks by heating materials directly and reducing interdiffusion between the source and crucible. In this process, a thermionically emitted e-beam is generated by a heated filament and accelerated by high voltage (keV), and focused with a magnetic field onto the source material [242]. The kinetic energy of the electrons vaporises the target material, with the deposition rate governed by the vapour pressure. The source is housed in a water-cooled Cu hearth, where rapid cooling solidifies the outer layer of the target material. For enhanced thermal isolation, a low-conductivity liner can be added, enabling higher operating temperatures while preserving material purity. The primary e-beam source (Telemark 575) has six indexable pockets in a water-cooled Cu hearth, each with a unique target material. The source design incorporates electromagnetic coils to raster the electron beam across the evaporant material within the large hearth. This sweeping action promotes even heating and avoids localised overheating (burrowing), which is especially critical for materials with

poor thermal conductivity. Positioned 0.725 m beneath the sample stage, the extended throw distance minimises thickness variation across substrates, as the deposition geometry is approximated as a point-source emission profile, given by:

$$\frac{dm}{dA} \propto \frac{\cos\phi \cos\theta}{|\vec{r}|^2} \tag{4.4.1}$$

where $\frac{dm}{dA}$ is the deposited mass per unit area, $|\vec{r}|$ is the vector connected the source to a point on the surface, and ϕ and θ are the angles between $|\vec{r}|$ and the source material normal or substrate normal, respectively. Under high vacuum conditions, the mean free path is much greater than 0.725 m, ensuring little to no contamination during growth. The thickness of deposited materials is monitored with a quartz crystal microbalance, where growth of thin films changes in frequency of a quartz crystal resonator. The quartz crystal microbalance was additionally calibrated with x-ray reflectivity measurements of thin film thickness [242].

4.5 Scanning Electron Microscopy

Scanning electron microscopy (SEM) is performed in Chapters 5 to 7 to measure polymer and metallic quasiperiodic patterns. SEM is performed at the University of Liverpool SEM-Shared Research Facility, with the JEOL JSM 7001F FEG-SEM. Images produced are saved as tiff file extensions and are typically analysed with Inkscape or in-situ to evaluate nanolithography success. A focused e-beam is produced by a Schottky field emission source and lens configuration. Field emission uses a liberation effect, where the spherical point of a sharp tip of radius r with an applied voltage V, will have a strong electric field E according to $E = \frac{V}{r}$. With a sufficiently high electric field the work function is lowered such that the electrons easily tunnel out of suitable materials. Pure metal materials with easily producible sharp tips such as W would be suitable for field emission. The liberated electrons are then accelerated towards an anode and away from the cathode [139]. As electrons are accelerated towards the surface, a magnetic condenser lens deflects the electrons into a focused beam. The e-beam incident on a sample interacts with the surface to produce various signals, as shown in Figure 4.9, that can be constructed into a digital image. The SEM detects secondary electrons that are emitted from the surface following irradiation by the primary e-beam. Secondary electrons are electrons in the valance band that overcome the ionisation potential and are ejected from the ion. This ejection is an inelastic process and thus secondary electrons have a low energy (1-10eV [243]). As secondary electrons have low energy, they do not travel far in the bulk before recombining. As a result, secondary electrons detected are extremely surface sensitive, giving topology with nanoscale resolution. The SEM image formed is therefore a function of the valance band structure

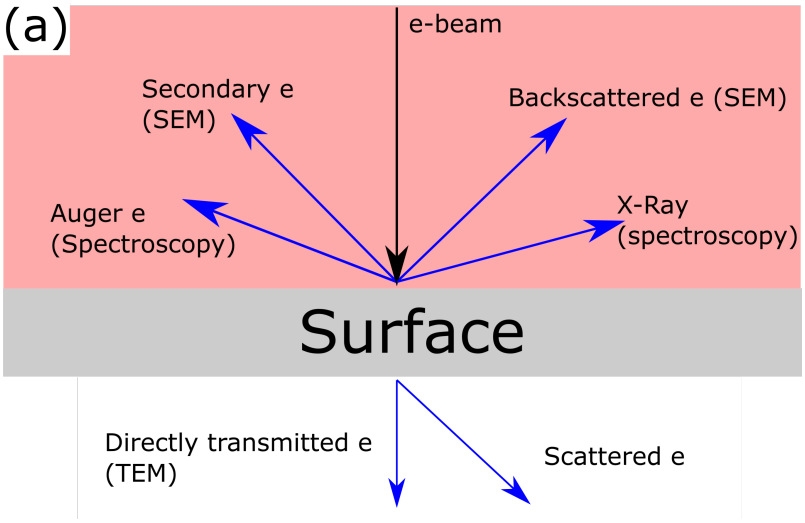

Figure 4.9: Graphic showing a primary e-beam interacting with a surface to produce a series of secondary species. Directly transmitted electrons through thin samples may be measured with transmission electron microscopy (TEM). Scattered electrons in the bulk are also indicated.

of the surface and topology.

SEM is complimentary with detecting other secondary species from the surface, such as backscattered electrons and characteristic X-rays. Backscattered electrons are primary electrons reflected from the surface. Heavier atoms more easily reflect the electron due to a high atomic number. Backscatter electron images thus form from samples of heavier and lighter ions. X-ray emission is caused when primary electrons create an inner electron vacancy, causing outer electrons to 'fall' in to fill the vacancy. Energy released from the vacancy can be a characteristic X-Ray, or sometimes a low energy auger electron is ejected. Energy dispersive X-Ray spectroscopy (EDX) is used in conjunction with an SEM to identify elements in a sample.

Figure 4.10 shows SEM images of the same region of fabricated QP detected with two different species: in (a) secondary elections, and in (b) backscatter electrons. Both images are greyscale but offer different information. In Figure 4.10(a), the e-beam inelastically interacts with the surface, producing secondary electrons. Darker areas are deeper areas, where electrons released from recesses close to features in the surface reabsorb before being detected. Sample preparation may be required for non-conductive samples, as the surface acts as an electron trap leading to bright white spots on the SEM. Charging effects can be caused where there is an imbalance between the primary electron beam and emitted electrons, combined with the inability of insulators to conduct away the excess charge. This causes SEM imaging of polymers to be difficult, and often metallic thin films must be deposited on the surface, or metallic clips near the imaging site, to increase charge flow. A charging effect will result in a dark black contrast along scanned sites, impeding

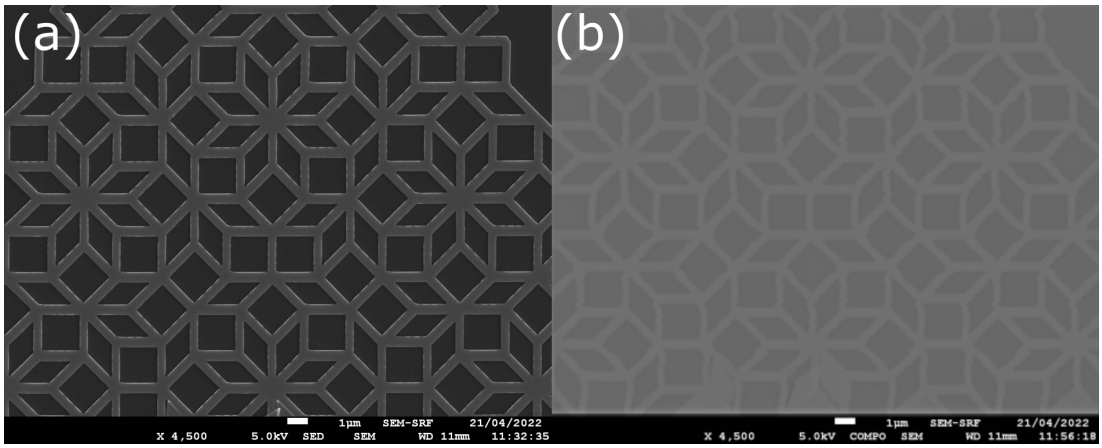

Figure 4.10: SEM images of the same region of fabricated QP tilings with two detection modes: (a) Secondary electrons, showing surface topology. (b) Backscatter secondary electrons, showing elemental composition.

imaging. Charging can also occur on metallic surfaces when the e-beam is focused to a high resolution spot size for prolonged periods.

Figure 4.10(b) shows the same region of tiling as in (a), with brighter areas corresponding to heavier elements, whereas the darker areas correspond to lighter elements. The backscattered electrons are elastically reflected into the detector from the surface. In this case the lighter areas are $Ni_{80}Fe_{20}$ and darker areas are Si. Backscatter electron microscopy is then useful for showing significantly differing composition on the surface layers.

4.6 Quasicrystal Surface Analysis Techniques

4.6.1 Surface Preparation and Molecular Evaporation

Ex-Situ

Quasicrystals are grown with Czochralski, Bridgman, Floating Zone, or Self-Flux methods [244, 245]. The *d*-Al-Ni-Co quasicrystal used in Chapter 8 was grown with the Czochralski method at the Ludwig-Maximilians-Universität München by Peter Gille [246]. In the Czochralski method, a measured quantity of feed materials, determined by the required crystal stoichiometry, is melted within a cylindrical crucible using resistance or radio-frequency heating. A seed crystal tip is then immersed into this melt. By withdrawing the seed slowly, crystallisation occurs at the interface between the seed and the melt, forming a new section of crystal. Precise regulation of the melt temperature, the rate at which the crystal is pulled upwards, and the rotation speed enables control over the final crystal's dimensions. In first experiments without a seed crystal, spontaneous nucleation at the tip of a Al_2O_3 ceramic rod is achieved by dipping into the melt rather than the seed

crystal [246].

Following growth of the *d*-Al-Ni-Co quasicrystal, the surface was polished with successively finer grades of diamond paste from 6 μm down to 0.25 μm, and cleaned in an ultrasonic methanol bath before being inserted into a UHV chamber with a base pressure of $\sim 1 \times 10^{-11}$ mbar. The research in Chapter 8 utilised an Omicron VT-STM UHV chamber, a variable-temperature scanning tunnelling microscopy (STM) system. The cleaned quasicrystal is mounted on a stainless steel Omicron sample plate, and held tightly in place via spot welding Ta wire straps around the edges. Finally, the sample plate is loaded into a vented load-lock.

In-Situ

UHV conditions are essential for measurements of crystal surfaces. Firstly, UHV conditions reduce contamination to prepared samples with clean surfaces, such as oxidation and other non-target particulates coating the surface. Secondly, the mean free path electrons can travel in the chamber without interacting with other gases is increased. Increasing the mean free path is important to reduce contamination-induced STM noise. To keep the VT-STM at low pressures many vacuum pumps are used in union across the chambers including: rotary pump, turbomolecular pump, Ti sublimation pump, and ion pumps. The VT-STM has three sample chambers: analysis, preparation, and load-lock. Each chamber is backed by a rotary and turbomolecular pump, with ion and Ti sublimation pumps in operation in the analysis and preparation chambers. After loading a sample into the load-lock, the chamber is pumped to high vacuum (10^{-7} mbar) with rotary and turbomolecular pumps. The sample is then transferred to the preparation chamber where in-situ sputter and anneal cycles of the surface can begin.

Sputtering involves the bombardment of the surface with noble gas ions, such as Ar^+, which physically remove surface layers. Sputtering helps to remove contamination from the top surface layers with hydrocarbon, oxide, and other species physically removed and pumped away. In the ion souce, electron ionisation of Ar species results in Ar^+ ions with a typical incident energy of 1-5 keV. Sputtering is monitored via a drain current from the sample stage, with a typical range of 4-6 μA. A sputter cycle time of 30-minutes is typically enough to remove all surface contaminants, but also significantly damages the surface structure.

Heating (annealing) the substrate is used to regain bulk composition at the surface layers. Joule heating a W filament in contact with the sample holder, and also with electron bombardment via a high-voltage potential difference between the plate and filaments, is used to increase the sample temperature. During anneal cycles, an anneal temperature of 700°C for 2 hours is typical, but temperatures as high as 850°C were recorded. Figure 4.11(a) shows a typical view of the pyrometer measuring the sample surface temperature.

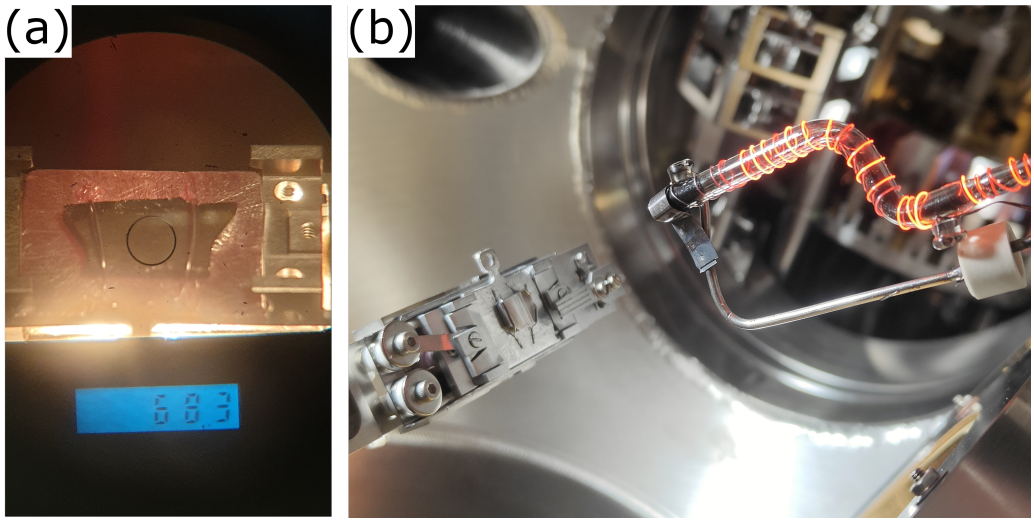

Figure 4.11: Photographs of the apparatus used for in-situ surface preparation. (a) A pyrometer optically focused on the *d*-Al-Ni-Co surface, with a measured temperature of 683°C. (b) The Pyrex tube containing C_{60} and wound with a heated W filament is aimed at the *d*-Al-Ni-Co surface.

A higher anneal temperature is expected to result in a more ordered surface, but the temperature is practically limited by the melting temperature of the crystal. A general rule is that the anneal temperature should be not be greater than two thirds of the sample melting temperature. In the preparation chamber, the temperature of the substrate is monitored with a pyrometer set to 0.35 emissivity, a value which is typically used for measuring the same surface in the literature [71, 247, 248]. Annealing and sputter cycles are typically performed in tandem, to restore order and stoichiometry at the surface.

Molecular Evaporation

Physical vapour deposition of C_{60} on the surface of *d*-Al-Ni-Co in Chapter 8 was performed in the VT-STM analysis chamber. High-purity materials are sublimed using filament heating. For materials with lower sublimation temperatures, such as C_{60}, a simple thermal source is sufficient. In this method, the evapourant is housed within a high-melting-point (Pyrex) tube. Heat is applied by passing an electrical current through a W filament wound around the cell, as shown in Figure 4.11(b), causing sublimation. The open end of the container is directed towards the substrate surface. The temperature of the substrate during annealing in the analysis chamber is monitored with a thermocouple.

4.6.2 Scanning Tunnelling Microscopy

Working Principle

Scanning tunnelling microscopy (STM) is an imaging technique where an atomically sharp tip is brought close to a conductive surface (< 1 nm), and the tunnelling current between the overlapping wavefunctions of the tip and surface are measured [249]. When a bias voltage is applied to the tip relative to the sample surface, it causes a quantum tunnelling current: electrons tunnel across the gap between the tip and the sample. A positive bias leads to electrons tunnelling from the tip to the surface, essentially probing empty surface states, while a negative bias probes filled states whereby electrons tunnel j from the surface to the tip. The tunnelling current j can therefore be expressed most simply as a function of the electron state densities D(V), the bias voltage V, the tunnelling gap d, and the effective barrier height ϕ_B:

$$j \propto \frac{D(V) \times V}{d} \times \exp(-\phi_B^{\frac{1}{2}} \times d) \tag{4.6.1}$$

The effective work function ϕ_B represents the average height of the energy barrier that electrons must overcome to tunnel between the tip and sample. It arises because electrons tunnel through a barrier shaped by the combination of the tip's work function and the sample's work function, rather than either alone. When a bias voltage shifts the Fermi levels of the tip and sample relative to each other, this effective barrier height determines how easily electrons can tunnel across the gap, which explains the exponential relation of the tunnelling current to distance. Figure 4.12(a) shows the energy diagram of the tunnelling contact of the tip to the surface [75]. The exponential relationship between j and d means that small variations in surface topology results in a sensitive change in the vertical resolution of j. As a result, the tunnelling current produced at each point of an STM image is primarily a function of the local density of states - if a surface of uniform height has an inhomogenous density of states, the measured heights of the surface will vary. Laterally, the resolution is limited by the probe apex dimensions, whereby an atomically sharp apex should allow for an STM image with lateral atomic resolution. Conversely, if the tip is more blunt than the lattice constant of the surface crystal, then the tunnelling signal from nearbouring atoms will convolve.

The key components of an STM are illustrated in Figure 4.12(b) [75]. The tip is typically fabricated from materials like W, Pt-Ir, or Au, via ex-situ physical shearing or electrochemical etching (W is used for this thesis's data collection) and is mounted on a scanning stage. This stage incorporates piezoelectric ceramics for fine control of tip motion in the x, y, and z directions through applied electric signals. Additional in-situ tip preparation techniques include tip sputtering, annealing, voltage pulses, and controlled tip-surface crashes. A coarse positioning system facilitates initial tip approach towards

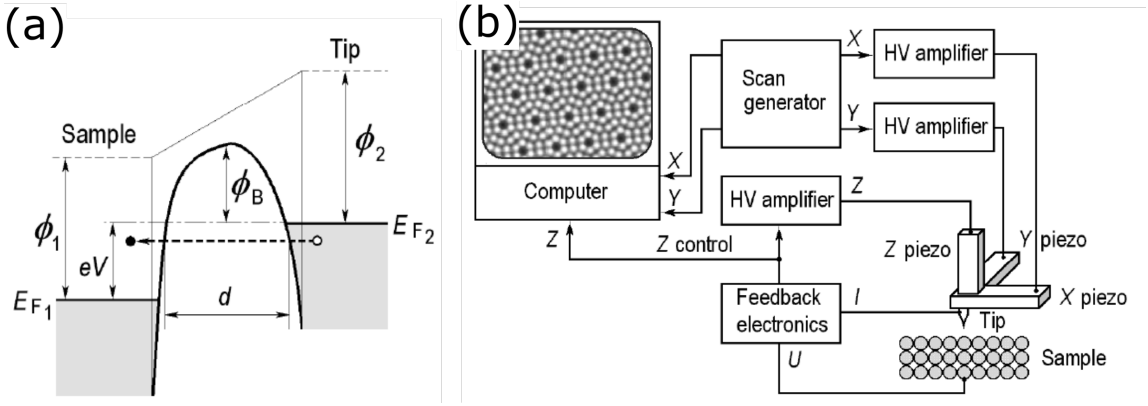

Figure 4.12: (a) Energy diagram of the tunnelling contact when a metallic tip, with Fermi level E_{f_2} and applied voltage bias, is brought into close contact (separated by d) with a metallic sample with empty states and Fermi level E_{f_1}. ϕ_1, ϕ_2, and ϕ_B, are the work functions of the sample, tip, and effective barrier height, respectively. (b) A schematic operation of a typical STM. Reproduced and modified from [75].

the sample, or retraction for sample transfer, enabling final fine positioning to within $<$ 1 nm separation. During operation, the stage is vibration-isolated using soft springs and magnets. A feedback electronics system continuously monitors the tunnelling current and regulates tip-sample separation. Acquired data is converted into images via a computer system, which also controls tip position and scanning parameters such as bias voltage, tunnelling current, scan size.

An STM image can be using either of two operational modes: constant height or constant tunnelling current. In constant height mode, the distance between the tip and surface is kept constant, and the changes in tunnelling current as a function of topology is measured. In constant current mode, which is utilised for work in this thesis, the tunnelling current value is set, and the apparent height as a function of topology is measured.

Analysis Techniques

Image processing of STM data is processed with WSxM [250]. Correcting for image artefacts or distortion is important to show real features of the substrate or adsorbate atoms. Firstly, a level plane is performed to correct distorted slopes due to the inclination between the tip and sample. A global level plane is suitable for correcting a surface which is expected to be flat, or local level planes of flat terraces may be utilised. A plane level with respect to the calculated substrate can also be made if adsorbates are present on a relatively flat surface. Secondly, scan line artefacts which do not represent the real surface and are caused by corruption or other interface interactions, may be corrected with a scar removal process. Finally, drift may be corrected for, caused by the surface moving relative to the tip during scanning, usually due to thermal expansion or relaxation,

Analysis of surface features is made with line scans, height histograms, thresholding, autocorrelation functions, and fast Fourier transforms (FFT). A line profile is a simple technique where a line is drawn between two or more points, and a graph plots height against distance. Line profiling is used for measuring inter-atomic and inter-molecular spacing, as well as determining step-height between flat terraces. Height histograms similarly plot recorded heights into bins, used for determining step-heights and molecular height differences. FFT deconvolves the signal into its harmonic sine and cosine harmonic components, represented in repriprocal space. Repeated separations and rotationally symmetry can be revealed by an FFT that may not be obvious to the eye in real space. Filtering high intensity regions of interest and performing a reverse FFT highlights these features in real space. The autocorrelation function is also useful to reveal repeated or ordered features, made by shifting the image and looking at the difference between the shifted and original image, highlighting repetitive patterns. Finally, thresholding is performed to determine molecular coverage. Molecular coverage is best determined by plotting calculated coverage against threshold height, and identifying the inflection point where the substrate is no longer visible.

4.6.3 Low Energy Electron Diffraction

Theory

Low energy electron diffraction (LEED) is a surface sensitive technique where electrons probe surface structure [75]. Electrons elastically scatter from a surface and collected on a detector, imaging the reciprocal space of the structure. Low energy electrons with E = 30 - 200 eV are suitable due to their low de Broglie wavelength $\lambda = \frac{h}{\sqrt{2mE}} = 0.1$ - 0.2 nm. As with SEM, the electron mean free path in the bulk is short, leading to only the surface layers being probed at low energies. The reciprocal lattice is a set of points defined by the following equation:

$$G_{hkl} = h\mathbf{a_1^*} + k\mathbf{a_2^*} + l\mathbf{a_3^*} \tag{4.6.2}$$

where h, k, and l are Miller indices, and $\mathbf{a_1^*}$, $\mathbf{a_2^*}$, and $\mathbf{a_3^*}$ are the reciprocal space vectors. The reciprocal and corresponding real space vectors are related by the following equations:

$$\mathbf{a_1^*} = \frac{2\pi a_2 \times a_3}{a_1 \cdot (a_2 \times a_3)},\ \mathbf{a_2^*} = \frac{2\pi a_3 \times a_1}{a_2 \cdot (a_3 \times a_1)},\ \mathbf{a_3^*} = \frac{2\pi a_1 \times a_2}{a_3 \cdot (a_1 \times a_2)} \tag{4.6.3}$$

The wavevector K_0 of the incident and K scattered electron beam are related to the set of points by $K - K_0 = G_{hkl}$, and under elastic scattering conditions $|K| = |K_0|$. For 2-dimensional surfaces where only the top layer is considered, perpendicular components can be ignored and the wavevectors reduce to the following equation:

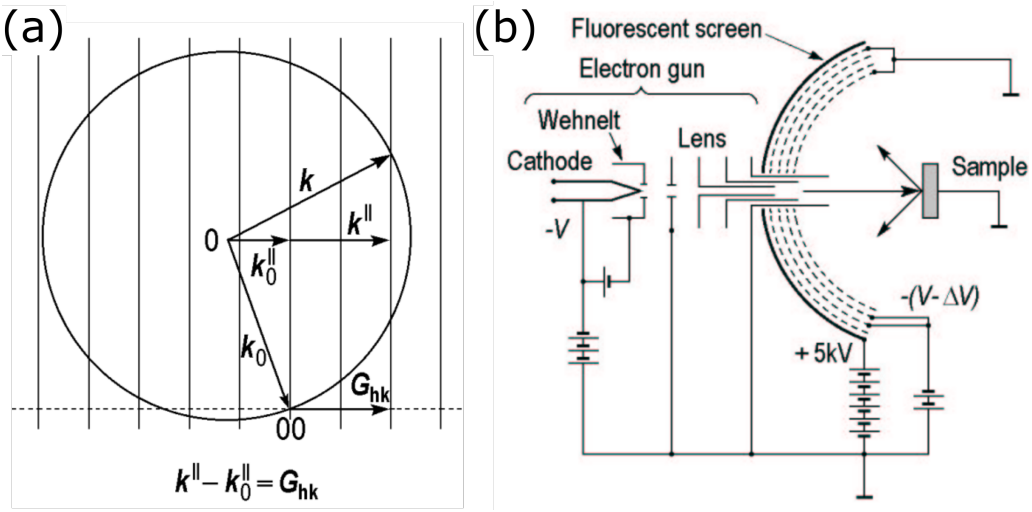

Figure 4.13: (a) Construction of the Ewald sphere from diffraction of a 2-dimensional surface. (b) A schematic diagram of a typical LEED setup. Reproduced and modified from [75].

$$K^{\parallel} - K_0^{\parallel} = G_{hk} \tag{4.6.4}$$

In this condition, only the parallel components of the incident and scattered beams relative to the surface need to be considered. The diffraction process can be illustrated with an Ewald sphere, shown in Figure 4.13(a), where each lattice point is projected as a rod perpendicular to the surface. Conceptually, a 2-dimensional lattice can be thought of as a 3-dimensional lattice with infinite periodicity perpendicular to the surface, with $|a_3| \to \infty$, and therefore $|a_3^*| \to 0$. The rods are therefore the infinitely dense lattice points along the normal direction, where K_0 terminates at the end of the rods, and K defines intercepts of the rods with the Ewald sphere [75].

LEED from a quasicrystal produces discrete diffraction vectors because despite lacking periodicity in 3-dimensions, they can be described as periodic in higher-dimensional space using more than three lattice vectors, as described in Section 2.5.2. During LEED, the Ewald sphere intersects these vectors just as with periodic crystals, resulting in sharp Bragg-like spots arranged with forbidden symmetries such as 5-fold rotation.

Experimental Setup

A schematic diagram of a typical LEED setup is shown in Figure 4.13(b) [75], with an example LEED image. LEED was performed in-situ with an Omicron VT-STM. An electron gun consists of a high voltage cathode with a beam of electrons fired towards the anode, a Wehnelt cyclinder for controlling emission and focusing, and a lens array for focusing. A hemispherical fluorescent screen, shielded from the lens array, operates at a high voltage

for post-acceleration of diffracted electrons. In front of the screen are a series of grounded and high voltage grids. The first and last grids are held at ground and shield electric fields from the second and third grids, which are held close to the lens voltage to reject inelastically scattered electrons. Adjusting the voltage of the second and third grids is useful for optimising the signal-to-noise ratio in the form of brighter or dimmer spots and background intensity.

4.7 Magnetic Measurement Techniques

In this section, magnetic microscopy, magnetometry, and micromagnetic modelling simulations are described for work undertaken in Chapters 6 and 7.

4.7.1 Magnetic Force Microscopy

The Atomic Force Microscope

The magnetic force microscope used for magnetic force microscopy (MFM) images in Chapter 6 adapts an Oxford Instruments Cypher atomic force microscope (AFM), offering an additional magnetically sensitive scanning mode. The AFM is operationally similar to the t-SPL imaging technique described in Section 4.3.2, but with an atomic force feedback loop rather than thermal-conductance. The behaviour of the tip-sample force depends on the proximity of the tip with the surface, influencing attractive Van der Waal or repulsive forces. The force-distance curve is described by the Lennard-Jones potential between two neutral atoms, shown in Figure 4.14 [251], with an attractive $-\frac{1}{r^6}$ term (green), and repulsive $\frac{1}{r^{12}}$ term (blue). The attractive term is due to long-range Van der Waal forces, specifically the London dispersion force between neutral atoms with permanent dipole moments. As the tip is brought closer, attractive metallic bonding may occur, then at even closer distances there is a repulsion between inner electron shells. Repulsion between overlapping inner shell orbitals is not purely electrostatic, as Pauli repulsion (the exclusion principle preventing two electrons from occupying the same state) begins to dominate. In Chapter 6, the probe is brought within 5 to 50 nm above the surface, where attractive forces dominate.

There are two operating modes, static and dynamic (oscillating). Figure 4.14(b) shows typical operation in static mode, where the surface is scanned (contact) so that either the tip-sample force (with cantilever deflection), or tip-sample distance (non-contact) is kept constant. By measuring either the changes in applied force to maintain deflection or constant height, a topographic map of the surface can be constructed [251]. Dynamic mode operates an oscillating cantilever either above the surface or in tapping mode, excited close to its natural resonance frequency. As the probe tip nears the sample surface, the interaction alters the cantilever's resonance frequency. Conceptually, this tip-sample force

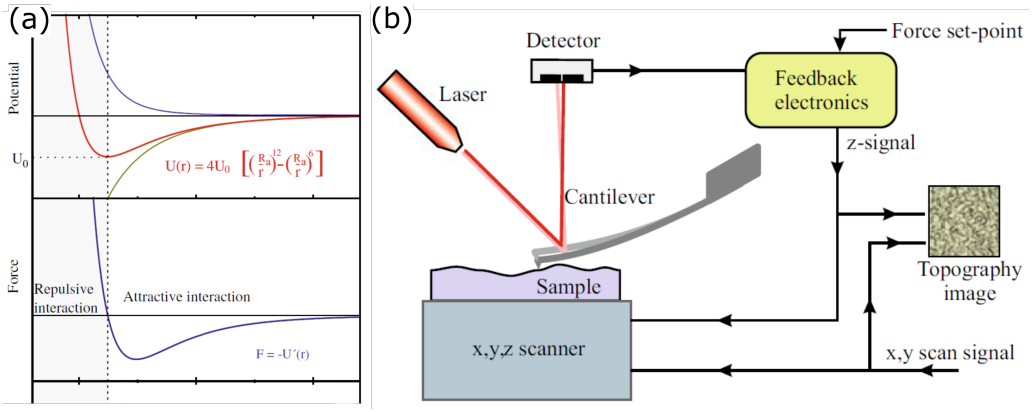

Figure 4.14: (a) The Lennard-Jones potential with attractive (green), repulsive (blue), and net potential (red). U_0 is the depth of the potential well, r is the distance between atoms, and R_a is the distance at which U(r)=0. Repulsive and attractive force regimes are labelled. (b) A schematic of typical atomic force microscopy operation. Reproduced and modified from [251].

can be approximated as a second spring acting in parallel with the cantilever's own spring constant. The presence of this additional spring modifies the overall resonance frequency, consequently changing the amplitude of the cantilever's vibration. This measurable amplitude shift provides the detection signal used as feedback to regulate the distance separating the tip and the sample [251].

The Magnetic Force Microscope

The MFM modifies an AFM probe with a ferromagnetic thin film coating sensitive to magnetic materials. A two-pass technique is employed where an AFM topography profile is firstly taken in dynamic tapping mode. On the second pass, the tip is raised 50 nm above features on the surface, where the magnetic field between the tip and surface may be attractive or repulsive, shifting the resonance frequency of the oscillating cantilever. A topographic magnetic map with varying resonent frequency of the cantilever can then be constructed in greyscale, with resonent frequency (grey) and shifted frequencies in black or white representing attractive or repulsive ferromagnetic interactions. The magnetic force between sample and tip is expressed with the following equation:

$$F = \mu_0(m \cdot \nabla)H \tag{4.7.1}$$

here m is the magnetic moment of the tip, and H is the stray field from the sample. Images produced are analysed and exported to .PNG using the Gwyddion software package [252].

4.7.2 Superconducting Quantum Interference Device - Vibrating Sample Magnetometer

Theory

The Superconducting Quantum Interference Device - Vibrating Sample Magnetometer (SQUID-VSM) combines the VSM and SQUID working princples into one instrument. During VSM operation, vibrating a sample through the centre of detection coils generates a time-varying magnetic flux. This induces an electromotive force (emf) in the coils proportional to the sample's magnetic moment, given by the following equation [253]:

$$V_{emf} = mAfS \tag{4.7.2}$$

where m is the total magnetic moment measured in emu, A and f are the amplitude and frequency of the oscillation, and S is the sensitivity function of the detection coils, determined by calibrating with a material of known magnetisation [253]. The induced emf signal can be improved by increasing the volume of m, and by increasing the amplitude or frequency of the oscillation. There is however a practical limit due to large frequencies producing eddy currents which will shroud emf measurements. Sensitivity can be increased by increasing the inductance of the detection coils, such as with a greater number of turns [242].

The SQUID technique introduces a superconducting wire with a magnetic field and Josephson Junctions to produce a sensitive magnetic field measurement instrument. A Josephson Junction occurs where two superconducting wires are separated by a thin metal barrier, where a superconducting current (zero resistance) may pass through the metal barrier without comprimising a drop in voltage [253]. The current i_s passing through the Josephson Junction is expressed with the following equation:

$$i_s = i_c \sin(\Delta\phi) \tag{4.7.3}$$

where i_c is the critical current of the superconductor wires, and $\Delta\phi$ is the phase difference between the two superconductor wires.

The SQUID-VSM incorporates a VSM with a specific coil configuration known as a second-order gradiometer. A second order gradiometer consists of three sets of coils: a central coil with N turns, and secondary upper and lower coils with $\frac{\mathrm{N}}{2}$ turns. The vibrating sample induces a current into these coils, and the turn ratios and opposite windings reject uniform field gradients such as the Earth's magnetic field lines. The SQUID is a separate set of superconducting coils placed within the gradiometer, which detects the amplified magnetic field generated by the secondary coils.

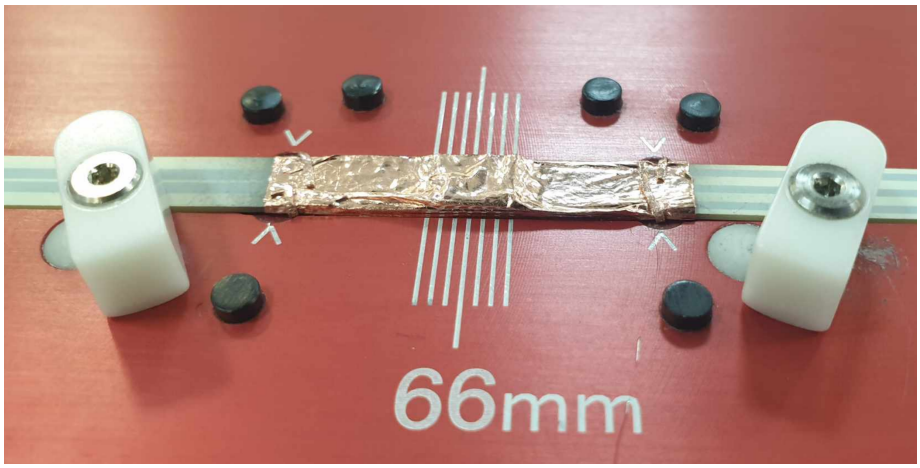

Figure 4.15: A wafer wrapped in a diamagnetic Cu film, clipped, and mounted on a straw, ready to be placed on a SQUID-VSM sample rod. The purpose of the Cu wrap is to hold the wafer in place

Experimental Setup

SQUID-VSM measurements are used to support sample preparation conditions in Chapters 6 and 7 of this thesis. Measurements of $Ni_{80}Fe_{20}$ thin films with 4, 6, 8, and 10 nm thickness were conducted using a Quantum Design MPMS3 instrument at the ISIS Materials Characterisation Laboratory, STFC Rutherford Appleton Laboratory. The instrument is sensitive to $1x10^{-11}$ Am^2, and can measure magnetisation in applied fields up to 7 T across a temperature range of 1.8 K to 1000 K. A high vacuum pressure is established with a cryostat vacuum pump. Samples under 5 mm^2 were loaded into a plastic straw, wrapped in a diamagnetic Cu film (Figure 4.15), and mounted on a long sample rod. A DC magnetisation calibration measurement was employed to precisely centre each sample within the detection coils prior to data collection. Samples were heated and measured in-operando with an oven between 300 - 1000 K, measured with a thermocouple. To normalise and determine total magnetisation (emu cm^{-3}) of samples, the surface area is measured by thresholding images in ImageJ, to determine the total volume of magnetic film (area $\times$ thickness).

4.7.3 X-Ray Magnetic Dichroism Photoemission Electron Microscopy

X-ray magnetic dichroism photoemission electron microscopy (XMCD-PEEM) is a magnetic imaging techique for measuring elemental magnetic domains in both space and time. An image is formed from photo-emitted electrons from a surface due to adsorption of an incident X-ray, which may be tuned for an element orbital specific measurement. For magnetic samples such as NiFe thin films measured in Chapter 7, adsorption of different photon helicities (their electric field rotates clockwise or anticlockwise as they propagate)

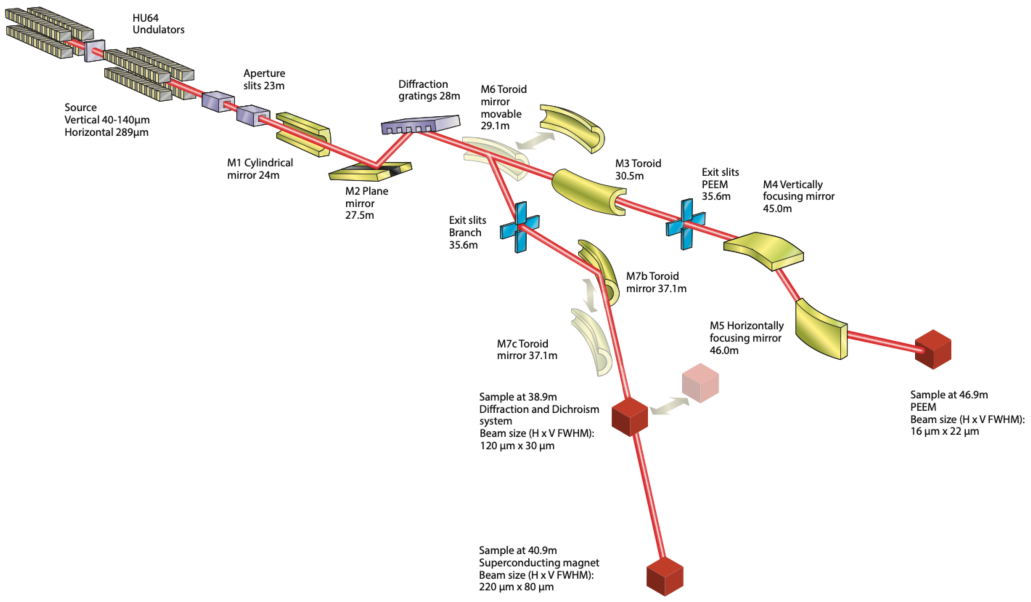

Figure 4.16: Schematic of the I06 beamline at the Diamond Light Source synchrotron. Reproduced from [255].

allows for magnetic contrast imaging [254]. XMCD-PEEM is performed at the I06 Diamond Light Source, Harwell. A schematic of the beamline is shown in Figure 4.16, starting with undulators consisting of four magnetic arrays which force electrons in the synchrotron ring into a helical path, emitting circularly polarised X-rays. The X-rays are then focused and monochromated, allowing selection of photon energies equivalent to the L3 Fe edge, corresponding to the orbital which gives Fe ferromagnetic properties. Finally, these X-rays are focused onto a sample with a spot size in the order of 30 µm.

To produce magnetic contrast, 40 images are taken at the L3 peak and pre-edge, shown labelled in Figure 4.17 [254]. At the L3 peak, 20 total images are taken with 10 at left circular polarisation (LCP), and 10 with right circular polarisation (RCP). At the pre-edge, another 20 total images are taken with 10 at RCP, and another 10 at LCP. Each image is stacked, drift corrected, and their combined intensity is used to produce magnetic contrast with the following equations:

$$X_+ = \frac{I_{L3+}}{I_{pre-edge}} \tag{4.7.4}$$

$$X_- = \frac{I_{L3-}}{I_{pre-edge}} \tag{4.7.5}$$

where I_{L3+} and I_{L3-} is the intensity of each pixel at the L3 peak of RCP and LCP X-rays, respectively, and $I_{pre-edge}$ is the intensity of each pixel at the pre-edge used for normalising variations in intensity. A final image of magnetic contrast is made with $D = X_+ - X_-$. A

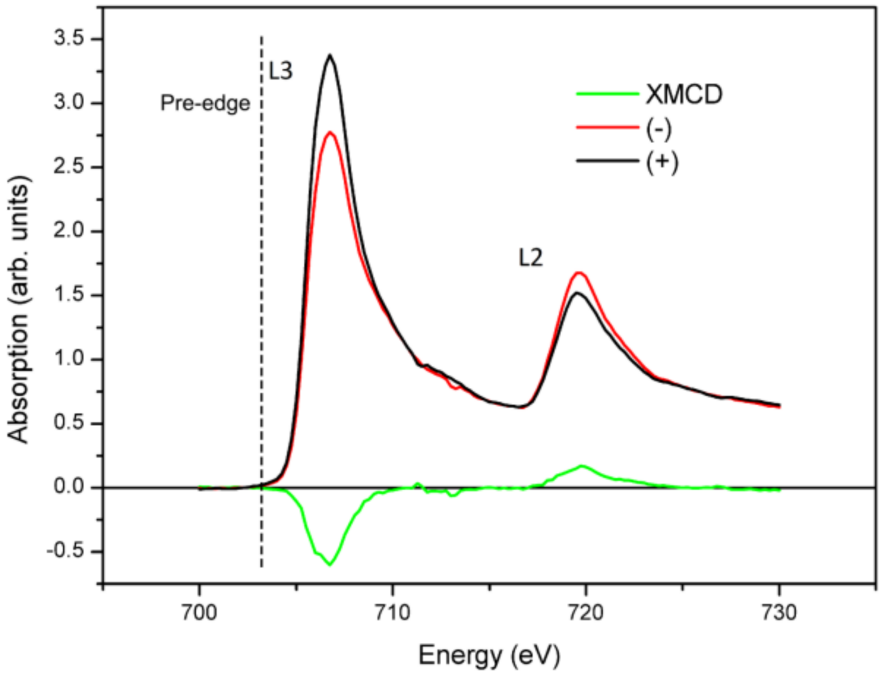

Figure 4.17: The Fe L3 and L2 edge as measured with XMCD-PEEM. The difference between adsorption of right circularly polarised X-rays (black) and left circularly polarised X-rays (red) produce magnetic contrast (green). Pre-edge adsorption is used to normalise images. Reproduced from [254].

bright contrast occurs when a component of a domain moment aligns parallel to the X-ray's in-plane wavevector, enhancing absorption of RCP more, while dark contrast arises when moments are antiparallel absorbing LCP more [256, 257]. Therefore, a positive D signal (bright) indicates moments aligned with the wavevector, and negative D signal (dark) shows the opposite.

XMCD-PEEM was performed on the 8-fold Ammann-Beenker tiling, with results shown in Chapter 6, and the 4-fold Square Fibonacci tiling in Chapter 7. In both results, the samples are annealed in-operando above the ferromagnetic to paramagnetic transition temperature, and cooled back to room temperature. Samples are heated radiatively through the back of the substrate, and the temperature is monitored with a W/Re thermocouple spot-welded and in thermal contact with the rear face of the sample. Magnetic contrast XMCD-PEEM images are produced shortly after measurements are taken by post-processing at a separate workstation.

Figure 4.18 shows room temperature XMCD-PEEM images before annealing, with different sample stage rotations to demonstrate how contrast changes relative to the X-ray wavevector (red arrow). After each acquisition, the stage is rotated by -45°, starting at +5°. On the left side a collection of images from each sample rotation are stitched together to cover the full ABT, showing no flipped moments between acquisitions. To

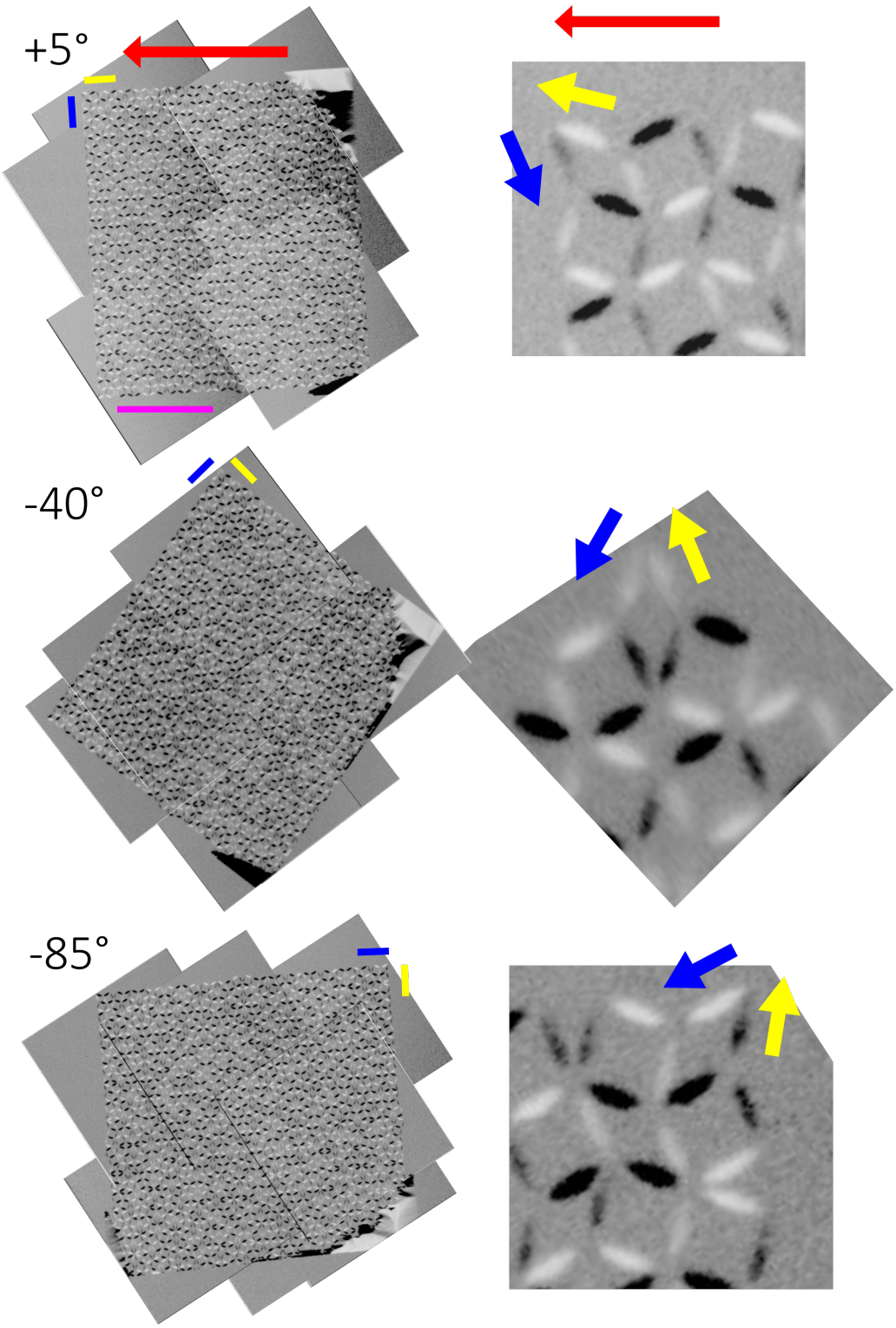

Figure 4.18: Stitched XMCD-PEEM images of the ABT at three different sample rotations at 45° to one another. The in-plane X-ray wavevector component is labelled with a red arrow. Blue and yellow bars (left) correspond to the same coloured arrows (right), indicating how moments appear different depending on their component to the X-ray wavevector. Pink scale bar top left equals 10 µm.

aid the reader, blue and yellow arrows on the right side magnified images (corresponding to bars on left demagnified images) are placed near the same moments at each sample orientation, which have different XMCD contrast depending on the sample orientation. Note, the XMCD technique cannot distinguish moments which are orthogonal to the X-ray wavevector having no parallel or antiparallel component, and in this case moments will have the same grey contrast as the background. At +5°, the blue moment is a darker grey whereas the yellow moment is a brighter white. As the X-ray wavevector is pointing from right to left, the blue moment must be orientated down and right, whereas the yellow moment is orientated left. As the sample is rotated by 45°, both blue and yellow moments are a light grey, as both now have moment components along the X-ray wavevector, while retaining the same orientations as before. Finally, with the final 45° rotation, the blue moment is now mostly aligned with the X-ray wavevector, giving it a bright white contrast, whereas the yellow moment is now oriented against the X-ray wavevector, giving it a dark contrast. Due to the 8-fold nature of the ABT, the structure can easily be rotated so that no moments are orthogonal to the X-ray wavevector, but some moments will be more alligned - leading to heavier contrasts.

4.7.4 Quasiperiodic Micromagnetic Simulations with MuMax3

In Chapters 6 and 7 micromagnetic simulations are performed for artificial spin-ice 8-fold Ammann-Beenker and 4-fold Square Fibonacci tilings. In these systems, thin single-macrospin nanomagnets are placed along the edges of tilings, and their interactions are measured. Simulations are utilised to calculate static ground state moment configurations of each vertex type, and time-evolved energy minimisation of discrete tilings. Micromagnetic simulations are performed with the MuMax3 software package [25], which integrates with Windows Command Prompt. This section covers the theory required to describe short-range exchange interactions which typically dominate these systems, the standard equations MuMax3 utilises, and the experimental modelling setup for Chapters 6 and 7.

Theory

Short-range exchange interactions have been determined to dominate experimental artificial spin-ice systems, as reviewed in Section 3.1. The exchange interaction occurs between nearest neighbour spin magnetic moments, a result of the Pauli exclusion principle and Coulomb interaction [258]. Heisenberg's nearest neighbour model describes the quantum mechanical exchange forces that develop from the interacting electron orbital configurations (Section 2.1.1). The exchange energy E_{exch} between nearest neighbour exchange interations is mediated by the exchange integral $J_{i,j}$, spin state S, and lattice parameter a, with the following equation:

$$E_{exch} = \int \frac{J_{i,j}S^2}{a}(\nabla M)^2 dr^3 \tag{4.7.6}$$

where $\frac{J_{i,j}S^2}{a} = A_{ex}$, the material specific exchange stiffness parameter. The E_{exch} can be used to estimate the probability P of a magnetic moment to flip with respect to its neighbour with the following equation:

$$P = \exp(-\frac{E_{exch}}{k_B T}) \tag{4.7.7}$$

where $k_B T$ is the thermal energy of the moment. For T $\rightarrow$ 0 K, P $\rightarrow$ 0, and the saturation magnetisation M_S (in the presence of an external field) of the system is maximised. As T increases up to the ferromagnetic to paramagnetic transition temperature T_C (Section 2.1.1), P $\rightarrow$ 1, as increasing $k_B T$ reduces the energy barrier for a spin flip. The ferromagnetic $Ni_{80}Fe_{20}$ thin films grown in this thesis have well-understood ferromagnetic properties, such as saturation magnesation $M_S = 8.6 \times 10^5 Am^{-1}$ and exchange stiffness constant $A_{ex} = 1.3 \times 10^{-11} Jm^{-1}$ [23]. With knowledge of M_S and A_{ex}, the distance that parallel alignment of spin magnetic moments is energetically favourable, l_{ex}, can be calculated with the following equation:

$$l_{ex} = \sqrt{\frac{2A_{ex}}{\mu_0 M_S^2}} \tag{4.7.8}$$

For $Ni_{80}Fe_{20}$, $l_{ex} = 1.67$ nm, and so for atomic nearest neighbours closer than this distance, magnetostatic field dominates atomic exchange interaction, and parallel magnetic domains form. Therefore, in each ferromagnetic nanoisland, a single macro-spin domain can form, with magnetic field lines which interact with neighbouring nanoislands.

Here, a summary of the relevant equations and terms used for calculating total energy and energy minimisation within MuMax3 will be given. In-depth explanations for derivations and equations used can be found in the literature [25, 259, 260]. MuMax3 uses the Landau-Lifshitz-Gilbert (LLG) equation to calculate magnetisation dynamics [25, 259]:

$$\dot{m} = -\gamma m \times H_{eff} + \alpha m \times \dot{m} \tag{4.7.9}$$

where γ is the gryomagnetic ratio ($\frac{q}{2m}$), m is a vector along the magnetisation direction, and $\dot{m}$ is the time derivative. α is the gilbert damping parameter, a material specific constant that quantifies the rate of energy dissipation in a magnetic system as its magnetisation relaxes towards equilibrium. The effective field H_{eff} is the functional derivative of the energy functional $H_{eff} = -\frac{1}{\mu_0}\frac{\delta E}{\delta M}$, and E is the volume integral over the local energy densities [259]. H_{eff} has multiple contributing terms, such as material intrinsic, sample geometry, and external fields. The $-\gamma m \times H_{eff}$ term causes precession, while the $\alpha m \times \dot{m}$

term causes dampning or relaxation.

Several common energy terms contribute to the effective field in our system: the Zeeman energy (E_{Zeeman}), exchange energy (E_{exch}), magnetostatic energy (E_{ms}), magnetocrystalline anisotropy energy (E_{anis}), and thermal fluctuations [260]. Zeeman energy is due to externally applied H_{ext} fields, minimised when magnetisation is aligned to the field. Zeeman energy is given by $E_{Zeeman} = -\mu_0 M \cdot H_{ext}$. The magnetostatic energy represents the energy from dipolar interactions between all magnetic moments (including self-interaction). This energy is minimized when magnetic flux forms closed loops entirely within the material, eliminating stray external fields. It is expressed as $E_{ms} = -\frac{1}{2} M \cdot B_{demag}$, where B_{demag} is the demagnetising field governed by Maxwell's equations [260].Magnetocrystalline anisotropy energy arises when the crystal lattice, via spin-orbit coupling, defines preferential magnetization directions (easy axes). In the simplest case (uniaxial anisotropy), one easy axis exists. The energy is $E_{anis} = -\frac{1}{2}\vec{B}_{anis}(K_{u1}) \cdot \vec{M} - \frac{1}{4}\vec{B}_{anis}(K_{u2}) \cdot \vec{M}$, where $\vec{B}(K_{ui})$ are effective field terms where only the first and second order uniaxial anisotropy constants are taken into account. MuMax3 calculates the summation of each energy term for static or dynamic cases as E_{Total}.

For the systems measured in this thesis, E_{Total} is typically increased with the number of total moments, which leads to more interactions, and vertices with more islands typically possessing a greater E_{Total}. The most interesting influence on E_{Total} within vertices with the same number of moments occurs when the interactions between moments have acute flux pathing. The effect of flux pathing leading to a change in E_{Total} is also known as flux shunting, which is discussed further in Chapter 6.

Modelling Setup: Ammann-Beenker tiling

An example code for calculating the E_{Total} of each configuration of an Ammann-Beenker tiling vertex type is given in Appendix A. In this section the code setup at each step is explained.

MuMax3 provides a finite-diffrence discretisation in space, whereby the geometry is divided into voxels of size set by the user. Quantities with volumetric dependence, including magnetisation and effective field, are computed at cell centers. Inter-cell coupling terms such as exchange strength, however, are assigned to shared faces between adjacent cells [25]. To begin, a suitable mesh is defined:

```
SetMesh(256, 256, 1, 4e-09, 4e-09, 4e-09, 0, 0, 0)
```

In this mesh, the field size is x = 256, y = 256, and z = 1 voxels in size, effectively producing a 2-dimensional scheme. Each voxel is set to be 4 nm in size along each axis, and so the field size is 1,024 x 1,024 x 4 nm. The field size is deliberately set to a power of 2 as this is reported to reduce computation time [25]. The final 0 values set no periodic

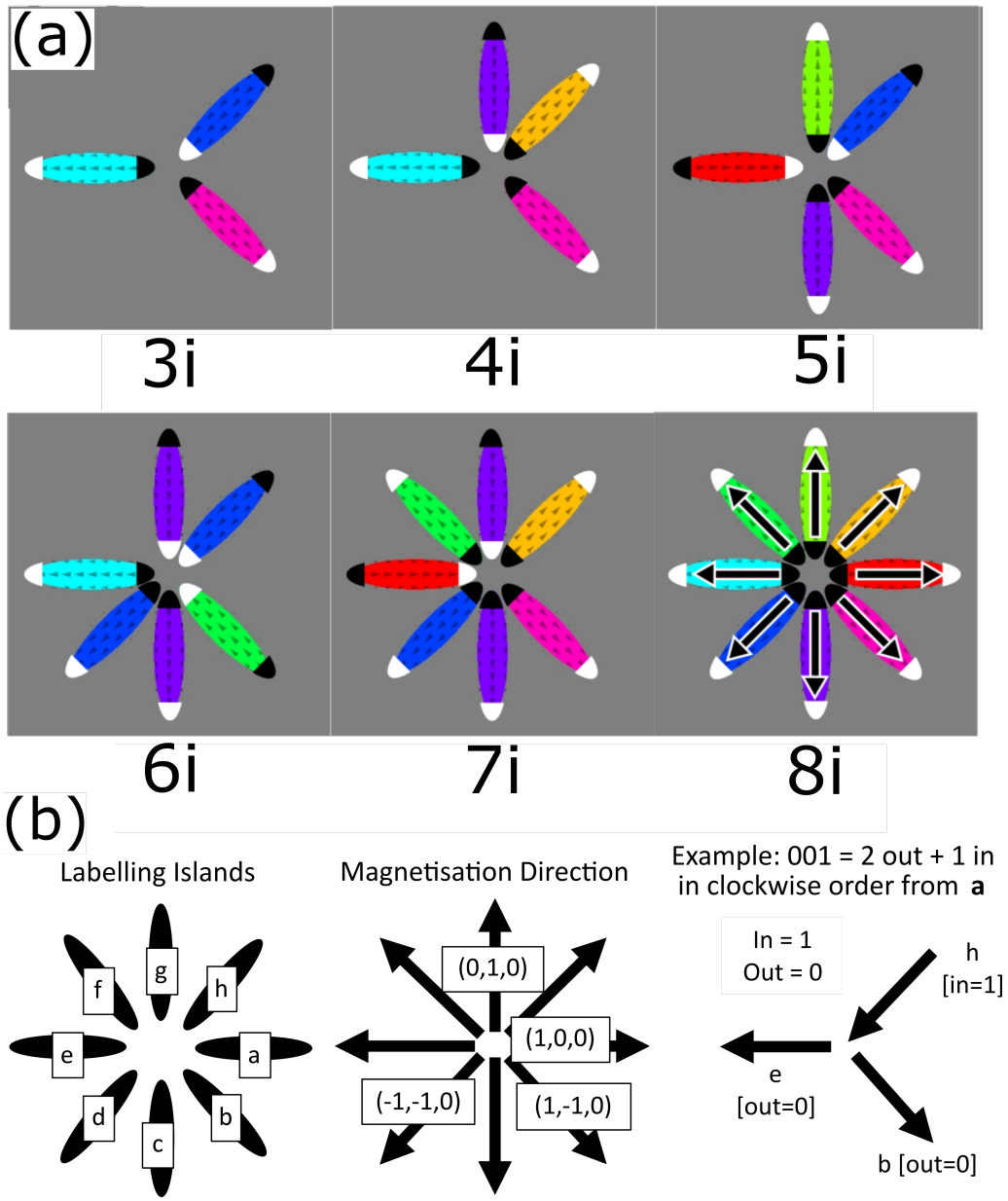

Figure 4.19

boundary conditions. Next, standard values for $Ni_{80}Fe_{20}$ are set: $M_S = 8.6 \times 10^5 Am^{-1}$, $A_{ex} = 1.3 \times 10^{-11} Jm^{-1}$, l_{ex}, and $\alpha = 0.5$ [23, 114].

Next, nanoislands specific to the Ammann-Beenker and Square Fibonacci tilings are constructed, with the goal of creating every possible combination of macro-spin configurations to sort by E_{Total}. Example configurations for each of the six vertex types of the Ammann-Beenker tiling are shown in Figure 4.19(a), labelled 3i to 8i corresponding to the number of nanoislands. Within MuMax3, it is possible to define, translate, and rotate shape objects within a mesh with the following command:

```
a := Ellipsoid(n, n/4, n/100).transl(q, 0, 0)
```

Here, n = 4 x 10^{-7} and q = 2.56 x 10^{-7} are defined for convinience. The object a is defined as an ellipsoid of length n, width $\frac{n}{4}$, and thickness $\frac{n}{100}$, corresponding to an ellipsoid island of length 400 x 100 x 4 nm. The nanoisland is translated from the centre in the (1, 0, 0) direction by q. Each nanoisland within a given vertex type needs to be defined, so that an independent magnetisation can be set. For this reason, a naming convention, shown in Figure 4.19(b) was created. For the Ammann-Beenker tiling, a maximum of 8 nanoislands populate each vertex type, and so 8 nanoislands are concentrically named from a to h (Figure 4.19(b)):

```
a := Ellipsoid(n, n/4, n/100).transl(q, 0, 0)
b := Ellipsoid(n, n/4, n/100).transl(q, 0, 0).rotz(-pi/4)
c := Ellipsoid(n, n/4, n/100).transl(q, 0, 0).rotz(-2*pi/4)
d := Ellipsoid(n, n/4, n/100).transl(q, 0, 0).rotz(-3*pi/4)
e := Ellipsoid(n, n/4, n/100).transl(q, 0, 0).rotz(-4*pi/4)
f := Ellipsoid(n, n/4, n/100).transl(q, 0, 0).rotz(-5*pi/4)
g := Ellipsoid(n, n/4, n/100).transl(q, 0, 0).rotz(-6*pi/4)
h := Ellipsoid(n, n/4, n/100).transl(q, 0, 0).rotz(-7*pi/4)
```

Now that nanoisland objects have been defined, they can be called into the mesh to create any of the six vertex types. For example, for the 3i vertex:

```
setgeom(b.add(e).add(h))
```

Magnetisation can now be set within each of the defined objects called into the mesh. As described previously in 4.7.4, each nanoisland can be treated to have a uniform macro-spin of aligned moments. Here, macro-spin moments either point 'in' towards the centre of the vertex, or 'out' from the centre. Combinations of various in and out need to be defined as a magnetisation vector, as the goal is to find the E_{Total} distribution for each vertex type. As such, an 'in' moment is defined as In = 1, and an 'out' moment as Out = 0 (Figure 4.19(b)), and magnetisation for a 001 configuration, for example, is defined as:

```
//001
m.setinshape( b, uniform(1,-1,0) )
m.setinshape( e, uniform(-1,0,0) )
m.setinshape( h, uniform(1,-1,0) )
```

The edge moments within a nanoisland are not expected to behave uniformly, and will follow stray field lines. However, the effect has a negligible contribution to the E_{Total} distribution. Magnetisation is defined in-plane with vectors in the form (x, y, z), where z

= 0 is always used. Next, total magnetisation is saved, a .jpeg image of the model is saved, and E_{Total} is calculated and added to a table with the following lines:

```
save(m)
snapshot(m)
tableadd(E_total)
tablesave()
```

This calculation is done for each combination and every vertex type. For the 3i vertex, there are $2^3 = 8$ unique combinations, while for the 8i vertex there are $2^8 = 256$ unique combinations. A simple script was developed by Dr Samual Coates to list each possible combination of m. The final table produced has each combination in binary (Examples: 001, 10110, 1000111), next to the calculated E_{Total}.

Modelling Setup: Square-Fibonacci tiling

The E_{Total} for each vertex type and a selection discrete tilings of the Square Fibonacci tiling were tabulated with a similar method as for the Ammann-Beenker tiling, but with new island lengths corresponding to experimental dimensions measured in Chapter 7. Another change was the use of the MuMax3 relax function in the form:

```
m = RandomMag()
relax()
save(m)
snapshot(m)
tablesave()
```

Here, RandonMag() removes the carefully configured parallel alignment of voxel moments, which essentially simulates a paramagnetic regime. The relax function allows MuMax3 to advance the LLG equation with explicit Runge-Kutta methods, to minimise E_{Total} [25]. The RK45 Dormand-Prince method is the default approach, which offers fifth order convergence for adaptive time step control. The effective field and moment vector of each voxel is stepped towards minimising E_{Total}, until a numerical noise floor is reached.

Chapter 5

Fabricating Quasiperiodic Tilings with Thermal-Scanning Probe Lithography

5.1 Introduction

Since the discovery of quasiperiodic materials, a major research effort has been undertaken to understand properties related to their structure [8,9]. However, characterising the physical properties of atomic-scale metallic-alloy quasicrystals poses several challenges. This is primarily due to the aperiodic arrangement of atoms, complicating structure determination and requiring advanced measurement techniques under UHV [10].

The repertoire of metallic-alloy quasicrystals available is limited to certain structures, such as icosahedral, decagonal, and dodecagonal systems. Metallic-alloy quasicrystals are grown with Czochralski, Bridgman, Floating Zone, or Self-Flux methods [244,245]. Growth conditions such as temperature, pressure, and composition are carefully controlled to produce high-quality quasicrystals with desired properties. Characterising the properties of the bulk and surfaces of quasicrystals is performed with various diffraction, spectroscopy, and microscopy techniques [78]. Pseudomorphic systems of atomic overlayers on quasicrystal surfaces have also been grown [194]. Overall, the preparation and characterisation of quasicrystals is challenging, spurring novel approaches.

Quasiperiodic tilings can be used to model the surface of quasicrystals, and have the potential to be fabricated with established nanolithography techniques, summarised in Chapter 2. Nanolithography techniques encompass artificial fabrication or manipulation of nanoscale structures to create patterns on a substrate. At the nano- to mesoscopic scale, nanolithography fabrication techniques open new possibilities for precisely engineering the size, shape, and arrangement of nanostructures, thus enabling tailored function-

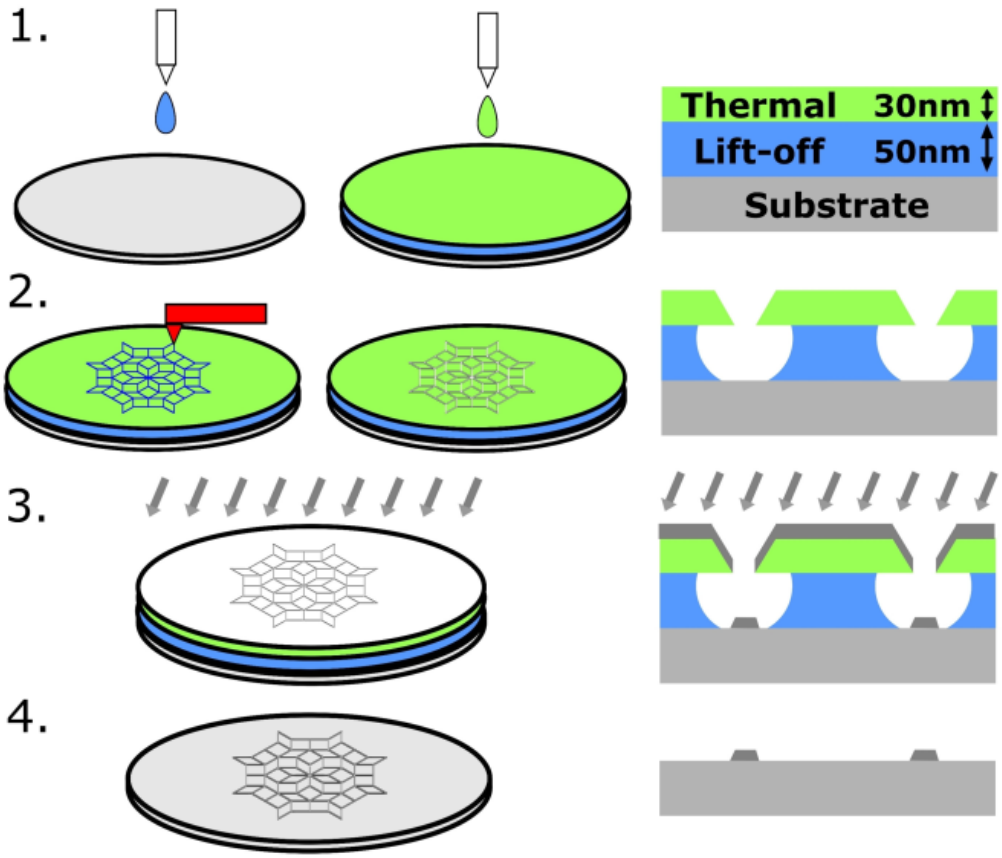

Figure 5.1: A graphic showing the procedure for thermal-scanning probe lithography. Step 1: Lift-off (bottom) and thermal (top) bi-layer polymer resists are deposited and spin-coated sequentially onto a clean atomically flat substrate. Step 2: A heated t-SPL tip sublimates surface molecules into a pattern in the thermal resist, a solvent then chemically etches (resist development) the patterned area which exposes the substrate, creating a mask. Step 3: A user-specified material, chosen for physical properties, is evaporated onto the masked sample. Step 4: The polymer resists are chemically removed in a lift-off process, leaving the desired pattern.

alities [115, 117, 118, 261]. Quasicrystalline nanostructures have demonstrated exceptional properties with enhanced solar efficiency [120, 121], improved catalytic performance [122], and thermoelectric applications [123–125].

The work contained in this chapter focuses on the design, chemical, and physical optimisations that are essential for a successful thermal scanning probe lithography (t-SPL) fabrication. t-SPL is a relatively novel scanning probe lithography technique compared to established electron beam and photolithography techniques, and so essential optimisations and written guides are still in their infancy, or only shared within research groups. Work recently published by the author briefly covered important optimisations [18], but there is still a need for a thorough and comprehensive discussion for new researchers to the field.

The majority of method improvements discussed in this thesis are related to fabricating

Stage	Description
Design (Step 2)	Tiling generation technique, coding, and tailoring
	Corresponding pixel density to pattern-by-pixel software (DPI and Figsize)
	Practical pixel limit
	Optimising throughput, and reducing waste
Chemical (Step 1)	Suitable substrate for needs (annealing or electrically sensitive measurements)
	Pristinely clean atomic surface of substrate
	Dicing substrates into suitable wafer sizes for experiment
	Reducing particulate distribution when scoring
	Plasma ash, pre-bake procedure, and resist uniformity
	PPA concentration and degradation
	Resist stack height for best resolution and metal thickness
Chemical (Step 2)	Undercut exposure time and solvent concentration
Chemical (Step 4)	Lift-off issues
Physical (Step 2)	Correct mounting, and avoiding damaging tip
	Adhesion length
	Cleaning tips
	Calibration corrections
	Applied voltage and feedback model
	Actual contact temperature
	Write temperature and pixel time
	Image analysis corrections

Table 5.1: Table summarising all essential optimisations required for a reproducibly high-quality t-SPL fabrication. Each optimisation is shown in chronological order as it would occur during the fabrication process and as ordered in this Chapter. Stages are broken down into Design, Chemical, and Physical optimisations, with indicated steps corresponding to the four steps in Figure 5.1.

the quasiperiodic 8-fold Ammann-Beenker Tiling (ABT), for the artificial spin-ice work carried out in chapter 6. All optimisations discussed are relevant for any fabrication work undertaken with t-SPL, and are pedagogically discussed and illustrated with microscopy images taken either during or after the nanolithography process.

For the purposes of providing a roadmap for this chapter, a standard t-SPL process is shown in Figure 5.1, also covered in the experimental methods in Chapter 4. Table 5.1 summarises all the essential steps for optimising the t-SPL process, relating each to the four

stages shown in Figure 5.1. Firstly, Section 5.2.1 goes into detail about how the design for a quasiperiodic tiling was chosen, including the coding required to generate tilings with the substitution method, and resolution optimisations to make the patterns ready to etch with t-SPL. Then, Section 5.2.2 covers the delicate optimisations and challenges overcome for the preparation of substrates, resist stack considerations, chemical undercut development, and the lift-off process. Finally, Section 5.2.3 focuses on the direct-write optimisation process of the t-SPL probe, including cantilever mounting, the actual tip contact temperature, tip cleaning, temperature and pixel times, software optimisations, and optimisations related to the write process. The combination of optimisations and fixes at every level of the nanolithography process lead to the final fabrication results are shown in Section 5.2.4.

5.2 Results and Discussion

5.2.1 Designing, Coding, and Resolution Optimisations

Tiling generation technique, coding, and tailoring

The t-SPL NanoFrazor [229] used in this research operates by etching structures directly from greyscale images uploaded to its software, with patterning performed pixel by pixel. As a result, it is crucial to carefully select and design the desired quasiperiodic tilings in greyscale, with tunable pixel resolution. To achieve this, Python scripts for substitution and dual grid methods were developed to generate quasiperiodic tilings. The chosen substitution method will be outlined, preferred due to its simplicity, direct visualisation, and ease of iteration control. To begin, a prototile is defined with an array of vertex points. For the ABT, these prototiles are the square and rhombus:

```
%    rhombA5 = [('rhombA5', (0,0), (1,0), array(rotatePoint(1,0,45))+(1,0),
%    rotatePoint(1,0,45) )]
%    squareA5 = [( 'squareA5', (0,0), (1,0), (1,1), (0,1) )]
%
```

Next, a deflation function with procedure shown in Figure 5.2(a-c) for the ABT, with the silver ratio for inflation, to define a new set of tiles with new vertex points. The function takes a list of tiles and an integer n, representing the number of deflation iterations. For each iteration (n times), the function processes every tile in the current list, then the deflation procedure (new vertex points) for the ABT square and rhombus splits the prototile into smaller tiles. Duplicates are removed by checking the centre of each tile, only tiles with unique centres are retained to avoid overlaps, ensuring the tiling remains valid. The final list plots a figure of tiles with vertices that may be rescaled incorporating Python's

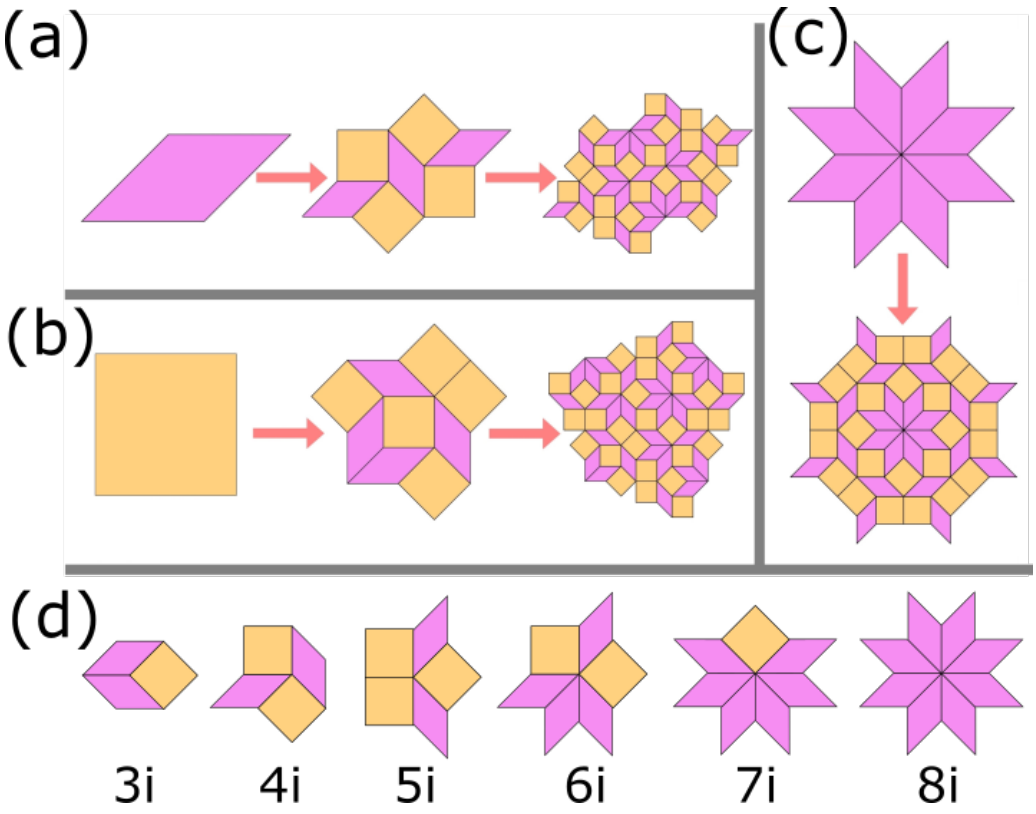

Figure 5.2: The substitution method for the ABT illustrated by the code written in the text. Rhombic and square prototiles are iteratively substituted twice in (a) and (b), respectively. (c) Eight rhombic prototiles are placed in a star and iterated with the substitution method, a design which is the basis for the majority of ABT structures fabricated in this Chapter. (d) The final six vertex types produced within the ABT and their surrounding tiles.

DPI (dots per inch) and figure size (in inches) plot functions. Figure 5.2(d) shows the six vertex types found in the final ABT, discussed further later in this Chapter and in Chapter 6. A broad range of quasiperiodic tilings, shown in Figure 5.3, were generated to identify the most suitable option for the research. The tilings considered include ABT, Square Fibonacci, and Penrose tilings.

Next, the design improvements for the ABT will be discussed. This tiling was chosen for its unique mirror symmetry and potential to investigate long-range nanomagnetic interactions in a geometrically frustrated quasiperiodic system. The results of this investigation are discussed in detail in Chapter 6. For now, the final design is shown in Figure 5.4. The increase in complexity from the initial ABT from Figure 5.3(a) to Figure 5.4(a) is due to an extra iteration in the substitution method. Most importantly, each edge is decorated with a nanoscale island, with width constrained to under 200 nm to ensure a single ferromagnetic domain [79]. Most importantly, in developing the design from Figure 5.3(a) to Figure 5.4(a), a white 8-fold star is placed at each vertex, to give the impression of isolated ellipsoidal islands with pointed tips. The initial design in Figure 5.4(a) was 48 µm in size,

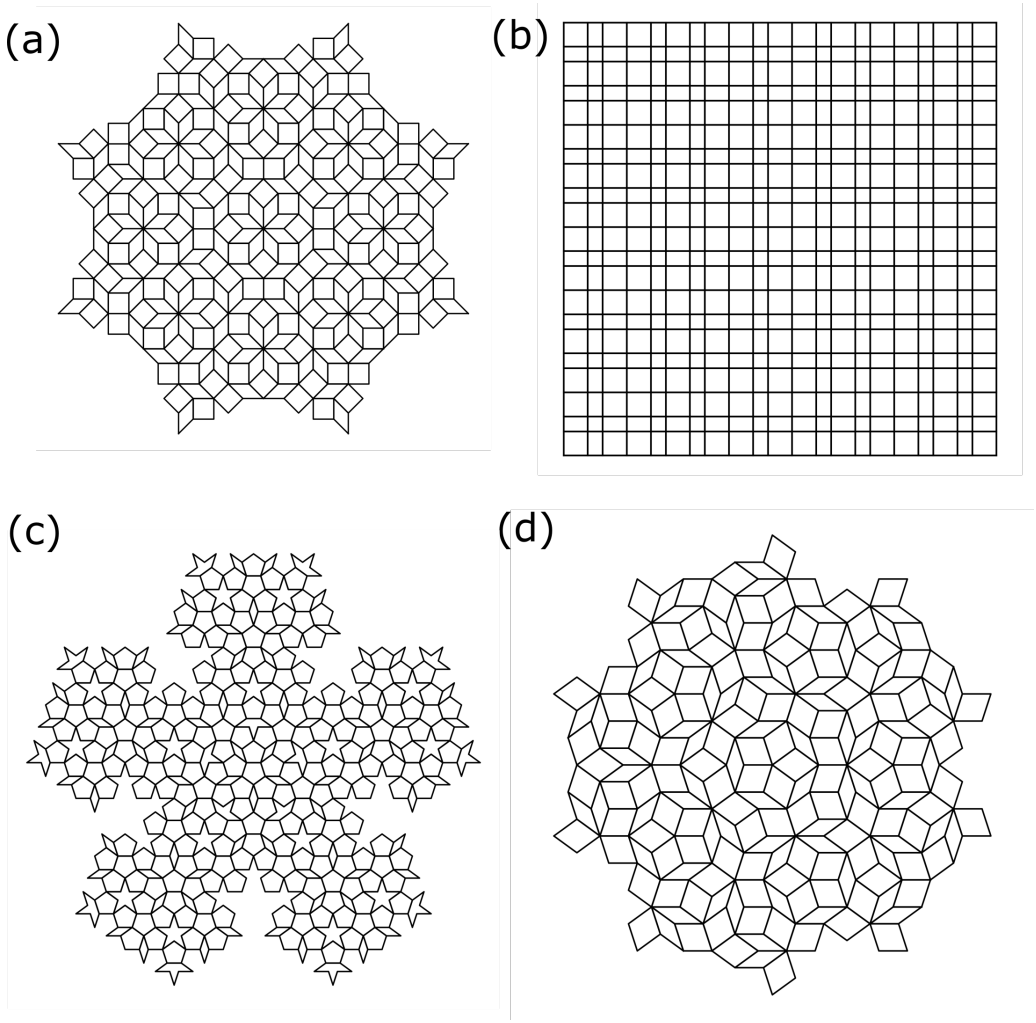

Figure 5.3: Generated quasiperiodic tilings made with Python: (a) Ammann-Beenker. (b) Square Fibonacci. (c) Penrose P1. (d) Penrose P3

close to the limit within a single t-SPL pattern window. Due to the size of the tiling, resist build-up increased on the t-SPL tip, leading to the tip more easily sticking. Additionally, level-plane corrections over a large pattern window were less accurate leading to over or under-etching, and each pattern took six minutes to etch. These t-SPL challenges are discussed further later in this chapter in section 5.2.3. The final design shown in Figure 5.4(b) is 36 µm in size, taking only three minutes to etch. The increase in throughput is due to a better utilisation of space over the entire pattern, and smaller pattern size, compared to Figure 5.4(a). Due to a shorter etching time, there are fewer nanolithography issues related to tip-lifetime such as degradation, resist build-up, and a more reliable level plane correction. A total pattern size of 36 µm is also suitable for measuring within a single magnetic force microscopy image (limited to ≈ 30 µm), rather than stitching several images together.

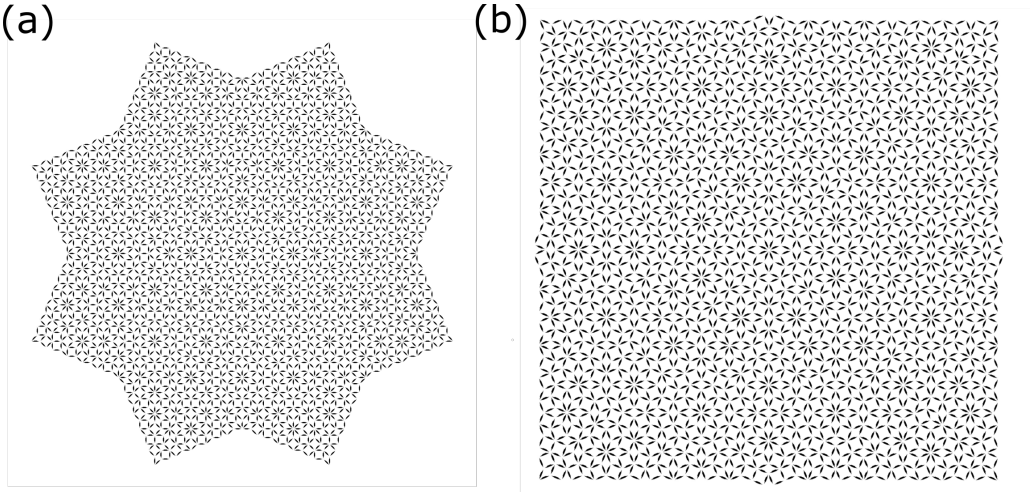

Figure 5.4: Final designs for creating artificial spin-ice patterns of the ABT. (a) The larger star-like pattern, shaped due to the substitution method used to generate the tiling. (b) The final square ABT, chosen due a faster etch time, fewer lithography defects, and appropriateness for measuring.

Practical Pixel Limit

The design is constrained by the practical resolution limit which can be achieved in one pixel by t-SPL. Firstly, the tip has a minimum apex which is physically blunted over time, lowering resolution. Additionally, heat transfer from the tip to the surface is primarily transferred via acoustic phonons [262]. Since the sharp tip apex has a diameter smaller than the phonon mean free path, increased scattering reduces thermal conduction with the surface. Blunt tips have a greater contact diameter and so greater thermal conductivity. A blunted tip therefore heats more easily with the same writer conditions, leading to a larger sphere of sublimation. Resist build-up on the tip is also inevitable, leading to the tip sticking to the surface, impacting the pattern quality. As a result, a practical limit for a typical bi-layer stack is 20 nm per pixel, which needs to be considered in the greyscale images uploaded to pattern. A higher resolution below 10 nm has been demonstrated in the literature with t-SPL using ultra-thin resist and SiO_2 stacks [263]. Another consideration is the t-SPL NanoFrazor tracks single etches within windows of 50 µm, so it is necessary to determine what combination of DPI and figure size in Python are suitable to keep the whole pattern within one window.

Corresponding pixel density to pattern-by-pixel software (DPI and Figsize).

Figure 5.5 demonstrates how the combination of DPI and figure size for a single-window pattern transfer impacts the final resolution. Given a single-window has a maximum size of 50 µm it is important to optimise what values of DPI and figure size are suitable. Patterns are intended to be close to this 50 µm, to increase the statistics available from

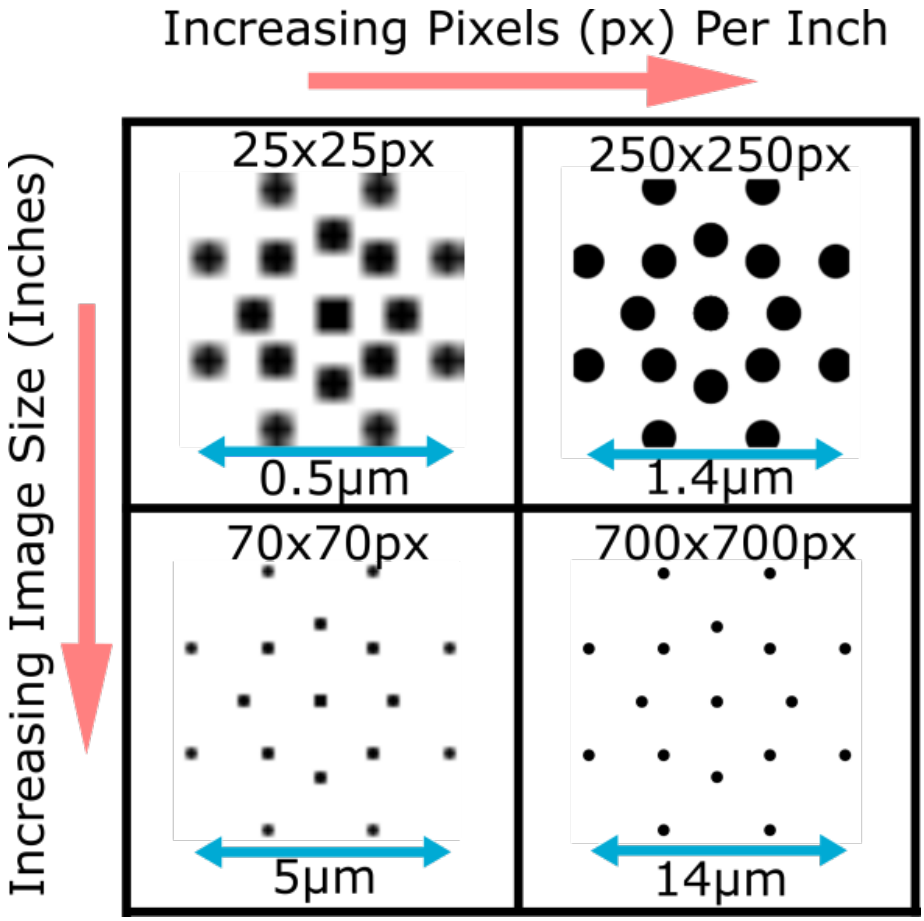

Figure 5.5: A graphical example of how an octagonal array of vertices varies with changes in the DPI and figure size set in Python, impacting the physical size of the final design given a 20 nm/pixel practical limit.

measurements, and to make patterns easier to find with microscopy techniques. The top left panel contains a 25 x 25 px dot pattern that is quite blurred, the physical etched size would be 25 pixels x 20 nm/pixel = 0.5 µm. This size would not be suitable for the tilings shown in Figure 5.3, as they would be too small. The top right panel multiplies the DPI by ten, to 250 x 250 px, and a physical size of 1.4 µm. The dots of the pattern are now around 200 nm in diameter and much clearer, but the canvas figure size is still too small. Finally, the bottom two panels multiply the figure size by ten, increasing the physical size from 0.5 µm and 1.4 µm to 5 µm and 14 µm, respectively. A pattern of the order of 14 µm is much closer to the nanoscale features hoped to be achieveed with designs from Figure 5.3.

Optimising throughput, and reducing waste.

Some optimisations can be made to a pattern design to improve throughput and reduce waste. Stitching patterns across multiple windows is possible, but this requires some align-

ment, as piezoelectric actuators have intrinsic errors in position, and etch time is also increased. Ideally, for a high-resolution pattern, fewer impressions per feature are desired for a higher throughput. For example, a dot made with a single 100 nm pixel etch would have a higher throughput than a dot made with several 20 nm pixel etches. Fewer impressions also improve the tip's lifetime, which is negatively impacted by several depressions into the resists per feature. Connected edge tilings can achieve 20 nm resolution, but at vertices there are several overlapping features causing heating proximity effects that overexpose the resists. With delicate designing, different tiling decorations are possible by plotting just vertices, plotting between vertices (connected edges), or disconnected edges (by plotting connected edges and then white stars on the vertices to create a disconnected appearance).

5.2.2 Optimising the Chemical Process

Chemical challenges are present at all stages of the nanolithography process, namely in substrate preparation, solvent exposure, and then chemical lift-off. This section will highlight these various challenges faced, and how they were overcome. To remind the reader, the full method is shown in Figure 5.1:

- **Step 1:** A clean, atomically flat substrate is prepared, and a bi-layer polymer resist is deposited with a micropipette. The bottom layer is a lift-off resist (PMGI), while the top layer is a thermal resist (PPA in Anisole). Both layers are deposited sequentially using spin-coating.
- **Step 2:** A heated tip in a t-SPL system sublimates surface molecules in the thermal resist, creating a patterned mask. A solvent is then applied to chemically etch the PMGI resist through the mask, exposing the underlying substrate and forming a mask for material deposition.
- **Step 3:** A material with chosen physical properties is selected and evaporated onto the masked sample, depositing it onto the exposed regions of the substrate.
- **Step 4:** The polymer resists are removed using a chemical lift-off process, leaving behind only the desired patterned material on the substrate.

Picking Suitable Substrates

The substrates first used for etching with this research are prime monocrystalline Si discs between 2-4 in (supplier: MicroChemicals GmbH), which have been mechanically polished to be atomically flat. An atomically flat substrate is essential for both continuous and mask-grown thin films, to avoid unintended raised or lowered features. It is critical to make the correct choice of wafer substrate for the research goals. For example, our system

may require annealing at higher temperatures to promote equilibrium conditions. With this need in mind, SiN substrates are chosen to reduce Ni interdiffusion during annealing [29], discussed further in chapter 6. Similarly, for sensitive applications such as in semiconductors, where high electrical resistance are essential, wafers designed to have a high ohmic resistivity would be chosen.

Pristinely clean atomic surface of substrate

It is critical that the substrate is pristinely clean before adding polymer resists, so that these resists can be applied uniformly and without streaking - caused by particulates on the substrate surface. The substrate is thoroughly cleaned in an acetone followed by an isopropyl bathe, and dried with an inert gas. There is not a significant change in final film quality between a bathe and thoroughly spraying the substrates, however the former allows ultra-sonication which aides removing particulates.

Dicing substrates into suitable wafer sizes for experiment

There is a decision to be made whether to dice substrates before or after spin-coating resist films, and to what size. Given the substrates are batched as 2-4 in discs, an appropriate cut is between 2-3 cm square, allowing for four or nine 1 cm wafers ready to coat. It is not sensible to coat a full disc at a time as this will produce twenty-thirty 1 cm wafers that would take too long to etch. This is because each square will take around 2 hours to etch patterns onto, therefore it is not encouraged to coat them all within 2 days. This time limit is set because it was found heuristically that patterns produced from etching soon after the batch is prepared were of highest quality. This may be due to the thermal resist beginning to degrade when stored at room temperature, or polymer mobility between layers. The degradation may be exaggerated by the very thin (14 nm) thickness of the thermal resist layer, reducing stability. One potential improvement would be to store coated wafers in a cooled desiccator that may increase the polymer lifetime.

Reducing particulate distribution when scoring

There is an issue that dicing Si substrates causes particles to scatter across the surface. These along with other particulates cause comet features to appear across the coated substrate when spin-coating the bi-layer resists. However, dicing the substrates into smaller wafers can be before or after coating. One solution is therefore to deposit a sacrificial resist onto the surface, dice substrates, then chemically remove the resist and any particulates. As the sacrificial resist is completely removed and the new smaller wafers are clean, the bi-layer resists can be coated with little to no defects. This does introduce a throughput issue however, as the user would have to juggle coating each square with the resists individually.

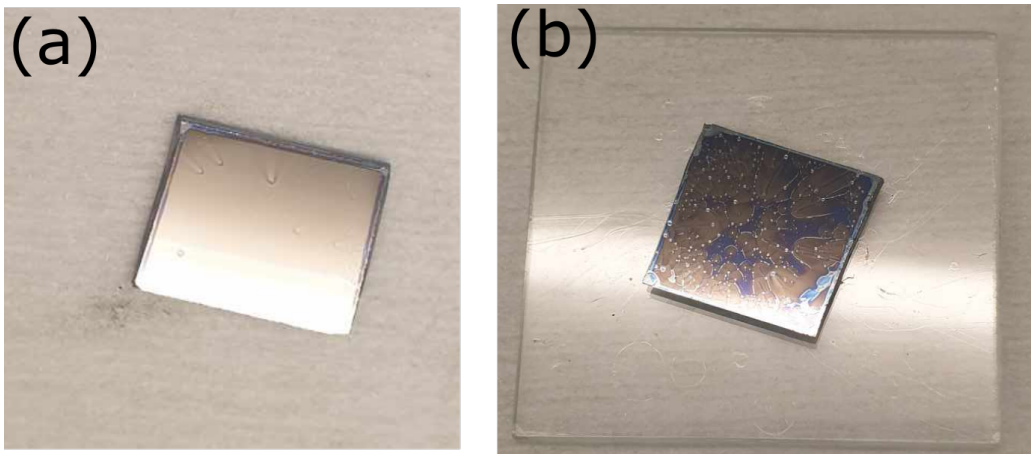

Figure 5.6: Two 1 cm Si wafers with different preparation and final bi-layer resist stack quality. (a) A good quality finish due to proper cleaning and preparation. (b) A poor quality finish due to poor cleaning and preparation.

In a typical batch of four squares it could take up to four times as long to coat in this manner. There is then a decision whether it is more convenient to just batch spin-coat, then dice substrates into squares and clean each with isopropyl. This research settled with using a sacrificial resist to dice the 2-4 in discs into $\approx$ 2 cm square wafers, chemically removing the resist, spin-coating the correct bi-layer resists, and finally dicing into 1 cm wafers and spraying particles off with Ar or N.

Figure 5.6 shows how dicing the substrate and preparation can easily change final resist coating results. Figure 5.6(a) shows a 1 cm square wafer with a bi-layer resist that was correctly cleaned before spin-coating, whereas Figure 5.6(b) shows a poor quality coating. There are two main features which indicate Figure 5.6(b) to be poor quality - comet streaks from the centre outward, and patches of grey and blue blotches. Firstly, the comet streaks are caused by particulates shielding the resist from uniformly coating outward as it is accelerated in the spin-coater. Secondly, the lighter grey blotches represent the top-layer of the resist stack, which appears uniformly in Figure 5.6(a). Also, the blue patches appearing suggests the top layer solution may have been improperly prepared, or the substrate was not correctly baked between depositions.

Plasma ash, pre-bake procedure, and resist uniformity

As discussed in Chapter 4, bi-layer polymer resists are spin-coated, but the preparation and properties of these resists are not the same. Figure 5.1 shows the bi-layer PMGI:PPA resist stack used for this research. The PMGI (lift-off) resist is referred to as the bottom layer as it is deposited and spin-coated first, and the PPA (thermal) resist the top layer because it is deposited and spin-coated atop the PMGI layer.

Preparing the resists presents new challenges. The PMGI (supplier: Kayaku) layer must

be coated uniformly for the PPA deposited atop to also be uniformly coated. Several issues can arise from a poor PMGI coating: comet features, poor adhesion with the substrate and PPA layer, and a non-uniform layer can all have knock-on effects for the nanolithography process. As discussed, comet effects are caused by raised particulate features on the surface, leading to the PPA deposited atop to not coat uniformly. Poor adhesion is due to not activating the surface correctly via an O_2 plasma ash, or by not correctly soft-baking (annealing) the wafer on a hot plate. Activating the surface involves O_2 plasma bombarding the surface leaving exposed high-energy broken bonds, which more readily accept the PMGI polymer for adhesion. Baking above 100 °C before plasma ashing is also important to remove any water molecules on the surface. Finally if the PMGI layer thickness is not reproducibly uniform, then the exposure time needed by the TMAH:isopropyl solution will vary greatly between patterned wafers, leading to over or underexposed patterns that are wasted.

PPA concentration and degradation

There is additional preparation required for the PPA resist compared to the PMGI resist, leading to additional challenges. PPA is delivered in powder form (supplier: Allresist), which must be kept in a freezer to increase lifetime - the manufacturer recommends storing in $-18\,°C$ that keeps the PPA stable for at least a year. The main challenge occurs when dissolving the PPA powder in anisole. It is important to calculate and measure the correct concentration of PPA in anisole, as the concentration is directly correlated to the thickness. If the solution isn't properly filtered or sonicated, mesoscopic PPA particles are visible on the surface making large-scale patterning difficult. If not properly filtered or sonicated, the film quality will look similar to Figure 5.6(b). Another consideration is how sensitive the correct concentration of PPA in anisole is to the resist thickness. For example, a concentration of 0.85% PPA in anisole would be expected to produce a 14 nm resist layer when accelerated to 2,000 rpm in the spin-coater, whereas a 2.5% concentration would be expected to be a 45 nm thick layer with the same spin speed. The concentration therefore needs to be carefully measured, as there is significant variation in the resist thickness with a small change in concentration. Another challenge is although PPA is metastable at room temperature, making it ideal for t-SPL to sublimate surface molecules with a hot tip, it will begin to degrade even at room temperature. Degradation is especially sensitive for nanoscale layers such as the 0.85% PPA in anisole concentration, so a new batch should be made regularly for high-resolution pattern transfers. The PPA also binds rapidly to a pre-baked substrate, so spin-coating should begin immediately after deposition.

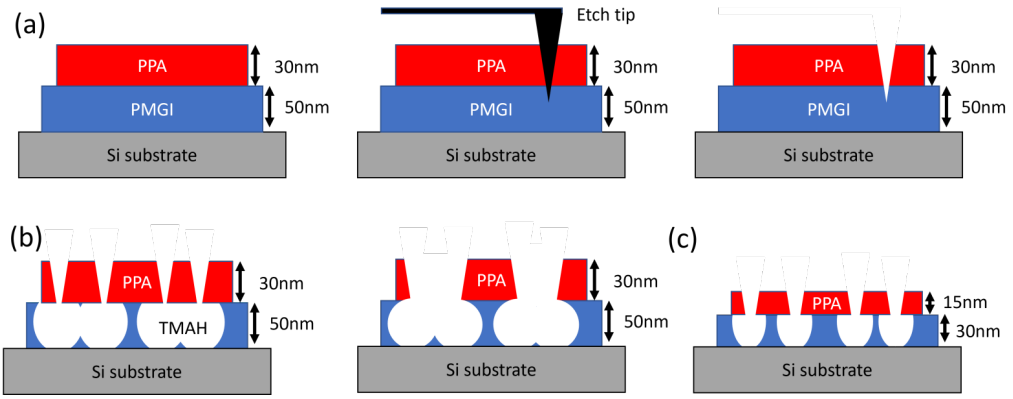

Figure 5.7: Graphically comparing undercut exposure with two different bi-layer resist stack thicknesses. (a) A 50 nm PMGI / 30 nm PPA stack showing an exposed area via t-SPL sublimation. (b) The undercut following TMAH exposure, whereby features too close together have collapsed. (c) A 30 nm PMGI / 15 nm PPA stack with features that have not collapsed due to a thinner lift-off resist.

Resist stack height for best resolution and metal thickness

The minimum achievable resolution that can be etched as a pattern is sensitive to the thickness of the PMGI:PPA stack. Initially, a 50 nm PMGI: 30 nm PPA stack was chosen as a standard thickness stack recommended by the manufacturer. However, it was found to be hard to achieve 20 nm precision on denser features of Figure 5.4(a). Figure 5.7 demonstrates why this may be the case. As the TMAH solvent develops isotropically with a defined speed, etched features that are much closer than 50 nm may cause the PPA resist layer to collapse due to an undercut. Once the stack collapses the resolution of the pattern cannot be recovered. It is possible to undercut 20 nm spaced features with a 50 nm lift-off layer, but the window for the undercut exposure time is vastly reduced. Instead, as seen in Figure 5.7(b), a 30 nm / 15 nm stack allows for the TMAH to develop into a thinner lift-off resist, leaving higher resolution designs. There is an additional benefit to thinning to stack thickness as less of the t-SPL tip is etching into the top layer, improving the lifetime. The downside is that less metal can be grown onto the surface with a thinner lift-off resist, and the develop time for the undercut is much faster. If too much metal is deposited onto a thinner stack, cross-linking between features will make it difficult to lift-off the desired pattern.

Undercut exposure time and solvent concentration

We will now discuss how the exposure time of the TMAH:isopropyl solvent effects the undercut quality. The exposure is performed after t-SPL etching (discussed next in section 5.2.3). The undercut exposes the Si substrate before material deposition, but can cause the resist stack to collapse if overexposed. Overexposure causes the undercut overhang to be

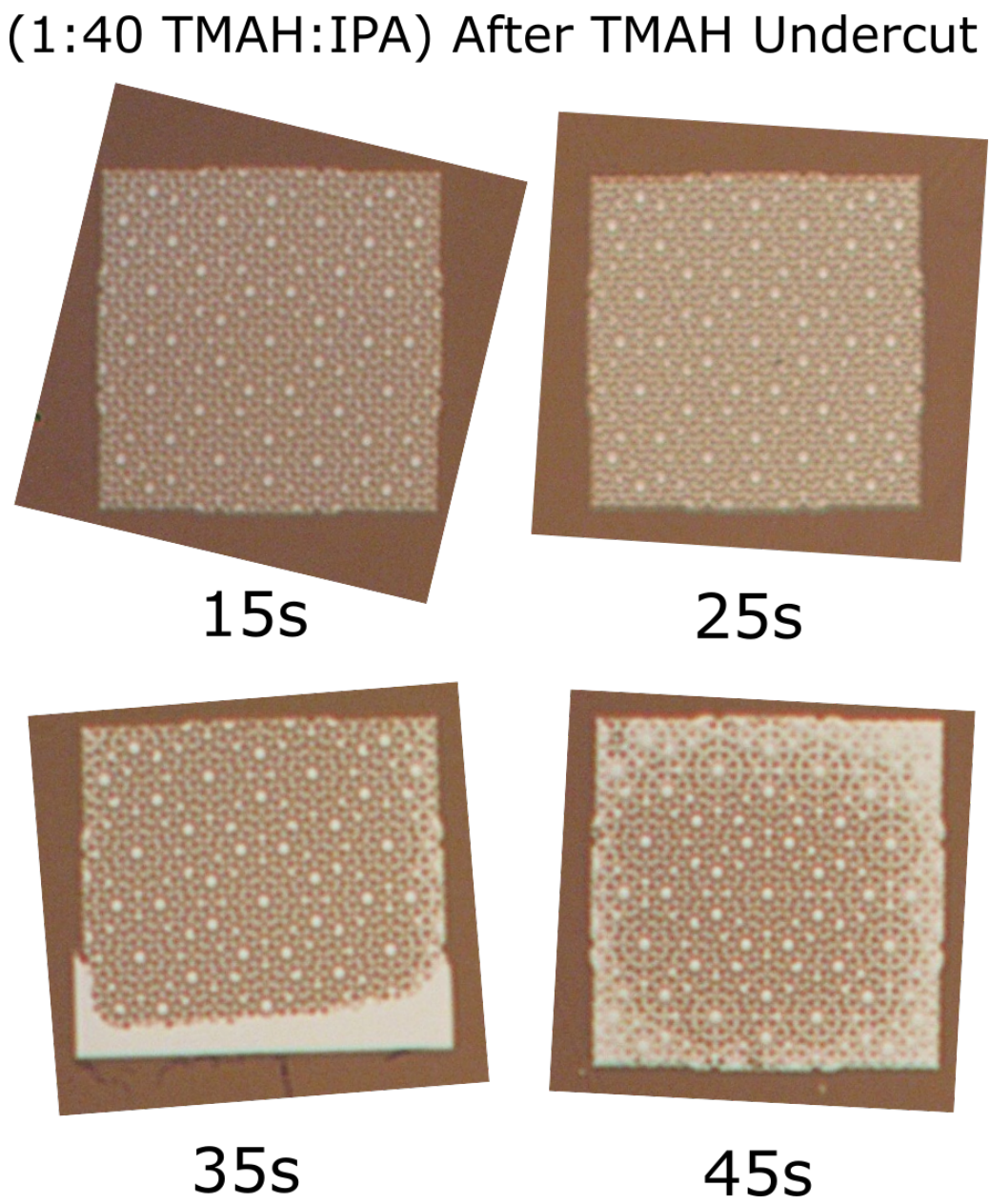

Figure 5.8: A range of Etched ABTs with four different undercut exposure times of 1:40 TMAH:isopropyl, from 15 s to 45 s. Images taken with an optical microscope. The purpose of imaging in this way is a quick test of an appropriate undercut time without damaging the etched patterns.

too great, leading to the resist stack collapsing. The concentration of TMAH:isopropyl can be varied to control undercut development. For resists under 50 nm this typically ranges from 20 - 60 seconds, whereby a greater concentration of TMAH increases the etch rate. A sensible dissolution rate of roughly 1 nm/s is made by mixing 1:40 of 2.38% TMAH with isopropyl. There is significant variation in the dissolution rate of new batches, so exposure time should be first trialled with test samples. Even a few seconds of under-exposure will spoil the metallised pattern. This is because the deposited metal would not fuse to the surface, and be effectively removed following the DMSO lift-off exposure. Similarly, over-exposure would spoil the pattern resolution due to the resist stack collapsing. One option is if the undercut exposure window is found to be too short or long, would be to vary the TMAH:isopropyl concentration between 1:20 - 1:80, to either increase or decrease the time needed to develop the lift-off resist.

A critical step is deciding the undercut time for a given TMAH:isopropyl concentration. As batches of TMAH:isopropyl are made with a single concentration, for example 1:40 or 1:60, it is essential to test what length of time to waft each wafer in the solution for. In figure 5.8, four different exposure times from 15 s to 45 s are shown with an optical microscope. Due to the optical diffraction limit, nanoscale features and defects are not visible with this method, but the colour and appearance of the undercut can tell enough of a story. For example, it is possible to adjust focus between the substrate and etched pattern to determine etch depth - though this technique has a lot of uncertainty. The best use of the optical microscope is to observe macro effects of under or over-exposure to TMAH. By trivially comparing the 15 s and 25 s exposure times, to 35 s and 45 s, it is clear that increasing exposure time leads to a pattern with leeched features. At 35 s, the solid bar along the base corresponds to a deeper etch via t-SPL, in this region the Si substrate is completely exposed and the pattern has been lost. Also, around the edges of both the 35 s and 45 s patterns there are leeched features, whereby overlap between neighbouring features has led to the substrate being overexposed. It is not clear why the edges are more exposed, one explanation may be in how the TMAH travels around the whole structure, or the edges being over etched via t-SPL. From these images, it is sensible to conclude an exposure time range between 10 - 20 s.

In Figure 5.9, a 1:60 concentration after the undercut of a different set of samples is shown with SEM, again with four exposure times ranging from 15 s to 45 s. The purpose is to investigate how over-exposing the substrate leads effects nanoscale features, before metallisation. Note as performing SEM is expected to delaminate layers from the polymer photoresist, the samples will be sacrificed. The SEM method is therefore typically recommended for only metallised structures, after completely chemically removing the resist layers. The TMAH exposure time range is typical to develop into a 30 nm PMGI thickness to expose the Si substrate with around 1 nm/s. Ideally, the pattern should

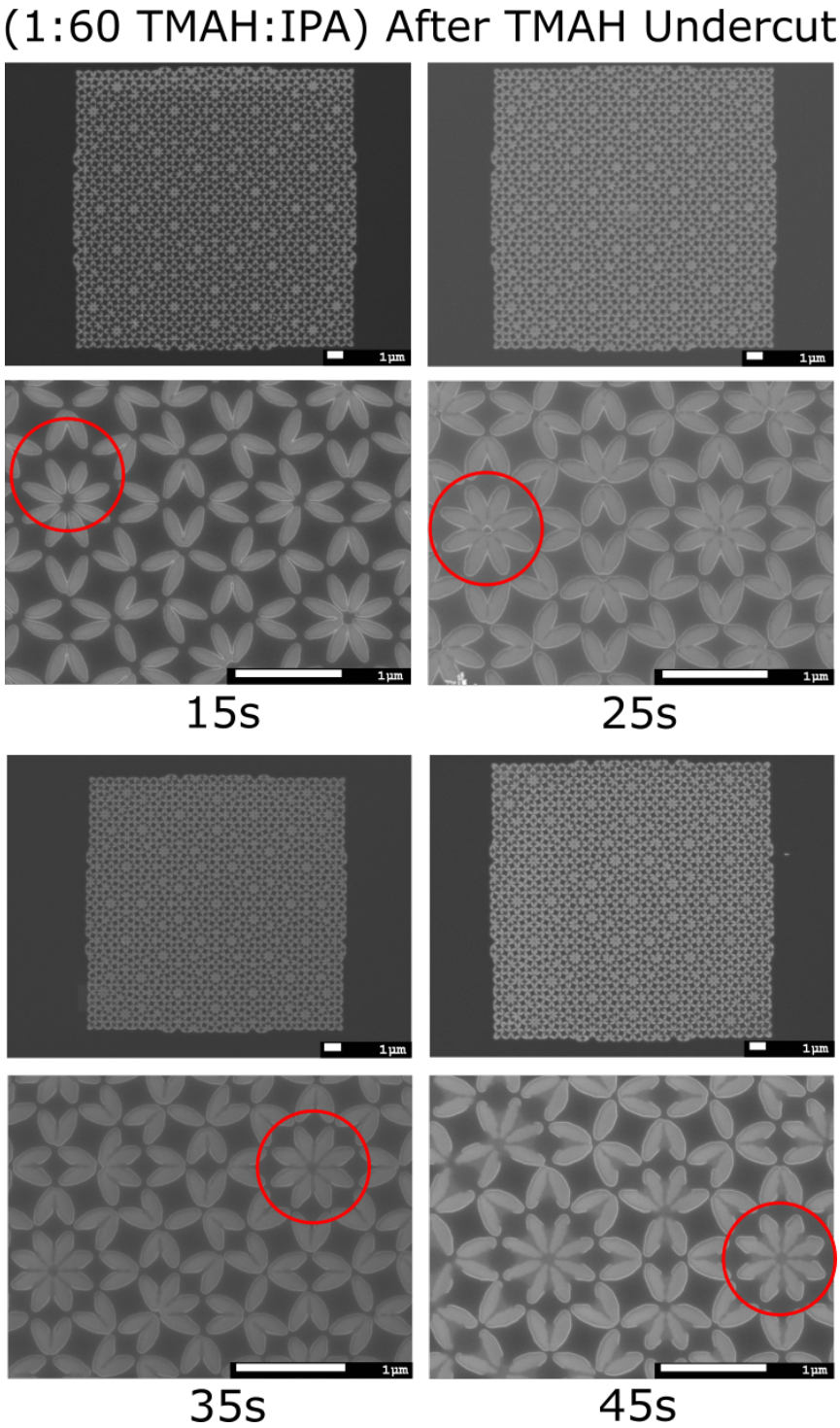

Figure 5.9: Etched ABTs with a range of 1:60 TMAH:isopropyl undercut exposure times, showing both the entire pattern and an X 20,000 magnification SEM image. This demonstrates how increasing exposure time in the range 15 - 45 s causes features to coalesce, and therefore not be suitable for metallisation.

appear close to Figure 5.4 (b), as in each island must be separated from one another. Looking at the demagnified SEM images in Figure 5.9(a) from 15 s - 45 s, there is no obvious discernable difference. The 45 s square does appear denser compared to the 15 s square, supporting that more of the substrate is exposed with a longer chemical bathe. There is a much clearer change comparing the magnified images, for example after 15 s each island appears separated and has lighter edges surrounding the island. The separation between the majority of islands at 15 s exposure suggests metal layers deposited on the surface would create separated nanoislands. There is some overlap between the tips of a handful of islands, suggesting an even shorter exposure time may be sensible. If there was a substantial amount of lift-off resist remaining, there would not be as clear an SEM image, due to the lack of secondary electrons released from a non-metallic surface. Vertices circled in red especially demonstrate how increasing exposure time causes fused features. Looking sequentially at the longer exposure times, it is clear that islands are gradually fusing together, such that any deposited metal film would give overlapping island features. This is caused by the lift-off resist being overexposed to the TMAH solution. Therefore, a suitable chemical exposure time for this TMAH batch and 30 nm of PMGI, would be between 10-15 s. Given this is quite a short window, a less concentrated mix of 1:80 TMAH:isopropyl is recommended, to reduce user error.

Lift-off issues

We will now discuss the challenges and defects that may occur after material deposition and chemically removing all resist stack layers. In principle this leaves the patterned metallised structures, but diagnosing issues and defects is needed to optimise the process. The chemical lift-off requires less optimisation, but it is important to expose with the correctly suggested solvents from the resist manufacturer, to avoid damaging the sample. For thin films, completely removing the resist stack within the patterned structure may be difficult for a few reasons. Firstly, it may be difficult for the solvent to reach under features that are close together, especially when the thin metal film has fused between these features. One solution is to gently cycle the solvent atop the wafer with a micropipette, aiding to remove the resist and connecting metal between features. If, despite spending several hours on this process, the film still clings between features, an ultrasonic bath with the solvent for a few minutes may finally convince the resist stack to let go. It is also possible that the resist stack was too thin, and the deposited metal has fused to the surface and across features too strongly, and therefore cannot be removed. Additionally, if the resist polymers are hard-baked (overheated), cross-linking between polymer chains will strengthen the lift-off resist becoming more rigid and harder to remove.

Figure 5.10 shows SEM images of examples of failed fabrication such as excess thin-film deposition, and over-exposure of the resist development solvent. Figure 5.10(a) shows a

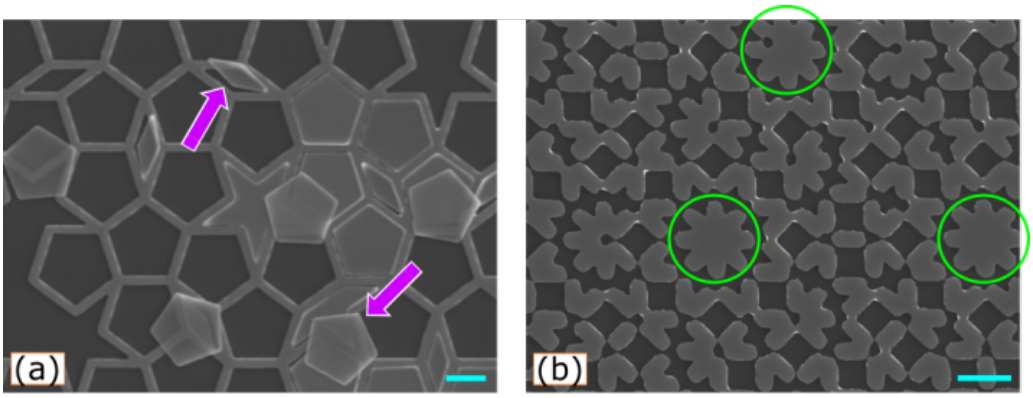

Figure 5.10: SEM images of failed fabricated tilings using t-SPL. (a) A 10-fold Penrose tiling, purple arrows indicate ultra-thin defect tiles scattered on the surface. (b) An 8-fold ABT with disconnected edges, where the edges have bloated defects due to development overexposure. Green circles indicate collapsed stars. Scale bars 1 µm.

fabricated Penrose tiling with permalloy edges. Ultra-thin pentagons, rhombuses, and star tiles are formed where deposited permalloy fuses between etched features, which should have been removed following the final lift-off. Pentagon and Rhombus tiles displaced on the surface are indicated with purple arrows. The permalloy film deposited may have been too thick with respect to the resist thickness and fused across etched features, or total resist removal has not occurred. The PMGI lift-off resist is probably still under these fixed tiles and will out-gas under high vacuum. Some of the pentagon and rhombus tiles are knocked slightly out of place, which may have occurred during transport, cleaning, or when exposed to high vacuum. With physical bombardment or ultra-sonication these tiles may be removed but could damage the intended edge structure the tiles are fused to. Further lift-off resist removal and cleaning is also a potential option to remove any remaining resist.

Figure 5.10(b) shows an ABT intended to have disconnected edges but instead has development overexposure. This structure is how Figure 5.9 with 45 s TMAH exposure would be expected to look like if metallised. The disconnected edges appear bloated as the undercut was too great and the thermal resist likely collapsed before or during permalloy deposition. It is also possible the original pattern dimensions were poorly designed for the resist thickness. As discussed, if the resist solvent develops isotropically, and the horizontal distance between features is much less than the vertical distance of the resist, the stack will collapse. This collapse can be seen in the thick stars in Figure 5.9(b), indicated with green circles. The collapse could also be caused by overestimating the spin-coated PPA thickness, whereby the set depth of the conically shaped t-SPL tip over etches into the second resist layer that may be thinner than expected. In summary, small changes in resist concentrations and thickness, and TMAH exposure time, will lead to significant variations in the final quality of the pattern transfer.

5.2.3 t-SPL Optimisation

Correct mounting, and avoiding damaging tip

Once a substrate is ready to pattern, similar to the one shown in Figure 5.6(a), the t-SPL write process is ready to start. This section will cover challenges and optimisations of that process. Starting with mounting the t-SPL cantilever, the tip must be mounted parallel to the holder, such that the prongs of the holder are in contact with the read and write junctions - as shown in Figure 5.11(a). A thorough description of the t-SPL setup and principles is given in Section 4.3.2. Most importantly, the read heater, located on a separate leg of the cantilever to the write heater and tip, determines proximity to the surface via heat exchange as a function of the air gap to the surface.

It is essential to handle the cantilever on the sides (one side indicated in blue in Figure 5.11(a)), to not physically damage the tip of the cantilever. The tip of the cantilever is conically shaped with half angle θ, a nanoscale apex of finite width w_0, and etch width w a function of depth d and etch broadening width Δw according to the equation [130, 235]:

$$w(d) = w_0 + 2(dtan\theta + \Delta w) \tag{5.2.1}$$

Etch width is broadened by thermo-mechanical interactions between the tip and resist broaden etch width such as heat diffusion, mechanical deformation, and time-dependent material responses, as well as tip contamination during etching. Later, the effects of varying the writer contact temperature and pixel contact time are discussed. If the tip is poorly mounted, the NanoFrazor software is capable of correcting off-centred mounting, but the threshold is related to small imperceptible human error. Tip malfunctions will become obvious during the IV approach calibration curve, whereby feedback from the thermistor cannot determine tip deflection, and an error will read in the software. The first option is to visually inspect the tip for damage or whether it is off-centre, with respect to Figure 5.11(a). A common error is placing the cantilever too far or shallow into the holder. Some tips - described as 'dead tips', have either too much damage or another defect that halts the feedback loop from being completed. It is important to thoroughly test and check before labelling a tip as dead, to avoid waste.

Adhesion Length

An important measure of a quality tip is the adhesion length, relating the vertical deflection distance between the cantilever and the surface before the tip loses contact with the surface [264]. High adhesion length is a universal challenge for t-SPL fabrication, previous works in the literature have identified adhesion force to be important for reproducibility [235, 265], while some authors briefly identify an adhesion length greater than 35 nm to be no longer optimised for 2D patterning [264]. Here, it is observed in detail how adhesion length,

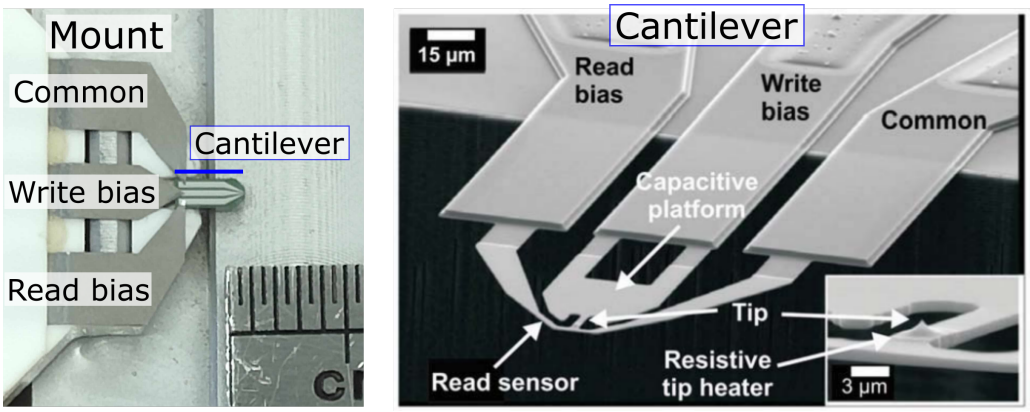

Figure 5.11: The t-SPL mount and cantilever. (a) The cantilever (blue) is shown correctly mounted. The common, write, and read bias junctions of the mount are aligned to the corresponding conductive strips of the cantilever. (b) An SEM micrograph of the cantilever (Image source: [236]). The tip is heated via the write bias voltage, with a capacitive platform for electrostatic actuation. The read sensor is located separate from the heated tip. A read field is performed by measuring heat exchange of the read sensor with the surface, directly proportional to the air gap between the sensor and surface. A magnified image of the tip and tip heater is shown inset.

calculated with a piezoelectric approach and retract calibration before each etched pattern, critically effects the final pattern quality, and how to improve adhesion length with chemical cleaning.

In order to fully understand how adhesion length is determined, Figure 5.12 demonstrates the approach and retract behaviour with respect to the read heater signal and the tip height above the surface. In Figure 5.12(a), the tip approaches the surface in 0.5 nm increments via piezoelectric actuators which deflect the cantilever towards the surface, eventually making contact (black cross in Figure 5.12(b)). Note, if one does not mechanically approach the tip to within 100-200 nm of the surface before this operation, then it will take a long time for the piezoelectric approach to reach the surface. The approach models an applied voltage (cantilever deflection) vs tip height above surface relationship, with the read heater signal is zeroed at contact, for use in estimating tip height on retraction. Retraction is shown in Figure 5.12(c). The tip is still elastically in contact with surface polymers and residual particulates that have not sublimated away form a meniscus around the tip. The result is that despite a lower applied voltage, which would model a greater tip height, the tip is actually much closer to the surface and still in contact. As the tip is closer to the surface, the small air gap between the read heater and surface facilitates heat exchange, causing the read heater signal to remain low. Once the applied voltage is reduced enough such that the adhesion force no longer keeps the tip in contact, the tip rapidly raises above the surface to the same deflection position set by the applied voltage on approach - indicated with a second black cross in Figure 5.12(d).

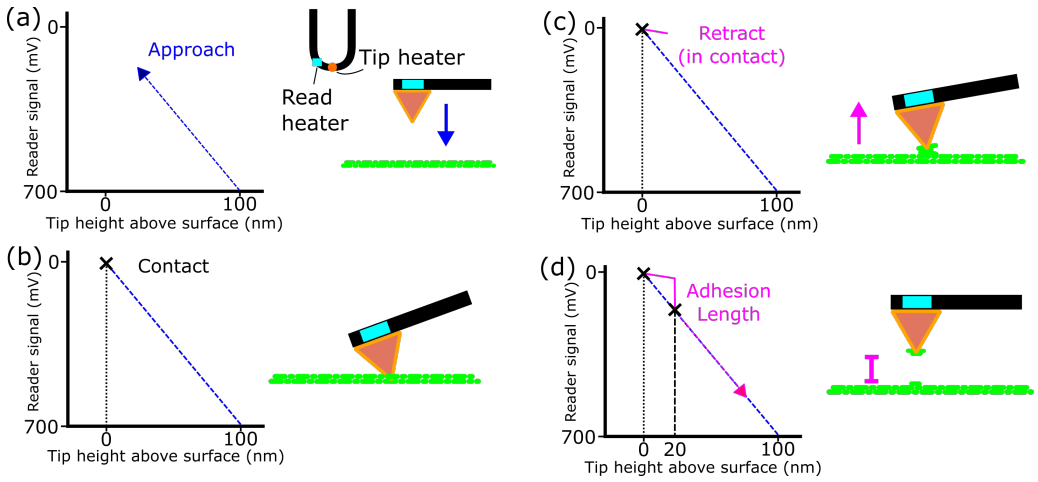

Figure 5.12: A schematic diagram modelling the tip position relative to the surface on approach and retraction, for determining adhesion length. (a) Approach. (b) Contact. (c) Retraction. (d) Adhesion length measured as the vertical deflection where the tip loses contact with the surface.

In Figure 5.13, a piezoelectric approach and retract is used to determine the adhesion length of three subsequent pattern calibrations before each pattern is etched, by measuring the knee point on retraction (indicated with a black arrow on the 3rd pattern). As previously discussed, the knee point relates to the tip remaining in contact with the surface, despite decreasing deflection of the cantilever corresponding to a greater read heater temperature (reader signal). The adhesion length from the first to third pattern increases over time, from 10.35 nm to 25.46 nm, corresponding to the tip sticking to the surface more easily. This is primarily due to resist build-up on the tip that is not sublimating under the $\approx$ 1000 °C write heater temperature. The resist build-up is most likely lift-off resist, as it is not easily thermally stimulated to sublimate. If the adhesion length is increasing too much between patterns, one diagnosis would be over-etching (the set etch depth is too great) into the lift-off resist, and vice versa. As the adhesion length increases, the achievable resolution reduces, which is especially sensitive for our artificial spin-ice applications that require 20 nm/pixel resolution. If the adhesion length is too great the tip will remain in contact scratching the surface and features will leach together, especially seen in the corners of Figure 5.15(a), indicated with purple arrows. The higher adhesion length is caused by residual lift-off resist built-up on the tip, a degradation or lack of uniformity of the thermal resist, or a blunted tip. There is also significant variation in the adhesion length with different areas on the surface, partially due to optically invisible mesoscopic particles. If high-resolution patterning is needed a new tip would be expected to have a much lower adhesion length.

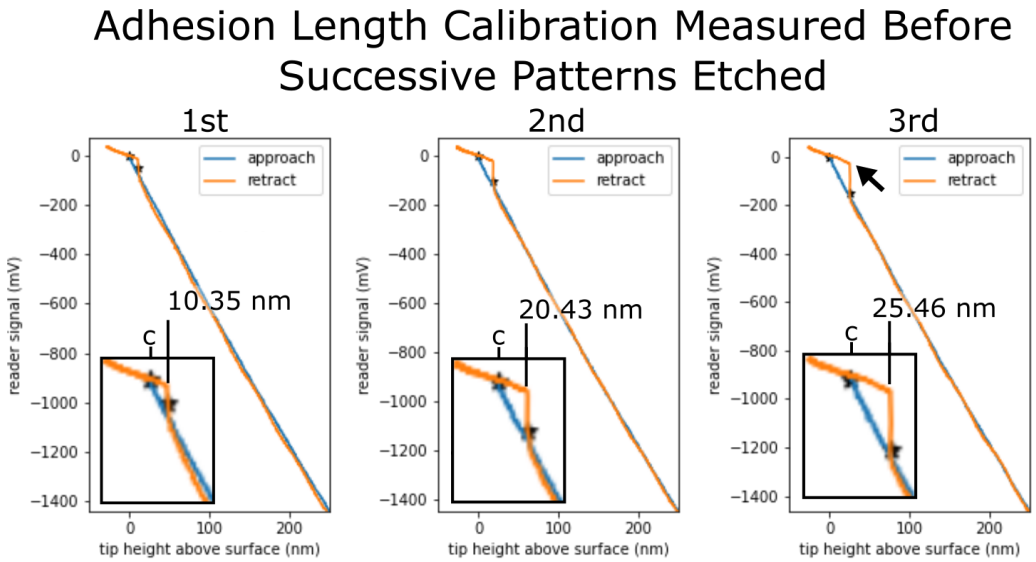

Figure 5.13: Graphs showing the measured adhesion length of the t-SPL tip sticking to the surface, from the 1st-3rd pattern. Adhesion length is determined by the knee-point on retraction, indicated with a black arrow on the 3rd pattern.

Cleaning procedure to extending tip lifetime

As adhesion length is clearly important for high-resolution patterning, it is important to optimise the lifetime of the tip. It has been demonstrated in the literature that cleaning spoiled tips in a bath of chloroform extended the lifetime in cell culture experiments, for bone tissue replicas [266]. With this in mind, suspending used tips in the resist solvent DMSO is experimented with. Any solvent of the resist polymers can, in principle, be effective in restoring high-resolution patterning. Figure 5.14 shows thermal-conductance feedback microscopy images (tc-FM) and the adhesion length of successive etched patterns on the same substrate before and after cleaning the tip in DMSO. In this session, the initial adhesion length was very low (< 5 nm), and increased to 39 nm with around an hour of patterning (nine patterns). The etched pattern before first cleaning (Figure 5.14(a)) shows signs of tip sticking in the darker top area, indicated with a blue arrow. This is also shown by the corresponding etch depth (green line right of the blue arrow) not recovering to base depth, compared to the initial first 40 µm into the pattern. The wet cleaning procedure is simple: suspend one (or a batch) of tips in a beaker of DMSO, and gently stir for 2-3 minutes to remove residual resist. It is essential that the solvent is entirely cleaned off with isopropyl and a dry blow with Ar, as to not contaminate the substrate resist surface with resist solvent. Note, it is sensible to heat samples atop a hot plate (to encourage DMSO resist removal) to ≈ 110 °C for 2-3 minutes, but in practice the heating was not found to significantly accelerate the cleaning efficacy. Ultra-sonication is also an option, but was found on occasion to damage the tip. Looking at Figure 5.14(b), after the first

clean, adhesion length is reduced from 39 nm to 22 nm, quantitively showing how cleaning improves the sticking coefficient. After the first clean, it took around 30 minutes (five patterns) of patterning before sticking effects plague the pattern again. This is evidenced by Figure 5.14(c) with the tc-FM image showing horizontal leeching between features along the top few lines, due to the tip sticking to the surface too easily. Just as after the first clean, after the second clean (Figure 5.14(d)), adhesion length is decreased, this time from 40 nm to 30 nm - but clean etches were only observed for a further two patterns, suggesting mitigating returns on cleaning. These mitigating returns may be due to the bluntening of tips over time, or a cumulative residual resist that is not being effectively removed by the solvent. In practice, the tip patterning lifetime is extended by almost double by cleaning with the resist solvent, continuing to produce high quality etched patterns. This is important because to date no other works have published a cleaning protocol for t-SPL tips, which are costly and may only be suitable for a few hours patterning before cleaning is needed.

Calibration corrections

Even with the availability of clean, high-quality tips, the quality of the sample surface is of key importance. A flat field plane, which scans in a window to estimate height offsets in x and y, is performed, so etching is parallel to the thermal resist. If the resist has poor uniformity this will cause under and over-etching, as even over a single window small variations in resist height will negatively affect the final pattern. For example, in Figure 5.15(b) the darker, deeper, left side of the etch image, indicated with a green arrow, appears too deep, but the etch depth of the vertices are still reaching up to 30 nm (the expected thickness of the thermal resist layer from spin-coating). Figure 5.15(c) shows an inverted 3D rendering of Figure 5.15(b), giving a clearer illustration of an uneven surface, with green arrows corresponding to the same region as in Figure 5.15(b). In the green arrow region, there is a drop in the surface up to 30 nm and then a flat plane. In this case, the thermal resist does not uniformly cover the surface, so areas of the lift-off resist were already or too easily exposed. Regions of thickness can be identified with an optical microscope, due to an optical effect of the finite thickness of the resist films. It is also possible to measure thin film roughness with ellipsometry [267].

Applied voltage and feedback model

Once both the tip and the sample are of high quality, the write feedback mode is chosen. In Figure 5.15(a) the first 5 µm from the base, indicated with a red arrow, has thinner edges, which is not a consequence of the flat plane but of the voltage the tip is being pulsed with. The default NanoFrazor write mode uses Kalman feedback, adjusting the applied voltage until the desired etch depth matches the thermal conductance feedback

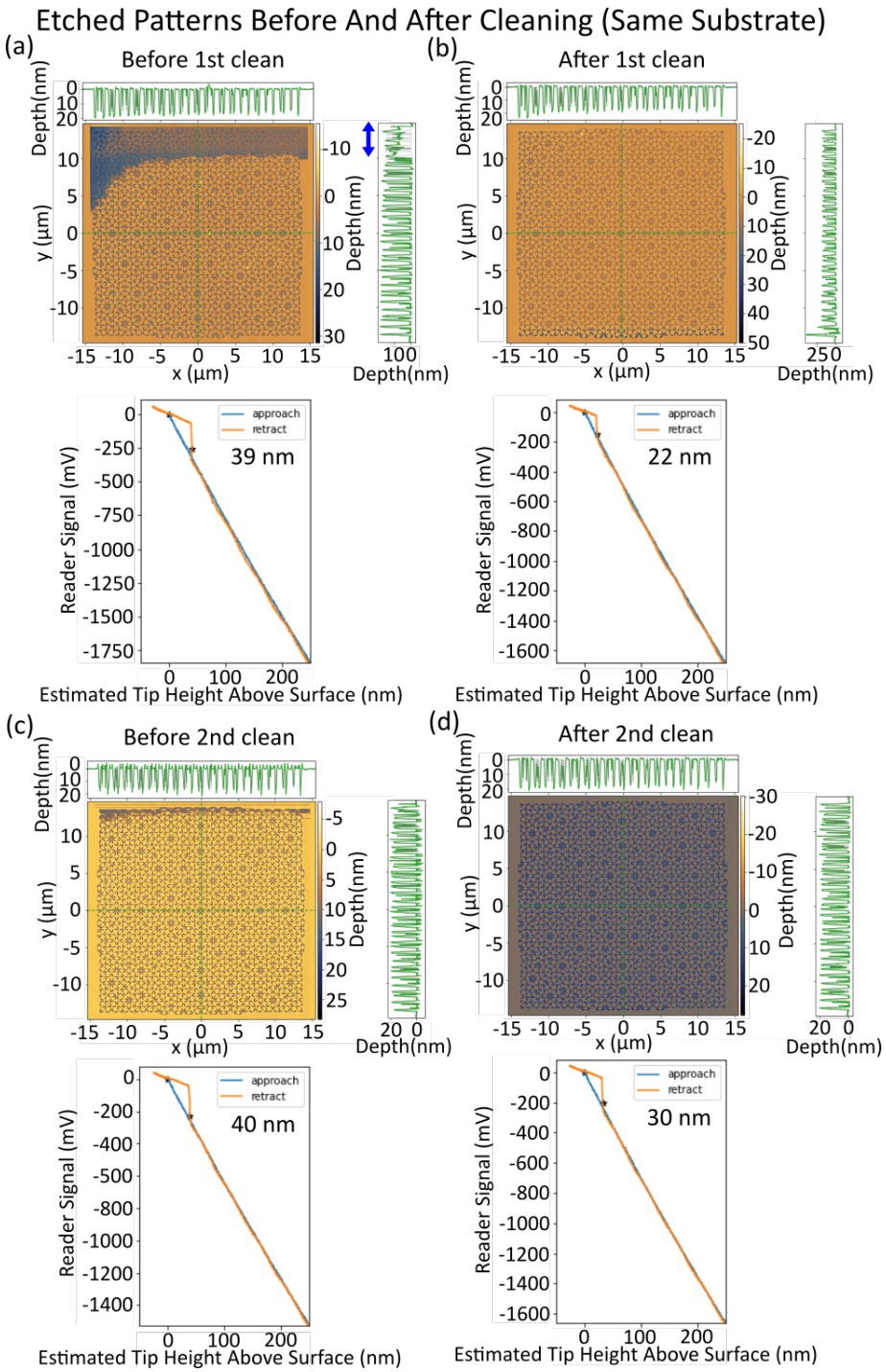

Figure 5.14: tc-FM images and adhesion length graphs showing the effects of cleaning the t-SPL cantilever in beakers of DMSO, the resist solvent. The before and after images of two stages of cleaning demonstrate how quickly cleaning the cantilever can extend the lifetime of high-quality tips.

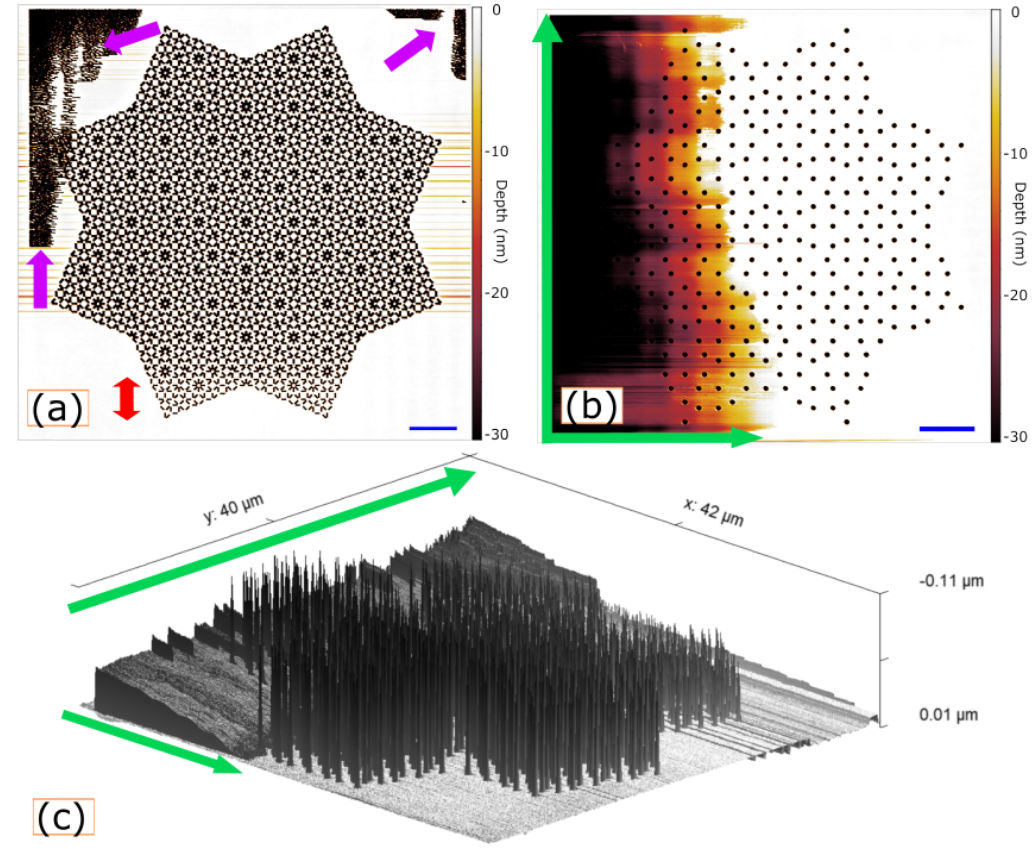

Figure 5.15: Thermal-conductance feedback microscopy images. (a) A disconnected 8-fold ABT, purple arrows highlight a dragged tip on the top corners. The red arrow points to the first 5 µm etch discussed in the text. (b) A vertices-only etched 8-fold ABT, with green arrows highlighting a trench along the left side. Blue scale bars 5 µm. (c) An inverted 3D view of (b), green arrows showing the trench

depth. Applied voltage ranges from 0 to 9V, and in Figure 5.15(a) voltage at the base of the red arrow is pulsed at 3V, and then increases to 5V at the top of the arrow, leading to a greater etch depth. As the tip is conical, a greater applied voltage also broadens the etch width, consequently broader and deeper features are observed for the rest of the pattern. Unfortunately, if the calibration of the tip centre is poor, or any other feedback issue, the thermal-conductance feedback may incorrectly over or underestimate the real etch depth. This in turn leads to over-correcting the applied voltage, changing the breadth and depth of features. As a consistent depth is essential, the best solution is to run a Kalman feedback for the first pattern, and identify the most appropriate voltage for the depth that corresponds to the correct etch depth by eye. Then, a linear voltage model is applied across the whole pattern for constant depth. Another solution are calibration pattern lines at the beginning of the pattern, to improve the Kalman feedback before the real pattern begins, reduce the variation in feature size.

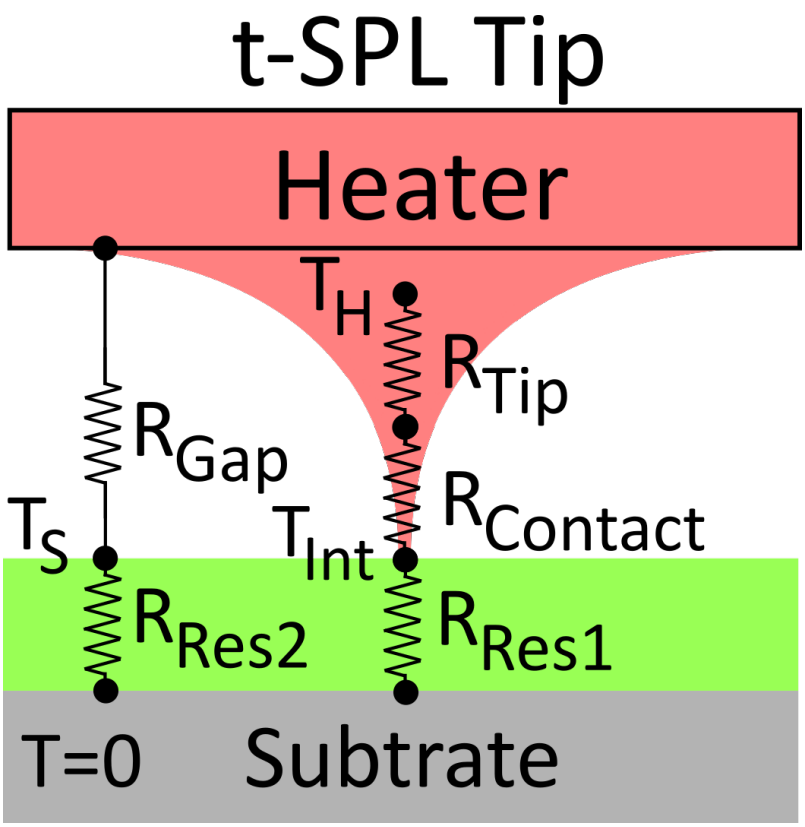

Figure 5.16: A diagram showing the tip - surface interface with thermal resistances and temperatures labelled. T_S refers to the temperature of the surface which modulates heat exchange between the read heater and surface, to estimate tip - surface separation. T_{Int} refers to the actual contact temperature at the interface between the tip and resist surface.

Actual contact temperature

As previously established, both the writer temperature and pixel contact time significantly influence the etch width and depth when using the NanoFrazor system at a constant cantilever actuator voltage. The NanoFrazor operates within a typical write heater temperature range of T_H = 800-1200 °C during writing. However, the actual contact temperature between the tip and the surface interface T_{Int} is much lower, as shown in Figure 5.16, with temperature of the surface T_S [129, 265, 268]. To emphasize the difficulty in estimating T_{Int}, a simple resistive model, developed by Holzner [269], can be followed:

$$T_{Int} = \frac{R_{Res1}}{R_{Tip} + R_{Contact} + R_{Res1}}(T_H - T_S) + T_S \tag{5.2.2}$$

Where R_{Res1} and R_{Res2} are the thermal resistance of the resist substrate under the tip contact and under the air gap, respectively. R_{Tip} and $R_{Contact}$ are the thermal resistances of the tip and tip-sample contact, respectively. Thermal resistance limits the heat flow Q between two bodies ($\Delta T = Q \times R$). Equation 5.2.3 is developed by considering the T_{Int}

as the sum of the original surface temperature, plus the temperature contribution from T_H considering the combined thermal resistances (heater efficiency). Firstly, $R_{Contact}$ can be approximated by considering the nanoscale dimensions of the tip with opening angle θ and apex diameter d. As d is lower than the effective mean free path of acoustic phonons in Si ($\lambda_{eff} \approx 70$ nm assuming no oxidation), phonon boundary scattering plays a much greater role, and the upper part of the tip cone hardly influences the T_{Int} [269]. For similar Si tips to those used in this chapter, $R_{Contact}$ was experimentally measued in the literature to be 2.0×10^8 K/W [268]. Also in the literature, oxidation of the Si tip was experimentally found to dominate R_{tip}, estimated to be between 10^7 - 10^8 KW^{-1} [270]. Finally, R_{Res1} is inversely proportional to d, and the thermal conductivity of the sample k_{resist}. In essence, a smaller tip apex reduces contact area making heat dissipation less efficient, increasing R_{Res1}. R_{Res1} was analytically determined with numerical computer models in the literature [269, 271], described by the following equation:

$$R_{Res1} = \frac{1}{2k_{resist}d_{eff}} - \frac{1}{2\pi k_{resist}t_{resist}} log\left(\frac{2}{1+\frac{k_{resist}}{k_{substrate}}}\right) \tag{5.2.3}$$

Whereby the thermal conductivity of the resist k_{resist} is comparable to typical thermal conductivity of a polymer, between 0.1 - 0.6 $Wm^{-1}K^{-1}$ [270]. Next, the thermal conductivity of the Si substrate $k_{substrate} = 150$ $Wm^{-1}K^{-1}$ [272], the effective diameter of the tip $d_{eff} = 20$ nm, and the thickness of the resist $t_{resist} = 50$ nm. This delivers a value of between $R_{Res1} = 0.4 \times 10^8$ - 2.4×10^8 KW^{-1} for $k_{resist} = 0.1$ - 0.6. The value of R_{Res1} is in the same order as R_{Tip} and $R_{Contact}$ but has a broad range relating to the uncertainty over the thermal conductivity of the resist polymer. This, along with the thermal resistance of the tip varying between 10^7-10^8 KW^{-1} [270], allows us to calculate T_{Int} with $T_H = 950$ °C and $T_S = 20$ °C as $T_{Int} = 148$ - 558 °C. The large range in possible interface temperatures is due to the range in possible R_{tip} and k_{resist}, which are hard to reproducibly quantify. There are a few options to overcome this challenge. Firstly, T_H is adjusted to ensure the correct etch depth if the surface is being under or overheated. Secondly, regularly replace or clean tips to ensure consistent R_{tip}. Thirdly, changing the conductivity of the substrate, for example SiN instead of Si, which is more insulating - and therefore there will be less heat loss to the substrate. Most important is to run process calibration tests for each batch to ensure etch depth is being met.

Write temperature and pixel time

While increasing the writer temperature enhances the sublimation rate (due to improved vertical heat transfer into the polymer), it also broadens the etch width through lateral heat diffusion, compromising resolution. This trade-off allows higher temperatures to reduce

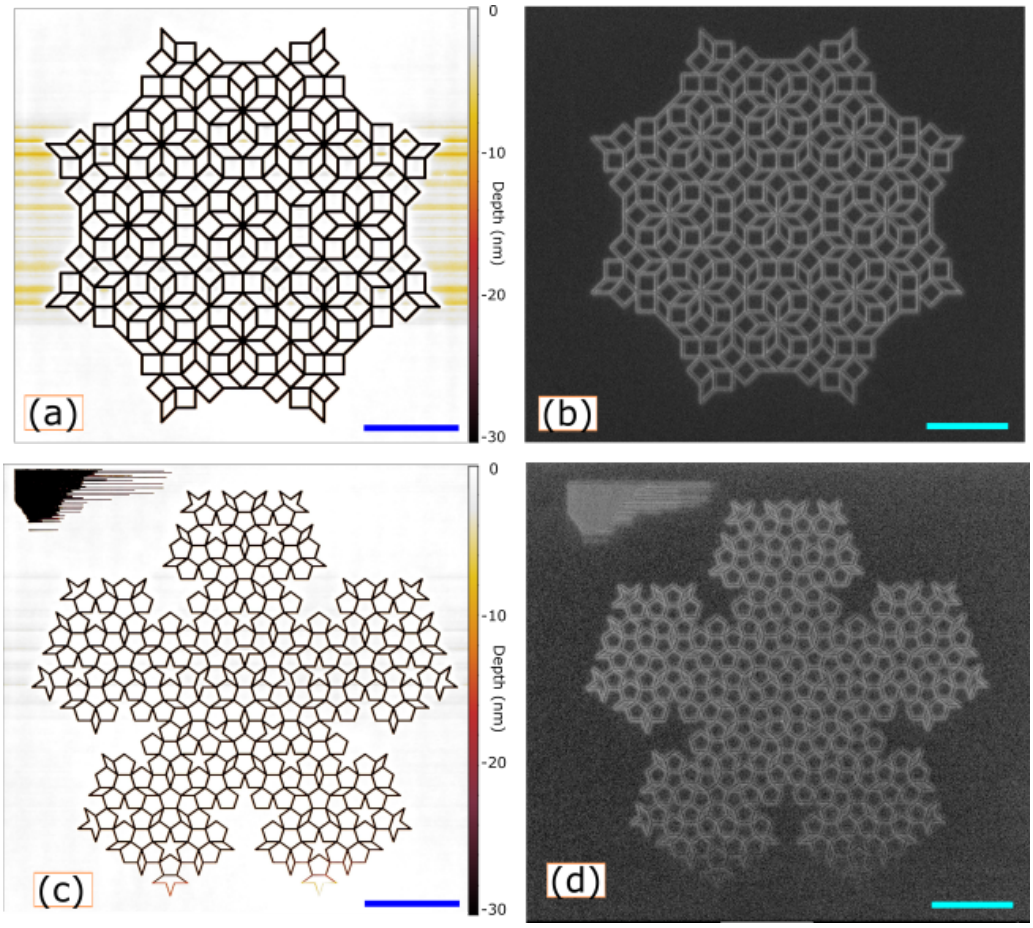

Figure 5.17: (a) The initial etch of an ABT with thermal conductance microscopy, and (b) an SEM of the same area with no further alterations taken 1 week later. (c) The initial etch of a Penrose tiling with thermal conductance microscopy. (d) An SEM of the same area as (c). Scale bars 10 µm.

pixel time, improving throughput and sublimation efficiency. However, excessively high temperatures risk damaging the tip or inducing unintended polymer cross-linking (local hard-baking) instead of clean sublimation. Conversely, increasing the pixel contact time at a fixed temperature extends thermal exposure, amplifying both feature width and depth via prolonged sublimation. Strategically varying pixel time within a single pattern enables the creation of 3D nanostructures with depth variations or tailored viscoelastic responses in polymers [273]. If the feedback mode dynamically adjusts the voltage applied to the cantilever actuator (rather than maintaining a constant voltage), changes to the writer temperature or contact time will have a diminished impact on etch depth. This is because the feedback system compensates for these changes by modulating the voltage to maintain consistent interaction forces or tip-sample height.

Image analysis corrections

Another challenge is relying on the accuracy of the tc-FM images produced by the NanoFrazor, with respect to the actual structures etched, especially in terms of the etch depth. For example, as heat exchange is a function of the sample material and the tip wears over time, there is great uncertainty in the calibration of these images. This is especially true because the manufacturer recommends calibrating the tc-FM images with another microscopy method due to potential inconsistencies. Therefore, images should be at least be tested in conjunction with another microscopy method. SEM was performed on samples after etching and before any solvent exposure or metallising, to check the accuracy of the thermal microscopy images with respect to the dimensions of the actual etch. Figure 5.17 shows a comparison of connected Ammann-Beenker and Penrose tilings with thermal conductance microscopy and the same regions with SEM. The SEM in Figure 5.17(b) shows a similar structure and lateral dimensions as the thermal microscopy image of the ABT in Figure 5.17(a), with clearly defined edges and no loss in the pattern quality. However, due to the greyscale nature of SEM images the physical geometry is hard to quantify. Horizontal streaks seen in Figure 5.17(a) do not appear in 5.17(b). These are likely image artefacts in the read scan direction and not part of the structure.

Similar comparisons are made between Figure 5.17(c) and 5.17(d), showing a connected Penrose tiling with thermal conductance microscopy and then an SEM of the same area. The snowflake-like shape of the pattern is a result of the substitution method implemented to design the tiling. The dark marks in the top left of Figure 5.17(c) are likely caused by a high adhesion length, as discussed with Figure 5.15(a) and previously in this section. This feature can be easily identified in the corresponding SEM in Figure 5.17(d). Also noteworthy is the lighter etch in the first few µm from the bottom of Figure 5.17(c), with a measured depth closer to 15 nm than the programmed depth 30 nm. This shallower edge depth occurs because the initial voltage applied to the tip was not enough to achieve the programmed depth but was then corrected by the feedback loop increasing voltage. The SEM agrees with this depth profile, as the first few µm appear lighter than the rest of the pattern, which implies a shallower indent.

SEM does not give absolute depth values for a sample, so etch depth is only inferred and should be calibrated via atomic force microscopy. However, similar feature comparisons are found among all structures, reinforcing that the tc-FM images produced via the t-SPL NanoFrazor can, in general, be trusted for their accuracy between the microscopy image produced and the real structure patterned.

5.2.4 Fabrication Results

Once all these challenges are overcome, high-quality quasiperiodic tilings may be produced with nanoscale precision. In this section, a range of both patterned and metallised

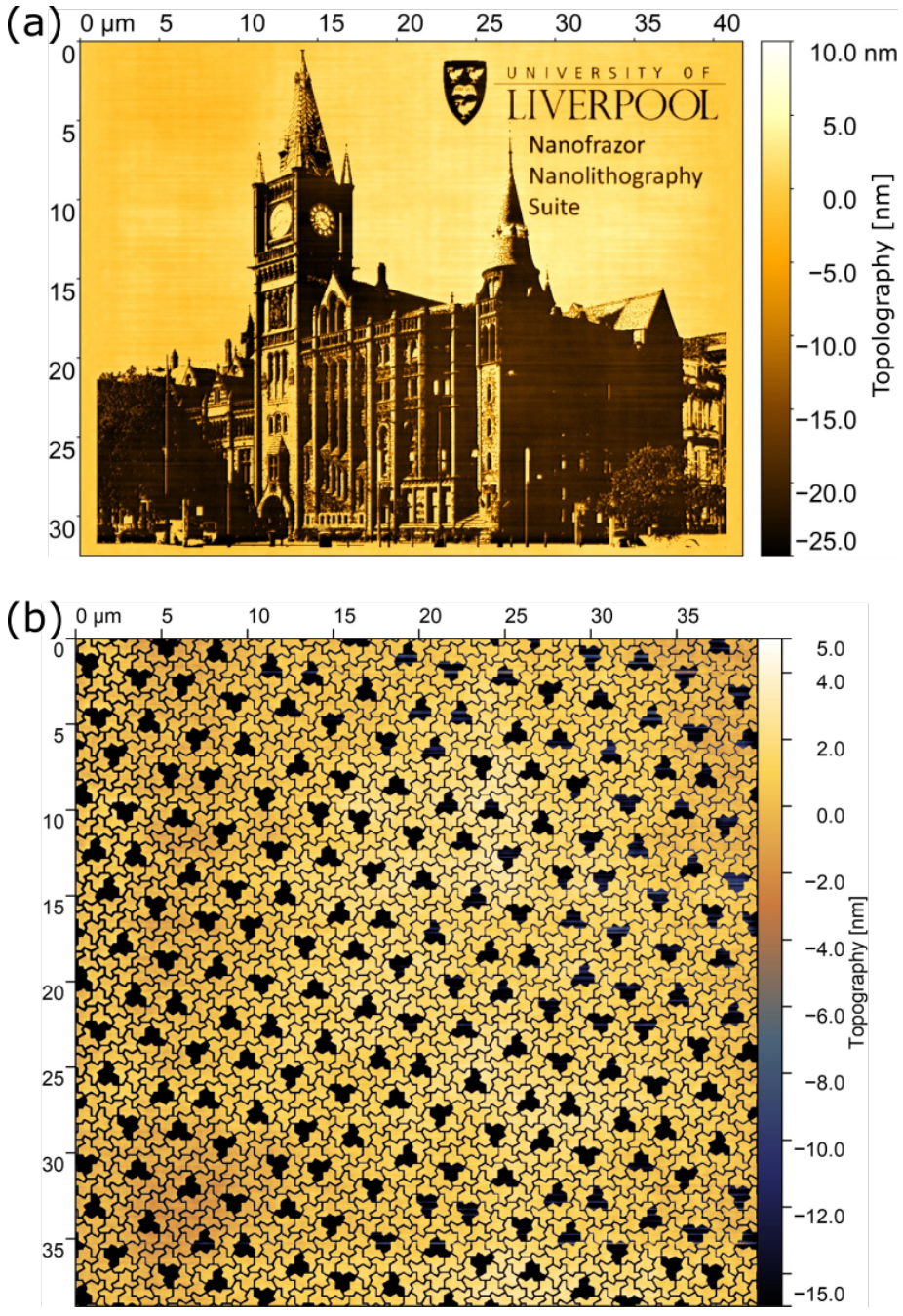

Figure 5.18: tc-FM images of novel architectures etched with t-SPL. (a) The University of Liverpool Victoria Building. (b) The aperiodic mono-tiling also known as the Hat Tiling.

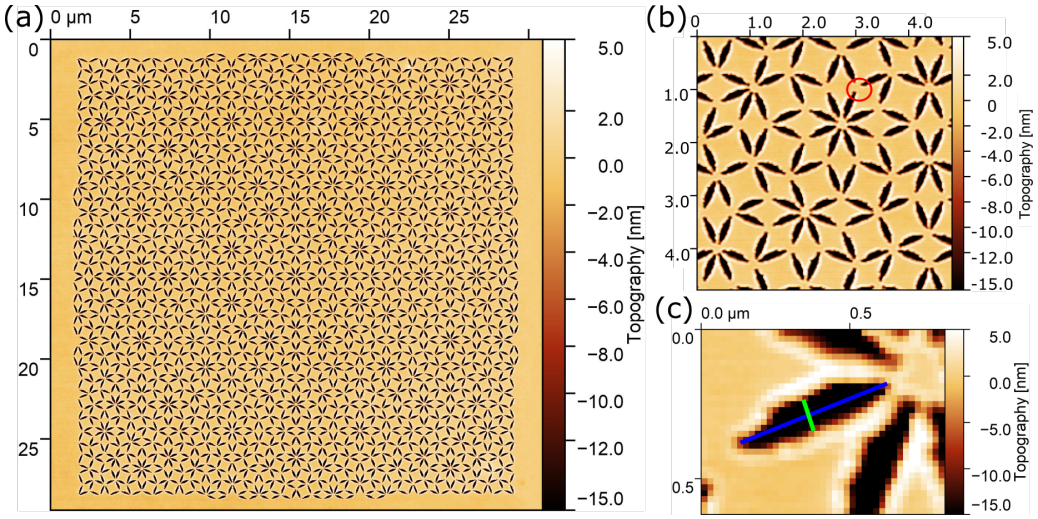

Figure 5.19: tc-FM images of a typical etched ABT etched for artificial spin-ice applications. (a) The full etch, demonstrating good uniformity and a high-quality etch. (b) A magnified section, showing no overlap between islands. A red circle indicates the furthest island tip-tip distance discussed in the text. Nearest neighbour islands have closer tip-tip distances than the red circled islands. (c) A further magnified section of a single island, with long axis (blue) and short axis (green) measured distances discussed in the text.

quasiperiodic tilings are presented. One novelty of this research is the ability to rapidly and easily create tailor-made quasiperiodic architectures, previously undemonstrated by direct-write probe nanofabrication. Figure 5.18 shows two examples of tailor-made architectures, fabricated with t-SPL and imaged with tc-FM. Figure 5.18(a) shows a 41 × 32 µm tc-FM image of the University of Liverpool Victoria Building, with the university's logo and the Nanofrazor Nanolithography Suite labelled. Although practical applications for this technique may be limited, it showcases the ability to take a photograph with a camera and efficiently etch a nanoscale impression of that photograph. Figure 5.18(b) shows a 40 × 37 tc-FM image of a section of the famous array of aperiodic monotiles, nicknamed the Hat Tiling, discovered in March 2023 [274]. To date, no nanofabricated version of this tiling or its variants exists in the literature. The Hat Tiling is an excellent example of what can be trivially etched with t-SPL, but would be much more difficult to produce with photolithography or EBL techniques due proximity effects and the design's aperiodicity.

Figure 5.19 shows a tc-FM image of a t-SPL patterned ABT, designed as an artificial spin-ice of interacting nanomagnets once metallised. The largest constraint for producing single-domain nanomagets is minimising the width of islands to under ≈ 200 nm to avoid multi-domain effects [79]. Figure 5.19(a) is a typical example of an artificial spin-ice array which can be reproducibly patterned, following the optimisations discussed so far in this chapter. Darker features indicate the islands which have been etched at least to -15 nm into the resist stick. In this case the thermal resist layer was coated to be 14 nm thick,

and for this reason all tc-FM images shown have a range up to 15 nm. When patterning in real time, the best way to evaluate whether the correct depth is being reached is to measure between -12 nm to -18 nm. This is because in theory etched between 0 to -14 nm (the top layer thickness) should not be reaching the PMGI lift-off resist, and so when undercut these features will not expose the Si substrate. The most important feature of these arrays is to have each island separated from one another, so the etch must not have overlapping features. If there is overlap around the -14 nm etch depth, then the final metallised structures will not be useful for artificial spin-ice measurements.

Figure 5.19(b) shows a magnified view of 5.19(a), which includes all six vertex types of the ABT (discussed in Section 5.2.1). Due to the quasiperiodic nature of the ABT, it is important to note that there are several different ways of measuring the lattice constant and nearest neighbour distances. Here, the lattice constant is measured along the edges of tiles between vertices, which each have a decorated island. At a given vertex, there can be between three and eight islands connected. For the ABT, the vertex-vertex lattice constant is always the same - in essence, each edge length of the tiling is equal. The vertex-vertex lattice constant measured in 5.19(b) is 760 $\pm$ 40 nm, representing the range of distances measured over many islands. Figure 5.19(c) shows an magnified view of an individual island, with long axis (blue) and short axis (green) dimensions indicated. As each edge is the same length, each island has nominally the same dimensions. The long axis (blue) measures 520 $\pm$ 20 nm in length, and the short axis (green) measures 130 $\pm$ 20 nm in width. The minimum uncertainty is related to the variation in island length observed, and the 20 nm per pixel resolution limit of the t-SPL probe. With this in mind, the minimum distance between vertices (lattice constant $-$ long axis) was $\approx 760 - 520 = 240$ nm. However, the minimum separation between acutely separated nearest neighbour island tips will be much closer. In combination with the 3i - 7i vertices (with three - seven islands to vertex) having missing islands from the population, means the actual minimum separation between island tips may be significantly different. In the case of the ABT, the minimum separation from island tip to island tip will change for each vertex type, and the specific island in the vertex. The closest distance between the tips of the 8i vertex is 100 $\pm$ 20 nm, whereas the furthest - circled in red on Figure 5.19(b), is 240 $\pm$ 20 nm. This is a significantly large variation between nearest neighbour distances, a characteristic of the tiling design rather than a nanolithography issue. In principle this is interesting to investigate as an artificial spin-ice partly due to the nearest neighbour distance variation.

Moving onto final metallised structures, Figures 5.20 and 5.21 show SEM images of a collection of quasiperiodic tilings, with a range of tailored permalloy decorations. Permalloy is deposited via a physical vapour deposition method discussed in Chapter 4. In principle, any material which can be grown on a crystal surface may be evaporated into the mask to produce the tailored decoration. For example, it would be relatively simple to switch

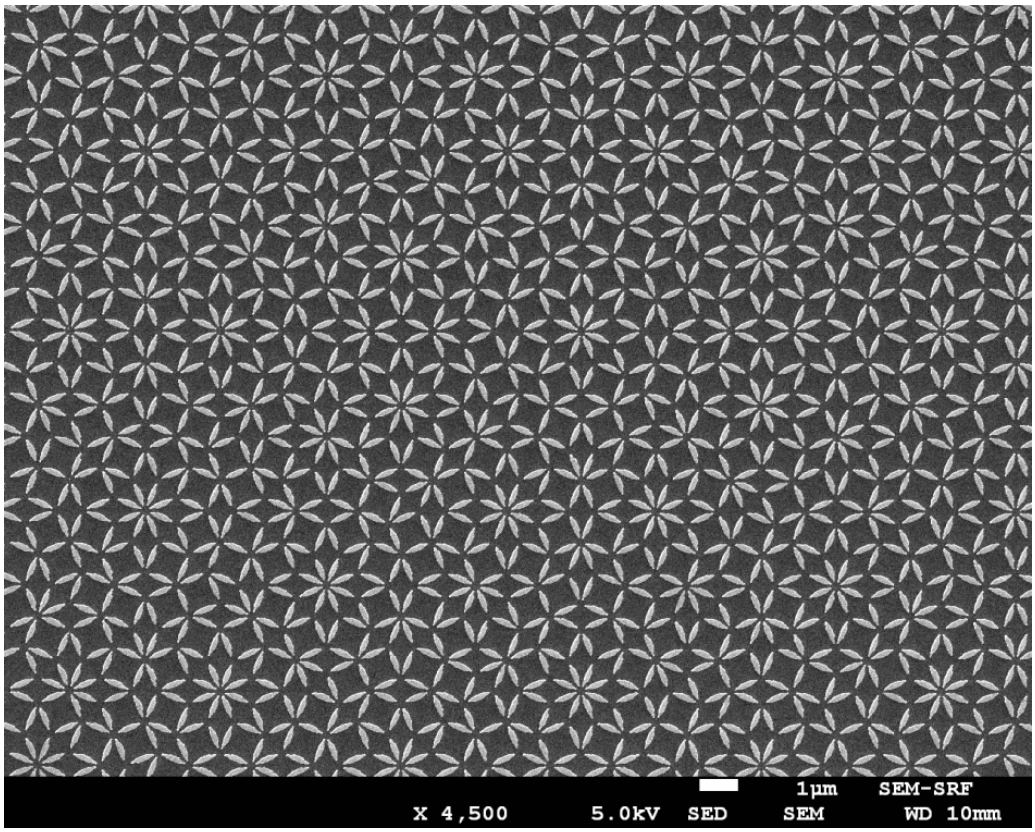

Figure 5.20: An SEM image of a metallised Ammann-Beenker artificial spin-ice tiling fabricating with t-SPL. This section of the array includes several hundred islands of $Ni_{80}Fe_{20}$, all individually separated from one another.

to grow a metal which exhibits antiferromagnetic or out-of-plane magnetisation, assuming their growth conditions are well-understood. Figure 5.20 shows a large array of a metallised ABT, the design discussed throughout this chapter. Each island in this array is nominally the same size, 600 ± 20 nm (long axis), 150 ± 20 nm (short axis), and 10 nm thick. These are slightly larger than the island dimensions measured with tc-FM, which may be due to wider features following the undercut. For artificial spin-ice, the most important dimension is the short axis that limits a ferromagnetic material to a single-domain. If the short axis is much greater than 200 nm, the domain will fragment into a split domain, leading to each island to not behave as a single nanomagnet. Similarly, the long axis : short axis ratio should be an elliptical 4:1 for artificial spin ice. In Figure 5.20, the edge around each island ellipses is smooth. This is good as it reduces the chance for a large local charge density to cause stray fields away from the island tips. This array is therefore suitable for the artificial spin-ice measurements shown in Chapter 6.

Next, a range of fabricated tilings which were metallised as part of this research are shown, which are relevant to the context of the broader nanofabrication field, with possible applications and investigations. Figure 5.21(a) shows an area from a connected ABT with

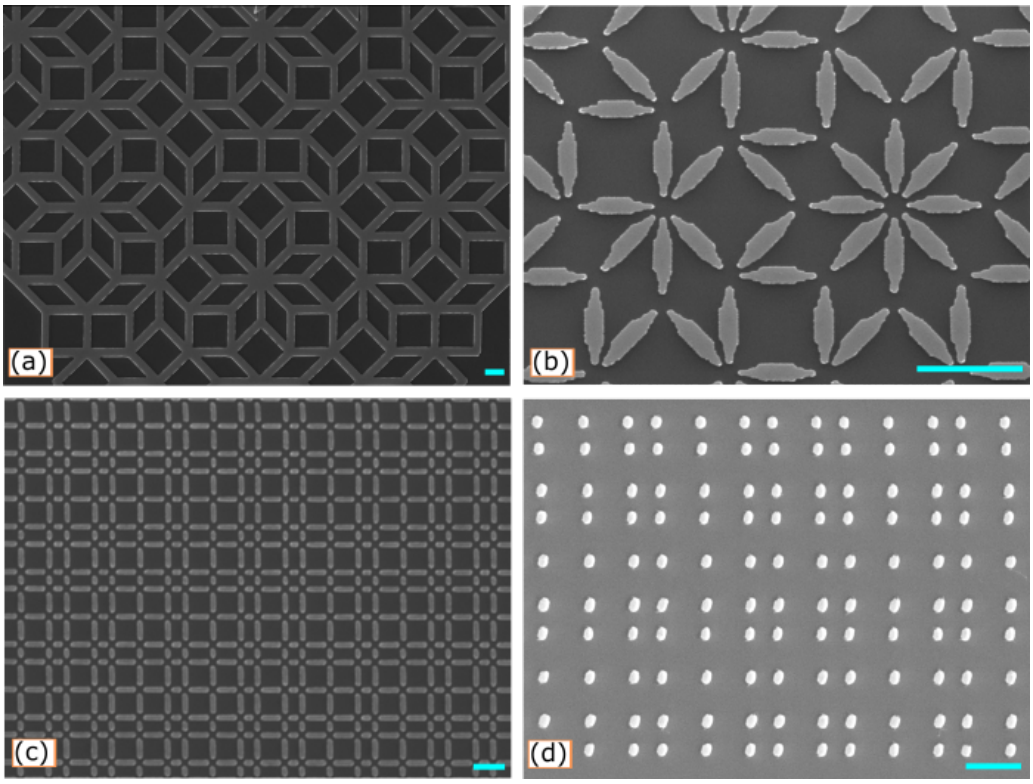

Figure 5.21: SEM images of 25 nm permalloy arranged into various quasiperiodic tilings with tailored decorations. (a) Connected 8-fold Ammann-Beenker. (b) Disconnected 8-fold Ammann-Beenker 10 nm thick (c) Disconnected 4-fold Square Fibonacci tiling. (d) Vertices of the 4-fold Square Fibonacci tiling. Scale bars 1 µm.

2.2 µm edge lengths and 25 nm thick permalloy. These edges are a higher resolution than similar work in the literature [141], where the authors investigated broadband and narrowband ferromagnetic resonance of a similar ABT. Narrow-band (0 - 2000 Oe) results revealed 8-fold ferromagnetic adsorption peaks, confirming the importance of patterning design on static and dynamic magnetic response. Fabricated tilings are of course not limited to these materials, with great flexibility over the substrate and deposition method or material.

Figure 5.21(b) shows an artificial spin-ice ABT, similar to the design of Figure 5.20. A fabricated quasiperiodic artificial spin-ice has been reported before in the literature, but only of a 5-fold Penrose tiling [114]. These authors produced a permalloy P3 Penrose tiling, and identifed a long-range skeleton of fixed moments of 5-fold symmetry with simulations and MFM observations. This work is discussed in-depth in Chapter 2. They showed a degenerate ground state with this skeleton existed, which is interesting for fundamental nanomagnetic interactions. That study serves as the basis for further investigations in this work in Chapter 6.

The Square Fibonacci tiling presented in Figure 5.21(c) has two edge lengths and order

approximated by the golden mean, with the long edge length equal to 1 µm and short 625 nm. This array would also be suitable for artificial spin-ice measurements, the results shown in Chapter 6. One can note the islands of the Square Fibonacci tiling are much shorter with long length 660 nm and short 300 nm, due to the spacing introduced by disconnecting the edge. It was found via micromagnetic simulation and XMCD-PEEM measurements that this Square Fibonacci tiling produced trapped vortices. These trapped vortices are an interesting application of neuromorphic computing - programmable vortices could simulate neural network connections, where the location and state of vortices represent synaptic weights or neuron states [275].

Finally, Figure 5.21(d) shows a Square Fibonacci tiling with permalloy dots decorated at the vertices, with diameter 180 nm and 25 nm thickness. The smallest resolution these dots could be achieved by the t-SPL NanoFrazor is 20 nm due to practical limits. Features this small can be difficult to find on an optical microscope due to the diffraction limit. Scratching the surface near the arrays, bunching large patches together, or reducing the distance between the vertices, would improve visibility. Other authors found applications for quasiperiodic dot arrays [120]. Those workers fabricated a layer of quasiperiodic holes in a solar cell, to reduce reflected photons and improve efficiency.

5.3 Conclusion and Outlook

This chapter presents a comprehensive methodology for fabricating quasiperiodic nanostructures using thermal-scanning probe lithography (t-SPL), systematically addressing design, chemical, and physical challenges inherent to the technique. By developing reproducible protocols for tiling generation, resist stack optimisation, and probe-surface thermal management, the work resolves critical barriers to achieving high-resolution, large-area quasiperiodic architectures. The chapter's significance lies in its integration of practical solutions, such as strategies to mitigate resist collapse, tip degradation, and thermal broadening, into a cohesive framework. These optimisations, rarely documented in detail elsewhere, lower the entry barrier for researchers adopting t-SPL and similar techniques for complex geometries. The successful fabrication of artificial spin-ice arrays and aperiodic tilings demonstrates the method's versatility and reliability. By bridging the gap between theoretical quasiperiodic models and experimental nanofabrication, this work provides a foundational resource for studying emergent phenomena in geometrically frustrated systems, topological photonics, and tailor-made systems. The systematic approach ensures applicability to a broad range of materials and structures, making it a critical reference for advancing nanoscale aperiodic engineering.

Chapter 6

Magnetic Ordering and Frustration in Ammann-Beenker Artificial Spin-Ice

This chapter explores magnetic ordering and frustration of the Ammann-Beenker Tiling, fabricated with techniques developed from Chapter 5. To begin, micromagnetic simulations are utilised to find candidate ground states for isolated vertex types. Next, by combining magnetic force microscopy and model magnetic ordering regimes, it is determined that vertex types with odd-coordination numbers are forced into excited states.

6.1 Introduction

Quasiperiodic (QP) systems exhibit long-range order without translational symmetry, and have interesting fundamental physical applications, from quasicrystals in materials science [10] to photonic structures [120] and magnetic interactions [114, 141]. Unlike periodic crystals, QP arrangements feature forbidden rotational symmetries such as 5- or 8-fold, and self-similar scaling, enabling unique electronic and magnetic behaviours [18, 36]. These systems offer platforms to study quasiperiodic geometric frustration and emergent phenomena in condensed matter physics.

An artificial spin ice (ASI) is an array of fabricated nanoscale ferromagnetic islands arranged in any lattice, and is an established technique for exploring fundamental magnetic frustration [80, 93]. By definition, an ASI can be any lattice including periodic and QP geometries, but only a limited amount of work in the literature explores fabricated QP tilings [132, 152], and only the Penrose ASI has been explored [114]. The overwhelming majority of ASI research to date has focused on periodic systems such as the square and kagome, and derivations of these structures [79]. In periodic ASIs, frustration arises

from competing short-range dipolar interactions constrained by lattice geometry [26], leading to ground states where the ice rule enforces vertex charge neutrality or monopole-like excitations [29]. As periodic systems are defined by repeating unit cells, there are open questions on ground state domain ordering, forced frustration, and long-range interactions when translational symmetry is removed, but the system is still ordered. QP ASI enables the study of self-similar hierarchical frustration and long-range ordering without translational symmetry, facilitated by overlapping pseudo-unit cell moment clusters inherent to QP tilings [276, 277].

In this chapter, the ground-state ordering and emergent forced frustration of the 8-fold Ammann-Beenker tiling (ABT) is investigated [45]. This system is chosen due to its evenly divisible mirror planes, and the reduced local geometric frustration of vertices compared to the Penrose tiling. A combination of these factors are expected to experimentally encourage a closer to ground-state ordering, and emergent forced frustration as a result of quasiperiodicity. The ABT is built from square and rhombic prototiles, featuring six distinct vertex types (termed 3i to 8i), global 8-fold symmetry, and local 8-fold symmetry sites. Unlike the Penrose tiling, the ABT was recently found to permit perfect dimer coverings and exhibits reduced geometric frustration at even-moment vertices, suggesting potential for unique magnetic ordering [175, 176, 183]. The hierarchical structure of the ABT has discrete scale invariance related by the silver ratio $\phi = 1 + \sqrt{2}$, which may enable self-similar long-range interactions to propagate.

The ABT is fabricated with a thermal-scanning probe lithography (t-SPL) process, where single-domain Permalloy ($Ni_{80}Fe_{20}$) nanoislands are arranged and fabricated along the edges of the ABT. Magnetic force microscopy (MFM), and micromagnetic simulations (MuMax3) techniques were used to reveal distinct ground state (GS) behaviours in the ABT system, compared to the more frustrated Penrose tiling. Later, experimentally thermalising the ABT array is performed with magnetometry and XMCD-PEEM (X-ray magnetic circular dichroism - photoemission electron microscopy), motivated by the need to access a global minimised energy state.

As part of the experimental analysis, three model regimes are discussed for analysing QP ASI: the Vertices-Only Model, the Skeleton Model, and the Correlation Model:

Firstly, the Vertices-Only Model is an established technique for examining the energy distribution of individual vertices in periodic ASI, by comparing their experimentally observed values to theoretical calculations [79, 80, 87, 278, 279]. The model has been used as a foundation to describe high-energy domain walls between ground-state vertex domains as ground-state excitations [29, 31, 87, 280, 281], and to determine ground-state occupation through relaxation procedures [81, 84, 101, 282]. Here, anomalous vertex populations are identified in odd-moment vertices with MFM, where excited states dominate despite low energy barriers.

Next, the Skeleton Model was recently developed for the 10-fold Penrose Tiling with decagonal clusters [114]. The model is built from the lowest-energy configuration of overlapping pseudo-unit cell moment clusters characteristic of QP systems [276, 277], forming a long-range fixed-moment skeleton. In this chapter, the Skeleton Model is generalised by applying it to the 8-fold Ammann Beenker Tiling with octagonal clusters. Experimental results find excited odd-moment vertices from the isolated Vertices-Only model exist within skeleton GS domains. GS domains are groups of GS vertices connected to one another that share the same chirality. This result suggests nearest neighbour moments or long-range QP order may be forcing excited states. Finally, forced frustration between competing chiral networks leads to high-energy domain wall formation.

Lastly, the Correlation Model is another established technique for measuring periodic ASI. The approach considers the nearest neighbour nanoislands for each vertex type, accounting for flux closure loops formed around each vertex type to minimise the total interaction energy [30, 80, 84, 283–286]. The Correlation Model explains the cause of previously identified excited vertices within GS domains, and explains open flux loops within GS domains. Results show that GS domains are stabilised by high-energy pinning centres, and that flux closure loops play a significant role in a minimised energy state.

6.2 Experimental and Modelling Details

Generation of Ammann-Beenker Tiling

The ABT used in this research is generated via a substitution method [18], where square and rhombus prototiles are iteratively replaced until the tiles effectively cover space. The design and generation of the ABT for fabrication with nanolithography is shared in detail previously in Section 5.2.1.

Experiment Details

Samples were fabricated using thermal-scanning probe lithography (t-SPL) and a physical vapour deposition process. Undoped Si substrates were spin-coated with a bilayer polymethylglutarimide (30 nm PMGI)/polyphthalaldehyde (14 nm PPA) resist, and baked at 200°C and 110°C, respectively. During t-SPL a heated tip raster scans the surface, indenting and sublimating a pre-programmed pattern into the PPA resist layer, exposing the PMGI layer. The PMGI layer is chemically etched with a controlled exposure time of 12-18 s in a 1:40 tetramethylammonium hydroxide (TMAH):isopropyl alcohol solution - exposing the substrate in the patterned regions to produce a mask. Permalloy ($Ni_{80}Fe_{20}$), chosen for its suitable ferromagnetic properties, is then deposited in a base pressure of 1×10^{-9} mbar at a rate of 0.4 $Å s^{-1}$ through the mask via electron beam evaporation, with a thickness of 10 nm and source purity of 99.9%. The physical dimensions of fabricated

structures are 600 nm long, 150 nm wide, and 10 nm thick, imaged with scanning electron microscopy (SEM). Any nanolithography defects in the structures are indicated in the text. Magnetic force microscopy (MFM) is employed to investigate the magnetic properties of the sample as-grown.

Modelling of Magnetic Interaction

The micromagnetic simulator MuMax3 is used to model the energy levels of moment combinations for each vertex type [25]. $M_S = 8.6 \times 10^5 Am^{-1}$ and $A_{ex} = 1.3 \times 10^{-11} Jm^{-1}$ standard values for Permalloy were used for simulations [114]. Each nanoisland was modelled as a 600 nm long, 150 nm wide, and 10 nm thick ellipsoid, with single-domain magnetisation aligned along its long axis. A width-to-length ratio of 1:4 is typical for ASI systems [79]. The total interaction energy for every possible combination of moments was then calculated and ordered in terms of their total interaction energy.

6.3 Results and Discussion

6.3.1 Square Artificial Spin-Ice

As an illustration of the Vertices-Only and Skeleton models, the periodic square ASI will be described here. Fabricating a standard square ASI tiling on the same substrate as other tilings is a valuable control tool to evaluate the energy distribution of those vertices, and compare them to accepted models within the literature - those distributions then support the validity and conclusions of new lattice distributions.

Applying the Vertices-Only Model to the Square Artificial Spin-Ice

The Vertices-Only model starts with MuMax3 by evaluating with the possible energy level of each vertex which populates the tiling. The real distribution of vertices within an ASI can then be assigned an energy level, and in many cases a colour-coded energy map can be generated. At this point, GS domains may be spotted where a collection of the lowest possible energy levels follow head-to-tail with no excited vertices. Next, the Boltzmann distribution $p(n) = \frac{e^{-\beta E_i}}{Z}$ [287] may be used to estimate and compare expected occupation for each microstate by vertex type. The Boltzmann distribution is a valuable tool for determining whether the moments in an ASI are arranged in the GS and for identifying any forced phenomena within the array.

The simulated energy levels for the square ASI are shown in the grey inset in Figure 6.1(a). These energy levels are in agreement with established work in the literature, with the GS following a typical 2-in, 2-out sequence [29, 79].

Figure 6.1(b) presents a 20 µm section MFM image and energy map for the square ASI. The MFM image is converted into an energy map by colour-matching simulated vertex energy levels (determined with MuMax3), the GS in blue, up to the most excited states in orange, as shown in Figure 6.1. The occupations of these observed states can then be plotted against the MuMax3 simulated Boltzmann distribution, as shown in Figure 6.1(a).

Figure 6.1(a) shows the Boltzmann distribution plot, which compares the predicted (red) and observed (black) distributions. The array is approaching equilibrium but is not fully thermalised, as the observed GS population is much lower than expected. It is important to note that the predicted distribution reflects how an isolated vertex would populate, which may differ from that in a tiling. If the distribution for isolated vertices differs significantly from that observed, it could be attributed to long-range order within the tiling. This comparison suggests that while the square ASI system is nearing equilibrium, it needs further thermalisation to increase the GS occupation.

The observed GS population of the square ASI is 69.5% (210 vertices). These GS vertices follow head-to-tail (black-white-black) in horizontal and vertical directions as expected. The GS population is similar GS populations found following AC-demagnetisation protocols (70%) [81]. This result is very important for the validity of the ABT GS population distribution analysis, which is expected to show a higher degree of frustration. This is because as a high proportion of vertices in the square GS (on the same substrate) form a large GS domain, it indicates the possibility of an experimentally realised thermal annealing during thin-film deposition. This effect has previously been observed in the literature [102]. For comparison, in a randomly distributed square ASI, only 12.5% of vertices would be in the GS [80]. For a single GS domain covering the entire tiling, the theoretical GS population is 100%. Experimentally it is hard to achieve that occupation due to defects in fabrication and the formation of high-energy domain walls constructed of excited vertices [29].

With this colour-map approach, the two possible GS cannot be easily distinguished, which may be important if there are several separated GS domains and the chirality between them is being compared. The concept of chirality is better demonstrated with the Skeleton Model, discussed next.

Applying the Skeleton Model to the Square Artificial Spin-Ice

The Skeleton Model, recently developed for the 10-fold Penrose Tiling [114], maps GS domains in QP systems with pseudo-unit cell moment clusters characteristic of the tiling [276,277]. A simple skeleton model is shown overlaid on the square ASI in Figure 6.2. The simple skeleton is constructed by first identifying GS vertices, and overlaying the square unit cell with coinciding moments. Unit cells of the same network colour (blue or pink) are placed alternately with white and black heads. If a white head cannot be placed after a

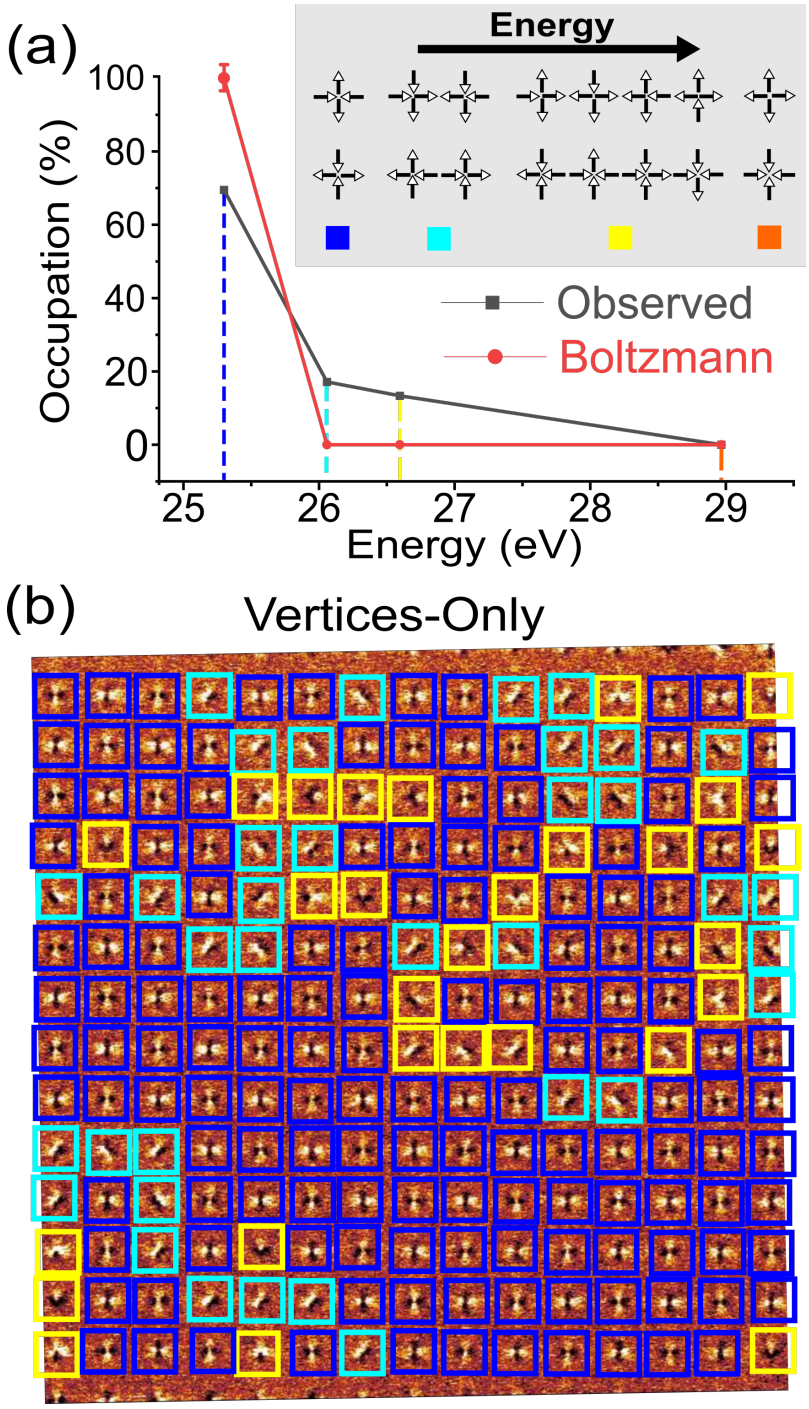

Figure 6.1: The Vertices-Only Model for the square ASI, fabricated on the same sample as the ABT ASI. (a) The (grey inset) MuMax3 calculated energy levels for the square ASI, with coloured boxes indicating their energy level, from the GS in blue, the 1st excited state in cyan, the 2nd excited state in yellow, and most excited state in orange. The Boltzmann distribution for the square ASI measured in (b) is shown, with the observed distribution (black) and the predicted distribution for isolated vertices (red). (b) An MFM of the square ASI, with coloured boxes around vertices following the same colour scheme for the calculated vertex energies. The most excited states do not appear.

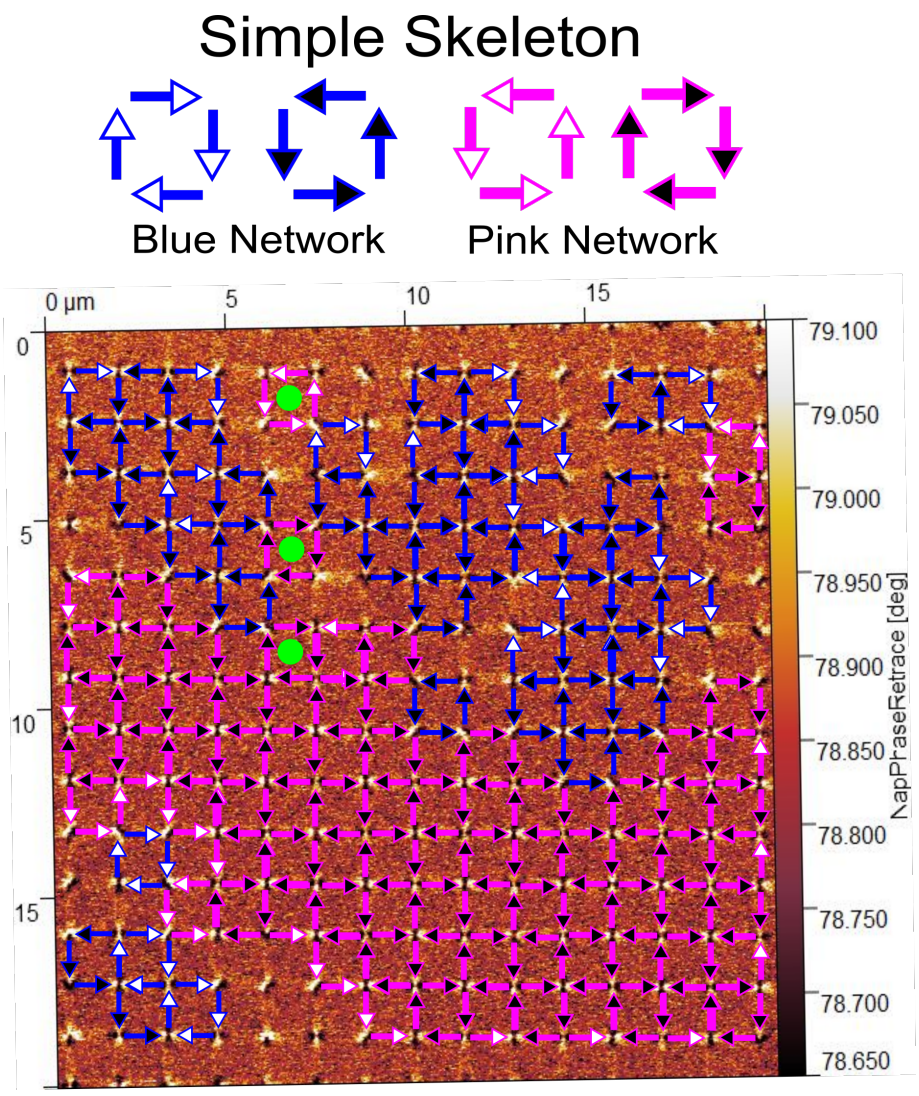

Figure 6.2: The simple skeleton model for a standard square ASI. Chirally related blue and pink network unit cells can decorate GS vertices to decorate GS domains. An MFM of the square ASI with decorated networks is shown, and in areas with excited vertices there are fewer unit cells placed. Green dots indicate parts of the network discussed within the text.

black head, due to moments not coinciding, then the next area is moved to. For example, in Figure 6.2, two black and then a white unit cell are indicated with green dots, showing how alternately coloured heads of the same network would be placed. If the moments from, for example, a pink network unit cell do not coincide with the correct head colour, then a blue network unit cell is placed. The concept that one network cannot fully coincide with another is also described as chirality. The result is two chirally related GS domains, coloured blue and pink. GS domains are groups of GS vertices connected to one another that share the same chirality.

Similar to the Vertices-Only Model for the square ASI, the theoretically maximum

possible GS occupation is 100%, though for the same reasons the experimentally possible GS occupation will be lower. The observed population of GS moments with the Skeleton Model in Figure 6.2 is 86.5%, which is notably higher than the Vertices-Only approach. This is because while a vertex may be excited, the majority of surrounding moments can still find a minimised energy state within the Skeleton Model.

6.4 Ammann-Beenker Tiling Artificial Spin-Ice

An SEM image showing a section of a 50 µm fabricated ABT ASI is shown in Figure 6.3(a). ASI structures are constructed with an array of single-domain ferromagnetic permalloy ($Ni_{80}Fe_{20}$) nanoislands. Each nanoisland is placed along the edge of a tile, uniformly sized at 600 nm long, 150 nm wide, and 10 nm thick, with an inter-vertex distance of 850 nm. As nanoislands are closely orientated at $\frac{360}{8} = 45°$, the tips between them must be delicately fabricated to ensure the system operates in the strongly coupled regime while avoiding overlap and multi-domain effects.

6.4.1 Magnetic Imaging

Figure 6.3(b) presents a magnetic force microscopy (MFM) image of the same area as Figure 6.3(a). Limiting nanoisland width ensures single-domain behaviour of nano-ferromagnets, with bright and dark spots in the MFM image representing dense field-line concentrations at each pole. Nanoislands therefore act as single-moment macrospins, analogous to nano-magnets, pointing either inward or outward toward a vertex. The MFM image in Figure 6.3(b) therefore demonstrates single-domain magnetisation of the nanoislands along their long axes, as each nanoisland has a corresponding white and dark spot at each pole.

Figure 6.3(c) shows the six ABT vertex types, labelled 3i to 8i (so-called for the number of associated nanoislands), with simulated moments generated in MuMax3. The white and black tips at each end of the nanoislands shown correspond to how they would appear in an MFM image. A colour wheel for MuMax simulations is shown overlaid on the 8i vertex type, with eight outward pointing moments. The vertex types are a distinctive feature of the ABT, characterised by odd and even-numbered moments across six unique vertices, each with at least one mirror symmetry plane. Combining these vertex types into the same system results in a highly symmetric yet geometrically frustrated QP ASI playground.

6.4.2 MuMax3 Micromagnetic Simulation Results

Figure 6.4(a) presents the calculated energy levels for each vertex type and every possible combination, revealing significant degeneracy due to inversion and mirror plane symmetry. With 2^n microstates for n nanoislands, vertices like the 8i vertex have up to 256 possible combinations, compared to only 8 for the 3i vertex. The calculated energy levels exhibit a

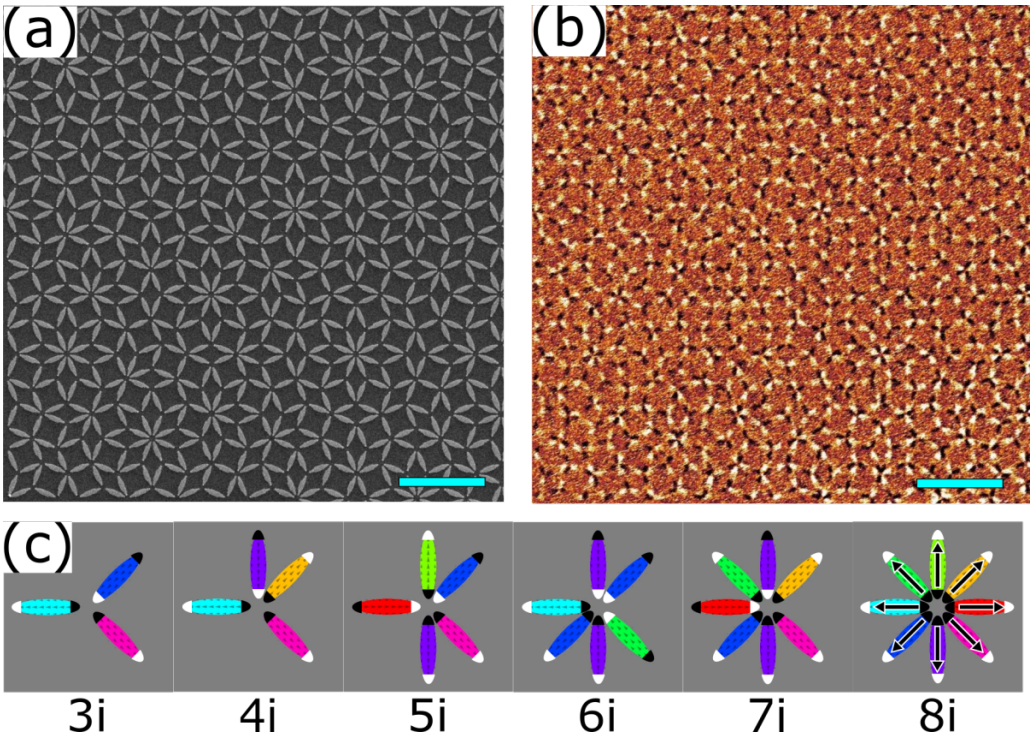

Figure 6.3: (a) An SEM of the 8-fold Ammann-Beenker Tiling (ABT) used for this research. Blue scale bar 2 µm (b) The corresponding MFM image for the same area as (a), demonstrates Ising-like single moments in each edge of the ABT with positive and negative white and black poles at the nanoisland tips. (c) The six vertex types found in the ABT are labelled 3i to 8i. From 3i to 8i there is an nanoisland added increasing the total moments around the vertex until eight total (= 8i). A colour wheel is shown at the 8i vertex with each moment pointing out from the centre. Arbitrary Moment configurations are shown for the 3i to 7i vertices, with the associated black and white coloured tip that would appear on an MFM image as in (b).

typical sigmoidal curve [93], with the GS corresponding to the moment combinations with the lowest interaction energy. Each vertex type has two or four degenerate GS depending on their geometry. Due to mirror symmetry, the ABT system is highly degenerate, with some 8i configurations having up to sixteen equivalent energy levels. Higher energy vertex types, such as the 8i vertex, have a greater total moment and higher overall interaction energies, with energy ranges up to 25 eV (black arrow in Figure 6.4(a)), compared to only 2 eV for the 3i vertex. This overlap results in certain GS configurations of the 8i vertex having lower total interaction energy than the most excited 6i states, for example. This same trend is seen for each of the 4i to 8i vertices. Micromagnetic modelling therefore reveals a rich relationship between geometry, symmetry, and degeneracy in the ABT system.

Figure 6.4(b) compares the calculated energy curves of ABT 3i-5i vertices to a standard square ASI vertex, the latter fabricated on the same substrate as a control (see Figure 6.1) [29, 80]. While the energy range widens progressively from the 3i to 5i vertex, the

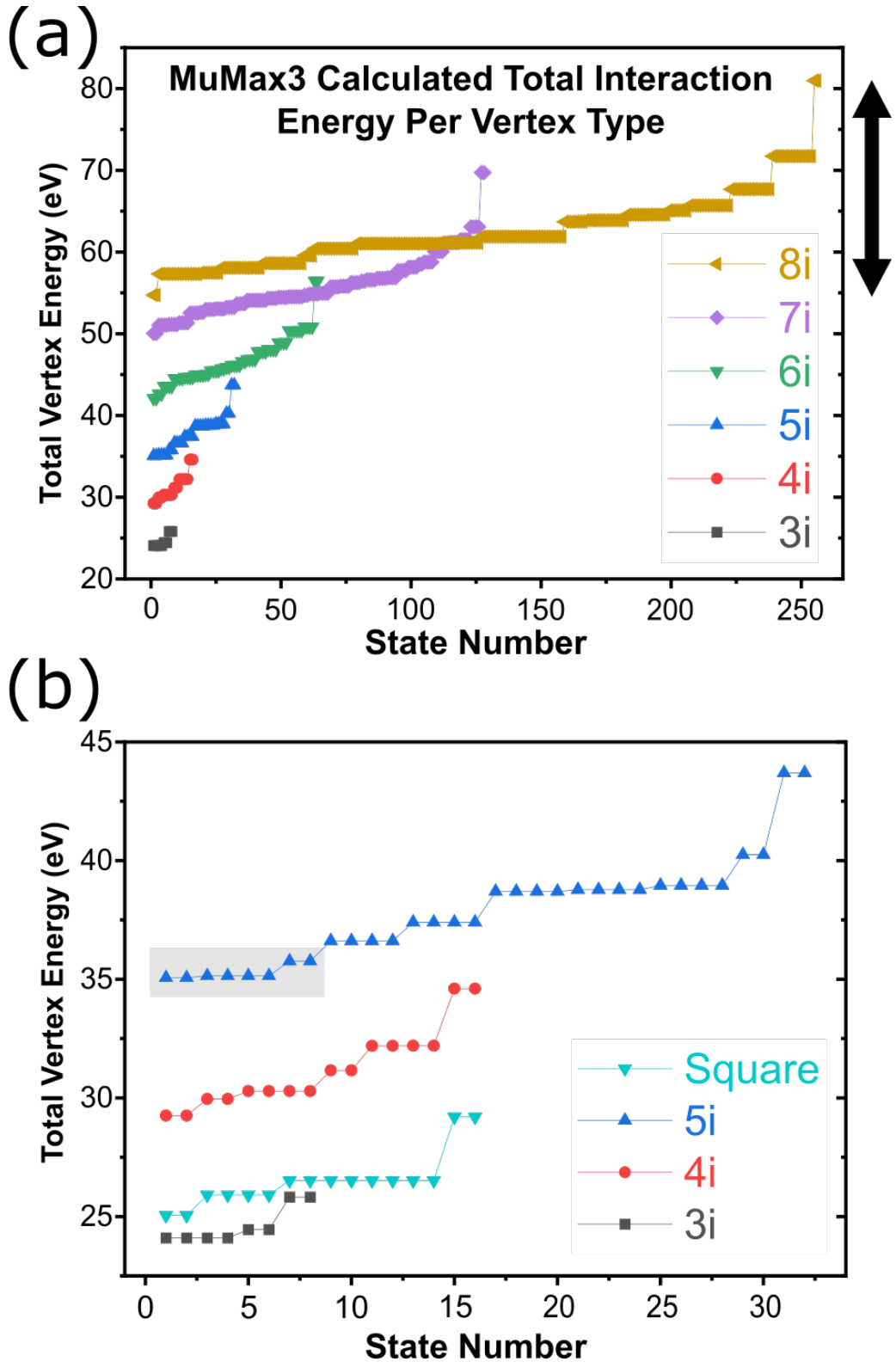

Figure 6.4: (a) Mumax3 Calculated total vertex energy for each vertex type in the ABT, ordered from lowest to highest energy. The double-head black arrow indicates the 25 eV energy range of the 8i vertex. (b) an enlargement of (a) highlighting 3i to 5i and adding the square vertex energy levels. The grey-coloured box indicates the lowest 5i energy states discussed in the text.

square ASI vertex deviates from this trend: despite having four islands, its energy range is comparable to the 3i vertex. This contrast arises from the square vertex's reduced geometric frustration, with its evenly spaced right angles between moments, compared to the 3i vertex's acute and obtuse angle moments. The 3i vertex further distinguishes itself with three discrete energy levels. The GS is four-degenerate (24.10 eV), enabled by inversion symmetry and a flippable 'F moment' along its sole mirror axis (a symmetry plane where flipping a moment preserves the energy). The 1st excited state (24.45 eV), and highest excited state (25.82 eV), are two-degenerate retaining only inversion symmetry and no F moment. The 4i (29.25 eV) and 5i (35.06 eV) GS vertices also lack F moments, with only inversion symmetry leading to two-degeneracy. This absence of a 'moment mirror plane' - a symmetry axis that hosts degenerate F moments, prevents isolated higher-order ABT vertices from replicating the 3i vertex's GS degeneracy, despite their structural mirror planes.

Frustration and degeneracy is most pronounced in odd-numbered vertices. Figure 6.5(a) maps the GS and 1st excited states of 3i-8i vertices, with the moment indicated with a pink circle serving as a fixed reference for defining 'in' and 'out' combinations. For even-order vertices (4i, 6i, and 8i), the GS adopts a simple in-out sequence to minimise interaction energy. Odd-number vertices, however, cannot achieve such conflict-free arrangements. Figure 6.5(b) shows all combinations of the GS, 1st, and 2nd excited states. The 5i GS (35.06 eV - blue border), for example, adopts an in-out-in-out-in sequence, forcing an in-in pair between its first and last moments (separated by 90°). This geometry incurs lower interaction energy compared to adjacent out-moments separated by 45°, as opposing field lines concentrated at 45° angles amplify repulsion. Moments interacting an acute 45° angles are therefore more influential to total interaction energy than wider right-angle or obtuse angles. Also, the orange-bordered leftmost moment at 35.06 eV cannot be degenerately flipped because it is not aligned along a moment mirror plane; flipping it would result in an excited in-out-[out]-out-in sequence. Crucially, the 5i vertex's first excited state (35.14 eV - green border) reintroduces F moment degeneracy: the out-in-[in]-out-in sequence can flip into an out-in-[out]-out-in sequence. Four-degenerate configurations at 35.14 eV therefore emerge via a flippable F moment along a moment mirror plane, absent in the GS, and via inversion symmetry. These states lie just 0.08 eV above the GS, in contrast to the 0.41 eV gap between its 1st and 2nd excited states. A similar trend appears in the 7i vertex, whose two-degenerate GS (30.96 eV) is accompanied by eight near-degenerate 1st and 2nd excited states (31.63 and 31.68 eV, respectively).

These results demonstrate that ABT vertices engineer degeneracy through selective symmetry breaking. Unlike the square ASI, the ABT suppresses moment mirror planes in the GS while allowing their reemergence in excited states. This suppression is driven by odd or even geometry, enabling precise control over magnetic state multiplicities. For

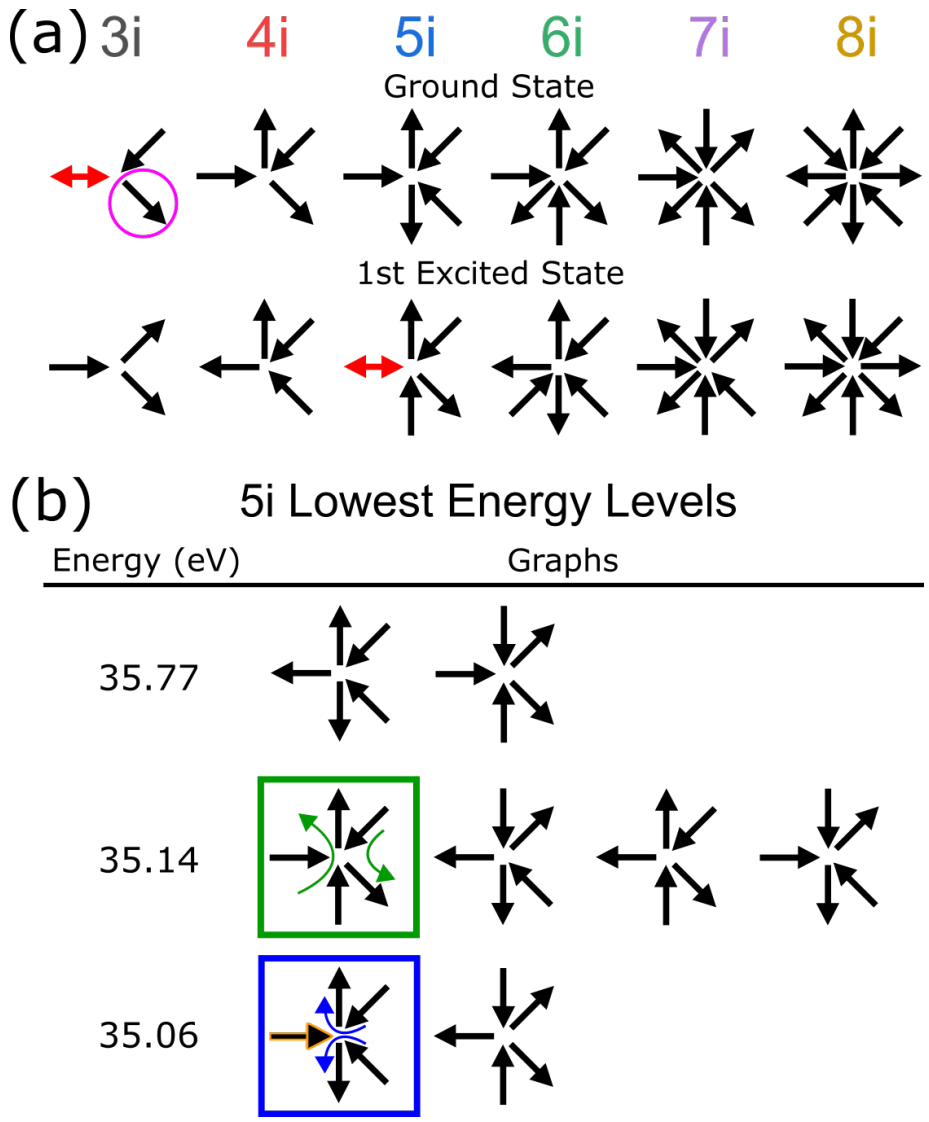

Figure 6.5: (a) The GS and 1st excited state for each vertex type, calculated with MuMax3 simulations. Black arrows indicate fixed moments, red arrows indicate degenerately flippable moments. (b) The 5i lowest energy levels, highlighted in grey from Figure 6.4(b), demonstrate both inversion and mirror symmetry degeneracy.

instance, the 3i vertex's four-degenerate GS, the 5i vertex's near-degenerate excited quartet, and the 7i vertex's near-eight-degeneracy all stem from symmetry-mediated frustration, a mechanism distinct from conventional periodic lattice designs. By decoupling degeneracy from strict periodicity, ABT-related vertices offer a platform for designing reconfigurable spin systems with on-demand state multiplicities, critical for applications in neuromorphic computing and magnonics [288].

Possible preferred long-range moment ordering (pathing) is worth noting, evident from the directional pathways of magnetic moments (indicated by green and blue arrows in Figure 6.5(b)), revealing distinct flux-shunting behaviour in the lowest-energy 5i states.

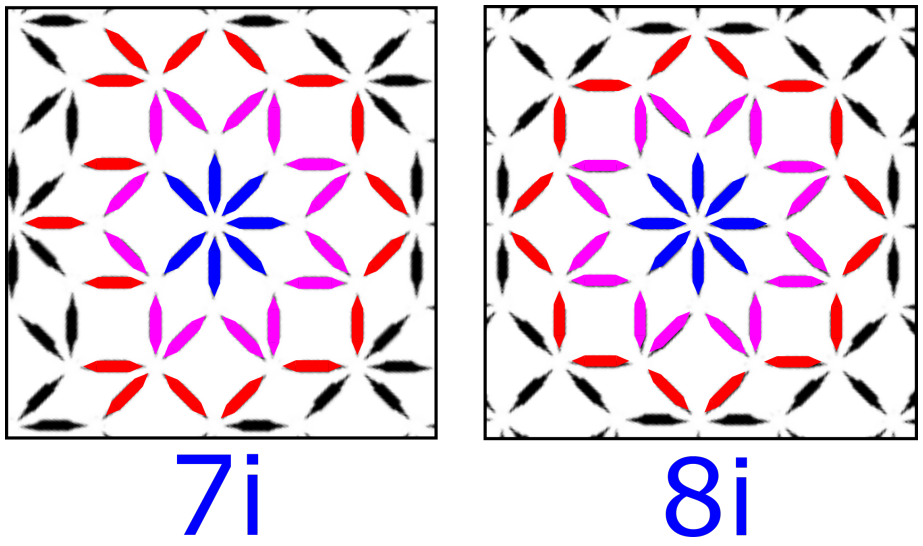

Figure 6.6: The 7i and 8i vertices in blue, with their neighbour nanoislands coloured based on their proximity: nearest neighbours in pink, next nearest neighbours in red, and elsewhere in black.

Flux shunting occurs when magnetic flux from one moment bypasses a frustrated neighbour and instead propagates along a path of lower energy, effectively redirecting the flux to influence the state of non-adjacent elements. A low-energy pathway is a path through aligned magnetic moments where flux propagates with minimal energy cost, typically along chains of moments oriented head-to-tail. Conversely, a high-energy pathway is a blocked path where flux encounters a high energy penalty due to magnetic conflict (head-to-head or tail-to-tail moment alignment), forcing frustration or redirection. For instance, the 5i GS (blue border) exhibits two adjacent 'in' moments (blue-green) at the right of the vertex, forming an acute angle between the top and bottom moments. This geometry forces flux to shunt through a high-energy pathway, as competing interactions between the 45°-separated moments amplify local repulsion. The second degenerate GS configuration, generated by global moment inversion, mirrors this flux-shunting pathway in reverse. In contrast, the 1st excited state (green border) adopts a lower-energy flux distribution: the right-hand moments align into a conflict-free sequence, while the vertical moments reorient to minimise repulsion. This reconfiguration reduces frustration, stabilising the excited state despite its slightly higher energy (GS = 35.06 eV, 1st = 35.14 eV). Flux-shunting dynamics are typically quantified using correlation functions, measuring how individual moments align with their neighbors to minimise interaction energy [30, 80, 283].

Due to the lack of translational periodicity in QP ASI systems, a generalised pairwise correlation function cannot be defined, as these rely on repeating unit cells to define neighbour interactions. However, by anchoring the analysis to specific vertex types, for example, selecting a reference nanoisland within a discrete vertex, a localised correlation function

can be computed that evaluates the alignment of nearest neighbour moments. This vertex correlation model is tailored to vertex types of QP systems, treating each vertex type as a quasi-independent unit, bypassing the need for periodicity-derived assumptions. In the ABT, the approach is particularly critical for the 5i vertex, where the minimal energy gap (0.08 eV) between GS and 1st excited states renders the system highly sensitive to flux-shunting perturbations. Such sensitivity suggests that long-range correlations may be mediated by symmetry-selective frustration. Higher-order vertex types (7i and 8i) are surrounded by a fixed set of vertices within three nearest neighbours, as shown in Figure 6.6. A minimised energy interaction for these moments can be computed to explore, for example, how increasing the lattice constants in an equilibrium system might reduce the correlation. Yet, such analyses remain inherently limited: the QP structure for lower-order vertex types generates a combinatorial explosion of unique nearest-neighbor configurations, while the focus on rarer 7i and 8i vertices (9% of the lattice) neglects the dominant 3i-5i vertices (91% of the lattice). A vertex correlation model considering all vertex types, therefore captures the dominant energy-minimising interactions immediately surrounding each of the ABT vertices, offering a pragmatic framework to quantify how geometric frustration and flux-shunting pathways affect GS formation.

6.4.3 Vertices-Only Model

Figure 6.7(a) shows a vertex energy map of a real ABT ASI measured with MFM, shown in Figure 6.7(b). Vertices in the calculated GS (green) and excited states (black) are displayed. The white gap in the top left is a physical defect from the nanolithography process. The overall GS occupation for the 3i to 8i vertices in this array is 64.8%, spanning 1811 vertices. Table 6.1 provides the GS population for each vertex type shown in Figure 6.7(a). In our system, the observed GS population of 69.5% suggests that the system is nearing equilibrium but has not fully thermalised. Figure 6.7(a) displays all GS vertices with a single colour to represent all vertex types regardless of their relative energies and degenerate states. As such, information is removed as different GS domains of GS vertices are not considered. As the ABT system has six vertex types of different degeneracy, defining a GS domain with a Vertices-Only approach is not trivial.

The excited states (black) in Figure 6.7(a) can be identified to form limited string-like

	3i	4i	5i	6i	7i	8i	Square
GS (%)	76.6	66.5	26.5	69.6	25	79	69.5
Total	773	606	268	92	24	48	210

Table 6.1: The GS population for each vertex type in Figure 6.7(a), including square vertices measured on the same substrate.

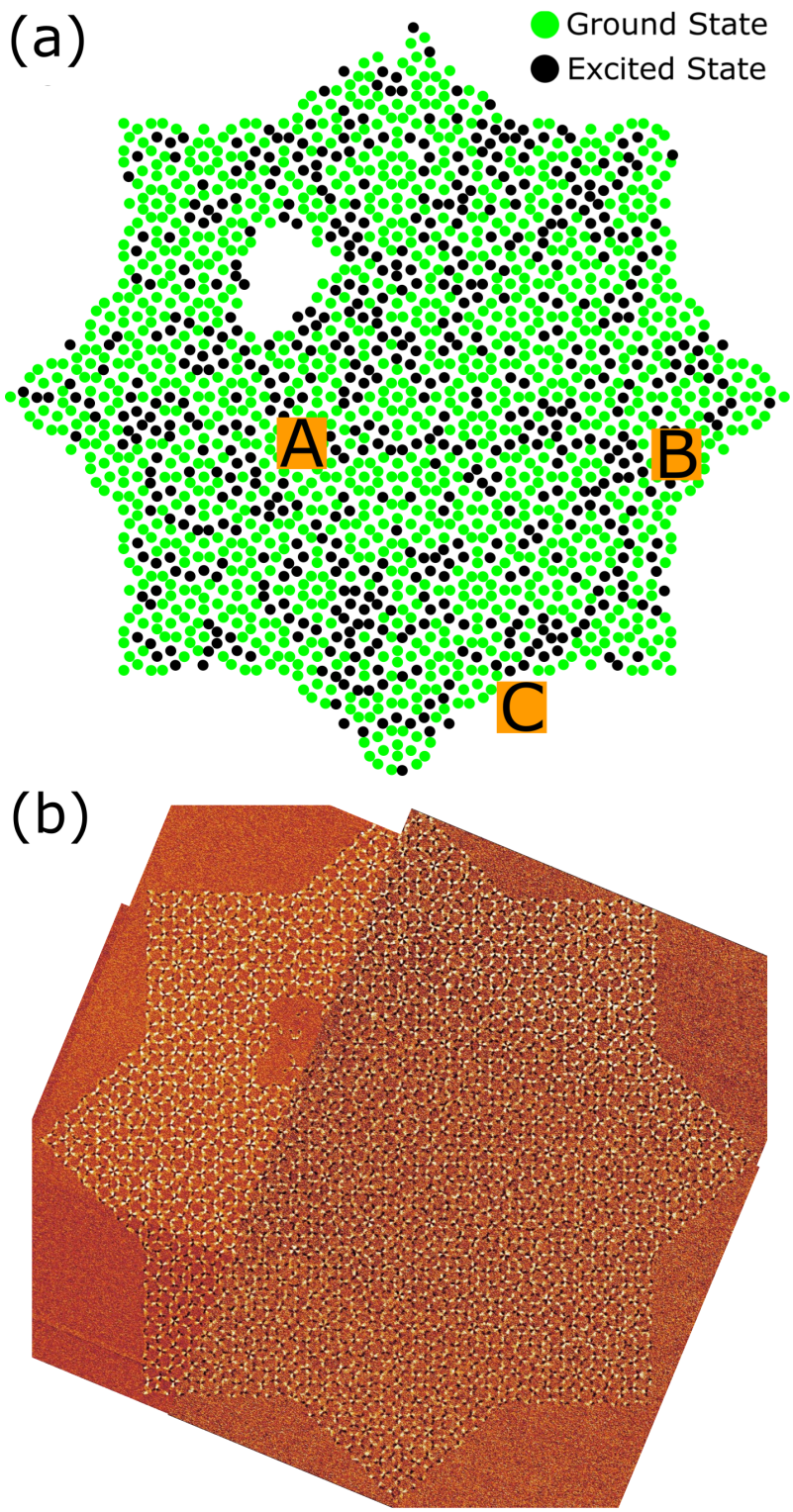

Figure 6.7: (a) An energy map of GS (green) and excited state (black) vertices in a real system 50 µm across. Orange A, B, and C indicate an example string of excited vertices which appear to form across the tiling. (b) The correspinding MFM image of the energy map from (a), stitched with four images.

paths across the full length of the tiling. An example string is indicated between the orange A - B - C path. These strings may suggest an approach toward separating long-range GS domains as high-energy domain walls in an incompletely thermalised system. A domain wall is typically made of excited vertices and separates domains of GS vertices [26, 29, 79]. Table 6.1 shows that the global GS occupation for the 3i, 4i, 6i, and 8i vertices ranges from 66.6% to 79%, which is expectedly high for a geometrically frustrated system [30, 114, 289]. These GS vertices tend to cluster in regions 3-5 µm in size, surrounded by the proposed high-energy domain walls.

The odd-numbered 5i and 7i vertices exhibit comparatively very low GS occupations of 26.5% and 25%, respectively. Including the GS ($n = 71$) and 1st excited state ($n = 167$) of the 5i vertex, previously noted as energetically close, increases the occupation to 88.9%. The total count of 5i vertices $N = 268$ has a relative uncertainty of $\frac{\sigma}{N} = 0.061$, which can be relied upon for broad statistical trends. However, the low GS occupation of the 7i vertex is susceptible to low counting statistics with $N = 24$ and $\frac{\sigma}{N} = 0.204$, though similar to the other higher-order 6i ($\frac{\sigma}{N} = 0.104$) and 8i ($\frac{\sigma}{N} = 0.144$) vertices, which also have low counts. The anomalous GS distributions of odd-numbered 5i and 7i moment vertices warrant further investigation with the Skeleton and Correlation Models, discussed later.

Figure 6.8 compares the expected Boltzmann distribution for each isolated vertex type with the observed distribution in the ABT. Figure 6.8 compares the predicted Boltzmann distribution for each independent ABT vertex type with the observed distribution in the ASI. The observed distributions for the 3i, 4i, 6i, and 8i vertex types closely follow the predicted Boltzmann populations, suggesting the system is approaching equilibrium at these sites. Additionally, there is strong evidence for all vertices nearing their minimum energy states by considering the lowest and highest energy occupations. While the total GS occupation is 64.8%, the GS plus 1st excited state occupation is 91.2%, and only 0.4% of total vertices are in their highest energy states. However, the experimental occupation of the GS and 1st excited states still fall outside several statistical standard deviations from the predicted populations, even with a statistically significant $N = 1519$ microstates, indicating some degree of excitation within the ASI. Since the system is measured as-grown rather than annealed, it is possible these excitations are not equilibrium results, which would explain the observed populations.

Interestingly, the 5i vertex with $N = 268$ shows the strongest deviation from the predicted distribution in the first two energy levels. The 5i GS and 1st excited state are predicted to populate with 77.4% and 22.6%, respectively, but instead are observed with 26.5% and 62.3%. The calculated 5i GS and 1st excited states are shown in the 5i panel of Figure 6.8. Note there is only a small energy gap between the 5i GS and 1st excited state (35.06 eV - 35.14 eV). Combining this trend with the conclusions from Table 6.1 and Figure 6.5, anomalous behaviour of the 5i and 7i vertices may be explained by symmetry-

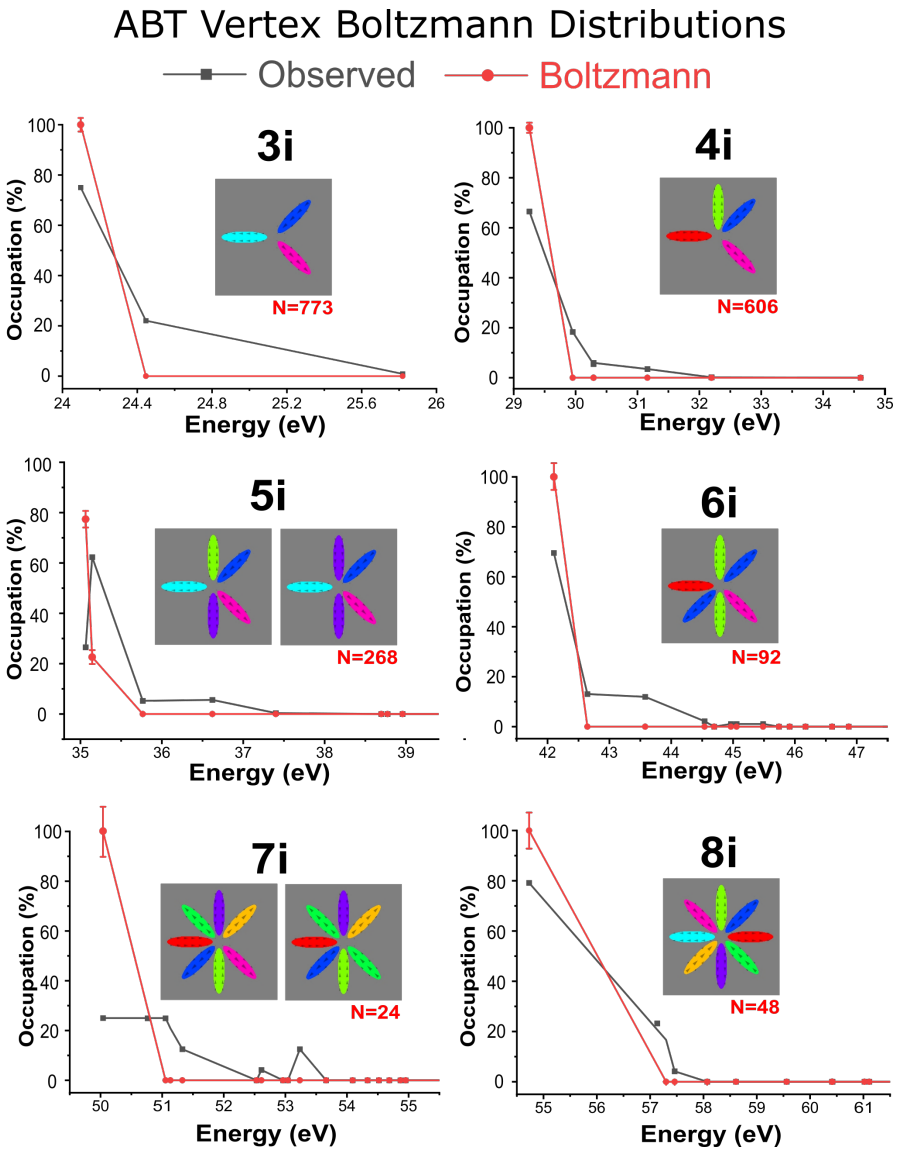

Figure 6.8: The observed vs predicted Boltzmann curves for each vertex type within the ABT. The 3i, 4i, 6i, and 8i graphs show one GS combination, while the 5i and 7i graphs also include the 1st excited state due to their observed population.

mediated flux-shunting. This may be because excited states with F-moments are preferred due to a lower-energy flux distrbution between nearest neighbours than in the isolated GS vertices.

6.4.4 The Skeleton Model

Applying the Skeleton Model to the Ammann-Beenker Tiling

In this section, the skeleton model approach is extended to the 8-fold ABT, which has overlapping octagonal clusters that act as quasi-unit cells. The octagon GS, shown in

Figure 6.9(b), can be calculated by placing fixed or F moments, with all vertices in their GS and minimised cluster energy. The total octagon moment GS is confirmed with MuMax3. This octagon cluster of moments is then mapped across the entire tiling. The construction produces a fixed 'skeleton' of moments, alongside a selection of F moments, predicting QP long-range ordering.

Figure 6.9(a) illustrates the Skeleton Model applied to a section of the ABT, with fixed moments represented in pink and F moments in red. The skeleton exhibits double degeneracy, forming two networks, denoted pink and blue in Figure 6.9(b), with opposite chiralities. Each F moment is individually double degenerate. However, when situated in 7i and 8i vertices, this degeneracy is lifted by the mutual dipolar interaction between neighbouring F moments. Additionally, in the ABT, a 5i vertex is always paired with another 5i, sharing an F moment. Taking into account the degeneracy of these F moments, the total number N of globally degenerate GS can be calculated:

$$N = 2 \times 2^{\frac{5i}{2}+7i+8i} = 2 \times 2^{134+24+48} = 2^{207} \tag{6.4.1}$$

The model therefore predicts 2^{207} unique but energetically degenerate global GS, far more than periodic square and kagome systems [114]. This is then extended to calculate the entropy:

$$S = k_B ln(N) = k_B \times 207 \times ln(2) \approx 143 k_B \tag{6.4.2}$$

and entropy density (the number of accessible microstates per vertex sites):

$$\rho = \frac{S}{N_{Spins} \times k_B} = \frac{143 k_B}{4608 k_B} \approx 0.031 \tag{6.4.3}$$

expressing a high degree of disorder within the system.

Figure 6.9(b) illustrates the construction blocks of the Skeleton Model, shown in pink and blue, for each chiral network. Octagon clusters are composed of the calculated GS vertices from Figure 6.4, and overlap to fully decorate the tiling. As a result of these overlapping clusters, a new set of GS vertices for each network are produced from this model and are displayed next to the clusters, labelled 3i to 8i.

Figure 6.9(c) demonstrates an arbitrary construction of the ABT from a single octagon (grey shade) into a larger array. Points A, B, and C highlight how the 5i, 6i, and 7i vertices, respectively, are formed. At point A, four overlapping octagons result in fixed moments where the octagon moments coincide. An F moment is placed along the outside edge of two octagons with opposite fixed moments, forming a 5i vertex with a two-in, two-out configuration and one F moment. At point B, another four octagons contribute to the formation of the 6i vertex. The two central top moments are flippable, but the fixed edges of the outer octagons force a fixed moment, resulting in the fixed 6i configuration.

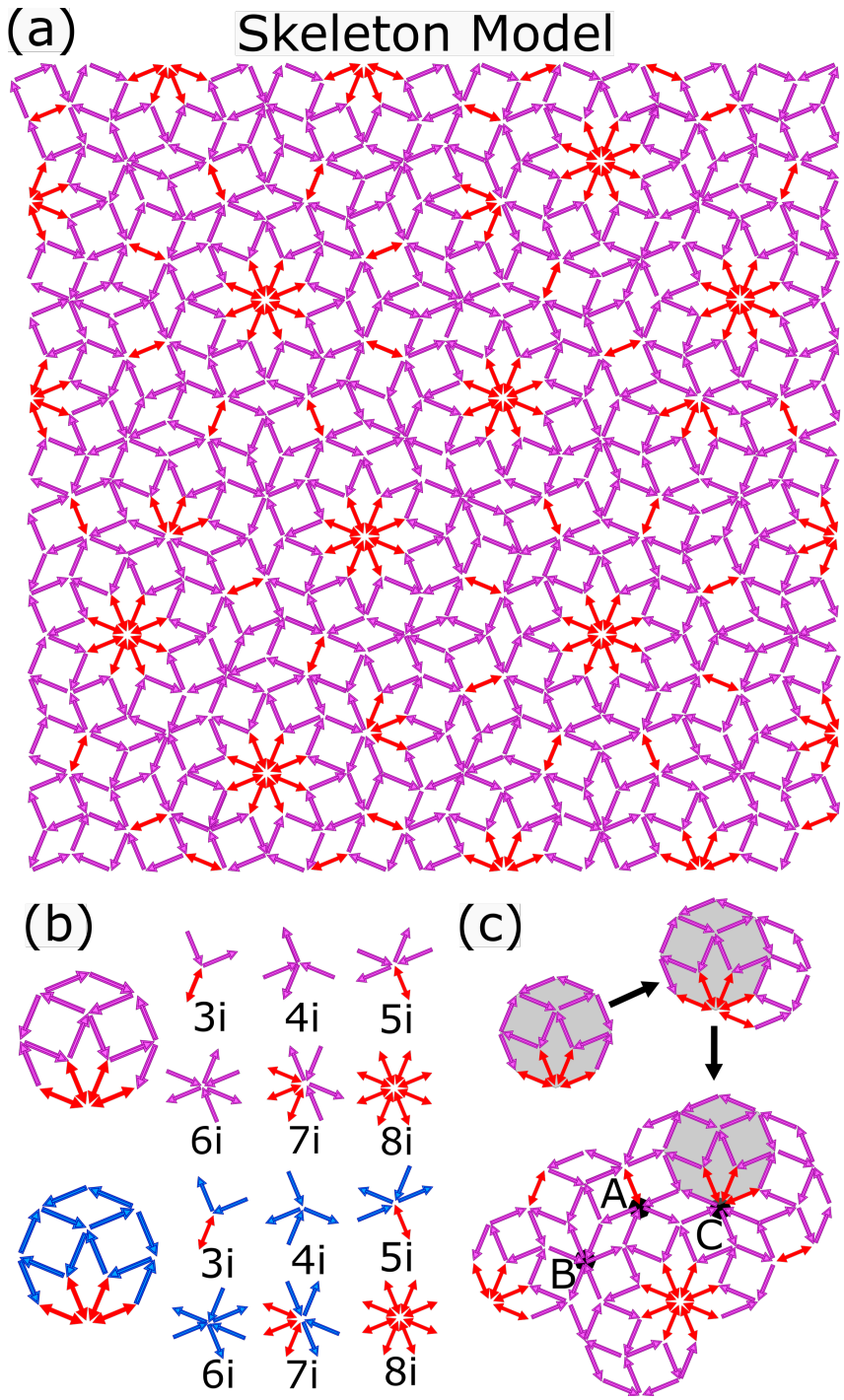

Figure 6.9: The Skeleton Model for mapping GS domains. (a) The theoretical model for the pink network includes fixed pink moments and flippable red moments. (b) The octagon cluster is the base construction block that the model is made from. Pink and blue networks have opposite chirality. The final vertex configurations from (a) are shown for each network labelled 3i to 8i. (c) The method for generating an arbitrary tiling by combining the octagon cluster (grey) with other overlapping octagons. Points A, B, and C in the final step indicate 5i, 6i, and 7i vertices discussed in the text.

Finally, point C illustrates the construction of the 7i vertex using six octagons. While five moments are flippable in theory, overlapping moments from the 6i vertex constrain two of them to be fixed. As a result, the 5i, 6i, and 7i vertices exhibit reduced entropy with fewer F moments, a consequence of long-range ordering not immediately evident from the base octagon structure.

Experimental Results and Discussion

Figure 6.10 shows the application of the Skeleton Model to the real ABT ASI system. Pink and blue moments are placed where their networks coincide with the measured moments, and green moments are placed where neither network surrounds a vertex. Excluding red flippable moments, which may belong to either network, there are 2600 blue, pink, and green moments placed in Figure 6.10. The total coverage is 1408 blue (54.2%), 1144 pink (44.0%), and 48 green (1.8%) moments. The total coverage of pink and blue moments being 98.2% indicates the model is a very good fit for illustrating the behaviour of each domain. It also indicates that a larger part of the ASI is in the GS than previously determined via the Vertices-Only model (64.8%).

High-energy vertices (black dots) from Figure 6.7(a) are overlaid on Figure 6.10. The high-energy vertices are predominantly found at the boundary between pink and blue networks. This further supports the conclusions from Figure 6.7(a) that strings of excited states may be high-energy domain walls between pink and blue domains.

The most interesting result is the distribution of 5i and 7i high-energy vertices in Figure 6.10. Some of these excited vertices are found within the blue or pink GS networks, for example the excited 5i vertices, which are highlighted with orange-white bordered dots. This is because the isolated 5i and 7i GS exhibited by the Skeleton Model are not the same as the isolated GS calculated in Figure 6.4. These excited vertices instead correspond to the skeleton vertices in Figure 6.9(b), with F moments in the 5i and 7i, supporting the previous conclusion that anomalous excited states with F-moments are stabilised due to a lower-energy flux distrbution than isolated GS vertices. These observations bridge the gap on why fewer of the calculated GS 5i and 7i vertices in Table 6.1 are observed in the real ASI than predicted by the Vertices-Only model. By combining the Boltzmann distribution evidence in Figure 6.8 for the 7i and especially 5i vertices preferring an excited state over the GS; there is strong evidence for reconfigurable excited states within GS domains as a result of symmetry-mediated multiplicity. Additionally, the fixed skeleton of moments, constructed from short-range flux-shunting, demonstrates long-range QP order.

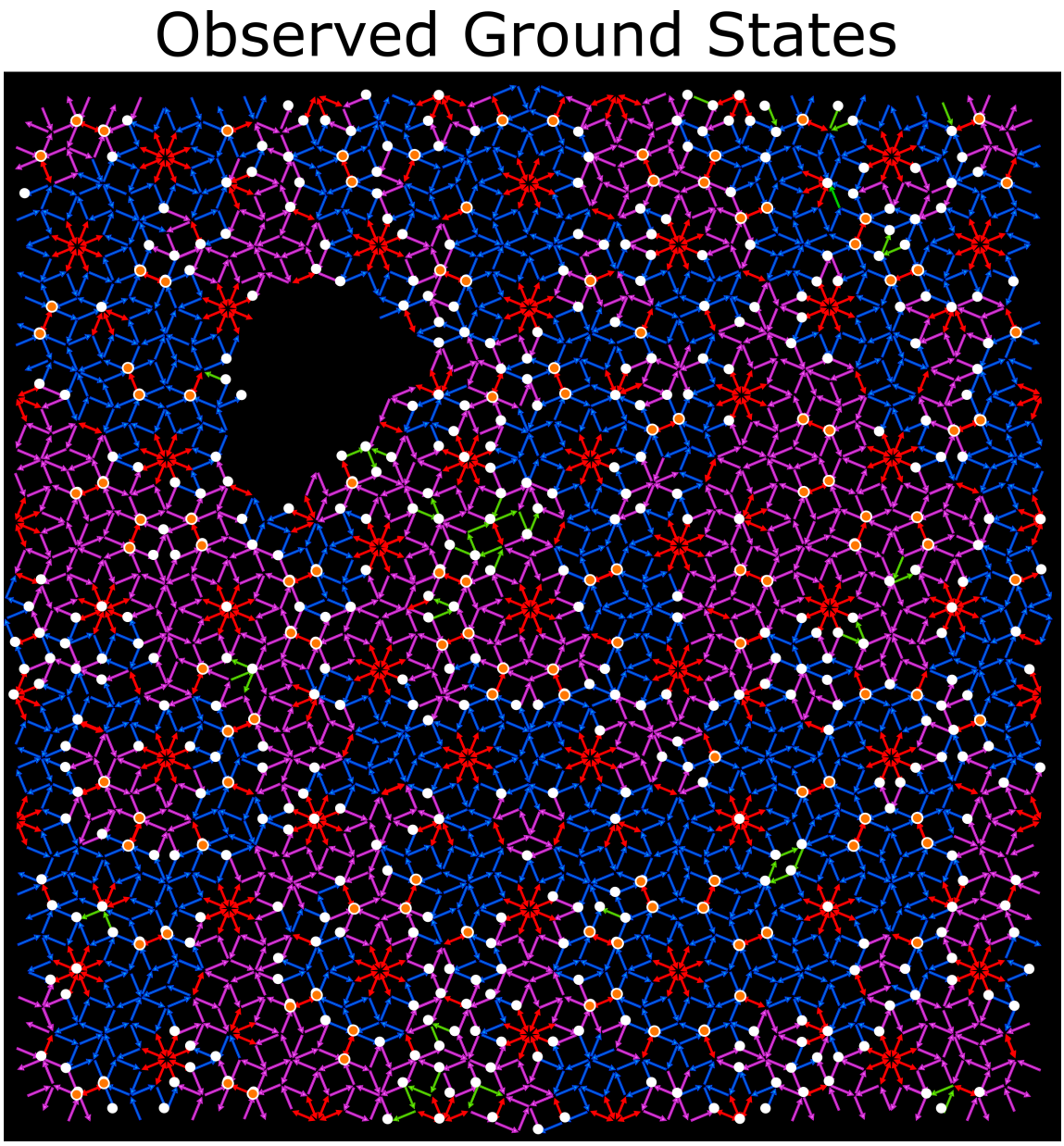

Figure 6.10: The observed GS in a real ASI system with the Skeleton Model. Pink and blue moments are part of the GS domains. Green arrows are placed where moments do not coincide with either domain. Overlaid white dots are high-energy vertices. Orange dots with white borders indicate high-energy 5i vertices found within GS domains.

6.4.5 The Correlation Model

Applying the Correlation Model to the Ammann-Beenker Tiling

Finally, for completeness, a vertex correlation model is considered, depicted in Figure 6.11. This model includes the nearest neighbour moment for each vertex type, accounting for the flux closure loops formed around each vertex type to minimise the total interaction energy [30, 80, 84, 283–286]. Flux closure loops occur when moments surrounding a tile follow the same rotational direction, coloured light-blue or pink with an open loop, and blue or purple with a closed loop. While the Vertices-Only and Skeleton Models describe vertex and moment distribution well, they struggle to fully capture the complexity of flux closure loops around tiles particularly in the 5i and 7i vertices. Earlier, a generalised correlation model was dismissed within the Vertices-Only framework due to the lack of a periodic unit cell. However, a correlation model can be applied to each individual vertex type in QP ASI. These models will be referred to as tilings, for example, the 3i tiling. Note square and rhombic tiles will continue to be called tiles. Figure 6.11(a) shows the correlation model for vertex types 3i to 8i including one nearest neighbour for both blue and pink chiral networks. Each tiling is constructed using either the MuMax calculated or Skeleton Model GS vertices, whichever minimises the number of open flux loops. Closed flux loops indicate the formation of a complete loop of moments around a tile; if any moments oppose the chirality, the loop remains open. For all vertex types except the 5i and 7i, the MuMax calculated GS is used, while the 5i and 7i vertices utilises the Skeleton Model GS. This choice is made because the MuMax calculated 5i and 7i GS results in more open flux loops compared to the Skeleton Model GS.

Figure 6.11(b) shows a predicted Correlation Model at the boundary between the two chiral blue and pink GS domains. Model tilings are placed manually with the following procedure: start with the highest-energy tiling (8i), and place until all 8i vertices are occupied. Then, sequentially place lower-energy tilings atop their vertices, from 7i down to 3i. When placing new tilings, all new moments must coincide with existing (placed) moments; otherwise, the vertex is skipped, and the next area is considered. This method is chosen as the higher energy (6i to 8i) tilings are considered pinning centres, as their total calculated interaction energy is greater than the lower energy (3i to 5i) tilings. Therefore, the energy required to flip moments in the higher energy tilings would be greater. Starting with lower energy tilings is discussed later.

With this approach one chiral tiling domain cannot completely coincide in one GS domain with the other, as seen along the boundary between the blue and pink network in Figure 6.11(b). For example, at the orange mark within enlarged area B, the 3i vertex between the blue and pink network is forced into the highest 3-out energy state. A frustrated domain wall of excited vertices is then present in all arbitrary constructions of the

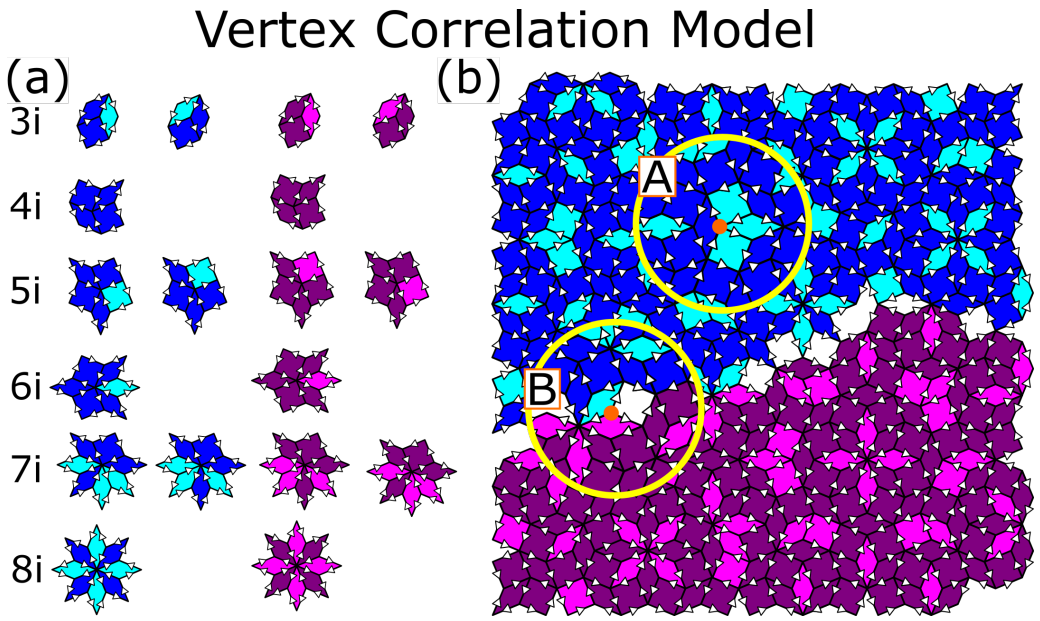

Figure 6.11: The vertex correlation model for mapping GS domains around each vertex type. (a) The correlation model for each vertex type 3i to 8i in each domain (blue and pink), minimised to reduce the number of open flux loops in tiles immediately surrounding the vertex. Moment mirror planes in the 3i, 5i, and 7i models lead to a second equivalent GS for each. (b) The vertex correlation model shows both domains in a discrete section of the ABT. Each domain is constructed starting with the highest energy 8i tilings, then 7i, 6i... until all space is effectively filled. Enlarged areas A and B highlight discussion points within the text.

Correlation Model, and must therefore exist between each chiral tiling domain.

Interestingly, the 5i vertex to the right of the orange mark in area B is the same as the Mumax3 calculated 5i GS, observed much less frequently in Figure 6.7(a) than the more populated 1st excited state. It was earlier established that short-range flux-shunting effects contributed to long-range QP order in the Skeleton Model, preferentially forcing the 1st excited 5i state in GS domains. In some cases at the boundary between domains, Mumax3-calculated 5i and 7i GS vertices are observed. Although this result may be determined to be a coincidence, these GS vertices could act as nucleation points for two coexisting domains, increasing the amount of long-range frustration in the system.

Another significant assertion from the Correlation Model in Figure 6.11(b) is forced frustration of exciting tilings. Locally excited tilings exist where more open flux loop tiles are constrained within a GS tiling domain. For example, at point A, the 4i tiling (orange mark) should have no open flux loops (see 4i in Figure 6.11(a)), but instead contains two open squares and one open rhombic flux loop. Note the open flux loop tiles are still constructed of GS vertices, and follow tiling construction rules. The open flux loop excitation is due to the surrounding 5i and 6i tilings constraining moments before the 4i tile is placed. This same effect is seen throughout model and real GS domains for 3i and

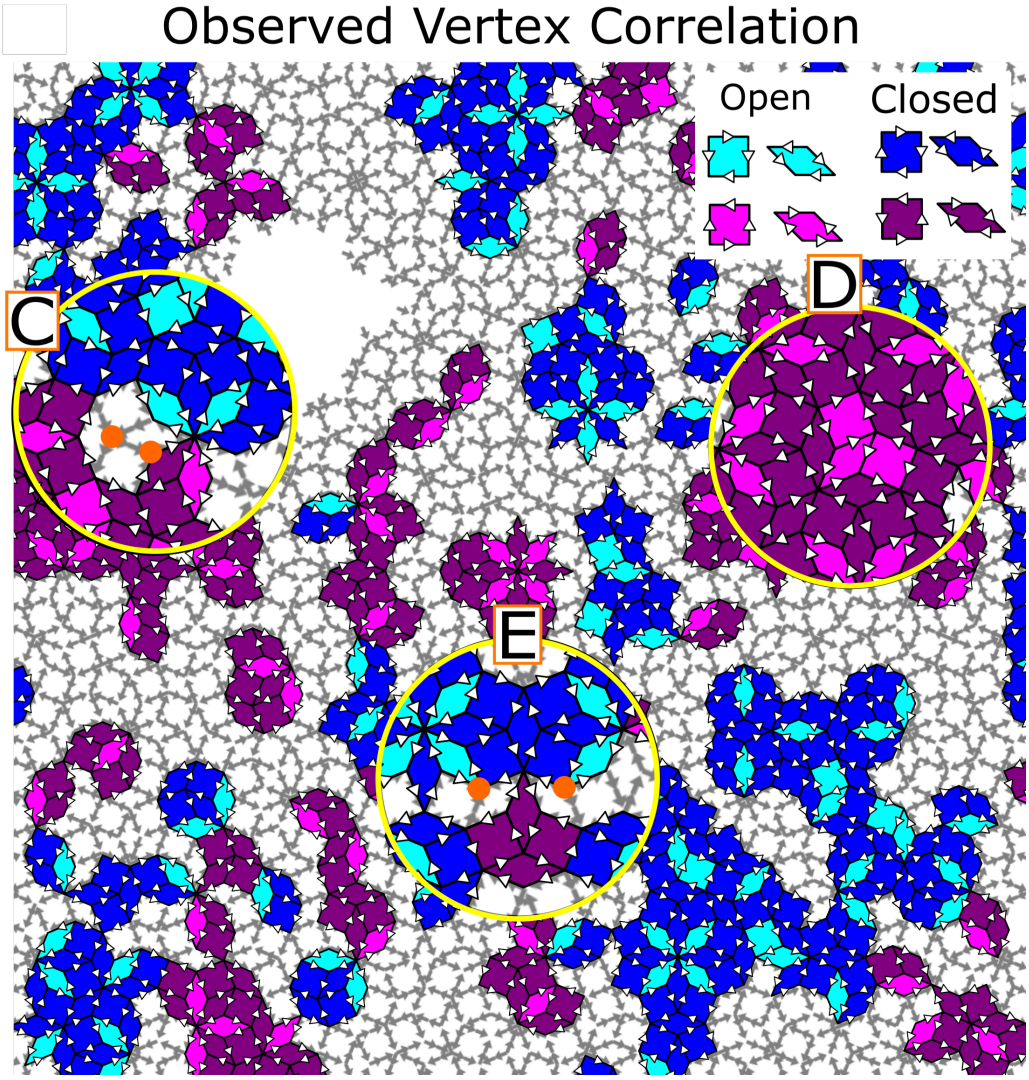

Figure 6.12: Observed vertex correlation models within our ABT ASI system. Coloured open and closed flux loops for each domain are shown inset. Enlarged areas C-E again indicate discussion points within the text.

4i tilings.

In construction, the ABT is almost entirely covered by the 5i to 8i tilings before 3i to 4i are placed. This strongly suggests a global GS domain would be dominated by nucleation from the higher energy tilings, and by extension why the 3i and 4i tilings become excited. Conversely, if tilings are placed arbitrarily or starting with 3i and then 4i, excited high-energy vertices become trapped surrounded by GS tiling domains in a stochastic manner. Since trapped high-energy vertices do not occur when placement begins with the 8i tiling, the formation of a global GS tiling domain with GS vertices is concluded to require higher-energy tilings like 8i to act as pinning nucleation centres. This process leads to a global GS domain dominated by nucleation from higher-energy tilings, forcing tile excitation in

the lower energy 3i and 4i tilings.

Experimental Results and Discussion

The Correlation Model is now applied to experimental results of the real ABT, as shown in Figure 6.12. When applying the Correlation Model to a real system, placed tilings must coincide with real lattice moments. Tiling placing is then the same operation as described previously. Of the 1636 loops available, 736 (45.0%) are covered by the Correlation Model tilings, indicating these tilings can only describe limited patches compared to the Skeleton Model (98.2%). The lower coverage is attributed to incomplete thermalisation of our system, and missed coverage in GS tiles within tilings that are not accounted for. Firstly, due to incomplete thermalisation, fragmented GS nucleation is expected from many areas, including lower energy 3i and 4i tilings. As previously discussed, when lower energy tilings are placed first, it leads to a stochastic array of smaller GS tiling domains surrounded by high energy vertices. Similar arrays of GS tiling domains are observed in Figure 6.12. This supports that the Correlation Model does correctly describe these GS areas well, but is poorer than the Skeleton Model at describing stochastic GS nucleation. Secondly, coverage is poorer than the Skeleton Model because all moments in the placed tiling must coincide with the real lattice moments. With this method, some tiles in tilings do coincide, but the full tiling includes one or two flipped moments, meaning the tiling cannot be placed. The combination of these factors contributes to the observed Correlation Model tilings having a low coverage.

Another interesting result is the distribution of open and closed flux loops varies dramatically between the interior and exterior of GS tiling domains. Within the tiling domains, there are a total of 763 loops, of which 570 are closed (75%) and 193 are open (25%). However, on the exterior, there are a total of 900 loops, 393 (44%) are closed and 507 (56%) are open. This suggests that outside GS tiling domains there are far more excited open flux loop tiles than within domains. These excited loops could only be quantified by the Correlation Model.

The highlighted areas of Figure 6.12 demonstrate forced frustration behaviour GS tiling domains in our real ABT, in terms of locally excited open flux loops and domain wall formation. Point D shows the centre of a tiling domain $\approx 10\,\mu m$, with an excited 4i tiling similar to the model 4i at point A in Figure 6.11(b). Several of these 4i, and by extension 3i, tilings are observed across the real ABT, demonstrating forced frustration due to QP long-range order. Additionally, points C and E show where two tiling domains meet, with excited vertices indicated with orange dots. The excited vertices are forced into high-energy states by the surrounding tiling domains, as their presence is necessary for the two domains to coexist.

Model	Real ABT (%)	Ideal ABT (%)	Real Square (%)	Ideal Square (%)
Vertices-Only	64.8	100	69.5	100
Skeleton	98.2	100	86.5	100
Correlation	45.0	100	NA	NA

Table 6.2: Table comparing the GS occupation for the real experimental ASI and the theoretically ideal occupation, for the ABT and square tilings.

6.5 Summary of Model Regimes Analysis

Three model regimes for analysing ASI have been explored: Vertices-Only, Skeleton, and the Correlation Model. Table 6.2 shows a summary of the GS occupation of each regime for the experimentally measured ASI, and the theoretically ideal occupation. Each of the ideal GS can in principle have 100% occupation, however nanolithography defects and the formation of high-energy domain walls constructed of excited vertices forbids an experimentally true global GS.

The Vertices-Only model found the GS occupation for the real ABT to be 64.8%, which is slightly lower than the 69.5% GS occupation for the real Square. However, analysis combining all models revealed that the isolated 5i and 7i GS vertices calculated with MuMax3 are not present in a global GS, as they force nearest neighbours into opposite chiral GS domains. The actual ideal ABT occupation has excited 5i and 7i vertices, leading to an occupation of the ideal ABT = 83.9%. As a result, the ratio $\frac{\text{Real}_\text{i}}{\text{Ideal}_\text{i}}$ for the ABT is $\frac{\text{Real}_\text{ABT}}{\text{Ideal}_\text{ABT}} = 0.77\%$, which is greater than $\frac{\text{Real}_\text{Square}}{\text{Ideal}_\text{Square}} = 69.5\%$. It was asserted in Section 6.3.1 that a GS occupation of 69.5 % for the square ASI may be thermalised during growth, which can also explain the high GS occupation of the ABT. Note the correlation model is not performed for the square ASI, as the defining feature of the GS in a simple system such as the square ASI is the formation of closed flux closure loops, which is quantified with the skeleton model.

A generalised Skeleton Model was developed to analyse QP ASI. As the ABT ASI is decorated with overlapping octagonal clusters, degenerate competing chiral domains of fixed moments with long-range order are produced. These fixed moments are mediated by short-range interactions, and map 98.2 % of observed moments in our system in the GS, close to the ideal GS occupation. Combining the Vertices-Only and Skeleton Model reveals that odd-moment vertices (5i and 7i) stabilise degenerate excited states within GS domains, via favoured nearest neighbour flux-shunting pathways. Flippable 'F moments', which occur due to moment mirror planes, increase degeneracy and are unique to odd-numbered vertex types with greater geometric frustration. Additionally, degeneracy reemerges selectively in excited 5i and 7i states containing F moments, where there is a suppression of moment mirror planes in the 5i and 7i GS.

The Correlation Model demonstrates that flux closure around vertices stabilises a global GS of tilings by adopting GS skeleton vertices containing F moments. Additionally, high-energy 8i vertices act as pinning centers for GS tiling domain construction. The edges between tiling domains form high-energy domain walls of excited vertices between chiral networks. These results position the ABT as a platform to design reconfigurable magnetic states in odd-numbered moment vertices, where degenerate F moments may be susceptible to long-range QP order, opening pathways for magnonics and neuromorphic architectures reliant on controlled metastability. Overall, results show the quasiperiodicity of the ABT forces frustration through competing chiral networks, and is stabilised by the local 8-fold symmetry sites which act as high-energy pinning centres.

6.6 Magnetometry and XMCD-PEEM

Results in Section 6.3 indicated the need for thermalised arrays to fully understand the experimental GS behaviour. This section shares magnetic imaging and magnetometry studies of the ABT taken at the Diamond Light Source, and ISIS Neutron and Muon Source, respectively. The goal is to establish a protocol for thermalising quasiperiodic ASI.

X-ray magnetic circular dichroism - photoemission electron microscopy (XMCD-PEEM) is a soft X-ray technique that utilises X-ray adsorption spectroscopy to produce in-situ spectroscopy imaging, and ex-situ magnetic imaging. By probing at the Fe or Ni L3 edge, which is a function of the materials ferromagnetic properties, magnetic contrast images can be produced while annealing or magnetising samples. A full method is given in Section 4.7.3 and 4.7.4 and is recommended to read before this section. With this technique it is possible to observe the cascade of GS moments forming in ASI as they are annealed, as energy barriers to flipping are lowered and the system is brought into equilibrium. To start, the Curie Temperature (T_C) for the ferromagnetic to paramagnetic regime is determined, to identify the temperature range needed for samples while measuring with XMCD-PEEM. T_C is measured via a vibrating sample magnetometry - superconducting quantum interference device (VSM-SQUID), by heating and then cooling within either field-cooled and zero field-cooled regimes. Next, XMCD-PEEM of the ABT is first shown at room temperature (RT), then in steps up to the T_C transition, and back to RT.

6.6.1 Experimental Techniques

Continuous thin films of permalloy ($Ni_{80}Fe_{20}$) with thicknesses of 4, 6, 8, and 10 nm were grown via a shroud physical vapour deposition process in UHV. Following permalloy deposition, a 3 nm Al capping layer was deposited to act as a capping layer to prevent Ni or Fe oxide surface growth in air. The films were all grown on the same clean, atomically flat, 400 µm thick and undoped SiN substrates. UHV deposition is performed in a base

pressure of 1×10^{-9} mbar, with a growth rate of 0.4 $\text{Å}\text{s}^{-1}$, and source purity of 99.9%. Following growth, substrates were scored according to their thickness grade, diced into 5 mm^2 batches, and normalised by thresholding the surface area of the thin film with ImageJ. Magnetometry is performed by VSM-SQUID with in-situ annealing from 300K up to 900K at the ISIS Neutron and Muon Source, Rutherford Appleton Laboratory, to determine T_C. The heating and cooling rate is set to 20 Kmin^{-1} for all magnetometry anneal measurements, and zero-field cooled unless otherwise stated in the text. XMCD-PEEM at the Fe L3 edge (708 eV), confirmed by XAS, was performed at the Diamond Light Source, Oxford. Samples were annealed from RT through T_C and back to RT, measured in-situ with X-PEEM, and post processed shortly after into XMCD-PEEM images. The temperature of samples were recorded via a thermocouple mounted to the back of samples on the sample holder, and heating is radiatively applied to samples over 6 hours.

6.6.2 Results and Discussion

Determining Curie Temperature of Permalloy Thin Films

Determining T_C is an important part of the method for measuring ASI. One method is with a VSM-SQUID, which measures magnetic moments on a sample mounted between pick-up coils on an vibrating rod with a constant frequency in a helium flow cryostat. By measuring change in magnetic flux in the coils during vibration, the total moment measured in emu of the sample can be calculated. By varying the temperature of the sample via joule heating, a graph of temperature against total moment can be plotted. Despite the sensitivity of VSM-SQUID in measuring total moment, ASI with around 100 μm^2 of magnetic material per 1 cm^2 have too low a signal-to-noise ratio for accurate moment measurements. For this reason a continuous unpatterned film sample, grown in the same batch of ASI samples during metal deposition, is instead measured. This will result is a small overestimate of T_C as ASI nanoislands will have smaller ferromagnetic domains compared to a continuous film, and therefore a lower energy barrier to transfer into the paramagnetic regime. In this section, VSM-SQUID measurements of a wedge film of continuous permalloy are presented, with 4, 6, 8, and 10 nm thick sections, to plot T_C as a function of film thickness and anneal temperature.

Figure 6.13 shows cooling curves which measure magnetisation as a function of temperature for each thickness of permalloy with zero applied field. The thickest (8, 10 nm) samples were annealed from 300 to 900K, and then cooled back to 300K. Cooled curves give a better estimate of T_C as the system has gone through equilibrium, where heating curves behave more stochastically and are more of a function of the unpredictable starting condition of domains. The samples therefore begin with zero total magnetisation in a total paramagnetic state. As the sample cools, coupled ferromagnetic exchange between neighbouring spins becomes more influential as thermal energy decreases. The inflection

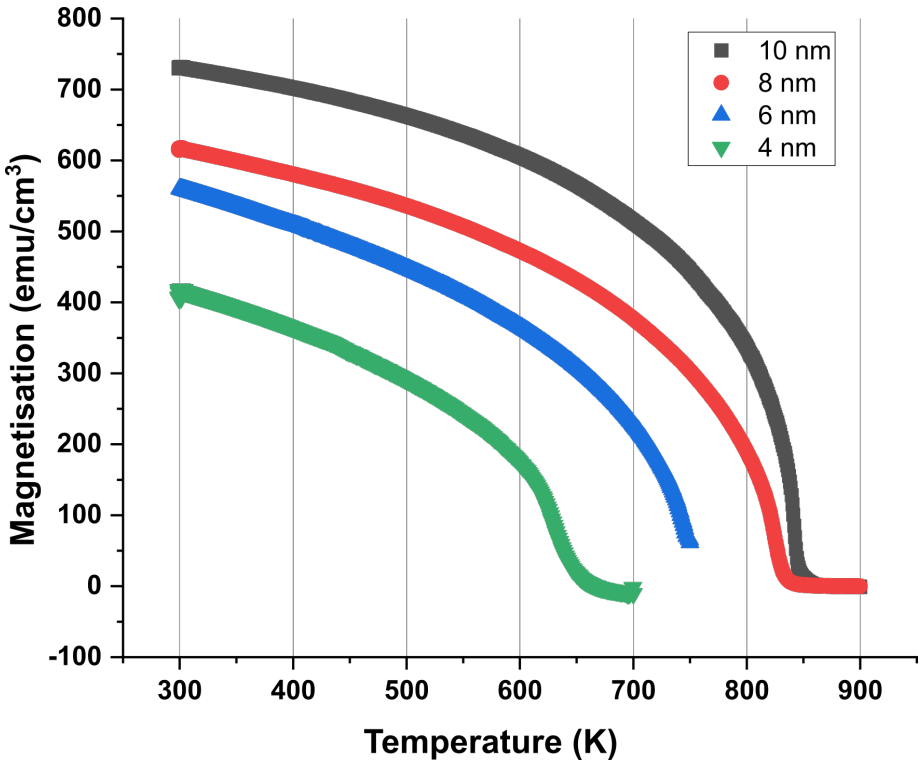

Figure 6.13: Measured magnesation as a function of temperature for a range of permalloy thicknesses. Samples are heated to their maximum temperature, discussed in the text, and therefore curves on the graph show cooling starting from the maximum temperature.

point of the curve ($\frac{dM}{dT}$ minimum) is where the transition from the paramagnetic to ferromagnetic regime begins, and ferromagnetic domains of parallel moments form. Physically, as thermal energy is reduced, the energy barrier to paramagnetic behaviour is increased and thermal disruption of spin alignment reduces, increasing the total magnetisation [101]. These characteristic curves from 900 to 300 K can be seen at 8 and 10 nm thicknesses in Figure 6.13, with an estimated T_C between 810 and 860 K. When heating the 6 nm sample to 900 K, delamination or interdiffusion effects caused an irreperable loss in magnetisation, so a lower final anneal temperature for thinner films was chosen. The curve for the 6 nm sample in Figure 6.13 shows the cooling from 750 to 300K, which begins with a slight inflection but above 0 total magnetisation, so T_C can be extrapolated to between 725 and 775 K. The 4 nm sample is cooled from 700 to 400K, finding an inflection point between 625 and 675 K. Finally, due to Al capping, there is a possibility of alloying at the interface of Al and Ni/Fe when heating to higher temperatures, which may explain less sharp transitions to zero magnetisation. However, alloying of this type is not known to have negatively effected the ferromagnetic properties of previous ASI studies.

An estimate of T_C to the most accurate value can be made by plotting $\frac{dM}{dT}$ against temperature around the inflection point, as shown in Figure 6.14(a), with all sample thick-

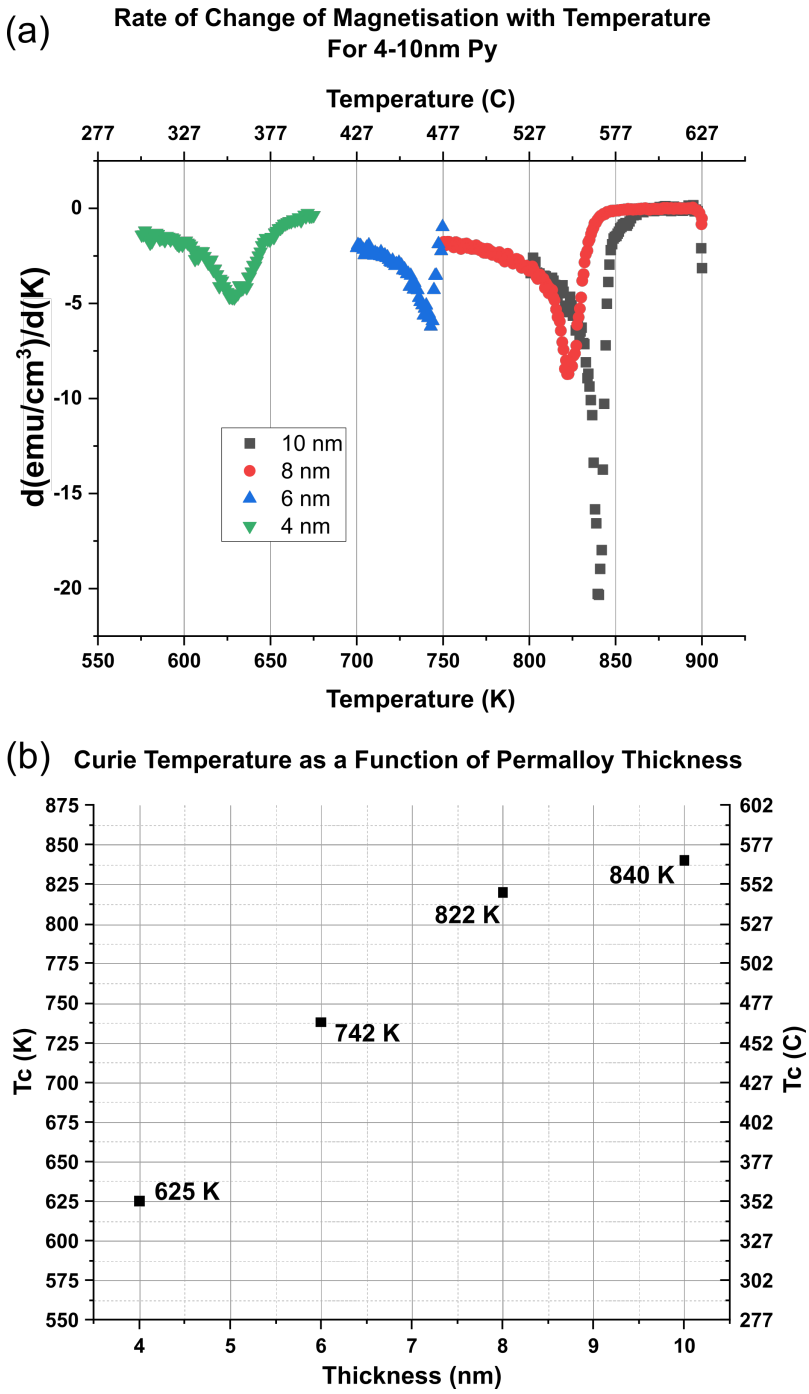

Figure 6.14: (a) Rate of change of magnesation plotted against anneal temperature for each sample thickness. Thicker samples are shown to correlate with an increases $\frac{d(Mag)}{d(Temp)}$ minimum, leading to an increased T_C. (b) A plot of T_C as a function of thickness, estimated from the inflection point of magnesation as a function of anneal temperature.

nesses from 4 to 10 nm. The inflection point at the $\frac{dM}{dT}$ minimum represents the transition between ferromagnetic and paramagnetic regimes. Well below T_C, a small increase in temperature leads to a small decrease in total magnetisation, primarily associated with an increase thermal energy disrupting spin alignment. Approaching T_C, the $\frac{dM}{dT}$ gradient increases, whereby a small change increase in temperature leads to a rapid decrease in magnetisation. The rapid decrease may be caused by ferromagnetic domains reducing in size as exchange energy becomes less influential, as well as an increase in spontaneous flipping of domains. At the $\frac{dM}{dT}$ minimum, the thermal energy between moments is enough to overcome the ferromagnetic exchange interaction, collapsing domains and the sample entering the paramagnetic regime with rapid moment switching. Immediately above T_C, total magnetisation rapidly reduces, until flatlining where there is no directional ferromagnetic behaviour. Figure 6.14(b) shows the final graph of T_C as a function of permalloy film thickness, with labelled T_C values. While there are only four points, a slight curve is observed for thinner films and a plateau approaching 850 K for thicker films approaching the bulk value (820 K [101]). This knowledge of T_C as a function of film thickness provides a guide for choosing the anneal temperature for later ASI investigations.

XMCD-PEEM Anneal Study

In this section, XMCD-PEEM is performed on the ABT ASI, with the sample annealed from RT, through T_C, and back down to RT. Accurate temperature measurements are very important to this work. Temperature is recorded with a thermocouple mounted to the back of samples on the sample holder, and samples are heated radiatively in close proximity. As this setup is limited to monitoring temperature at the back of samples, any temperature gradiant between the back and surface cannot be measured. SiN has a thermal conductivity of 10 - 40 $Wm^{-1}K^{-1}$, compared to Cu which has 147 - 370 $Wm^{-1}K^{-1}$, so it is possible the recorded temperature at the back will be slightly higher than at the surface of the sample [290]. In the previous section, T_C was estimated to be 840 K for a 10 nm permalloy film, but previous works with the same composition and thickness identified a value closer to 800 K [101]. Overall, considering the thermocouple accuracy, our magnetometry measurements, and the literature, a ferromagnetic to paramagnetic transition is expected to occur between 800 - 860 K.

Figure 6.15 shows a series of XMCD-PEEM images of the ABT ASI from RT, through T_C, and back down to RT. The red arrow in the top left panel indicates the X-ray wavevector. At RT, each nanoisland has a single domain macrospin, with each having enough of a parallel component with the X-ray wavevector to show their domain orientation. Heating is applied and acquisitions were taken every 25 K over a period of 6 hours. At 725 K, similar domains to at RT are observed below the T_C. At 775 K, domain contrast is mostly lost, but topological magnetic contrast is still visible. One explanation could be

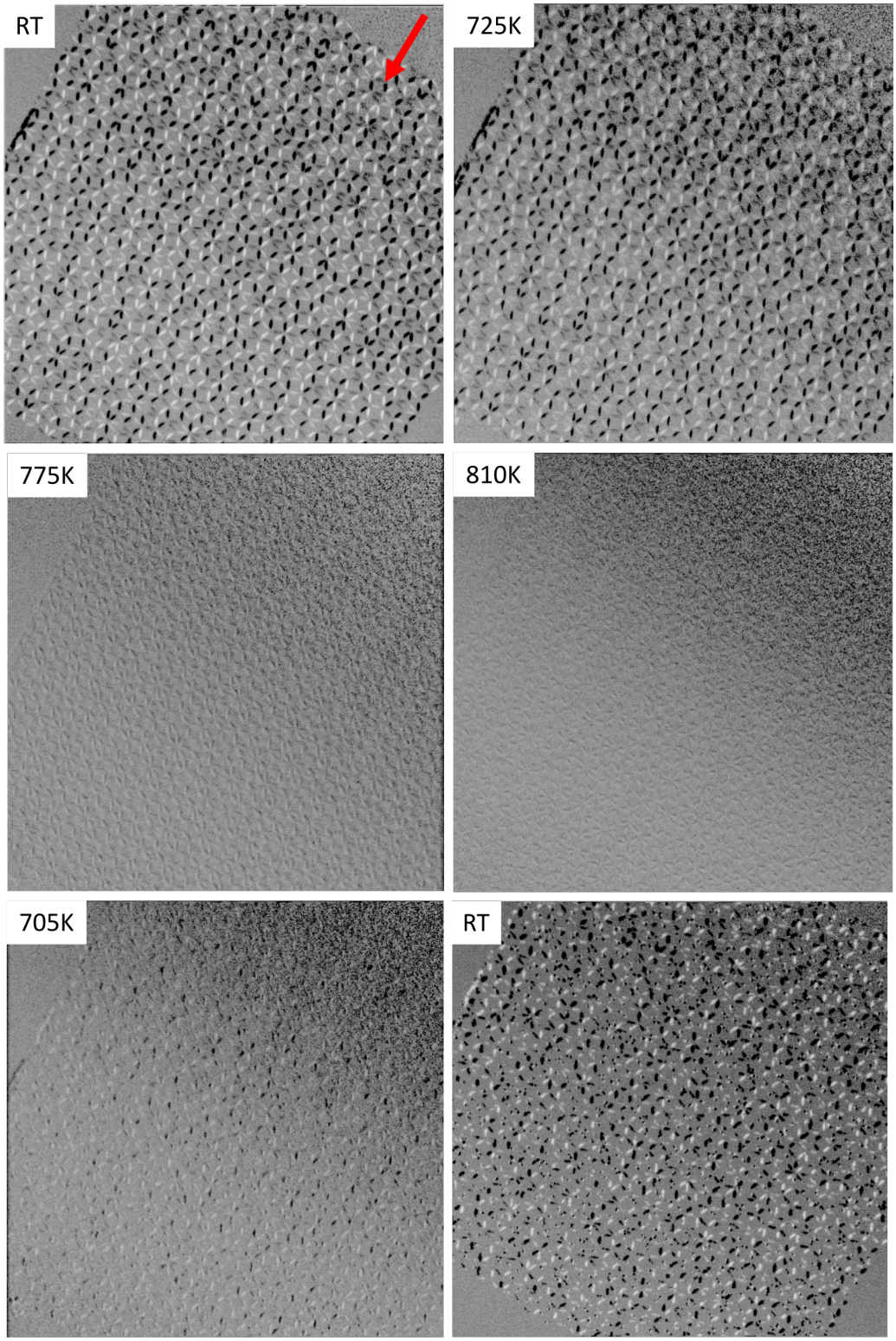

Figure 6.15: XMCD-PEEM images acquired while heating the ABT ASI, from RT up past the T_C to 810 K, and back to RT. The X-ray wavevector is indicated with a red arrow.

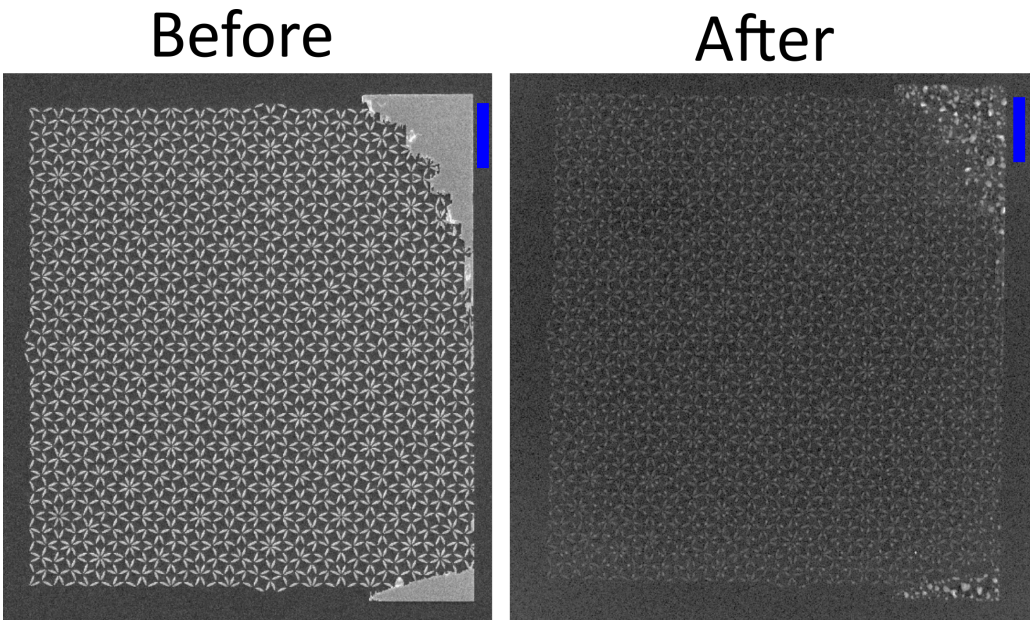

Figure 6.16: SEM images of the sample structure as in Figure 6.15, before and after annealing. The blue bar corresponds to features discussed in the text.

that the ASI has entered a superparamagnetic regime, where rapid flipping of moments shorter than the image acquisition (0.25 s) can cause the average effect of no net macrospin moment. At 810 K, most of the topological contrast is lost as the ASI passes through T_C and individual moments within nanoislands overcome strong exchange interactions and behave paramagnetically. The maxiumum recorded temperature was 830 K before cooling began. Upon cooling to 705 K, magnetic contrast was regained at a lower temperature than expected, and macrospin moments appeared smaller and more diffuse. One possible explanation for poor signal quality may be due to misaligned optics as the stage, sample, lens, and other components undergo slight thermal expansion or drift. Finally at RT, is it clear that the sample has undergone many defect transformations, no longer exhibiting a majority of single domain macrospins.

To explain the loss in both XMCD-PEEM signal and lack of distinct macrospins, SEM acquisitions with the same probe conditions from before and after XMCD anneal imaging is shown in Figure 6.16. SEM does not provide a thickness profile but is surface sensitive, and a couple of factors indicate the thin film thickness has decreased. Firstly, the brightness of the permalloy before annealing is much greater and each nanoisland can be distinguished, suggesting a thicker and better quality ASI film. Secondly, nanolithography defects of continuous permalloy thin film areas are indicated with a blue bar in the before and after pictures. Before annealing these indicated structures are continuous, but after annealing have become significantly fragmented. The leading explanation for sample degradation is delamination or thermal diffusion either laterally or into the substrate. It has been

reported that Ni may diffuse into the substrate of SiN, and especially Si, as a drop in saturated magnesation, when annealed to 870K [29]. As the ASI permalloy constitutes a much lower surface area than the continous film annealed with VSM-SQUID, it is possible diffusion of Ni could have occured significantly damaging the surface permalloy structure. Despite damaging the permalloy thin film, the study was still able to image domains at RT, as well as observing the T_C threshold crossing.

6.7 Summary of Anneal Studies

To summarise this section, fabrication of ABT ASI which exhibit single-domain edges when measured with magnetic microscopy techniques has been demonstrated. To support anneal protocols, the T_C of continuous thin films of graded thickness was determined with magnetometry measurements. Despite structural degradation of the ABT post annealing, XMCD-PEEM was able to show ferromagnetic contrast being lost and regained as the structure moved through T_C. Knowledge of the degradation will also be useful for future beamtimes by collaborators.

6.8 Conclusion

The 8-fold ABT ASI has been explored with micromagnetic modelling, and MFM and XMCD-PEEM magnetic imaging techniques, to attempt to fabricate and measure an experimentally minimised global energy state. At room temperature, ground state domains demonstrate how quasiperiodicity leverages symmetry to engineer frustration and degeneracy. With an isolated vertex approach, specific vertex types (5i and 7i) with excited states can be found within 'ground state' domains. These excited states can be explained by flux-shunting behaviour between nearest neighbour vertices, which leads to a re-defined global ground state of fixed skeletal moments. Finally, high-symmetry mirror planes unique to QP systems, and hierarchical self-similar geometry of the ABT, enable symmetry-induced multiplicity of specific vertex types (3i, 5i, 7i, and 8i) to satisfy a global ground state. An anneal study was performed with magnetometry and XMCD-PEEM to establish a protocol to thermalising quasiperiodic ASI. While the anneal study caused irreperable damage to the ABT ASI, attributed to delamination or thermal diffusion effects, important lessons were gained in managing thermalising ASI. It is expected that a thicker thin film would be more robust to diffusion effects, as found as the Square Fibonacci tiling ASI measured in Chapter 7.

Chapter 7

Magnetic Ordering and Frustration in Square-Fibonacci Artificial Spin-Ice

In this Chapter, the physical nanomagnetic properties of a fabricated Square-Fibonacci tiling (SFT) are investigated with magnetic microscopy, supported by micromagnetic simulations. This work is an extension of nanomagnetic investigations made in Chapter 6.

7.1 Introduction

The Square-Fibonacci tiling (SFT) is a 4-fold quasiperiodic structure formed by superimposing two orthogonal 1-Dimensional Fibonacci chains. This superimposing creates tiles with long (L) and short (S) edge lengths, related by the irrational golden mean $\tau = \frac{\mathrm{L}}{\mathrm{S}}$ [46, 291]. The SFT introduces quasiperiodic order within a square-like framework, enabling comparable studies of fundamental magnetic ordering between periodic and quasiperiodic analogues.

The advent of nanolithography has enabled the fabrication of single-macrospin ferromagnetic domains, which can decorate the edges of tilings such as the periodic square lattice [18]. Fabricated systems of single-macrospin ferromagnetic domains are known as artificial spin-ice (ASI), where periodic systems have been fabricated and measured exhaustively with magnetic microscopy techniques [79]. The global ground state (GS) of periodic square ASI exhibit vertex arrangements with enforced charge neutrality and an absence of excitations [29,79]. While atomic square-lattice thin films are well-demonstrated on periodic substrates [292], the growth of a fullerine SFT on an Al-Pd-Mn quasicrystal surface is a recent achievement [194]. Furthermore, the recent development of endohedral metallofullerene molecular nanomagnets may facilitate the growing of an SFT thin film

functionalised with magnetic moments [293]. Given the established capability to fabricate ASI via nanolithography, studying a nanomagnetic phenomena in an SFT system is now accessible without sacrificing precision. Such research could directly probe quasiperiodicity effects and motivate efforts to grow metallofullerene thin films on quasicrystal surfaces.

In this chapter, the magnetic properties of the SFT ASI are investigated with X-ray magnetic circular dichroism - photoemission electron microscopy (XMCD-PEEM), at the Diamond Light Source, Oxford. Experimental results are supported by micromagnetic simulations with MuMax3 of the SFT. XMCD-PEEM is a soft X-ray technique that utilises X-ray adsorption spectroscopy to produce in-situ spectroscopy imaging, and ex-situ magnetic imaging. By probing at the Fe or Ni L3 edge, which is a function of the materials ferromagnetic properties, magnetic contrast images can be produced while annealing or magnetising samples. By annealing ASI through the Curie Temperature (T_C), energy barriers to moment flipping are lowered, and the system is brought into equilibrium. It is therefore possible to observe the formation of GS moment configurations in the ASI as they are annealed and cooled.

XMCD-PEEM and MuMax3 simulations reveal trapped vortex states in the SFT ASI. Trapped vortex states are localised excitations pinned by the tiling's QP geometry. These states are absent in periodic square analogues, demonstrating how quasiperiodicity imposes geometric confinement. Such trapped states suggest pathways to engineer magnetic metastability, with potential applications in neuromorphic computing architectures [294].

7.2 Experimental and Modelling Techniques

7.2.1 Experimental Techniques

XMCD-PEEM of a 25 nm thick permalloy ($Ni_{80}Fe_{20}$) SFT was performed at the Fe L3 edge (708 eV), confirmed by X-ray adsorption spectroscopy, at the Diamond Light Source, Oxford. The sample was annealed from RT through T_C and back to RT, measured in-situ with X-PEEM, and post processed shortly after into XMCD-PEEM images. The temperature of samples were recorded via a thermocouple mounted to the back of samples on the sample holder, and heating is radiatively applied to samples over 6 hours.

7.2.2 Modelling Techniques

The micromagnetic simulator MuMax3 is used to model the energy levels and time-evolved magnetic state of moment combinations for SFT geometries [25]. $M_S = 8.6 \times 10^5 Am^{-1}$ and $A_{ex} = 1.3 \times 10^{-11} Jm^{-1}$ standard values for Permalloy were used for simulations [114]. Unless otherwise stated in the text, two nanoisland dimensions characteristic of the SFT are modelled, with long island dimensions equal to 660 x 120 x 25 nm^3, and short island dimensions equal to 300 x 120 x 25 nm^3.

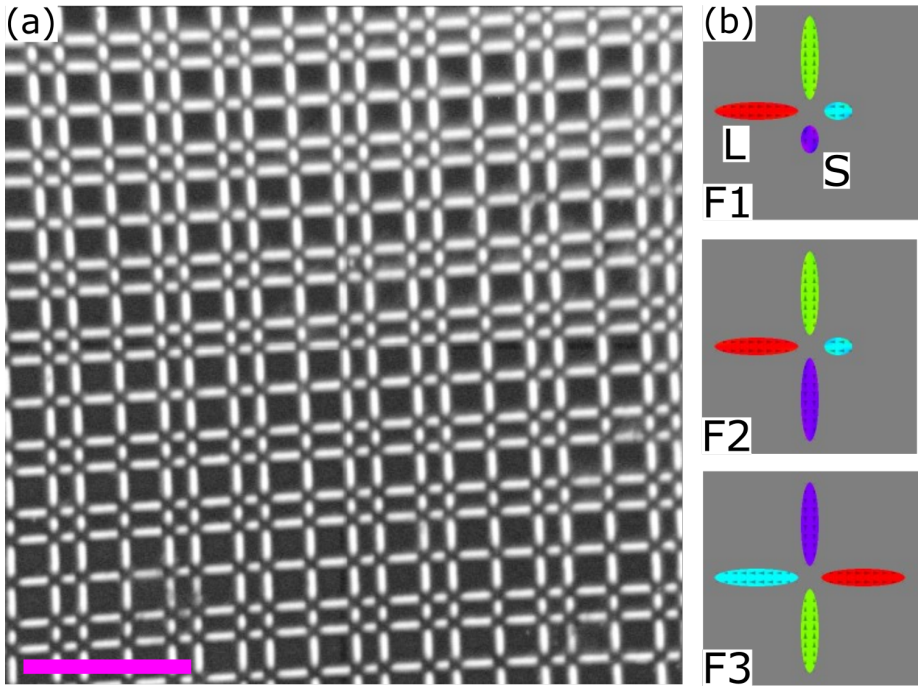

Figure 7.1: (a) X-PEEM image at 708eV of a 25 nm thick SFT ASI. Pink scalebar 5 µm. (b) The three vertex types of the SFT simulated with MuMax3, and labelled F1 to F3. L and S correspond to long and short lengths of nanoislands with quasiperiodic scaling.

7.3 Results and Discussion

The structure of an area of the SFT is shown in Figure 7.1(a), imaged with X-PEEM at 708 eV. The three vertex types for the SFT are shown labelled F1 to F3, with MuMax3 simulations in Figure 7.1(b) [25]. Labelled L and S correspond to two different quasiperiodic nanoisland lengths: L = 660 x 120 nm^2 and S = 300 x 120 nm^2. Note the intervertex lengths are set to $L_v = S_v$ x τ, a characteristic quasiperiodic scaling ratio, with L_v = 1 µm and S_v = 625 nm. The spacing difference is introduced by disconnecting the edges to form nanoislands. The three vertex types F1, F2, and F3, have four nanoislands each, with F1 having two L, F2 having three L, and F3 having four L nanoislands. As recommended with Chapter 6, a full method is given in Section 4.7.3 and 4.7.4 and is recommended to read before this section.

7.3.1 Micromagnetic Modelling Results

The distribution of total vertex energy for each configuration and vertex type is shown is Figure 7.2(a). The distribution follows a typical sigmoidal curve, similar to modelling results for the ABT vertex types in Chapter 6. Figure 7.2(b) shows the GS configuration for each of the F1, F2, and F3 vertices, as simulated with MuMax3 with a similar procedure to the ABT ASI. Arrows are overlaid over the top of F3 vertices corresponding to the colour

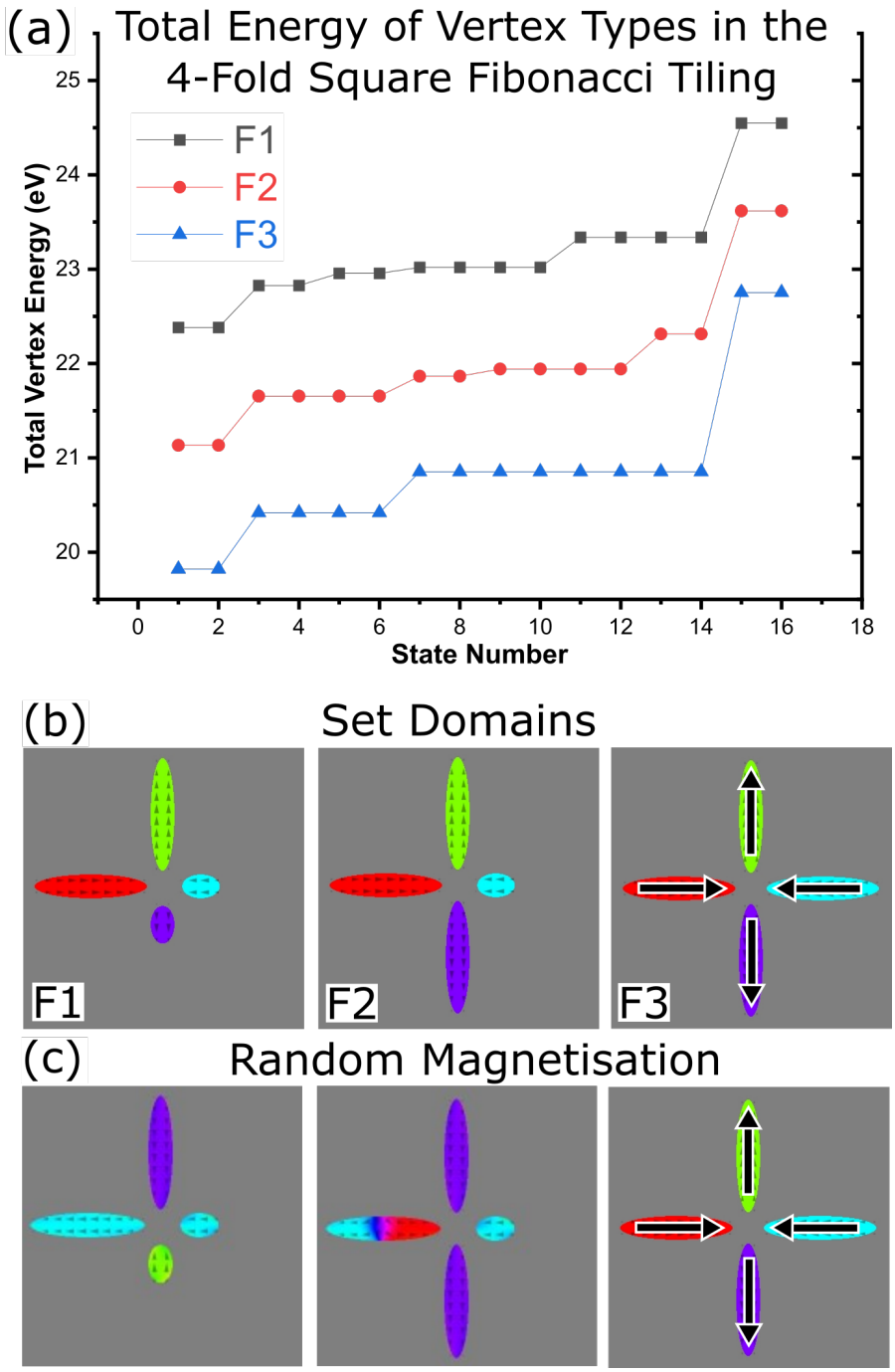

Figure 7.2: (a) Total energy of each combination of the three vertex types in the SFT. The vertex types are labelled F1 to F3 corresponding to in as in (b). (b) The GS configurations determined by setting magnesation within domains and finding the lowest interaction energy, labelled F1 to F3. (c) Moment configurations simulated by the MuMax3 Runge-Kutta method for advancing the Landau-Lifshifz equation. Each nanoisland is initially set to have random magnesation corresponding to a paramagnetic state. In (b) and (c), arrows are overlaid over the top of F3 vertices corresponding to the colour wheel flux vector.

wheel flux vector. Similar to the periodic square ASI simulated in Chapter 6, the lowest GS corresponds to a sequential in-out sequence for each of the three vertex types of the SFT.

Figure 7.2(c) shows the results of a second test, to randomise the magnesation of each nanoisland, and perform a relax function with MuMax3. The relax function employes a Runge-Kutta method to minimise magnesation by advancing the Landau-Lifshift equation [25] (See Chapter 4 for more detail). This simulation forces domains to behave as if they have been initialised in a paramagnetic state above T_C, before cooling and finding an energetically optimum ferromagnetic state. This method is however susceptible to quenching due to random fluctuations in how domains are initially formed. Quenching refers to the process where a system (like ASI) is rapidly cooled or evolved, trapping it in a metastable state instead of allowing it to reach the true GS. This occurs because random fluctuations during initialisation or dynamics cause the system to settle into a local energy minimum, preventing it from finding the global optimum configuration. For example, in Figure 7.2(c), the F1 vertex relaxes into an excited state. This behaviour may arise because the island tips are spaced too far apart to control formation of magnetic domains, or that L nanoislands are far more influential in determining magnetic domain formation in S nanoislands. Consequently, the domains nucleate metastable pseudo-GS. These states later become energetically excited, and remain unresolved by the Runge-Kutta solver during time-stepping, as a local energy minimum is found and there is insufficient numerical advancement to find the true GS. A similar quenching also occurs in the F1 vertex, which does not find a sequential in-out formation when using the relax function.

The most interesting result of simulations shown in Figure 7.2(c) is the presence of a

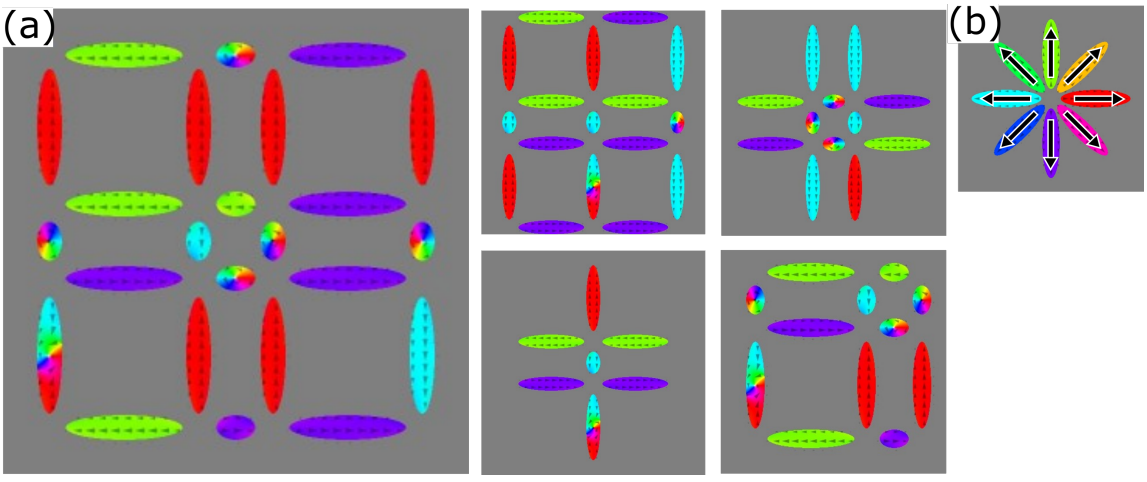

Figure 7.3: (a) A selection of tiles found within the SFT simulated with MuMax with the same procedure as in Figure 7.2(c). Single coloured domains within nanoislands correspond to single macrospin domains, while rainbow-coloured spirals correspond to trapped frustrated vortex states. (b) A colour wheel with eight example colour directions indicated.

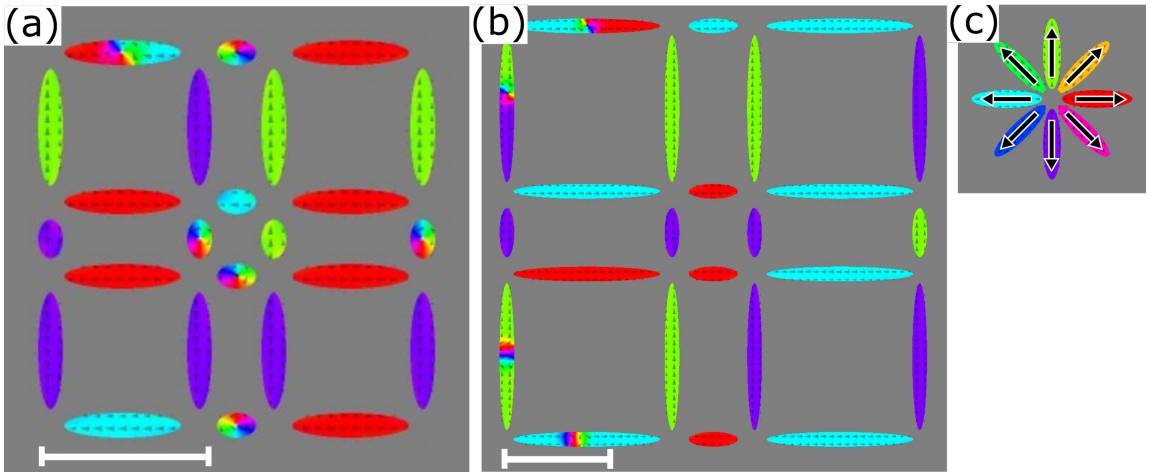

Figure 7.4: Tiled sections of the SFT exhibiting several L and S length nanoislands, with (a) having half the nanoisland lengths of (b). (a) L = 660 x 120 nm, S = 300 x 120 nm. (b) L = 1320 x 120 nm, S = 600 x 120 nm. (c) A colour wheel with eight example colour directions indicated.

vertex state at the centre of one of the F2 moments. In the SFT, the vortex splits the L domains into two opposite moments, with an excited 31.52 eV of total energy compared to the set domain GS of 21.13 eV. Topological frustration is an interesting result, which can naturally be exaserbated by adding more vertices to increase frustration. Figure 7.3 shows a selection of tiled moments, with various L and S moment combinations which each have frustrated vortex states. In each simulation, a random magnesation is set and a relax function is advanced with the Runge-Kutta method. The result is that each tiling array forces frustration which is not observed with the regular square periodic tiling. Vortex states typically occupy S nanoislands, which may not be significantly elongated to develop a single domain macrospin, but vortex states are also located in some L moments. The presence of frustrated vortex states in both the S and L moments suggests a characteristic frustration of the SFT, which can be investigated further with XMCD-PEEM.

The final test is to simulate whether trapped vortex states are topological to SFT, or a result of the S nanoislands not being elongated enough for single domain macrospins. Figure 7.4(a) shows a tiling subset of L x L, L x S, and S x S nanoislands, and in Figure 7.4(b) each L and S are doubled in length but kept the same width. Doubling the lengths results in a new L = 1320 nm and new S = 600 nm. The same simulation procedure as in Figure 7.3 is then advanced for the new longer nanoislands in Figure 7.4. With a 5:1 length to width ratio, the new S nanoislands stop exhibiting vortex states, but these states do not disappear and are instead repopulated within L nanoislands. This result shows that vortex states within either L or S nanoislands are invariant of their dimensions, and instead are intrinsic topological properties of the SFT.

7.3.2 XMCD-PEEM Results

XMCD-PEEM is performed on the SFT ASI with a similar procedure as in Chapter 6 for the Ammann-Beenker tiling: starting at RT, annealing the sample through T_C to see ferromagnetic loss in signal, and returning to RT. The measured SFT sample has a permalloy thickness of 25 nm, compared to the 10 nm ABT previously measured. Therefore, a slightly higher T_C is expected, as the thin film may now have more bulk-like properties. XMCD-PEEM images acquired at different temperatures are shown in Figure 7.5, with the X-ray wavevector marked with a red arrow. At RT (top left panel), single domain macrospins can be observed in each of the L nanoislands, and the majority of S nanoislands. Note some S nanoislands have split white and black contrast domains, such as the S nanoisland indicated with a purple arrow in the magnified (blue border) view. These split domains can be explained by the vortex states, topological excitations which are characterised by an in-plane curling magnesation and a nanometer-sized centre with an out-of-plane magnetisation [295]. Previous studies identified vortex structures as useful for fundamental studies of nanoscale spin behaviour, neuromorphic computing, and in data storage [294–298]. Single domain moments within L nanoislands are visible up to 810 K. At 820 K ferromagnetic contrast is lost as the nanoislands enter the paramagnetic regime. Ferromagnetic contrast is recovered by 725 K before the sample returns to RT. Note, the final RT image after annealing has a continuous grey background as background signal has been removed via thresholding.

Upon cooling back below T_C, ferromagnetic contrast is regained, with a 'lollipop' contrast visible in both L and S nanoislands, such as the L nanoisland indicated with a yellow arrow in the magnified (orange border) view. These lollipop features may correspond to split domains or trapped vertex states, as each white and black area matches opposite polarity moments. Within Figure 7.5 at RT after annealing, 81.0 % of 322 L and 0.0 % of 256 S nanoislands are single domain macrospins. The rest are defined as lollipop states (vortex or split domain). This is in contrast to at RT before annealing, where 100 % of L and 95.9 % of S nanoislands are single domain macrospins. For both L and S nanoislands, annealing decreases the number of single domain macrospins, with S having the most significant drop in occupation to 0 %.

These results agree with modelling results in Figure 7.3, which show a significant amount of S nanoislands relax to a vortex state, and a lower fraction of L exhibit split domains or trapped vortex states. In the ABT ASI analysed in Chapter 6, of the 1811 moments measured, no split domains or vortex states were identified, as each moment in the ABT has uniform 600 x 150 nm^2 dimensions, which behave similar to L nanoislands here. The periodic square tiling also analysed in Chapter 6 with similar L nanoisland dimensions did not exhibit any lollipop states. However, as the ABT and periodic square tiling were only measured at room temperature, and not thermalised through T_C, it is more fair to

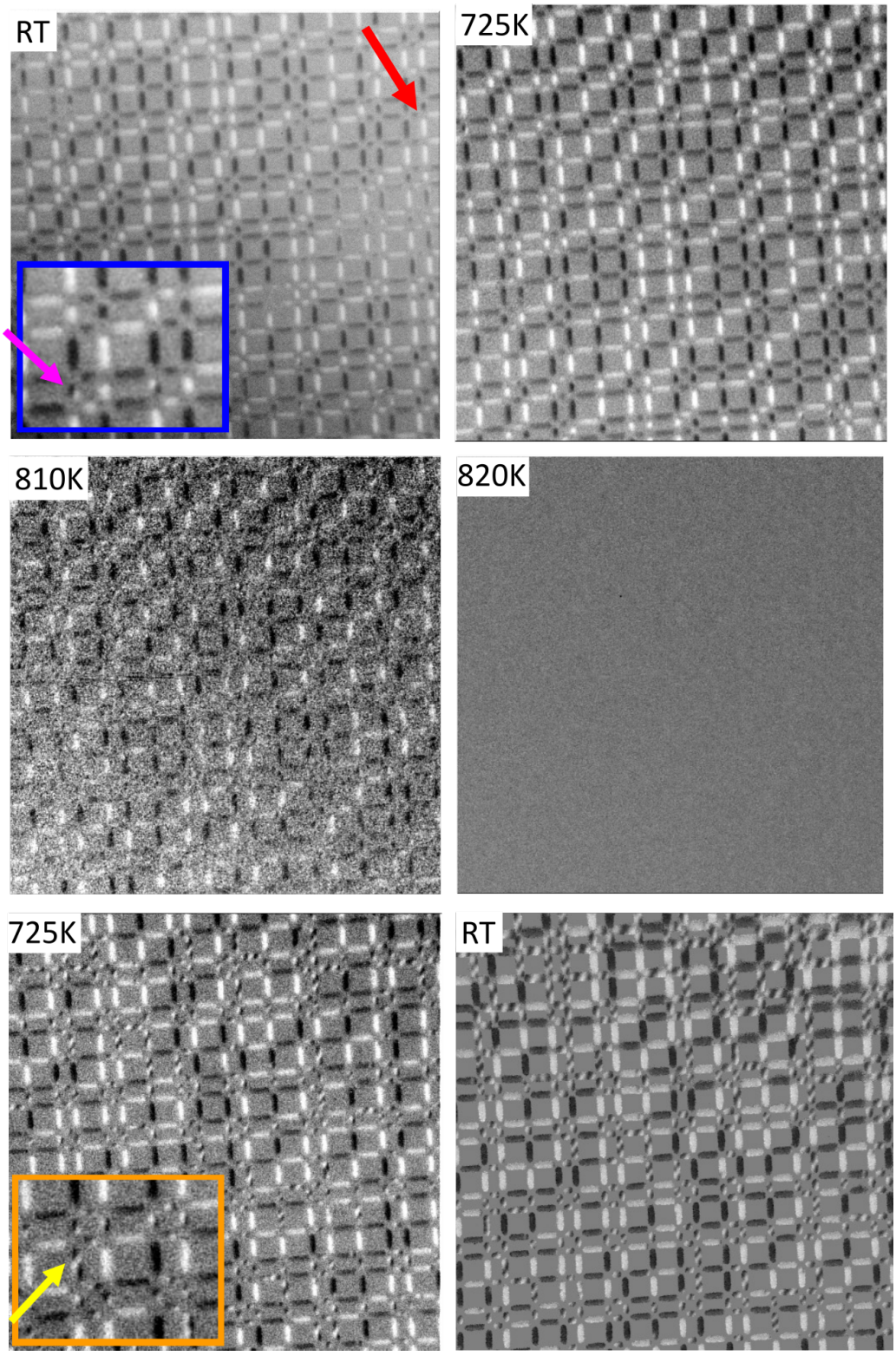

Figure 7.5: XMCD-PEEM images taken at the Fe L3 edge of a 25 nm thick permalloy SFT. The X-ray wavevector is shown with a red arrow. Images show the magnetic contrast of the sample surface as it is heated from RT through T_C, and back to RT. Multiple white and black contrast correspond to multi-domain ferromagnetism or vortex within nanoislands. Magnified sections with blue and orange borders indicate areas discussed in the text.

compare to the room temperature SFT imaging. The SFT at room temperature exhibited 4.1% of S and 0% of L nanoislands with lollipop features. It is therefore concluded that vortex states are a result of S nanoislands easily forming vortex states, and readily interacting with L nanoislands to form split domains or vortex states. These vortex states or split domains are therefore an intrinsic topological property of the SFT not found in the periodic square analogue, and with some tuning of lattice spacing these excited states may be programmable.

7.4 Conclusion

The SFT ASI was modelled with micromagnetic simulations, and imaged experimentally with XMCD-PEEM, with the aim to identify ground state dynamics. MuMax3 simulations identified trapped vortex states as excitations pinned by the tiling's inherent geometric frustration, dominating S nanoislands. The invariance of vortex states to larger nanoisland dimensions further supports their topological origin due to quasiperiodic geometry. XMCD-PEEM imaging with in-situ annealing revealed the proliferation of vortex state configurations in S nanoislands after annealing, and split domain behaviour in L nanoislands. It is therefore determined that the SFT exhibits emergent trapped vortex states following thermalisation, which are absent in the periodic square analogue. These results naturally compliment the conclusions from Chapter 6, which found excited states of odd-numbered vertex types could be found within ground state domains of the ABT. It is believed that the successful annealing of the SFT compared to the ABT can be attributed to the SFT thickness (25 nm) being much greater than the ABT thickness (10 nm), and so diffusion effects were not influential to surface layers over the duration of the anneal study. These findings position quasiperiodic ASI systems, and the SFT in particular, as a playground to explore frustration-mediated phenomena, with potential applications in neuromorphic computing architectures or data storage [294].

Chapter 8

Quasiperiodic Arrays of C_{60} Molecular Chains Induced by Anisotropic Growth

In previous chapters artificial QC have been grown, and their magnetic properties measured, to support fundamental applications research for real QC. In this chapter, there is a shift of focus to measure the adsorption properties of a real QC surface as a template for thin film growth, to identify potential practical applications.

8.1 Introduction

Quasicrystalline materials have no translational symmetry yet exhibit perfect long-range order [1], typically displaying rotational symmetries such as 5-, 8-, and 10-fold that are incompatible with periodicity. Quasicrystalline order has been observed in various materials, such as colloids [2, 3], soft-matter [4, 5], perovskites [6, 7], and originally, as inter-metallic alloys [1]. Inter-metallic alloy quasicrystals can be divided into two families: icosahedral (i) and decagonal (d). Icosahedral quasicrystals are isotropically quasiperiodic, exhibiting quasicrystalline order in all three dimensions. In contrast, decagonal quasicrystals feature a structure characterised by a stacking of quasicrystalline planes perpendicular to the 10-fold axis.

The surfaces of icosahedral and decagonal quasicrystals have been extensively studied using a variety of surface-sensitive techniques, as reviewed in the literature [163, 201, 299, 300]. Under appropriate preparation conditions, these surfaces form atomically flat terraces at specific bulk planes. These surfaces have been used as substrates for growing unique overlayer structures of single elements and molecules. For example, three-dimensional quasicrystalline films of single elements [217] and quasicrystalline molecular overlayers

have been reported [194–196, 222].

The adsorption of molecular thin films on quasicrystal surfaces is of particular interest [194–196, 222]. This is because quasicrystal surfaces exhibit a wide variety of adsorption sites with distinct electronic, chemical, and geometrical properties, leading to selective and patterned adsorption. Owing to the site-specific adsorption behaviour, molecules may also be used as chemical probes and can facilitate the development of functional thin-film materials [196].

In general, the growth of quasicrystalline molecular thin films is governed by a combination of several fundamental physical phenomena, including electron transfer between substrate atoms and molecules [194, 196, 196, 208, 222, 301], symmetry matching between adsorption sites and molecular facets [222, 224], molecular size compatibility with adsorption site spacing [194], and growth conditions including substrate temperature [195, 223]. For example, electron-accepting C_{60} molecules form quasicrystalline films when deposited onto surfaces with electron-donating minority constituents, such as *i*-Al-Cu-Fe and *i*-Al-Pd-Mn [194, 196, 222]. The minority constituents not only provide an electronically attractive site, but are also sparsely distributed at the surface, such that adjacent spacings are compatible with the size of the molecules, promoting long-range quasicrystalline order. Similar arguments have been made for electron-donating molecules atop electron-accepting constituents, such as pentacene on the *i*-Ag-In-Yb surfaces [196, 208, 301].

All previous studies on quasicrystalline molecular thin film growth have utilised substrates that are isotropically quasiperiodic. However, the 2-fold surface of the decagonal quasicrystal family is anisotropically quasiperiodic, comprising both periodic and quasiperiodic directions. Therefore, this surface provides a unique opportunity to simultaneously investigate the influence of quasiperiodically and periodically ordered adsorption sites. Here, the first such investigation is presented, reporting on the deposition of C_{60} molecules on the 2-fold surface of *d*-Al-Ni-Co. When dosed with the substrate held at elevated temperatures, the molecules are found to adsorb preferentially along the periodic direction, forming finite-sized quasiperiodically spaced chains. Chains appear to be dictated by a strong interaction between the molecule and the proposed adsorption sites.

8.2 Experimental Details

The *d*-$Al_{71.8}Ni_{14.8}Co_{13.4}$ quasicrystal was grown using the Czochralski method and cut along the 2-fold (10000) surface. *d*-Al-Ni-Co exists in several phases depending on the exact composition and temperature [58, 302]. The sample used in this study corresponds to the type I superstructure [62]. The surface was then polished with successively finer grades of diamond paste from 6 μm down to 0.25 μm, and cleaned in an ultrasonic methanol bath before being inserted into an ultra-high vacuum chamber with a base pressure of

$\sim 1 \times 10^{-11}$ mbar. The surface was prepared with 30-minute 2 keV Ar^+ sputter (drain current ~ 4 μA) and 2-hour 700°C anneal cycles measured with a pyrometer set to 0.35 emissivity. The surface was imaged using an Omicron VT-STM at room temperature, with continued sputter-anneal cycles until atomically flat terraces could be resolved with scanning tunneling microscopy (STM). STM bias voltage was typically -2 V, and tunneling current -0.2 nA, unless otherwise stated in the text. C_{60} was thermally evaporated from a Pyrex tube wound with a tungsten filament. The source and substrate temperatures during C_{60} growth were monitored via a thermocouple attached to the source and back of the sample. A substrate temperature during deposition of 250-300°C facilitated an ordered molecular overlayer.

8.3 Results and Discussion

8.3.1 Model Atomic Structure

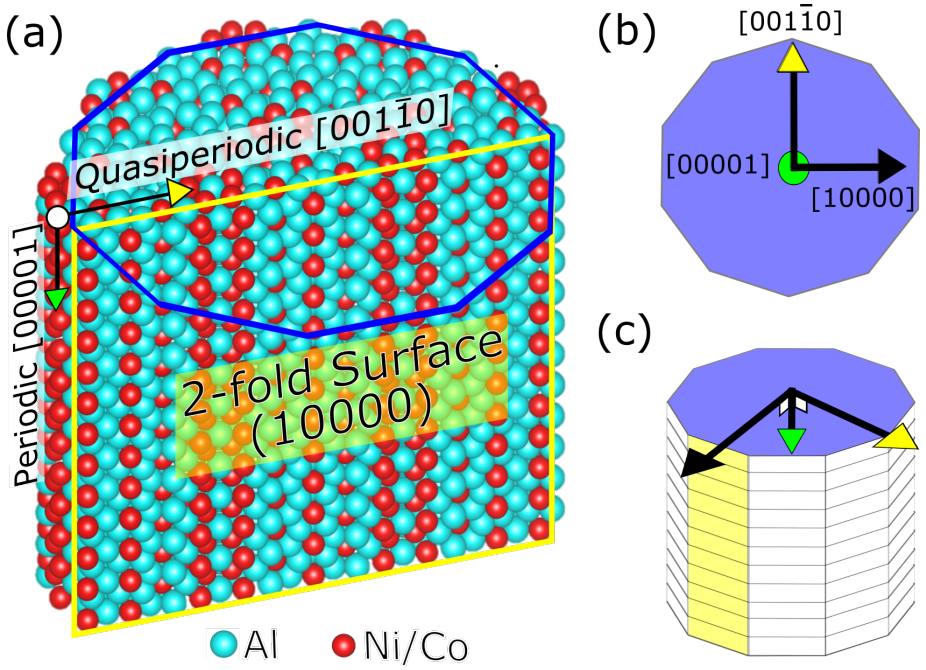

Figure 8.1: (a) The bulk structure model of the *d*-Al-Ni-Co quasicrystal [63, 64, 303], displaying the 10-fold (00001) (marked by a blue decagon) and 2-fold (10000) (marked by a yellow rectangle) planes. Periodic [00001] and quasiperiodic [001$\bar{1}$0] directions are indicated with arrows. Al atoms are coloured blue, and Ni/Co atoms coloured red. (b) Major periodic [00001] (green) and quasiperiodic [001$\bar{1}$0] (yellow), [10000] (black) directions are overlaid on the decagonal (10000) surface. The [001$\bar{1}$0] direction bisects the edge of two decagonal facets to form the (001$\bar{1}$0) facet. The [10000] direction produces the (10000) facet on each face of the decagon. Therefore, there are ten equivalent 2-fold facets for each direction. (c) Shows a 3D view of the decagonal crystal with coloured directions overlaid, with an example yellow (10000) surface orthogonal to the [10000] vector.

Figure 8.1 shows a bulk atomic model of the *d*-Al-Ni-Co crystal, where Al atoms are depicted by cyan spheres and Ni/Co atoms by red spheres [63, 64, 303]. The *d*-Al-Ni-Co crystal has 2-fold and 10-fold facets, with well-understood clean surfaces which have been studied by a variety of surface sensitive techniques [62, 68, 70, 71, 201, 304]. The periodic [00001] (green arrow head) and quasiperiodic [001$\bar{1}$0] (yellow arrow head) directions are shown in Figure 8.1. Orthogonal to the [00001] direction, 5-fold planes are alternately rotated by 36° in-plane and stacked, creating decagonal columnar clusters with an overall 10-fold symmetry in the [00001] direction. The periodic stacking of quasiperiodic atomic planes along the [00001] direction is 0.2 nm [58]. The resulting 10-fold quasiperiodic facet (blue outline) is shown in Figure 8.1. As a result of alternating 5-fold planes, two inequivalent 2-fold axes, (10000) and (001$\bar{1}$0), exist alternately at 18° perpendicular to the tenfold axis.

For this research, the (10000) surface, comprised of atoms from the periodically stacked [00001] direction, and the orthogonal quasiperiodic [001$\bar{1}$0] direction [62, 70, 303], was selected, also shown (yellow outline) in Figure 8.1. Therefore, this study provides the unique opportunity to study the influence of quasicrystallinity and crystallinity of the same material on the adsorption of C_{60}.

Figure 8.2(a) shows the model 10-fold *d*-Al-Ni-Co surface, with high density rows along the [001$\bar{1}$0] indicated with black lines. Indicated densely packed atomic planes in the model exhibit strong Bragg reflections and best support morphologically stable surface terminations [61]. 5-fold equivalence of the [001$\bar{1}$0] direction is observed in high density rows at 36° to one another as seen in Figure 8.2(a). This 5-fold equivalence of high density rows leads to ten equivalent (10000) and a different ten equivalent (001$\bar{1}$0) surfaces, rotated at 18° to one another with respect to the [00001] direction, as seen in Figure 8.1(b) and (c). In figure 8.2(a), perpendicular spacing between high density rows along [001$\bar{1}$0] are related by L = S×τ, with L = 0.75 nm and S = 0.47 nm, producing a section of a perfect Fibonacci sequence. High-density rows are determined with a similar procedure to the literature [61], identifying slices parallel to [001$\bar{1}$0] with a high concentration of atoms. Additionally, Al atoms at the centre of high-density slices also form a Fibonacci sequence of L and S, shown closer later. The yellow line corresponds to the (10000) surface outlined in yellow in Figure 8.1. Finally, the separation between high-symmetry decagonal cluster centres in the 10-fold (00001) plane is 1.978 nm.

Previous work determined that the (10000) surface can be considered as a bulk truncation through the centre of high-density planes, consisting of both Al and Ni/Co atoms, separated by step-terrace heights of L = 0.78 ± 0.03 nm and S = 0.47 ± 0.03 nm [61,65,71]. These step terrace heights correspond to perpendicular spacing between high density rows in Figure 8.2(a). Figure 8.2(b) illustrates an example of the atomic structure of one such plane in both side and top views. Atomic resolution is not reached with STM images,

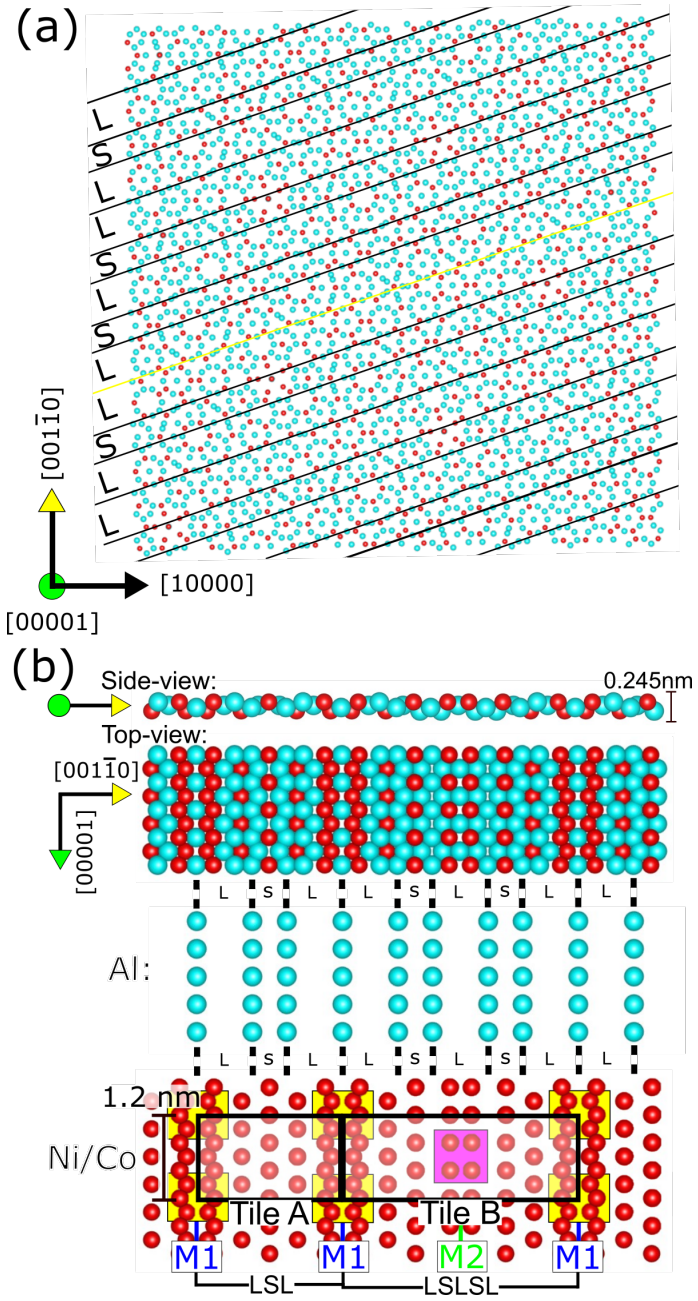

Figure 8.2: (a) The bulk structure model of the *d*-Al-Ni-Co 10-fold (00001) surface, with Al atoms in blue and Ni/Co atoms in red. High density atomic rows along one set of ten equivalent [00$\bar{1}$10] rows are indicated with black lines. The 2-fold (10000) surface terminates at these high density atomic rows, separated with terrace step heights related by L and S Fibonacci segments. The yellow plane indicates the surface corresponding to Figure 8.1. The three major directions are shown in the bottom left. (b) The atomic structure of the 2-fold (10000) surface. A 0.245 nm slice of the surface is selected at the centre of the high-density regions of the bulk. Al and Ni/Co atoms of the surface are shown separately. Al-atom columns are separated by short (S = 0.469 nm) and long (L = 0.750 nm) distances forming a Fibonacci sequence. M1 (blue) and M2 (green) indicate two different types of Ni/Co columns.

however, columns separated by τ-scaled segments are observed. For this reason, to improve clarity between the STM and model, only the centre slice of Al atoms (top view) which form an LSLLS ... Fibonacci sequence are shown in the middle of Figure 8.2(b). All Ni/Co atoms are shown in the bottom region of Figure 8.2(b). Due to the lack of atomic resolution, these Al atoms are essential for comparing STM features to the model. These columns of Al atoms in the model are separated by τ-scaled long (L = 0.759 nm) and short (S = 0.469 nm) distances, supported by experimental works [61, 65, 71].

As a tool to aid the discussion of C_{60} adsorption, the atomic surface structure is mapped using two rectangular tiles, Tile A and Tile B, shown in Figure 8.2(b). These tiles follow a Fibonacci sequence of long (L = 0.75 nm) and short (S = 0.47 nm) segments:

$$Tile\ A\ length = L + S + L = 1.97\ nm \tag{8.3.1}$$

$$Tile\ B\ length = L + S + L + S + L = 3.19\ nm\ (\tau \times Tile\ A) \tag{8.3.2}$$

Both tiles share a short edge of 1.2 nm in the periodic direction. The vertices of the tiles are decorated with squashed hexagonal motifs of Ni/Co atoms, labelled M1 motifs (yellow in Figure 8.2(b)). The vertices are located along high-density Ni/Co columns. M1 motifs repeat with a periodicity of 0.4 nm along the columns, enabling two motifs to fit along the short edge of a tile. Consequently, the tiling can be translated by 0.4 nm along M1 columns and still decorate a subset of M1 motifs. Additionally, M1 motifs include subsurface Ni/Co atoms (0.08 nm below the top layer; see Figure 8.2(b) side view). Next, the centre of Tile B contains a rectangular arrangement of Ni/Co atoms (purple in Figure 8.2(b)), termed M2 motifs. Unlike M1 motifs, M2 motifs consist solely of top-layer atoms. Tile B's structure is also overlaid on the Ni/Co model in Figure 8.2(b) and later correlated with C_{60} adsorption in Figure 8.9(b). The rationale for motif sites will be fully described later in the chapter.

8.3.2 Clean Surface

Our analysis begins by determining the step-terrace morphology of the clean surface (Figure 8.3). Terraces up to 20 nm in size in the $[001\bar{1}0]$ direction are typical for this surface with an anneal temperature of 650-700°C, with a high step-density. Terraces shown in Figure 8.3(a) and in 3D in Figure 8.3(b) are flat, disregarding adatoms. Note a tip effect causes some adatoms to appear 'T' shaped - indicated with blue marks in Figures 8.3(a) and (b). The line profile from A to I is shown in Figure 8.3(c) right, with the associated height histogram left. In addition to other step heights recorded on the clean surface, heights between sharp peaks can be separated into L = 0.8 ± 0.3 nm and S = 0.5 ± 0.3 nm segments. These values are in good agreement with the model separation between planes

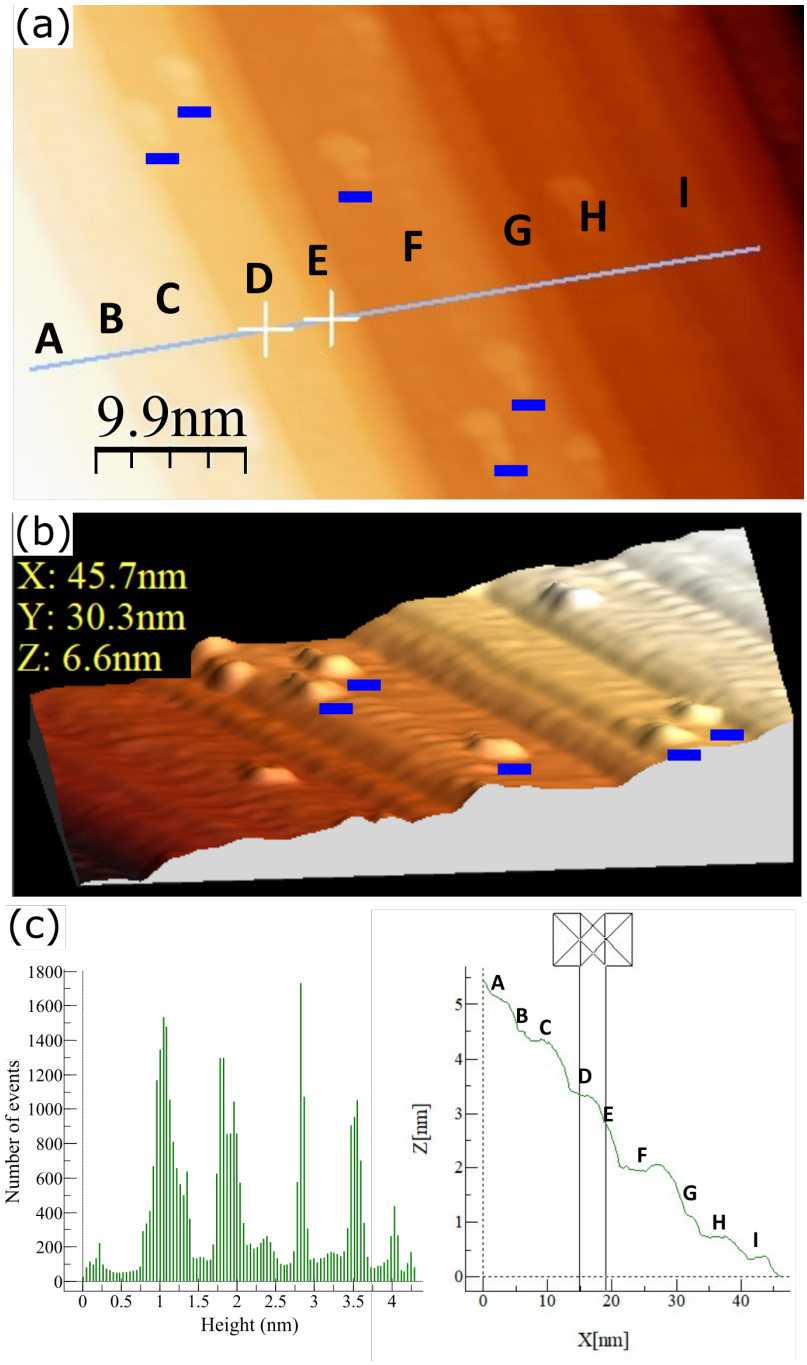

Figure 8.3: (a) A 32×52 nm STM image showing several flat terraces and step edges with height profile from A to I. Bias voltage = -2 V, and tunneling current = -0.248 nA. (b) The associated 3D image of (a). (c) Histogram and height profile from A to I.

of L = 0.75 nm and S = 0.47 nm. Peaks which have a larger full width half maximum are attributed to non-flat terraces. Flat terraces correspond to different high density atomic slices in the model (black lines Figure 8.2(a)). Step heights below 0.4 nm are attributed to inter-plane formations, caused by rapid quenching of the system post-anneal, or a low

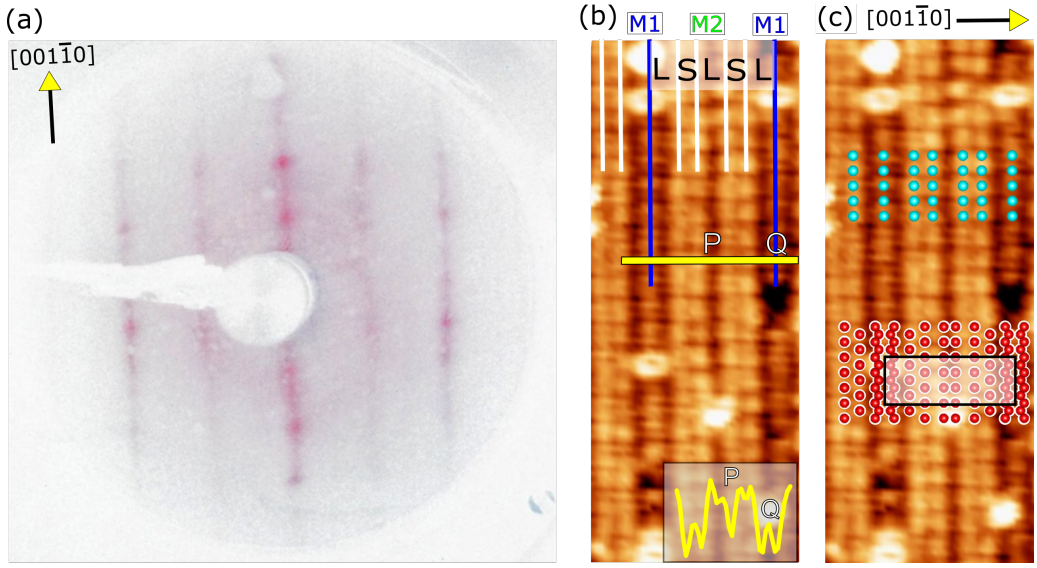

Figure 8.4: (a) A low energy electron diffraction image of the clean surface following several sputter-anneal preparation cycles. Dense Bragg peaks in the [001$\bar{1}$0] direction indicate long-range quasiperiodic order. (b) Magnified STM image of a clean section of the deposited surface, highlighting the substrate area and labelled columns M1 and M2. Bias voltage = -2 V, and tunneling current = -0.129 nA. (c) The same area as in (b), with Al and Ni/Co models overlaid.

anneal temperature, leading to step-edge defects and smaller terrace sizes. Overall, step-terrace morphology is in good agreement with the bulk model and the literature.

Long-range quasiperiodic order of the clean surface was demonstrated by low energy electron diffraction, as seen in Figure 8.4(a). A series of fringes represent a dense packing of atoms in the (yellow head) labelled [001$\bar{1}$0] direction. These densely packed atom fringes are orthogonally separated depending on the substrate periodicity. This result is in agreement with the literature, which identified columns of high density Bragg peaks in the [001$\bar{1}$0] and [10000] directions to be periodically separated by 0.4, 0.8, and 1.6 nm periodicity, or a multiple of these values [61, 70]. Upon deposition of C_{60}, shown later, a LEED pattern with resolvable diffraction peaks differing from the clean surface was not obtained. This is attributed to C_{60} adsorbing in columnar motifs on the surface, where molecules adsorb arbitrarily at periodically separated sites, leading to a diffraction pattern which has similar features to the clean surface. It may be possible to resolve C_{60} diffraction peaks with more dedicated LEED imaging in future work.

An enlarged STM image of a clean surface section of the surface is shown in Figure 8.4(b) and (c). Darker columns are indicated in blue, labelled M1, and lighter columns indicated in white, with a group labelled M2. These M1 and M2 columns relate to the model M1 and M2 shown in Figure 8.2. The decision for this labelling scheme is to aid C_{60} adsorption analysis, explained further later. L and S segments, aligned with the model

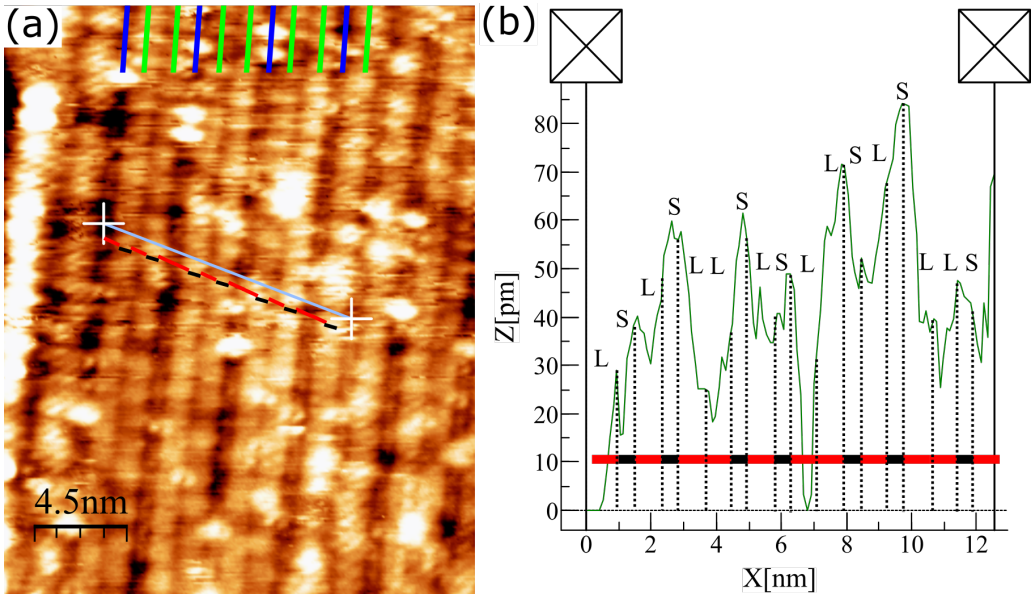

Figure 8.5: (a) An example STM image of the clean surface with quasiperiodically arranged dark (blue) and bright (green) indicated columns. Bright and dark columns are arranged in L (red) and S (black) segments, producing a Fibonacci sequence. Bias voltage = -2 V, and tunneling current = -0.129 nA. (b) The corresponding height profile for the line marked in light blue in (a). While atomic resolution is limited, dark and bright columns can be broken down into their respective L and S constituents. Dark columns are identified as LL segments, whereas bright columns as S segments. The brightness of columns is therefore attributed to a more densely packed convolved atomic signal.

separations, are labelled at the top, showing an LSLSL Fibonacci chain. Model Al atoms and Ni/Co of an LSLSL section corresponding to Figure 8.2(b) are overlaid corresponding to columns identified on the substrate in Figure 8.4(c). Therefore, columns observed with STM are attributed to Al atoms. The remaining model Al atoms in Figure 8.2(b) contribute to an inflated Fibonacci sequence, and are part of convolved signals of Al atoms, such as in the brighter columns observed later in Figure 8.9(b) (A model LSLSL section with all Al atoms is overlaid over these brighter columns). The model plane then explains why atoms in columns around the labelled M1 column appear darker than along M2 - due to a combination of topographical height (greater tunneling current along M2) and electronic contrast (lower density of Al along M1). These findings agree with our adsorption results, where C_{60} moleculaes appear brighter along M2 than M1, and previous STM studies of the clean surface [68, 71, 72]. Additionally, theoretical calculations [69] have demonstrated that the tunneling current in Al-based quasicrystals is predominantly contributed by the *s-p* electrons of Al atoms. As a result, Al atoms contribute more to the local density of states, and appear as brighter contrasts compared to Ni/Co atoms in the STM images.

As is typical of similar quasicrystalline systems, atomic resolution with STM of the clean surface is hard to achieve. The clean 2-fold surface has previously been investigated

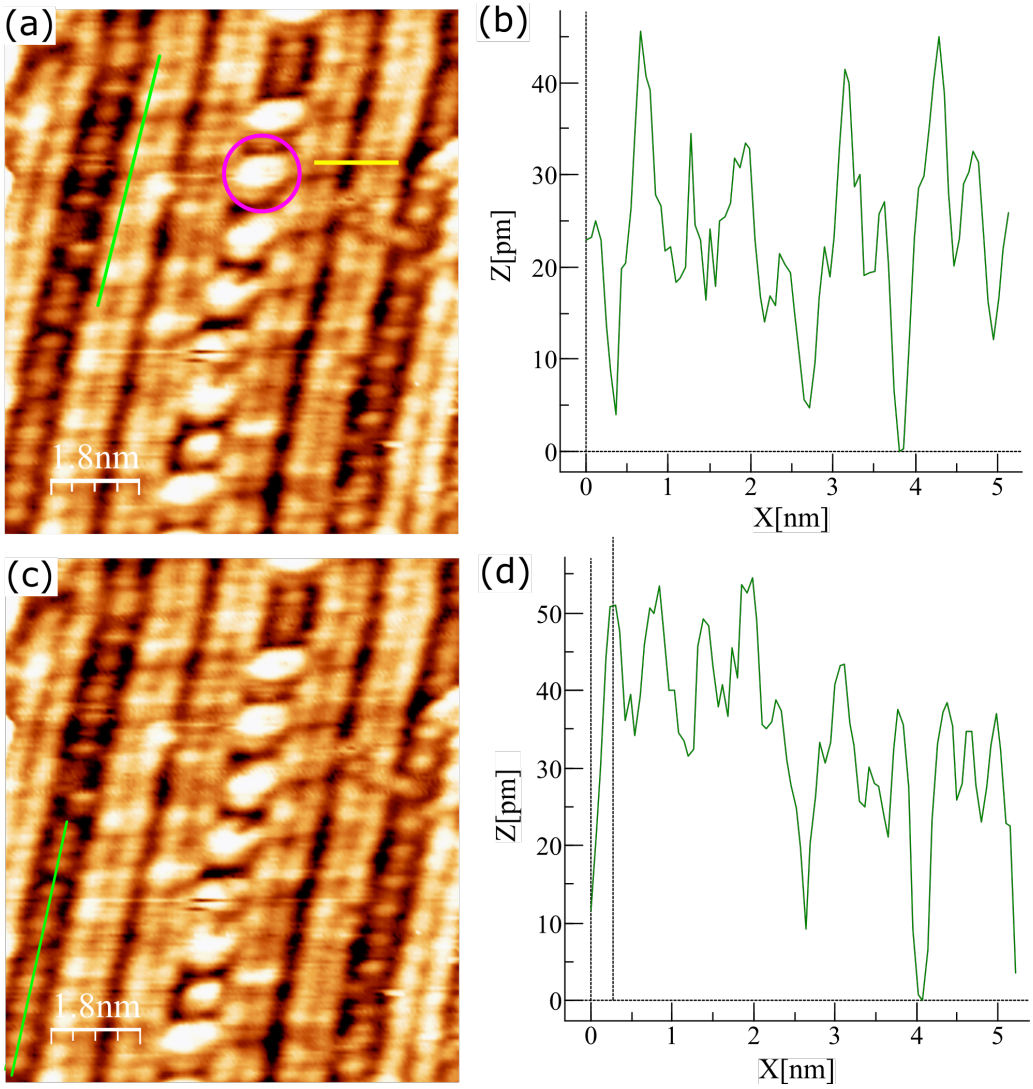

Figure 8.6: (a) and (c) STM images of a section of the clean surface with green height profile to analyse bright and dark column atomic separations, respectively. Bias voltage = -2 V, and tunneling current = -0.129 nA. (b) and (d) The corresponding height profiles for (a) and (c), respectively.

by several authors [68, 70–72]. τ scaled quasiperiodicity was found in the quasiperiodic directions, with the $[001\bar{1}0]$ direction scaled by L = 0.77 ± 0.03 nm and S = 0.47 ± 0.03 nm. Next, within the periodic direction, rows of atoms were found separated by 0.2 nm, with Al atoms separated by 0.4 nm, or multiples of these values, with larger separations attributed to surface reconstruction (doubling). These findings are in agreement with established *d*-Al-Ni-Co models [303]. Our aim is to identify parts of the surface which correspond to the model surface and to previous work, for use in analysis for C_{60} adsorption and modelling.

An example STM image (23 × 28 nm) of the clean surface produced by this research is shown in Figure 8.5(a). Quasiperiodically spaced columns are identified in the $[001\bar{1}0]$

direction. Overlaid coloured bars correspond to L (red) and S (black) segments identified in the height profile shown in Figure 8.5(b). Next, the STM surface is characterised by two types of columns: bright and dark, indicated by green and blue bars along the top of Figure 8.5(a). Despite a lack of atomic resolution, dark and bright columns can be easily distinguished and measured. By aligning the measured L (red) and S (black) segments of the line profile with the blue and green coloured bars, their local quasiperiodic order can be identified. A feature of bright columns are doublet peaks in line profiles such as in Figure 8.5(b), indicating two atoms in close-proximity whose tunneling signal convolve, making an accurate peak-peak measurement difficult. Instead, the width of bright columns is measured as 0.47 ± 0.05 nm, allocated to S segments (indicated in Figure 8.5(b)). Dark columns are typically more resolvable, with the centre to the edge of bright columns measured as 0.76 ± 0.05 nm, allocated to L segments indicated in Figure 8.5(b). Therefore, locally, blue coloured bars represent LL segments, and green coloured bars represent an S segment. The resulting sequence of L and S segments produces a Fibonacci sequence, characteristic of the quasiperiodic $[001\bar{1}0]$ direction.

Next, the spacing along the periodic [00001] direction is analysed in Figure 8.6. Figures 8.6(a) and (c) show a 10×9 nm section of the clean surface. Height profiles along the bright and dark columns are indicated with green lines. Figures 8.5(b) and (d) show the corresponding height profiles. Starting with the brighter column, the minimum width between peaks is 0.20 ± 0.05 nm, consistent with model separations. However, greater separations of 0.4 ± 0.1 nm and 0.6 ± 0.1 nm are also recorded. Similar separations have been recorded in the literature [68,70–72], and may be explained by surface reconstructions, vacancies, or a convolution of tunneling current from different features. Figure 8.6(d) shows the height profile measured in the dark column, with a typical separation between peaks of 0.4 ± 0.2 nm. The large uncertainty is due to a range of separations recorded between 0.2 - 0.6 nm. The range of recorded separations in the periodic direction of our STM images can be attributed to a few factors, such as a lack of atomic resolution, a low anneal temperature, drift, surface reconstruction or relaxation, or vacancies. However, it is still concluded that the surface has a [00001] periodicity consistent with the model bulk periodicity for both dark and bright columns.

Finally, there are larger and brighter spheres (purple circle) uniquely observed at the centre of Figures 8.6(a) and (c), following the periodic direction. As this is the clean surface, these spheres are not molecules, but raised atomic clusters. Note, as the surface is raster scanned horizontally, these raised features cause a tip effect to make some neighbouring atoms to appear brighter, such as indicated with the yellow bar in Figure 8.6(a). These raised features may be attributed to a raised atomic layer, or surface defects.

8.3.3 C_{60} Adsorption

In this section, STM images of the (10000) surface after deposition of C_{60} are presented. The distribution of C_{60} molecules is investigated, and an adsorption model is proposed. Most interestingly, the formation and modelling of anisotropic finite-sized C_{60} chains is described, with quasiperiodic tiles that map motif sites to the substrate. Firstly, it is shown that an elevated substrate temperature during deposition is required to form ordered columnar thin films of C_{60}. Experimental results show anisotropic adsorption sites, which combined the temperature dependence to create ordered thin films, the height differences of absorbed C_{60}, and the influence of local geometry, support the proposed adsorption model.

Temperature Dependence

Figure 8.7 shows a selection of STM images with deposited C_{60} at different coverages with a room temperature (RT) substrate in (a) and (b), and a raised substrate temperature of 250°C in (c) and (d). Coverage is determined by thresholding values above the flat surface until the substrate features were no longer visible. Bright circular features represent individual C_{60} molecules. Vertical columns correspond to substrate features previously identified on the clean surface.

Depositing at RT leads to molecules forming strong bonds on contact with the surface and not diffusing to a more energetically preferred site. As a result, many C_{60} molecules such as those indicated with black dots at 0.05 ML coverage in Figure 8.7(a) show no preference to a particular column. The remaining molecules at 0.05 ML coverage do, however, still adsorb atop darker columns - suggesting some preferential adsorption. At a higher coverage > 1.00 ML, molecular coverage is equally dispersed, however, columnar adsorption is clearly present, such as near light blue indicated lines.

In contrast, C_{60} molecules deposited on a raised substrate temperature of 250°C at all coverages results in templated anisotropic adsorption. These molecules preferentially position along substrate columns as displayed in Figure 8.7(c) and (d). Consequently, an elevated substrate temperature during adsorption is determined to help facilitate ordered adsorption. An ordered film is only found when the substrate is annealed between 250-300°C during deposition, a disordered film is produced at room temperature across all coverages. These findings are consistent with previous work [196, 222].

Analysis of Columnar Adsorption

Figure 8.8(a) shows an STM image at 0.20 ± 0.02 monolayer (ML) coverage (100×75 nm), and Figure 8.8(b) shows 0.65 ± 0.05 ML coverage in (45×65 nm). Both low and high coverage data suggest C_{60} molecules have templated anisotropic adsorption in the [00001]

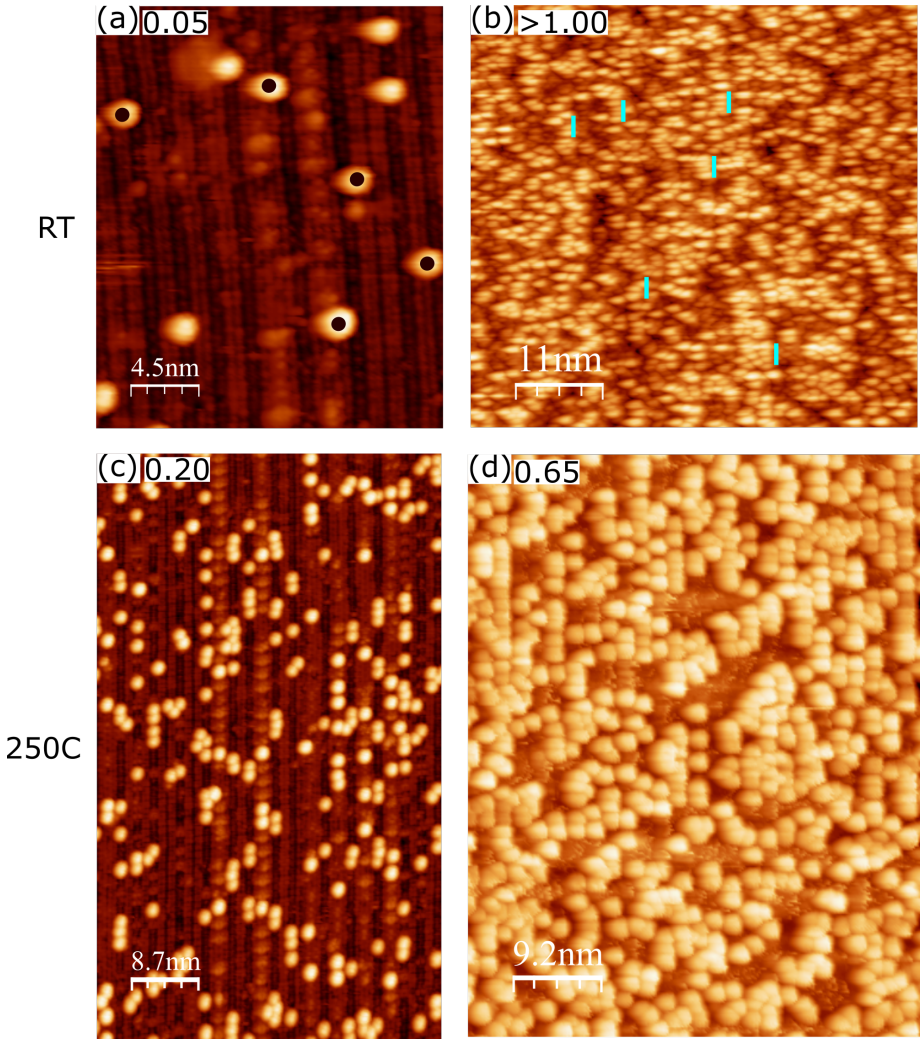

Figure 8.7: A selection of STM images with different C_{60} coverages prepared with the substrate at room temperature (RT) and at 250°C. Adsorption at RT results in a more scattered C_{60} distribution at low and high coverage, with some columnar adsorption such as indicated light blue lines. Adsorption with a substrate temperature of 250°C leads to more ordered anisotropic adsorption at both low and high coverage. Bias voltage = -2.1 V, and tunneling current = -0.268 nA.

direction, in quasiperiodically separated chains. Example chains are indicated in light blue in Figure 8.8(a).

To demonstrate site-specific adsorption, dark columns, previously labelled M1, are highlighted across Figure 8.9(a) with light blue lines. Separations between these columns have the same distance as Tiles A and B previously discussed, with Tile A = LSL (blue), and Tile B = $\tau\times$ A = LSLSL (red). These dark columns are essential for matching model substrate features to C_{60} motif sites. L and S separations in the $[001\bar{1}0]$ direction form a Fibonacci sequence across the substrate: within Figure 8.8(a), an unbroken Fibonacci sequence of 135 segments is observed, with the ratio of 84 L and 51 S close to τ, as expected

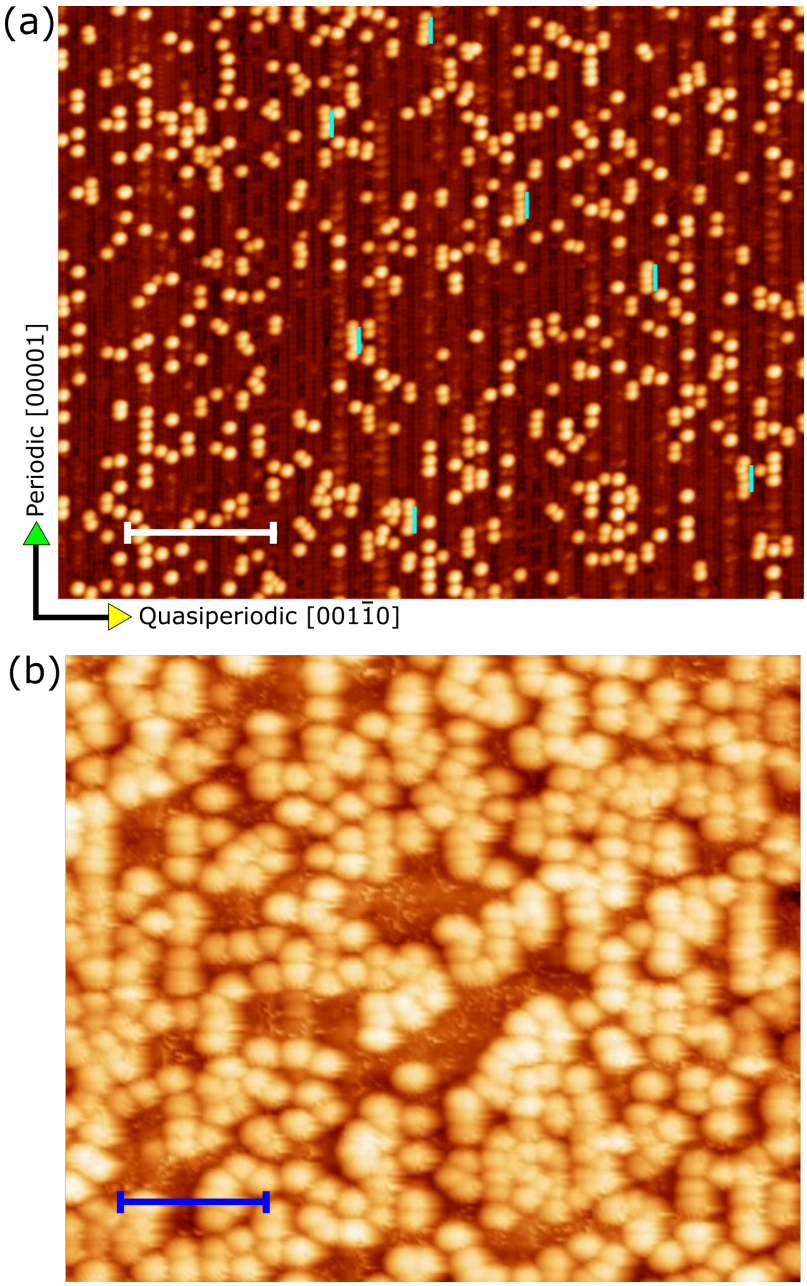

Figure 8.8: Two STM images of the 2-fold (10000) surface of*d*-Al-Ni-Co quasicrystal after deposition of C_{60} at two coverages. The quasiperiodic (yellow) and periodic (green) directions are indicated with arrows. Atomic columns form along the periodic [00001] direction. The atomic columns are separated by a Fibonacci sequence of short (S = 0.47 nm) and (L = 0.75 nm) segments. (a) Coverage is 0.2 ML with white scale bar = 20 nm. Bias voltage = -2.1 V, and tunneling current = -0.268 nA. (b) Coverage is 0.65 ML with blue scale bar 9.2 nm. Bias voltage = -1.7 V, and tunneling current = -0.122 nA.

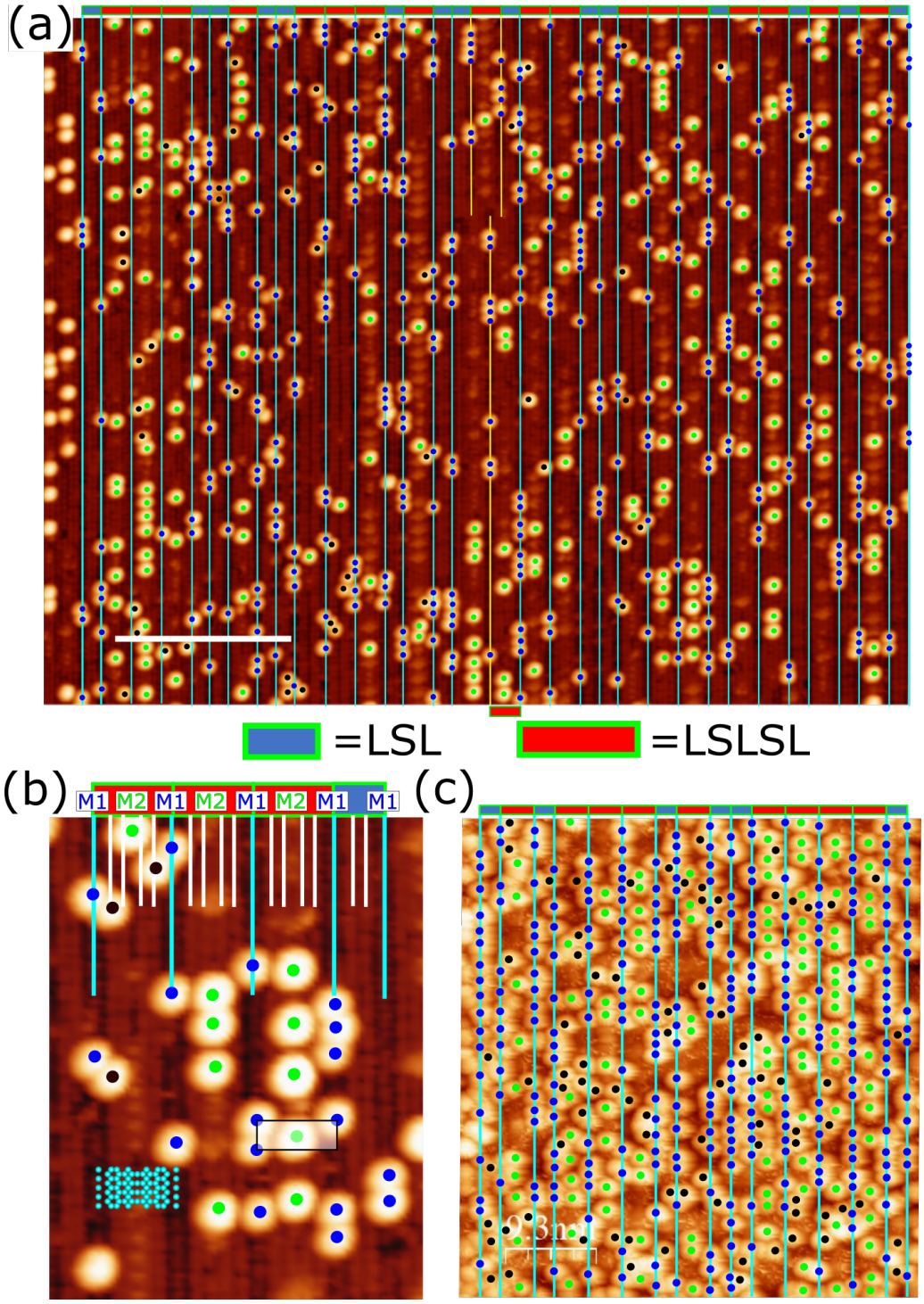

Figure 8.9: STM images with two different coverages: (a-b) 0.2 ML, and (c) 0.65 ML. Tiles A and B with lengths LSL and LSLSL respectively are placed between darker columns as a tool to model the surface. As a result, three distinct adsorption sites are identified: M1 (blue dots) along dark columns, M2 (green dots) along bright columns, and black sites (black dots) which adsorb elsewhere.

for a perfect Fibonacci sequence.

Overlaying the substrate model M1 and M2 columns on our data suggests that C_{60} molecules adsorb at three distinct sites marked in Figure 8.9(b): M1 columns (blue dots), M2 columns (green dots), and elsewhere termed black sites (black dots). Some C_{60} molecules on M1 columns form finite chains, separated by an average distance of 1.03 $\pm$ 0.06 nm, and a maximum observed chain length of five molecules (5.2 $\pm$ 0.2 nm) is observed. Similarly, C_{60} molecules on M2 columns also appear to form finite chains separated by 1.20 $\pm$ 0.04 nm, with a maximum observed chain length of three molecules (3.45 $\pm$ 0.2 nm). These chains are discussed in deeper detail later in this chapter. Finally, the molecules marked by black dots are typically adjacent to M1 molecules such that the distance between them is 1.00 $\pm$ 0.05 nm. Among the 611 C_{60} molecules observed in Figure 8.8(a), 63% are adsorbed atop M1, 28% atop M2, and 9% on black sites.

A similar anisotropic distribution of C_{60} molecules is observed at higher coverage in Figure 8.9(c). In the same procedure as for Figure 8.8(a), dark columns of the substrate are identified, and light blue lines are overlaid. Tiles A and B with LSL and LSLSL lengths can be perfectly placed between these dark columns, allowing us to model which site C_{60} molecules adsorb atop. Among 471 molecules observed in Figure 8.9(c), 59% are adsorbed atop M1, 24% atop M2, and 17% on black sites. The main difference between adsorption at higher coverage compared to low is an increase in the percentage of molecules which populate black sites. An explanation for the C_{60} adsorption frequency and distribution with an adsorption model will be given in a later section.

Finally, yellow indicated lines at the centre of Figure 8.9(a) are also M1 columns, but the top and bottom L and S sequence do not match. The top of yellow lines in Figure 8.9(a) represent two M1 columns, whereby an 'L[SL] LSL[SL] LSL' chain flips into a 'L[LS]LSL [LS]LSL' at the bottom yellow line, preserving total chain length and order. The latter 'LSLSL' is indicated with a red tile at the bottom of Figure 8.9(a). One possible explanation for this could be a phason flip, which causes two M1 columns to terminate into one M1 column. In quasicrystals, a phason flip or shift is produced by a translation of objects in $E_\perp$ and $E_\parallel$ in complementary space (see Figure 2.10 in Chapter 2), causing a local rearrangement of atoms that preserves quasiperiodic long-range order [305, 306].

Adsorption Model

Our experimental observations can be explained by the introduction of a C_{60} adsorption model which maps the frequency and distribution of molecules, their motif sites, the influence of local geometry, long-range order, height measurements, and high-temperature adsorption measurements.

The adsorption model is shown in Figure 8.10. Here, M1 absorbed molecules are marked in blue, M2 absorbed molecules marked in green, and molecules adsorbed elsewhere (black

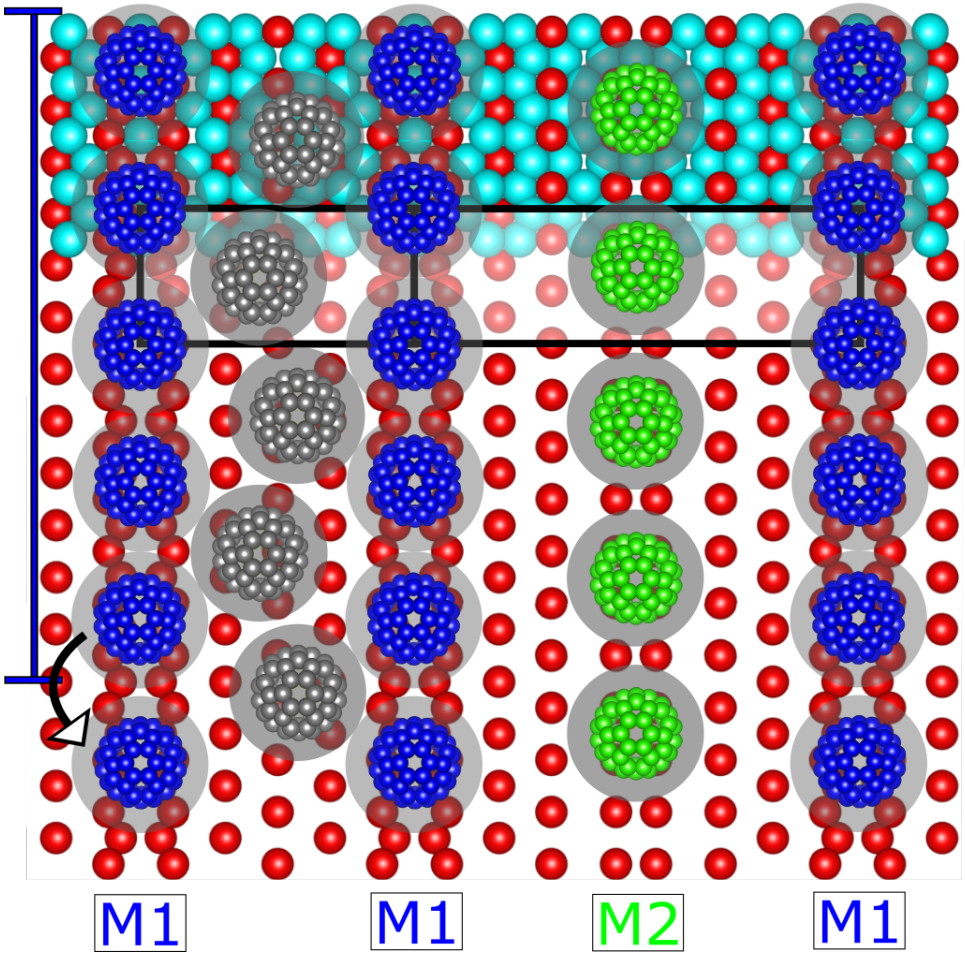

Figure 8.10: The model structure of the 2-fold *d*-Al-Ni-Co surface with C_{60} molecules decorated. The adsorption sites are extracted from STM images, whereby blue, green, and black C_{60} molecules represent molecules adsorbed at M1, M2, and elsewhere (black sites). Shaded circles indicate the Van der Waals diameter of the molecules. The top rows include both Al (cyan) and Ni/Co (red) atoms and the remaining rows show only Ni/Co atoms. Tiles A and B (black outline) from Figure 8.2(b) are placed such that M1 molecules are placed at the vertices and M2 molecules at the centre of Tile B.

sites) marked in black. The shaded circle around each molecule is set to the Van der Waals radius of C_{60} = 1.00 nm [195,307,308]. The adsorption model is consistent with our experimental STM data.

The expected coverage frequency of a single monolayer of C_{60} at each adsorption site can be calculated by generating an extended model (single layer, 26.3 nm × 29 nm) of Figure 8.10, including M1 (blue), M2 (green), and the remaining (black) sites, with 513 molecules. In this model, molecules are placed with no overlap: starting with occupying the M1 and M2 motifs first, then black sites which populate at least after M1 motifs are occupied. The model frequencies are: M1 = 54.6%, M2 = 24.4%, and black sites = 21%. The model distribution supports our experimental observations at 0.2 ML coverage (M1

= 63%, M2 = 28%, black = 9%), with a similar $\frac{M1_{Model}}{M2_{Model}} = 2.25$ and $\frac{M1_{0.2Exp}}{M2_{0.2Exp}} = 2.24$. The lower proportion of black sites observed at 0.2 ML coverage supports a stepwise adsorption at black sites after M1 motifs populate. The coverage of the model is further supported by comparing the experimental observations at 0.65 ML (M1 = 59%, M2 = 24%, and black = 17%) and $\frac{M1_{0.65Exp}}{M2_{0.65Exp}} = 2.25$. Between the model low and high coverage, the ratio $\frac{M1}{M2}$ remains constant. The most significant change in distribution as coverage tends from 0 to 1 ML is the increase in occupation of black sites. As previously explained, at equilibrium, molecules atop black sites are not preferred at low coverage, and only occupy sites in contact with already C_{60} occupied M1 or M2 motifs. As coverage increases, the number of available M1 and M2 motifs reduces, increasing the proportion of available black sites. The adsorption model therefore agrees with experimental observations at low to high C_{60} coverage.

Motif Sites and Influence of Local Geometry

The influence of local geometry is now introduced to describe most-favoured motif sites for C_{60} at equilibrium. Tiles A and B from earlier in the chapter are shown again in Figure 8.11(a). The squashed hexagons of Ni/Co atoms previously chosen for the vertices of Tiles A and B, are now revealed to act as the most-favoured site for the M1 motif. The hexagonal face of C_{60} is oriented in contact with the M1 motif, as in Figure 8.11(b). Next, the rectangle of Ni/Co atoms at the centre of Tile B, indicated purple in Figure 8.11(a), represents the M2 motif. Tiles and their vertices are important for describing the nature of finite chains discussed in the next section.

Figure 8.11(b) shows the proposed motif sites for C_{60} atop M1 and M2, with contact C atoms placed atop the best-matching surface Ni/Co atoms. Hybridisation of C atoms with the surface may be *s-p* or *s-p-d*, in relation to the fact that surface electronic density imaged by STM comes from Al atoms [222]. Further investigations varying the bias voltage between the STM tip and the surface are required to be more certain of how the C atoms bind with the surface atoms. In addition, obtaining molecular resolution STM images and DFT calculations would strongly improve the confidence of the proposed adsorption sites. Local symmetry and dimensions of M1 and M2 motif sites match those of C_{60} molecules. For example, the distances between Ni/Co atoms in M1 motifs (a = 0.289 nm and b = 0.241 nm) are close to the nearest-neighbour distances of C atoms in the hexagonal faces of C_{60} (A = 0.3 nm and B = 0.239 nm). Similarly, at M2 motifs, the Ni/Co - Ni/Co distances (c = 0.287 nm and d = 0.4 nm) match the second-nearest neighbour distances of C atoms in the hexagonal face of C_{60} (C = 0.3 nm and D = 0.466 nm). Both M1 and M2 motif sites occur every 0.4 nm in the periodic direction.

Despite motif sites occurring with the same periodicity, experimental observations at lower coverage show that adsorbed molecules are rarely exactly side-by-side, as seen earlier

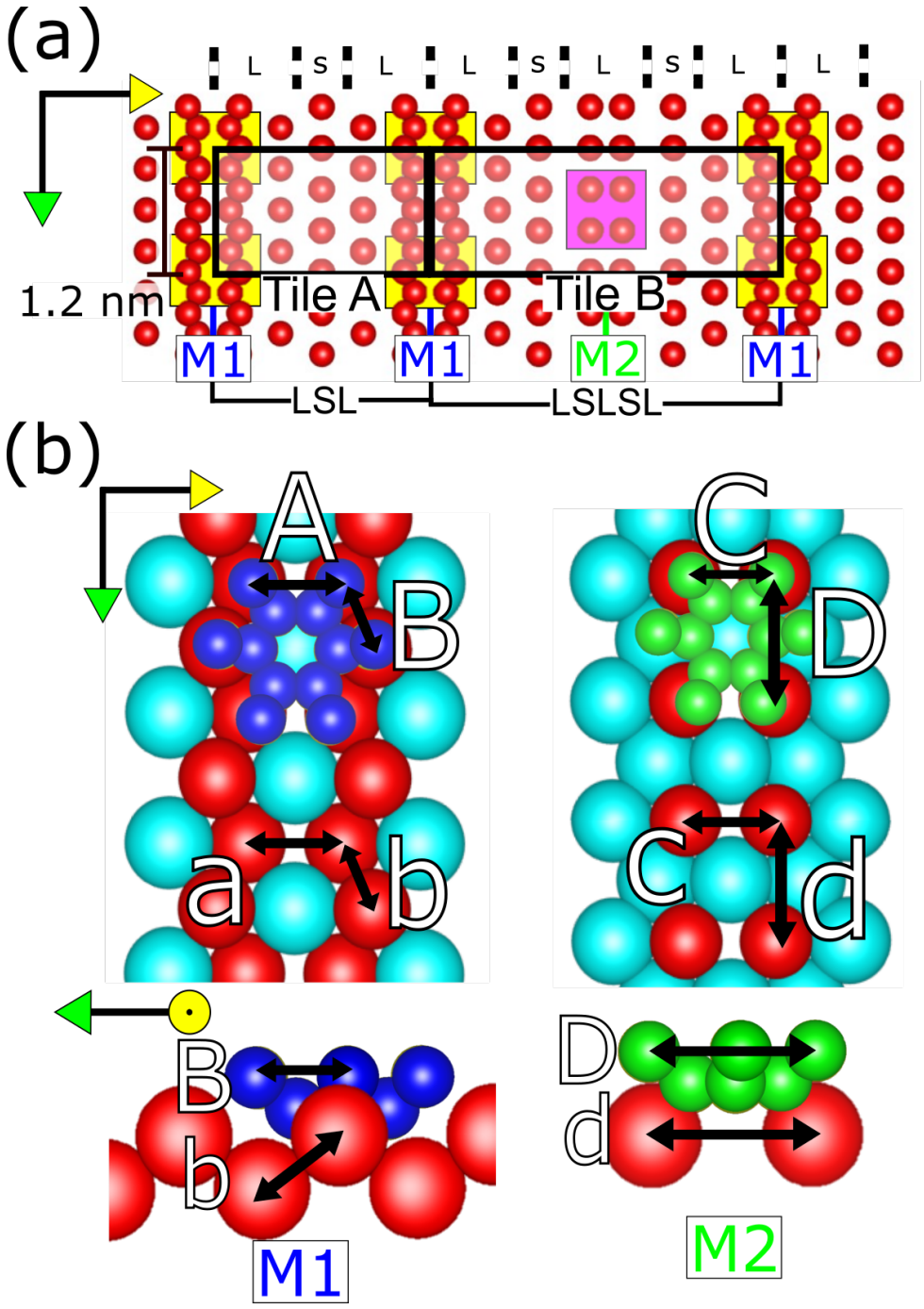

Figure 8.11: (a) A Ni/Co only section of the model previously shown in Figure 8.2(b). (b) A magnified view of the symmetrically parallel orientation of C_{60} molecules with the substrate Ni/Co atoms, at both the M1 and M2 motifs. Side-views are shown at the bottom. Distances between substrate atoms (a, b, c, and d), and C-C atom distances in C_{60} (A, B, C, and D) are marked.

in Figure 8.9(a). This behaviour can be explained by mobility of the substrate atoms and C_{60} atoms at room temperature, STM tip effects including drift, and a low C_{60} coverage.

By turning our attention to higher coverage data in Figure 8.9 it may be convinced that many M1 and M2 adsorbed molecules are side-by-side.

8.3.4 C_{60} Height Difference

There is a height difference observed such that C_{60} molecules atop M1 columns consistently appear 0.1 - 0.2 nm lower than those atop M2 columns. The height change is illustrated in an STM image of C_{60} molecules adsorbed on M1 and M2 motifs, along with the corresponding height profile, shown in Figure 8.12(a). Next, height difference is more thoroughly quantified on a larger scale by measuring the height difference of C_{60} molecules in Figure 8.8(a). Due to a large flat terrace, it is trivial to threshold above the surface, as shown in Figure 8.13. Figure 8.13(a) shows features 0.65 nm above the surface, with 0.041 ML coverage. At this threshold, all molecules atop M1 and M2 are observed to be visible, consistent with the expected height of C_{60} in the literature of $\approx$ 0.7 nm [307]. Most importantly, on average, molecules atop M1 (light blue lines) have a slightly smaller visible surface area at this threshold than those atop M2 (centre between light blue lines). Figure 8.13(b) shows features 0.75 nm above the surface, with a smaller 0.009 ML coverage. Firstly, fewer total molecules are observed at 0.75 nm compared to at 0.65 nm. Additionally, as expected with Gaussian-like peaks, the molecules at a 0.75 nm appear comparatively smaller. The most interesting feature is the location of C_{60} molecules - almost all of which are aligned atop M2 columns located at the centre between blue lines.

Figure 8.14 shows a histogram with observed heights against number of events for molecules observed in Figure 8.8(a). Number of events weakly peak around a height of 0.62 nm, which can be attributed to a combination of both M1 and M2 adsorbed molecules. Beyond 0.62 nm, there is a steep drop-off of events until around 0.77 nm with a small plateau before events drop to 0. These results reinforce the findings of Figure 8.13, as there are two height thresholds relating the more numerous M1 molecules at a lower observed height ($\approx$ 0.62 nm) than those at M2 ($\approx$ 0.77 nm).

The height difference between C_{60} molecules absorbed atop M1 and M2 columns arises from both the physical topography of the substrate and differences in electronic interactions between C_{60} and Ni/Co atoms. A minor contribution from topological substrate height can be seen in Figure 8.12(b) with the purple and yellow line profiles. The height difference between PQ is $\approx$ 0.05 nm, small enough to be within a measurement error interval, but is nevertheless still consistent with the model surface height difference. The much larger height difference between RS cannot be fully attributed to the substrate topology, but instead is mainly attributed to electriconic substrate-molecule characteristics. The model overlay is previously shown in Figure 8.2(b), exhibiting twice the concentration of Ni/Co atoms along M1 compared to M2. The extra contribution is provided by subsurface Ni/Co atoms only present along M1. There is a 0.08 nm height difference of these subsurface

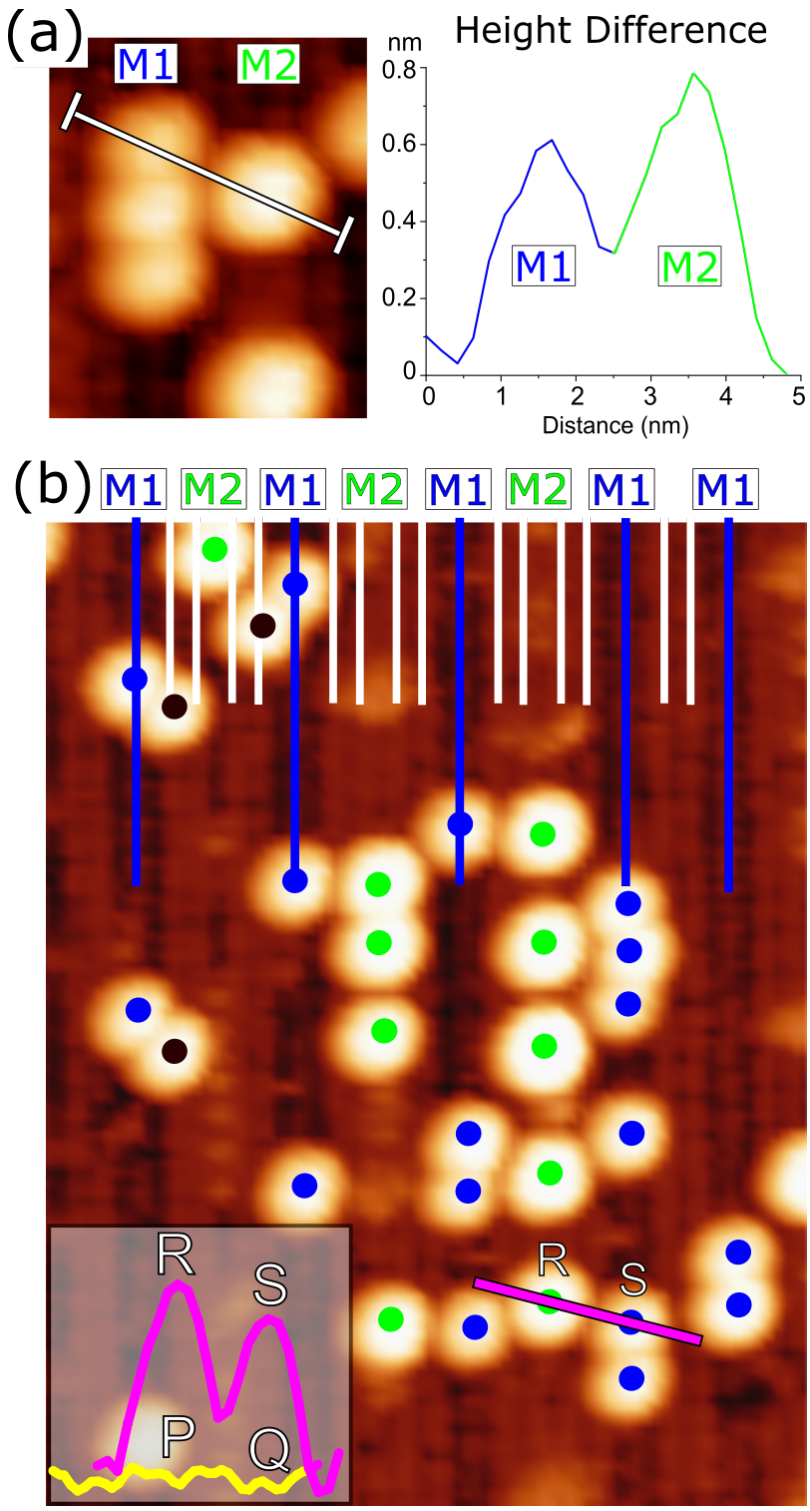

Figure 8.12: (a) An STM image showing the typical observed height difference between molecules atop M1 and M2. Observed height difference is attributed to topological substrate height and electronic characteristics.

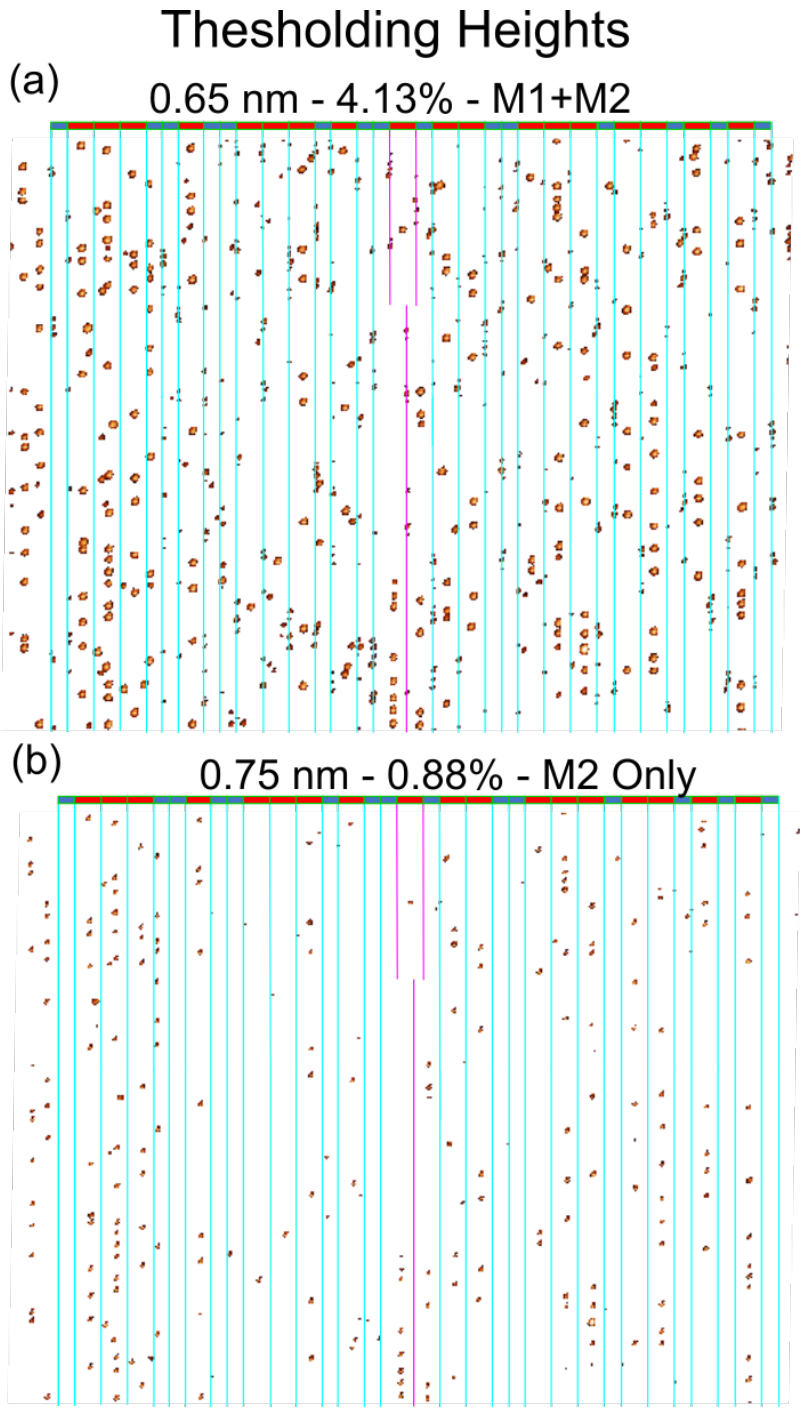

Figure 8.13: Features of Figure 8.8(a) observed at two height thresholds: (a) 0.65 nm, and (b) 0.75 nm. Coverage at this height suggests molecules atop M1 (light blue lines) are consistently lower than those atop M2 (centre between blue lines).

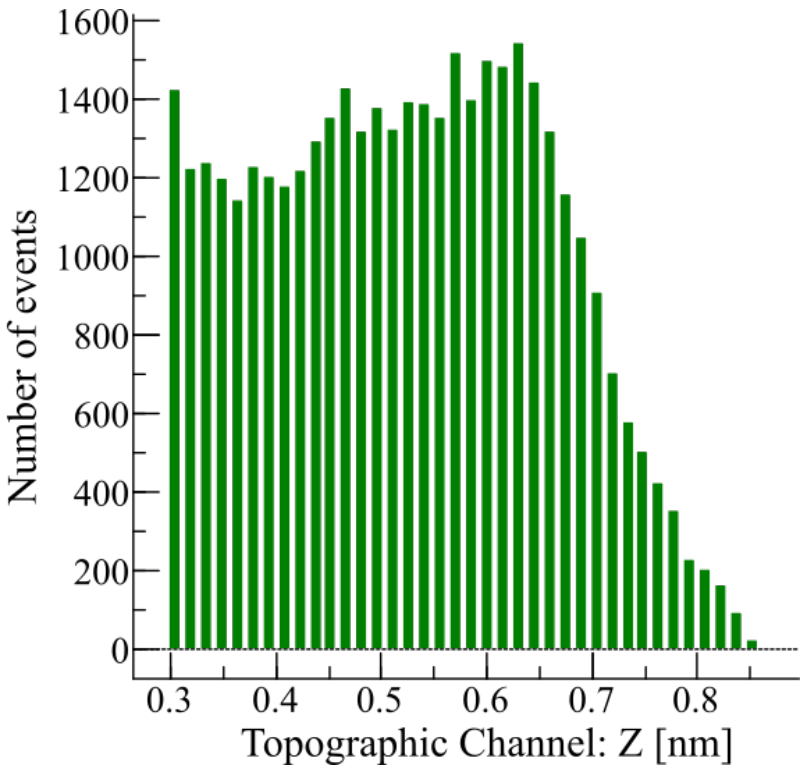

Figure 8.14: A histogram of observed heights for events measured in Figure 8.8(a). The distribution suggests a majority of events weakly peak around 0.62 nm (M1+M2), and then again around 0.77 nm (M2 - only).

Ni/Co atoms relative to the topmost layer. These subsurface Ni/Co atoms act as additional electron donors, bonding and pulling the C_{60} molecule closer, increasing the strength of the bond between the C_{60} molecule and substrate. A stronger covalently bonded C_{60} molecule will consequently appear dimmer due to a lower tunneling current between the surface and STM tip. M1 motif sites must therefore be rich in Ni/Co electron donors interacting with adsorbed C_{60} molecules. A combination of these factors leads to C_{60} molecules appearing darker when absorbed along M1, compared to M2, as seen with STM observations.

The explanation of observed C_{60} height difference is supported by the substrate requiring elevated temperatures during deposition. While subsurface atoms along M1 columns are not readily accessible at room temperature, annealing the substrate lowers the energy barrier, facilitating bonding with Ni/Co. M2 columns are less rich in Ni/Co donors but still facilitate a high Ni/Co density at M2 motif sites for a strong C_{60} - substrate interaction.

8.3.5 Finite-Chain Observations and Analysis

At medium to high coverage, chains of C_{60} molecules can be identified, within which molecules are observed at close proximity ($\approx$ 1.00 nm) to one another. Given the C_{60} Van der Waals separation of C_{60} is $\approx$ 1.00 nm, it is likely these molecules within chains have

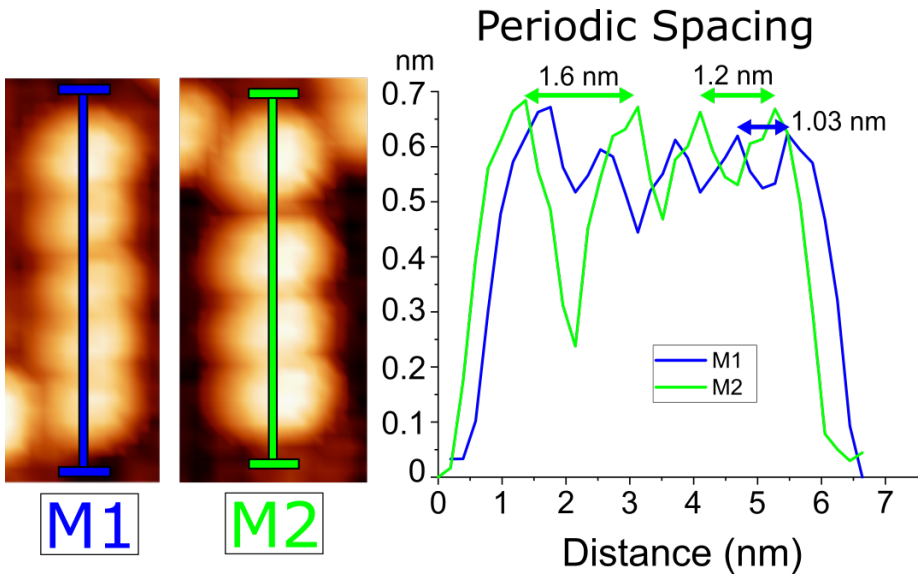

Figure 8.15: (Left) STM images showing example chains of molecules adsorbed at M1 and M2 motifs, coloured blue and green, respectively. (Right) Height profiles corresponding to blue and green lines marked on the STM images. Typical spacing between M1 is around 1.03 nm, whereas spacing between M2 molecules is larger at around 1.20 and 1.60 nm.

weak interacting bonds with each other [195, 307, 308]. In this section, the experimental evidence of these chains is shown, and provide models which describe the chains position, anisotropy, and finite nature.

Experimental Observations

Two sets of finite chains with different inter-molecular separations are observed, one set atop M1 and the other atop M2. The vertices of Tiles A and B skew to accommodate molecules within M1 and M2 chains, with up to 0.4 nm shifted centres from the M1 motif. The up to 0.4 nm shift allows for chains to be centred around any M1 motif, agreeing with STM observations. C_{60} molecules in chains therefore have competition between molecule - substrate and molecule - molecule interactions for their most-favoured adsorption sites.

Typical spacing between C_{60} molecules on M1 and M2 columns is shown in the line profiles in Figure 8.15, with STM images of the example chains produced at M1 and M2. Most importantly, spacing along M1 is close to the C_{60} Van der Waals separation, whereas spacing along M2 is slightly greater, suggesting different molecule - substrate interactions between these columns. For completeness, C_{60} molecules absorbed atop black sites are in close contact with M1 absorbed molecules, having a C_{60} - C_{60} separation similar to the Van der Waals radius of C_{60} [309].

Figure 8.16(a-c) shows histograms of C_{60} centre-centre separations in chains observed in Figure 8.8(a). The majority of chains are found to populate the M1 column, with 118 molecules, compared to 30 in M2 and at black sites. The favour of M1 motifs can be

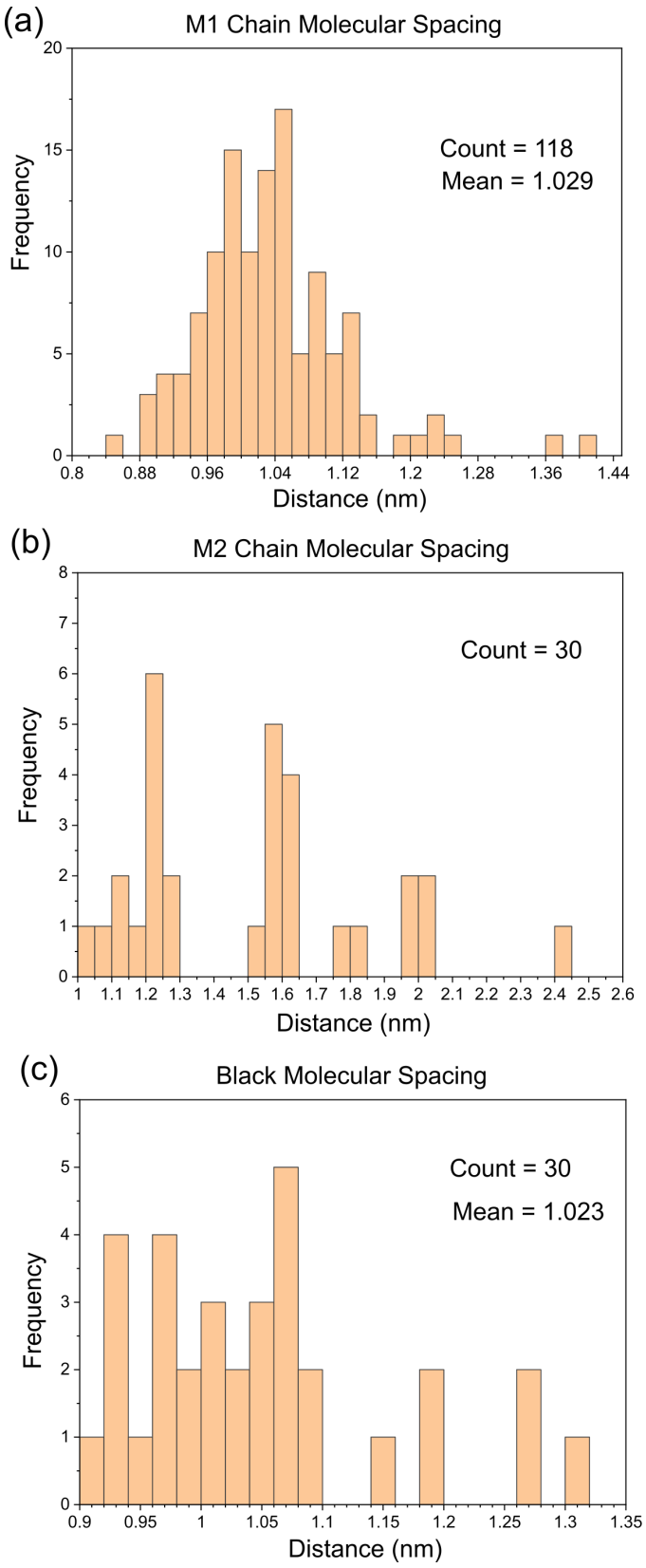

Figure 8.16: Histogram chain separations for C_{60} molecules observed in Figure 8.8(a). Histograms show separations chains atop: (a) M1, (b) M2, and (c) at black sites.

explained in two parts: a greater number of available M1 sites compared to M2, and that M1 adsorption is more electronically favoured compared to M2. There are more available M1 sites than M2 because of a higher frequency of M1 columns, for example, a 10:5 ratio of M1:M2 columns in our 26.3 nm x 29 nm adsorption model. The latter conclusion will be discussed further with our adsorption model in a later section.

In Figure 8.16(a) there are 120 separations listed, but the highest two separations greater than 1.36 nm are dismissed as anomalous. The estimated mean separation across M1 is 1.03 ± 0.06 nm, close to the Van der Waals separation of C_{60}. It therefore determined that chains adsorbed atop M1 have both molecule - substrate and molecule - molecule interactions, which force anisotropic adsorption.

At M2, molecule separations to not show one consistent value, but instead tend to populate around 0.2 or 0.4 nm multiples beginning with 1.2 nm. Though the count frequency is low, the majority (67%) of observed separations at M2 exist 1.2, 1.6, and 2.0 ± 0.05 nm apart. This in turn suggests that molecules atop M2 are more dominated by stronger molecule-substrate interactions which pull them to specific spaced motif sites.

Finally, chains were previously stated to only exist across M1 and M2, not black sites. The reason for close separations of black molecules is that these tend to adsorb in contact with M1 or M2 molecules after those molecules find their motif sites, and there is competition between too many C_{60} molecules chasing too few motif sites. This, along with our adsorption model, explains why molecules atop black sites are more populous at higher coverages. Molecular separation at black sites is found to be 1.0 ± 0.1 nm, close to the Van der Waals separation of C_{60}.

Molecular Chain Model

This section describes, within the adsorption model, the finite anisotropic nature of C_{60} molecules observed in chains at both low and high coverage. This begins by modelling chains along M1, and then move to M2 chains.

Firstly, finite chains along M1 can be explained by a compounded translational mismatch, caused by very strong substrate - C_{60} bonding, and supported by C_{60} - C_{60} interactions. This statement is justified by how observed C_{60} - C_{60} separation within chains along M1 of 1.03 nm is close to the C_{60} Van der Waals separation of ≈ 1.00 nm [195, 307, 308], suggesting these molecules are bonded with each other. To explain finite length of C_{60} chains, a model chain is proposed, illustrated in Figure 8.17, with Tile A and B motif colours matching Figure 8.11. Figure 8.17(a) shows the M1 chain begins with a molecule where six C atoms are aligned with the M1 motif, corresponding to the hexagon of Ni/Co atoms (marked as the centre). Additional C_{60} molecules are bidirectionally added along the periodic direction along the column, with yellow squares overhead corresponding to the vertices of Tiles A or B.

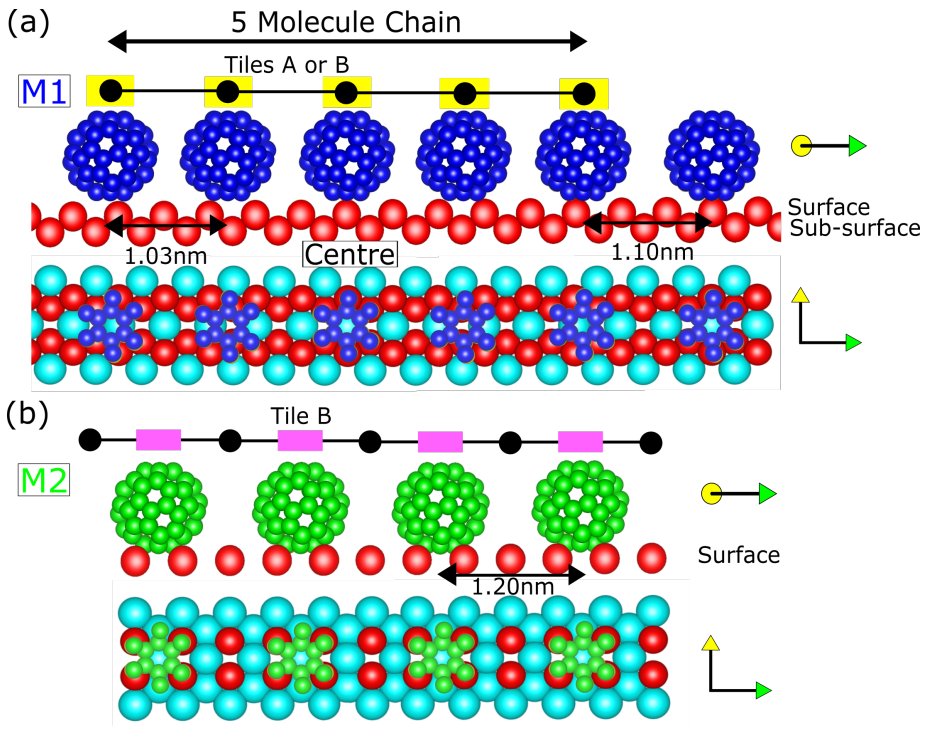

Figure 8.17: A model chain of C_{60} molecules at the (a) M1 (blue), and (b) M2 (green) sites are shown in side- and top-view. The distance between M1 molecules in chains is 1.03±0.06 nm, determined from STM data, which is close to the Van der Waals separation between molecules. Chains of up to five molecules are observed with STM. The next molecule in the chain (top right blue) shifts to the next most favourable M1 state away from the Van der Waals separation. Only the contact C atoms with the surface Ni/Co are shown in the top-view.

Tiles A or B stretch to accommodate C_{60} molecules away from M1 motifs within molecular chains. Previously, the distance between C_{60} molecule centres was set to the exact value determined from STM measurements (1.03 nm). Given the minimum Van der Waals separation of ≈ 1.00 nm and standard M1 motif spacing of 0.40 nm, if there was negligible C_{60} - C_{60} interactions, the expected minimum separation between two C_{60} is 1.20 nm (the sepration between M1 motifs). As the determined separation is 1.03 nm, the mismatch between the first site is $\delta = 1.20 - 1.03 = 0.17\ nm$. As the chain grows, the C atoms in subsequent molecules gradually displace further out of alignment with the M1 motif, until a critical displacement length Δ_{Crit} is reached, where the hexagonal face of C_{60} no longer matches the M1 motif hexagonal. Here, Δ_{Crit} corresponds to half the available M1 motif separation between the vertices of Tile A and B, $\Delta_{Crit} = \frac{1.20}{2} = 0.60\ nm$. If the chain is displaced by greater than 0.60 nm then the next molecule grown has too weak an interaction with the substrate and prefers to shift away from the chain and to the next available M1 motif site. With this information, it is possible to predict the number of molecules in a chain with a cumulative displacement equation that models the mismatch

between number of molecules n, δ, and Δ_{Crit}:

$$n_{crit} = \frac{\Delta_{Crit}}{\delta} = \frac{0.60\ nm}{0.17\ nm} \approx 3\ molecules \tag{8.3.3}$$

Therefore, our model predicts that bidirectionally only three molecules may grow along a chain, with a total chain length of five molecules (assuming the centre molecule is centred on an M1 motif site). The total critical length of a chain of C_{60} molecules along M1 is also 4.12 nm (1.03 nm $\times$ 4).

Experimentally, the critical length is also determined to be equal to five molecules, with centre-centre length of 4.12 $\pm$ 0.15 nm, derived from STM data (some chains indicated by blue lines in Figure 8.8(a)). Chains of up to five molecules are also observed in the high-coverage data (Figure 8.9(c)). No chain longer than five molecules with the minimum separation is observed at any coverage. The observed critical length of five molecules agrees with the determined n_{Crit} growing bidirectionally from a molecule centred on an M1 motif site. Once the chain reaches this critical length, the next molecule is dominated by molecule-substrate interactions, rather than C_{60}-C_{60} Van der Waals forces. These interactions pull the molecule to the next M1 motif site with a separation from the chain of 1.10 $\pm$ 0.05 nm, represented by the rightmost blue molecule in Figure 8.17. The critical threshold arises due to the cumulative translational displacement between the molecules and the substrate. Overall, interacting chains of C_{60} along M1 are bound to a finite length.

Turning to the M2 columns, close C_{60} - C_{60} absorbed on M2 motifs and black sites can also be explained in terms of the local geometry and electronic bonding. The molecular separation along M2 closely matches the separation between the centres of tile B (= 1.2 nm), coloured pink in Figure 8.11(a). This can be explained by the density of Ni/Co atoms only being sufficient at M2 motifs to facilitate equilibrium C_{60} adsorption. Without a contribution of subsurface Ni/Co between M2 motifs (that are found along M1), substrate - C_{60} bonding at M2 motifs dominate. This in turn leads to C_{60} absorbed along M2 to primarily reside atop the M2 motif. Molecules of C_{60} absorbed along M2 are therefore determined to be dominated by substrate - C_{60} interactions.

The only examples of dominating C_{60} - C_{60} interactions occur at the black sites (Figure 8.9), that are bonded to primarily M1 molecules via Van der Waals interactions. The adsorption behaviour of black site molecules can be explained by C_{60} existing in a metastable environment without a high-density Ni/Co motif, but still sufficiently satisfied to bond with both C_{60} and any substrate Ni/Co atoms. If the black site C_{60}-C_{60} interaction was as strong as the substrate interaction, longer chains would be expected to be seen.

8.4 Conclusions

The growth of C_{60} molecules on the 2-fold surface of a decagonal Al-Ni-Co quasicrystal was presented, studied using scanning tunneling microscopy (STM). This surface features both periodic and quasiperiodic directions. C_{60} is found to preferentially grow along the periodic direction, forming chains of C_{60} molecules separated by a Fibonacci sequence. The C_{60} molecules adsorb on Ni/Co sites, where the symmetry of these sites closely matches that of the hexagonal faces of C_{60}. Additionally, the separation of Ni/Co atoms was comparable to the C-C distance in the hexagonal face of C_{60}. The growth of these chains was governed by two competing interactions: substrate-molecule interactions and molecule-molecule Van der Waals forces, resulting in chains of finite length. This work highlights the role of quasicrystalline surfaces in directing molecular assembly, offering insights into the design of nanostructures and advancements in molecular electronics.

Chapter 9

Conclusions and Future Work

The aim of this thesis was to fabricate multiscale quasiperiodic architectures as a new avenue for investigating their electronic and magnetic properties, for potential applications. The work addressed the fundamental challenge of controlled fabrication of quasiperiodic nanostructures, through two complementary methods: nano-lithographed artificial spin-ice (ASI) quasiperiodic tilings, and templated atomic-scale molecular growth on a quasicrystal surface.

The development of thermal-scanning probe lithography (t-SPL) into an established nanofabrication technique for quasiperiodic tilings was key to results in Chapters 5 - 7. By carefully optimising protocols for quasiperiodic tiling generation, resist stack engineering, and thermal management, fabrication barriers such as resist collapse, tip degradation, and metallisation defects are resolved, which previously limited high-resolution fabrication of quasieriodic architectures. This methodology not only enabled the first experimental realisations of 8-fold Ammann-Beenker (ABT) and 4-fold Square Fibonacci (SFT) ASI tiling systems, but also created a reproducible, accessible framework for future researchers to build upon.

In Chapter 6 the ABT ASI was revealed to engineer unique magnetic degeneracy through mirror symmetries and hierarchical order. The development of a generalised Skeleton Model revealed how competing chiral domains achieve a global ground state (98.2% moment agreement) despite high degeneracy. Crucially, odd-moment vertices (5i and 7i) stabilised excited states via flippable 'F moments', while high-symmetry 8i vertices pinned chiral domain networks. The ABT is therefore a reconfigurable platform where degeneracy can be selectively harnessed, and demonstrates less local geometric frustration than the 5-fold Penrose tiling, resulting in more accessible long-range magnetic order and ground states without thermalisation.

In Chapter 7, the SFT ASI was found to exhibit emergent trapped vortex states, absent in the periodic square analogue. XMCD-PEEM imaging and MuMax3 simulations confirmed these excitations were topologically pinned by the tiling's geometry, dominating

small nanoislands at smaller scales. This demonstrates quasiperiodicity's role in stabilising non-trivial magnetic excitations, with implications for data storage and neuromorphic computing.

In Chapter 8, the first experimental realisation of anisotropically ordered molecular monolayers were imaged on the 2-fold surface of the decagonal Al-Ni-Co quasicrystal. C_{60} molecules were found to adsorb atop the surface, and preferentially diffuse to Ni/Co sites along the periodic direction upon annealing, forming chains of C_{60} separated by Fibonacci-scaled sequences in the quasiperiodic direction. The assembly of these chains was found to be mediated by two competing interactions: substrate-molecule interactions and molecule-molecule Van der Waals forces. This work builds on the established phenomenom of templated surface adsorption on quasicrystalline surfaces, with the future potential for advanced functional endofullerine monolayers to be similarly deposited on the surface.

Together, these results establish a structure for the fabrication of quasiperiodic systems, and reveal emergent phenomena inaccessible to periodic systems. Central to this achievement is the development of the t-SPL method, which enabled the first experimental realisation of high-resolution ASI in the 8-fold Ammann-Beenker (ABT) and 4-fold Square Fibonacci tilings (SFT). These systems demonstrate how quasiperiodic geometry tailors frustration: the ABT stabilises excited minimal energy at odd-number vertex states through symmetry, protected by chiral domains, while the SFT traps topological vortex excitations via hierarchical frustration. Complementing these nanomagnetic discoveries, atomic-scale templating of C_{60} on the 2-fold decagonal Al-Ni-Co surface demonstrates how quasiperiodic symmetry directs molecular self-assembly through selective site adsorption. By integrating artificial nanofabrication with advanced characterisation techniques, this work transcends natural quasicrystal limitations, and provides a reproducible framework to synthetically explore emergent phenomena in tailored quasiperiodic architectures, from frustrated nanomagnetism to molecular growth.

Future Work

The nanofabrication of various quasiperiodic thin film architectures during this work has opened new potential research directions. Generally, any quasiperiodic tiling can be fabricated with lithography, as shown with the fabrication of the hat tiling in Chapter 5. There are, however, practical limits in acute angles of higher rotational symmetries between nanoislands that realistically limits fabrication to structures such as the 12-fold square-triangle tiling [310]. There is a large range of quasiperiodic tilings available for fabrication into ASI, which could be fabricated and measured with the same protocol as in Chapters 5 to 7. Any arbitrary quasiperiodic tiling chosen will have its own unique potential for real applications. Following on from the interesting results of the τ-scaled square Fibonacci tiling, the τ-scaled trigonal or hexagonal Fibonacci ASI tilings would be

especially interesting to measure and compare to these results [51].

Next, while room temperature measurements of the ABT ASI in chapter 6 showed excited states within ground-stand domains, there is still a need to thermalise arrays to confirm these results and increase the ground state occupation, or size of ground state domains. By fabricating ABT ASI and investigating with the same protocol as for the SFT in Chapter 7, in essence with a thickness of 25 nm instead of 10 nm, thermalised results can be investigated. These results would substantially contribute to conclusions from room temperature analysis.

Additional interesting work on the ABT ASI could involve removing the 8i vertex types, which are found to be important pinning centres for ground state domains in Chapter 6. By investigating the change in magnetic ordering of the system, it may be possible by selectively removing specific 8i vertices (or other vertex types and arrangements) to create a programmable array. Another approach could be varying inter-nanoisland spacing, to see if for example quasiperiodic domain wall formation of high-energy vertices could be controlled.

The work on quasiperiodic ASI may be extending to include other metal materials with different magnetic properties. For example, it would be interesting to grow quasiperiodic ASI with out-of-plane magnetisation with a Co-Pt material, which may reveal novel interactions. Swapping the metal grown onto the mask during the nanolithography process is relatively trivial, not limited to just permalloy of ferromagnetic investigations.

Finally, following the succesful growth of anisotropically arranged C_{60} chains of the 2-fold Al-Ni-Co surface, it would be interesting to attempt to grow functional endofullerines on the same surface and investigate their magnetic or electronic properties for potential applications. Such systems may be doped C_{60}, or with functional endofullerines a ferromagnetic atom such as Fe may reside at the centre of the fullerine.

Bibliography

[1] Shechtman D, Blech I, Gratias D, Cahn JW. Metallic phase with long-range orientational order and no translational symmetry. Physical review letters. 1984;53(20):1951.

[2] Zhou W, Lim Y, Lin H, Lee S, Li Y, Huang Z, et al. Colloidal quasicrystals engineered with DNA. Nature materials. 2024;23(3):424-8.

[3] Fischer S, Exner A, Zielske K, Perlich J, Deloudi S, Steurer W, et al. Colloidal quasicrystals with 12-fold and 18-fold diffraction symmetry. Proceedings of the National Academy of Sciences. 2011;108(5):1810-4.

[4] Noya EG, Wong CK, Llombart P, Doye JP. How to design an icosahedral quasicrystal through directional bonding. Nature. 2021;596(7872):367-71.

[5] Dotera T. Quasicrystals in soft matter. Israel Journal of Chemistry. 2011;51(11-12):1197-205.

[6] Förster S, Meinel K, Hammer R, Trautmann M, Widdra W. Quasicrystalline structure formation in a classical crystalline thin-film system. Nature. 2013;502(7470):215-8.

[7] Förster S, Schenk S, Maria Zollner E, Krahn O, Chiang CT, Schumann FO, et al. Quasicrystals and their approximants in 2D ternary oxides. physica status solidi (b). 2020;257(7):1900624.

[8] Louzguine-Luzgin D, Inoue A. Formation and properties of quasicrystals. Annu Rev Mater Res. 2008;38(1):403-23.

[9] Thiel PA. Quasicrystal surfaces. Annu Rev Phys Chem. 2008;59:129-52.

[10] Steurer W. Quasicrystals: What do we know? What do we want to know? What can we know? Acta Crystallographica Section A: Foundations and Advances. 2018;74(1):1-11.

[11] Marder MP. Condensed matter physics. John Wiley & Sons; 2010.

[12] Coey JM. Magnetism and magnetic materials. Cambridge university press; 2010.

[13] Kittel C, McEuen P. Introduction to solid state physics. John Wiley & Sons; 2018.

[14] McMichael RD, Donahue MJ. Head to head domain wall structures in thin magnetic strips. IEEE Transactions on Magnetics. 1997;33(5):4167-9.

[15] Estévez V, Laurson L. Head-to-head domain wall structures in wide permalloy strips. Physical Review B. 2015;91(5):054407.

[16] Stier M, Neumann A, Philippi-Kobs A, Oepen HP, Thorwart M. Implications of a temperature-dependent magnetic anisotropy for superparamagnetic switching. Journal of Magnetism and Magnetic Materials. 2018;447:96-100.

[17] Harris MJ, Bramwell S, McMorrow D, Zeiske T, Godfrey K. Geometrical frustration in the ferromagnetic pyrochlore Ho 2 Ti 2 O 7. Physical Review Letters. 1997;79(13):2554.

[18] Chandler L, Barker OJ, Wright AJ, O'Brien L, Coates S, McGrath R, et al. Fabricating Quasiperiodic Tilings with Thermal-Scanning Probe Lithography. Israel Journal of Chemistry. 2023:e202300115.

[19] Harsha KS. Principles of vapor deposition of thin films. Elsevier; 2005.

[20] Reichelt K, Jiang X. The preparation of thin films by physical vapour deposition methods. Thin Solid Films. 1990;191(1):91-126.

[21] Guimarães AP, Guimaraes AP. Principles of nanomagnetism. vol. 7. Springer; 2009.

[22] Stefanita CG. From bulk to nano: the many sides of magnetism. vol. 117. Springer Science & Business Media; 2008.

[23] Gomez-Iriarte G, Gonzalez-Chavez D, Sommer R, Sinnecker J. Ferromagnetic resonance response in square artificial spin ice: Roles of geometry in vertex dynamics and magnetic configurations. Physical Review B. 2024;110(17):174435.

[24] The Object Oriented MicroMagnetic Framework (OOMMF) project at ITL/NIST; 2006. 'https://math.nist.gov/oommf/'.

[25] Vansteenkiste A, Leliaert J, Dvornik M, Helsen M, Garcia-Sanchez F, Van Waeyenberge B. The design and verification of MuMax3. AIP advances. 2014;4(10).

[26] Nisoli C, Moessner R, Schiffer P. Colloquium: Artificial spin ice: Designing and imaging magnetic frustration. Reviews of Modern Physics. 2013;85(4):1473.

[27] Heyderman LJ, Stamps RL. Artificial ferroic systems: novel functionality from structure, interactions and dynamics. Journal of Physics: Condensed Matter. 2013;25(36):363201.

[28] Farhan A, Saccone M, Petersen CF, Dhuey S, Chopdekar RV, Huang YL, et al. Emergent magnetic monopole dynamics in macroscopically degenerate artificial spin ice. Science advances. 2019;5(2):eaav6380.

[29] Zhang S, Gilbert I, Nisoli C, Chern GW, Erickson MJ, O'brien L, et al. Crystallites of magnetic charges in artificial spin ice. Nature. 2013;500(7464):553-7.

[30] Gilbert I, Chern GW, Zhang S, O'Brien L, Fore B, Nisoli C, et al. Emergent ice rule and magnetic charge screening from vertex frustration in artificial spin ice. Nature Physics. 2014;10(9):670-5.

[31] Gilbert I, Lao Y, Carrasquillo I, O'Brien L, Watts JD, Manno M, et al. Emergent reduced dimensionality by vertex frustration in artificial spin ice. Nature Physics. 2016;12(2):162-5.

[32] Shechtman D, Blech IA. The microstructure of rapidly solidified Al 6 Mn. Metallurgical Transactions A. 1985;16(6):1005-12.

[33] Bragg WL. The structure of some crystals as indicated by their diffraction of X-rays. Proceedings of the Royal Society of London Series A, Containing papers of a mathematical and physical character. 1913;89(610):248-77.

[34] Shechtman D. Quasi-periodic crystals—the long road from discovery to acceptance. Rambam Maimonides medical journal. 2013;4(1).

[35] Pauling L. Apparent icosahedral symmetry is due to directed multiple twinning of cubic crystals. Nature. 1985;317(6037):512-4.

[36] Lifshitz R. The symmetry of quasiperiodic crystals. Physica A: Statistical Mechanics and its Applications. 1996;232(3-4):633-47.

[37] Lifshitz R. Quasicrystals: A matter of definition. Foundations of Physics. 2003;33(12):1703-11.

[38] Lifshitz R. What is a crystal? Zeitschrift für Kristallographie. 2007;222(6):313-7.

[39] Lifshitz R. Symmetry breaking and order in the age of quasicrystals. Israel Journal of Chemistry. 2011;51(11-12):1156-67.

[40] Penrose R. The role of aesthetics in pure and applied mathematical research. Bull Inst Math Appl. 1974;10:266-71.

[41] Gardner M. Penrose tiles to trapdoor ciphers: And the return of Dr Matrix. Cambridge University Press; 1997.

[42] Frettlöh D, Gähler F. Tilings Encyclopedia; 2025. [Online; last accessed 11-02-2025]. `https://tilings.math.uni-bielefeld.de/`.

[43] Beenker FPM. Algebraic theory of non-periodic tilings of the plane by two simple building blocks: a square and a rhombus. Eindhoven University of Technology. 1982.

[44] De Bruijn NG. Algebraic theory of Penrose's non-periodic tilings of the plane. Kon Nederl Akad Wetensch Proc Ser A. 1981;43(84):1-7.

[45] Ammann R, Grünbaum B, Shephard GC. Aperiodic tiles. Discrete & Computational Geometry. 1992;8(1):1-25.

[46] Lifshitz R. The square Fibonacci tiling. Journal of alloys and compounds. 2002;342(1-2):186-90.

[47] Baake M, Frank NP, Grimm U. Three variations on a theme by Fibonacci. Stochastics and Dynamics. 2021;21(03):2140001.

[48] Baake M, Grimm U. Inflation versus projection sets in aperiodic systems: the role of the window in averaging and diffraction. Acta Crystallographica Section A: Foundations and Advances. 2020;76(5).

[49] Fang F, Hammock D, Irwin K. Methods for calculating empires in quasicrystals. Crystals. 2017;7(10):304.

[50] Socolar JE, Steinhardt PJ, Levine D. Quasicrystals with arbitrary orientational symmetry. Physical Review B. 1985;32(8):5547.

[51] Coates S, Koga A, Matsubara T, Tamura R, Sharma HR, McGrath R, et al. Hexagonal and trigonal quasiperiodic tilings. Israel Journal of Chemistry. 2024;64(10-11):e202300100.

[52] Steurer W, Deloudi S. Decagonal quasicrystals–What has been achieved? Comptes Rendus Physique. 2014;15(1):40-7.

[53] He LX, Wu Y, Kuo K. Decagonal quasicrystals with different periodicities along the tenfold axis in rapidly solidified Al 65 Cu 20 M 15 (M= Mn, Fe, Co or Ni). Journal of materials science letters. 1988;7:1284-6.

[54] Tsai AP, Inoue A, Masumoto T. A stable decagonal quasicrystal in the Al–Cu–Co system. Materials transactions, JIM. 1989;30(4):300-4.

[55] Tsai AP, Inoue A, Masumoto T. Stable decagonal Al–Co–Ni and Al–Co–Cu quasicrystals. Materials transactions, JIM. 1989;30(7):463-73.

[56] Lifshitz R. Quasicrystals - Introduction; Published 2007, Last accessed May 2025. website `https://www.tau.ac.il/~ronlif/quasicrystals.html`.

[57] Steurer W. Twenty years of structure research on quasicrystals. Part I. Pentagonal, octagonal, decagonal and dodecagonal quasicrystals. Zeitschrift für Kristallographie-Crystalline Materials. 2004;219(7):391-446.

[58] Ritsch S, Beeli C, Nissen H, Gödecke T, Scheffer M, Lück R. The existence regions of structural modifications in decagonal Al-Co-Ni. Philosophical magazine letters. 1998;78(2):67-75.

[59] Sharma HR. Structure, Morphology, and Dynamics of Quasicrystal Surfaces [Dissertation]. Free University of Berlin; 2002. Available from: `http://dx.doi.org/10.17169/refubium-13587`.

[60] Hiraga K, Ohsuna T, Sun W, Sugiyama K. Structural characteristics of Al-Co-Ni decagonal quasicrystals and crystalline approximants. Materials Transactions. 2001;42(11):2354-67.

[61] Franke KJ. Quasicrystal Surfaces: Morphology, Phase Transitions, and Epitaxy [Dissertation]. Free University of Berlin; 2004. Available from: `http://dx.doi.org/10.17169/refubium-11341`.

[62] Sharma H, Franke K, Theis W, Riemann A, Fölsch S, Gille P, et al. Structure and morphology of the tenfold surface of decagonal Al 71.8 Ni 14.8 Co 13.4 in its low-temperature random tiling type-I modification. Physical Review B—Condensed Matter and Materials Physics. 2004;70(23):235409.

[63] Yamamoto A, Weber S. Five-dimensional superstructure model of decagonal Al-Ni-Co quasicrystals. Physical review letters. 1997;78(23):4430.

[64] Deloudi S, Fleischer F, Steurer W. Unifying cluster-based structure models of decagonal Al–Co–Ni, Al–Co–Cu and Al–Fe–Ni. Acta Crystallographica Section B: Structural Science. 2011;67(1):1-17.

[65] McGrath R, Smerdon J, Sharma H, Theis W, Ledieu J. The surface science of quasicrystals. Journal of Physics: Condensed Matter. 2010;22(8):084022.

[66] Yuhara J, Klikovits J, Schmid M, Varga P, Yokoyama Y, Shishido T, et al. Atomic structure of an Al–Co–Ni decagonal quasicrystalline surface. Physical Review B—Condensed Matter and Materials Physics. 2004;70(2):024203.

[67] Ferralis N, Szmodis A, Diehl R. Diffraction from one-and two-dimensional quasicrystalline gratings. American journal of physics. 2004;72(9):1241-6.

[68] Kishida M, Kamimura Y, Tamura R, Edagawa K, Takeuchi S, Sato T, et al. Scanning tunneling microscopy of an Al-Ni-Co decagonal quasicrystal. Physical Review B. 2002;65(9):094208.

[69] Krajčí M, Hafner J, Mihalkovič M. Ab initio study of the surface of a decagonal Al-Co-Ni quasicrystal. Physical Review B—Condensed Matter and Materials Physics. 2006;73(13):134203.

[70] Sharma H, Franke K, Theis W, Riemann A, Fölsch S, Rieder K, et al. Investigation of the twofold decagonal Al71. 8Ni14. 8Co13. 4 (1 0 0 0 0) surface by SPA-LEED and He diffraction. Surface science. 2004;561(2-3):121-6.

[71] Mäder R, Widmer R, Gröning P, Deloudi S, Steurer W, Heggen M, et al. High-resolution scanning tunneling microscopy investigation of the (12110) and (10000) two-fold symmetric d-Al-Ni-Co quasicrystalline surfaces. Physical Review B—Condensed Matter and Materials Physics. 2009;80(3):035433.

[72] Park JY, Ogletree DF, Salmeron M, Ribeiro R, Canfield PC, Jenks C, et al. Atomic scale coexistence of periodic and quasiperiodic order in a 2-fold Al-Ni-Co decagonal quasicrystal surface. Physical Review B—Condensed Matter and Materials Physics. 2005;72(22):220201.

[73] Kossel W. Extending the law of Bravais. Nachr Ges Wiss Göttingen. 1927;143:135-43.

[74] Stranski IN. Zur theorie des kristallwachstums. Zeitschrift für physikalische Chemie. 1928;136(1):259-78.

[75] Oura K, Lifshits V, Saranin A, Zotov A, Katayama M. Surface science: an introduction. Springer Science & Business Media; 2013.

[76] Burnie DW. Icosahedral Ag-In-Yb surfaces: clean surfaces, atomic motion and adsorbate structures. The University of Liverpool (United Kingdom); 2022.

[77] Coates S. Quasicrystal systems with simple symmetries. The University of Liverpool (United Kingdom); 2019.

[78] Lüth H. Solid surfaces, interfaces and thin films. vol. 4. Springer; 2001.

[79] Skjærvø SH, Marrows CH, Stamps RL, Heyderman LJ. Advances in artificial spin ice. Nature Reviews Physics. 2020;2(1):13-28.

[80] Wang R, Nisoli C, Freitas R, Li J, McConville W, Cooley B, et al. Artificial 'spin ice'in a geometrically frustrated lattice of nanoscale ferromagnetic islands. Nature. 2006;439(7074):303-6.

[81] Nisoli C, Wang R, Li J, McConville WF, Lammert fPE, Schiffer P, et al. Ground state lost but degeneracy found: The effective thermodynamics of artificial spin ice. Physical review letters. 2007;98(21):217203.

[82] Nisoli C, Li J, Ke X, Garand D, Schiffer P, Crespi VH. Effective Temperature in an Interacting Vertex System:¡? format?¿ Theory and Experiment on Artificial Spin Ice. Physical review letters. 2010;105(4):047205.

[83] Wang R, , Li J, McConville W, Nisoli C, Ke X, et al. Demagnetization protocols for frustrated interacting nanomagnet arrays. Journal of applied physics. 2007;101(9).

[84] Ke X, Li J, Nisoli C, Lammert PE, McConville W, Wang R, et al. Energy minimization and ac demagnetization in a nanomagnet array. Physical review letters. 2008;101(3):037205.

[85] Li J, Ke X, Zhang S, Garand D, Nisoli C, Lammert P, et al. Comparing artificial frustrated magnets by tuning the symmetry of nanoscale permalloy arrays. Physical Review B—Condensed Matter and Materials Physics. 2010;81(9):092406.

[86] Kapaklis V, Arnalds UB, Farhan A, Chopdekar RV, Balan A, Scholl A, et al. Thermal fluctuations in artificial spin ice. Nature nanotechnology. 2014;9(7):514-9.

[87] Farhan A, Derlet PM, Kleibert A, Balan A, Chopdekar RV, Wyss M, et al. Direct observation of thermal relaxation in artificial spin ice. Physical review letters. 2013;111(5):057204.

[88] Budrikis Z, Politi P, Stamps R. Vertex dynamics in finite two-dimensional square spin ices. Physical Review Letters. 2010;105(1):017201.

[89] Budrikis Z, Politi P, Stamps R. Diversity enabling equilibration: disorder and the ground state in artificial spin ice. Physical review letters. 2011;107(21):217204.

[90] Lammert PE, Ke X, Li J, Nisoli C, Garand DM, Crespi VH, et al. Direct entropy determination and application to artificial spin ice. Nature Physics. 2010;6(10):786-9.

[91] Kohli K, Balk AL, Li J, Zhang S, Gilbert I, Lammert PE, et al. Magneto-optical Kerr effect studies of square artificial spin ice. Physical Review B—Condensed Matter and Materials Physics. 2011;84(18):180412.

[92] Rougemaille N, Montaigne F, Canals B, Duluard A, Lacour D, Hehn M, et al. Artificial kagome arrays of nanomagnets: a frozen dipolar spin ice. Physical Review Letters. 2011;106(5):057209.

[93] Mengotti E, Heyderman L, Fraile Rodríguez A, Bisig A, Le Guyader L, Nolting F, et al. Building blocks of an artificial kagome spin ice: Photoemission electron microscopy of arrays of ferromagnetic islands. Physical Review B—Condensed Matter and Materials Physics. 2008;78(14):144402.

[94] Budrikis Z, Morgan J, Akerman J, Stein A, Politi P, Langridge S, et al. Disorder strength and field-driven ground state domain formation in artificial spin ice: experiment, simulation, and theory. Physical review letters. 2012;109(3):037203.

[95] Siddharthan R, Shastry B, Ramirez A, Hayashi A, Cava R, Rosenkranz S. Ising pyrochlore magnets: Low-temperature properties,"ice rules," and beyond. Physical review letters. 1999;83(9):1854.

[96] Ramirez AP, Hayashi A, Cava RJ, Siddharthan R, Shastry B. Zero-point entropy in 'spin ice'. Nature. 1999;399(6734):333-5.

[97] Schroeder DV. An introduction to thermal physics. Oxford University Press; 2020.

[98] Tanaka M, Saitoh E, Miyajima H, Yamaoka T, Iye Y. Magnetic interactions in a ferromagnetic honeycomb nanoscale network. Physical Review B—Condensed Matter and Materials Physics. 2006;73(5):052411.

[99] Wills A, Ballou R, Lacroix C. Model of localized highly frustrated ferromagnetism: The kagomé spin ice. Physical Review B. 2002;66(14):144407.

[100] Möller G, Moessner R. Artificial square ice and related dipolar nanoarrays. Physical Review Letters. 2006;96(23):237202.

[101] Zhang X, Lao Y, Sklenar J, Bingham NS, Batley JT, Watts JD, et al. Understanding thermal annealing of artificial spin ice. APL Materials. 2019;7(11):111112.

[102] Morgan JP, Stein A, Langridge S, Marrows CH. Thermal ground-state ordering and elementary excitations in artificial magnetic square ice. Nature Physics. 2011;7(1):75-9.

[103] Brown Jr WF. Thermal fluctuations of a single-domain particle. Physical review. 1963;130(5):1677.

[104] Néel L. Théorie du traînage magnétique des ferromagnétiques en grains fins avec application aux terres cuites. In: Annales de géophysique. vol. 5; 1949. p. 99-136.

[105] Brown W. Thermal fluctuation of fine ferromagnetic particles. IEEE Transactions on Magnetics. 1979;15(5):1196-208.

[106] Weller D, Moser A. Thermal effect limits in ultrahigh-density magnetic recording. IEEE Transactions on magnetics. 1999;35(6):4423-39.

[107] Coffey WT, Kalmykov YP. Thermal fluctuations of magnetic nanoparticles: Fifty years after Brown. Journal of Applied Physics. 2012;112(12).

[108] Basso V, Beatrice C, LoBue M, Tiberto P, Bertotti G. Connection between hysteresis and thermal relaxation in magnetic materials. Physical Review B. 2000;61(2):1278.

[109] Porro J, Bedoya-Pinto A, Berger A, Vavassori P. Exploring thermally induced states in square artificial spin-ice arrays. New Journal of Physics. 2013;15(5):055012.

[110] Farhan A, Derlet P, Kleibert A, Balan A, Chopdekar R, Wyss M, et al. Exploring hyper-cubic energy landscapes in thermally active finite artificial spin-ice systems. Nature Physics. 2013;9(6):375-82.

[111] Drisko J, Daunheimer S, Cumings J. Fepd 3 as a material for studying thermally active artificial spin ice systems. Physical Review B. 2015;91(22):224406.

[112] Skomski R. Nanomagnetics. Journal of physics: Condensed matter. 2003;15(20):R841.

[113] Saccone M, Scholl A, Velten S, Dhuey S, Hofhuis K, Wuth C, et al. Towards artificial Ising spin glasses: Thermal ordering in randomized arrays of Ising-type nanomagnets. Physical Review B. 2019;99(22):224403.

[114] Shi D, Budrikis Z, Stein A, Morley SA, Olmsted PD, Burnell G, et al. Frustration and thermalization in an artificial magnetic quasicrystal. Nature Physics. 2018;14(3):309-14.

[115] Garcia R, Knoll AW, Riedo E. Advanced scanning probe lithography. Nature nanotechnology. 2014;9(8):577-87.

[116] Randall JN, Owen JH, Lake J, Fuchs E. Next generation of extreme-resolution electron beam lithography. Journal of Vacuum Science & Technology B. 2019;37(6).

[117] Mojarad N, Gobrecht J, Ekinci Y. Beyond EUV lithography: a comparative study of efficient photoresists' performance. Scientific reports. 2015;5(1):1-7.

[118] Achanta VG. Plasmonic quasicrystals. Progress in Quantum Electronics. 2015;39:1-23.

[119] Martın J, Nogues J, Liu K, Vicent J, Schuller IK. Ordered magnetic nanostructures: fabrication and properties. Journal of magnetism and magnetic materials. 2003;256(1-3):449-501.

[120] Mercier TM, Rahman T, Krishnan C, Khorani E, Shaw PJ, Pollard ME, et al. High symmetry nano-photonic quasi-crystals providing novel light management in silicon solar cells. Nano Energy. 2021;84:105874.

[121] Varadarajan V, Shekar C. Fabrication of two-dimensional photonic quasi-crystals with 18-and 36-fold by holography for solar application. IET Optoelectronics. 2016;10(6):217-20.

[122] Mishra S, Yadav T, Mukhopadhyay N, Srivastava O. Synthesis of fine skeletal structure on Al–Cu–Co decagonal quasicrystals for hydrogen production through steam reforming of methanol. International Journal of Hydrogen Energy. 2020;45(46):24491-501.

[123] Takagiwa Y. Thermoelectric Properties of Co-Substituted Al–Pd–Re Icosahedral Quasicrystals. Materials. 2022;15(19):6816.

[124] Vekilov YK, Chernikov MA. Quasicrystals. Physics-Uspekhi. 2010;53(6):537.

[125] Anand K, Fournee V, Prevot G, Ledieu J, Gaudry E. Nonwetting Behavior of Al–Co Quasicrystalline Approximants Owing to Their Unique Electronic Structures. ACS applied materials & interfaces. 2020;12(13):15793-801.

[126] Xu K, Chen J. High-resolution scanning probe lithography technology: a review. Applied Nanoscience. 2020;10(4):1013-22.

[127] Tseng AA, Notargiacomo A, Chen T. Nanofabrication by scanning probe microscope lithography: A review. Journal of Vacuum Science & Technology B: Microelectronics and Nanometer Structures Processing, Measurement, and Phenomena. 2005;23(3):877-94.

[128] Hu H, Kim HJ, Somnath S. Tip-based nanofabrication for scalable manufacturing. Micromachines. 2017;8(3):90.

[129] King WP, Bhatia B, Felts JR, Kim HJ, Kwon B, Lee B, et al. Heated atomic force microscope cantilevers and their applications. Annual Review of Heat Transfer. 2013;16.

[130] Howell ST, Grushina A, Holzner F, Brugger J. Thermal scanning probe lithography—a review. Microsystems & Nanoengineering. 2020;6(1):1-24.

[131] Liu X, Huang Z, Zheng X, Shahrjerdi D, Riedo E. Nanofabrication of graphene field-effect transistors by thermal scanning probe lithography. APL Materials. 2021;9(1):011107.

[132] Lassaline N, Brechbühler R, Vonk S, Ridderbeek K, Spieser M, Bisig S, et al. Optical Fourier surfaces. Nature communications. 2020;582(1):506-10.

[133] Collins LC, Witte TG, Silverman R, Green DB, Gomes KK. Imaging quasiperiodic electronic states in a synthetic Penrose tiling. Nature communications. 2017;8(1):1-6.

[134] IBM. A Boy and His Atom; 2013, last accessed May 2025. Website `https://youtu.be/oSCX78-8-q0?`

[135] Chen Y. Nanofabrication by electron beam lithography and its applications: A review. Microelectronic Engineering. 2015;135:57-72.

[136] Lawson RA, Robinson AP. Overview of materials and processes for lithography. In: Frontiers of Nanoscience. vol. 11. Elsevier; 2016. p. 1-90.

[137] Li P. A review of proximity effect correction in electron-beam lithography. arXiv preprint arXiv:150905169. 2015.

[138] Pala N, Karabiyik M. In: Electron Beam Lithography (EBL). Dordrecht: Springer Netherlands; 2016. p. 1033-57. Available from: `https://doi.org/10.1007/978-94-017-9780-1_344`.

[139] Ul-Hamid A. A beginners' guide to scanning electron microscopy. vol. 1. Springer; 2018.

[140] Bhat VS, Sklenar J, Farmer B, Woods J, Hastings JT, Lee S, et al. Controlled magnetic reversal in permalloy films patterned into artificial quasicrystals. Physical review letters. 2013;111(7):077201.

[141] Bhat VS, Sklenar J, Farmer B, Woods J, Ketterson J, Hastings JT, et al. Ferromagnetic resonance study of eightfold artificial ferromagnetic quasicrystals. Journal of Applied Physics. 2014;115(17):17C502.

[142] Bhat V, Woods J, Farmer B, De Long L, Hastings J, Sklenar J, et al. Observation of Robust FMR in Permalloy Quasiperiodic Arrays. IEEE transactions on magnetics. 2013;49(7):3101-4.

[143] Bhat V, Farmer B, Smith N, Teipel E, Woods J, Sklenar J, et al. Non-stochastic switching and emergence of magnetic vortices in artificial quasicrystal spin ice. Physica C: Superconductivity and its applications. 2014;503:170-4.

[144] Farmer B, Bhat V, Sklenar J, Woods J, Teipel E, Smith N, et al. Nonstochastic magnetic reversal in artificial quasicrystalline spin ice. Journal of Applied Physics. 2014;115(17):17E133.

[145] Farmer B, Bhat V, Sklenar J, Teipel E, Woods J, Ketterson J, et al. Magnetic response of aperiodic wire networks based on Fibonacci distortions of square antidot lattices. Journal of Applied Physics. 2015;117(17):17B714.

[146] Farmer B, Bhat VS, Balk A, Teipel E, Smith N, Unguris J, et al. Direct imaging of coexisting ordered and frustrated sublattices in artificial ferromagnetic quasicrystals. Physical Review B. 2016;93(13):134428.

[147] Sung D, Jung C, Cho BG, Jo W, Han HS, Lee KS, et al. Imaging the magnetic structures of artificial quasicrystal magnets using resonant coherent diffraction of circularly polarized X-rays. Nanoscale. 2018;10(27):13159-64.

[148] Bhat V, Grundler D. Angle-dependent magnetization dynamics with mirror-symmetric excitations in artificial quasicrystalline nanomagnet lattices. Physical Review B. 2018;98(17):174408.

[149] Watanabe S, Bhat VS, Baumgaertl K, Grundler D. Direct Observation of Worm-Like Nanochannels and Emergent Magnon Motifs in Artificial Ferromagnetic Quasicrystals. Advanced Functional Materials. 2020;30(36):2001388.

[150] Watanabe S, Bhat VS, Baumgaertl K, Hamdi M, Grundler D. Direct observation of multiband transport in magnonic Penrose quasicrystals via broadband and phase-resolved spectroscopy. Science Advances. 2021;7(35):eabg3771.

[151] Watanabe S, Bhat VS, Mucchietto A, Dayi EN, Shan S, Grundler D. Periodic and aperiodic NiFe nanomagnet/ferrimagnet hybrid structures for 2D magnon steering and interferometry with high extinction ratio. Advanced Materials. 2023;35(31):2301087.

[152] Bhat VS, Watanabe S, Kronast F, Baumgaertl K, Grundler D. Spin dynamics, loop formation and cooperative reversal in artificial quasicrystals with tailored exchange coupling. Communications Physics. 2023;6(1):193.

[153] Kemmler M, Gürlich C, Sterck A, Pöhler H, Neuhaus M, Siegel M, et al. Commensurability effects in superconducting Nb films with quasiperiodic pinning arrays. Physical review letters. 2006;97(14):147003.

[154] Jia P, Yang Z, Yang J, Ebendorff-Heidepriem H. Quasiperiodic nanohole arrays on optical fibers as plasmonic sensors: fabrication and sensitivity determination. Acs Sensors. 2016;1(8):1078-83.

[155] Butler TP, Butt H, Wilkinson TD, Amaratunga GA. Visible diffraction from quasicrystalline arrays of carbon nanotubes. Nanoscale. 2015;7(32):13452-7.

[156] Kasture S, Ravishankar AP, Yallapragada V, Patil R, Valappil NV, Mulay G, et al. Plasmonic quasicrystals with broadband transmission enhancement. Scientific reports. 2014;4(1):5257.

[157] Holman A, Xu Y, Sun X, Wu J, Wang M, Seo B, et al. Trapping of Single Atoms in Metasurface Optical Tweezer Arrays. arXiv preprint arXiv:241105321. 2024.

[158] Villegas J, Montero M, Li CP, Schuller IK. Correlation length of quasiperiodic vortex lattices. Physical review letters. 2006;97(2):027002.

[159] Langner A, Päivänranta B, Terhalle B, Ekinci Y. Fabrication of quasiperiodic nanostructures with EUV interference lithography. Nanotechnology. 2012;23(10):105303.

[160] Mahmood R, Ramirez AV, Hillier AC. Creating Two-Dimensional Quasicrystal, Supercell, and Moire Lattices with Laser Interference Lithography: Implications for Photonic Bandgap Materials. ACS Applied Nano Materials. 2021;4(9):8851-62.

[161] Lubin SM, Zhou W, Hryn AJ, Huntington MD, Odom TW. High-rotational symmetry lattices fabricated by moire nanolithography. Nano letters. 2012;12(9):4948-52.

[162] Materials A. Lithography Machines and the Chip-Making Process; Last accessed May 2025. website azom.com.

[163] Lifshitz R. Recent Advances in Quasicrystal Research. Israel Journal of Chemistry. 2024;n/a(n/a):e202412000. Available from: `https://onlinelibrary.wiley.com/doi/abs/10.1002/ijch.202412000`.

[164] Koga A. Superlattice structure in the antiferromagnetically ordered state in the Hubbard model on the Ammann-Beenker tiling. Physical Review B. 2020;102(11):115125.

[165] Thiem S, Chalker J. Long-range magnetic order in models for rare-earth quasicrystals. Physical Review B. 2015;92(22):224409.

[166] Thiem S, Chalker J. Magnetism in rare-earth quasicrystals: RKKY interactions and ordering. Europhysics Letters. 2015;110(1):17002.

[167] Araújo RN, Andrade EC. Conventional superconductivity in quasicrystals. Physical Review B. 2019;100(1):014510.

[168] Gottlob E, Schneider U. Hubbard models for quasicrystalline potentials. Physical Review B. 2023;107(14):144202.

[169] Fukushima T, Takemori N, Sakai S, Ichioka M, Jagannathan A. Supercurrent distribution on Ammann-Beenker structure. In: Journal of Physics: Conference Series. vol. 2461. IOP Publishing; 2023. p. 012014.

[170] Oktel MÖ. Strictly localized states in the octagonal Ammann-Beenker quasicrystal. Physical Review B. 2021;104(1):014204.

[171] Damanik D, Embree M, Fillman J, Mei M. Discontinuities of the integrated density of states for Laplacians associated with Penrose and Ammann–Beenker tilings. Experimental Mathematics. 2024;33(4):588-610.

[172] Zhang Y, Lan Z, Chen W, Li J. Dual-band topological Bott insulators in Ammann–Beenker-tiling square photonic quasicrystals. Journal of Physics: Photonics. 2025;7(1):015010.

[173] Peng T, Hua CB, Chen R, Xu DH, Zhou B. Topological Anderson insulators in an Ammann-Beenker quasicrystal and a snub-square crystal. Physical Review B. 2021;103(8):085307.

[174] Mao YF, Tao YL, Wang JH, Zeng QB, Xu Y. Higher-order topological insulators in three dimensions without crystalline counterparts. Physical Review B. 2024;109(13):134205.

[175] Singh S, Lloyd J, Flicker F. Hamiltonian cycles on ammann-beenker tilings. Physical Review X. 2024;14(3):031005.

[176] Lloyd J, Biswas S, Simon SH, Parameswaran S, Flicker F. Statistical mechanics of dimers on quasiperiodic Ammann-Beenker tilings. Physical Review B. 2022;106(9):094202.

[177] Jagannathan A, Duneau M. Properties of the Ammann–Beenker Tiling and its Square Periodic Approximants. Israel Journal of Chemistry. 2024;64(10-11):e202300119.

[178] Viebahn K, Sbroscia M, Carter E, Yu JC, Schneider U. Matter-wave diffraction from a quasicrystalline optical lattice. Physical Review Letters. 2019;122(11):110404.

[179] Jagannathan A, Duneau M. An eightfold optical quasicrystal with cold atoms. Europhysics Letters. 2014;104(6):66003.

[180] Sbroscia M, Viebahn K, Carter E, Yu JC, Gaunt A, Schneider U. Observing localization in a 2D quasicrystalline optical lattice. Physical Review Letters. 2020;125(20):200604.

[181] Wang N, Chen H, Kuo K. Two-dimensional quasicrystal with eightfold rotational symmetry. Physical review letters. 1987;59(9):1010.

[182] Wang N, Fung KK, Kuo K. Symmetry study of the Mn-Si-Al octagonal quasicrystal by convergent beam electron diffraction. Applied physics letters. 1988;52(25):2120-1.

[183] Flicker F, Simon SH, Parameswaran S. Classical dimers on Penrose tilings. Physical Review X. 2020;10(1):011005.

[184] Fisher ME. Statistical mechanics of dimers on a plane lattice. Physical Review. 1961;124(6):1664.

[185] Kasteleyn PW. The statistics of dimers on a lattice: I. The number of dimer arrangements on a quadratic lattice. Physica. 1961;27(12):1209-25.

[186] Temperley HN, Fisher ME. Dimer problem in statistical mechanics-an exact result. Philosophical Magazine. 1961;6(68):1061-3.

[187] Macé N, Jagannathan A, Kalugin P, Mosseri R, Piéchon F. Critical eigenstates and their properties in one-and two-dimensional quasicrystals. Physical Review B. 2017;96(4):045138.

[188] Varjas D, Lau A, Pöyhönen K, Akhmerov AR, Pikulin DI, Fulga IC. Topological phases without crystalline counterparts. Physical review letters. 2019;123(19):196401.

[189] Chen R, Chen CZ, Gao JH, Zhou B, Xu DH. Higher-order topological insulators in quasicrystals. Physical review letters. 2020;124(3):036803.

[190] Stanley HE. Dependence of critical properties on dimensionality of spins. Physical Review Letters. 1968;20(12):589.

[191] Blöte H, Nienhuis B. Fully packed loop model on the honeycomb lattice. Physical review letters. 1994;72(9):1372.

[192] Baxter RJ. Exactly solved models in statistical mechanics. Elsevier; 2016.

[193] Jaubert L, Haque M, Moessner R. Analysis of a fully packed loop model arising in a magnetic Coulomb phase. Physical review letters. 2011;107(17):177202.

[194] Coates S, Smerdon JA, McGrath R, Sharma HR. A molecular overlayer with the Fibonacci square grid structure. Nature communications. 2018;9(1):1-5.

[195] Ledieu J, Gaudry É, Fournée V, Smerdon J, Diehl RD. Fullerene adsorption on intermetallic compounds of increasing structural complexity. Zeitschrift für Kristallographie-Crystalline Materials. 2017;232(7-9):629-45.

[196] Smerdon J, Young K, Lowe M, Hars S, Yadav T, Hesp D, et al. Templated quasicrystalline molecular ordering. Nano letters. 2014;14(3):1184-9.

[197] Zangwill A. Physics at surfaces. Cambridge university press; 1988.

[198] Widjaja E, Marks L. Models for quasicrystal–crystal epitaxy. Journal of Physics: Condensed Matter. 2008;20(31):314003.

[199] Shimoda M, Sato T, Tsai A, Guo J. Epitaxial crystalline film with psuedo-tenfold symmetry formed by Au-deposition on a decagonal Al 72 Ni 12 Co 16 quasicrystal. Physical Review B. 2000;62(17):11288.

[200] Lüscher R, Erbudak M, Weisskopf Y. Al nanostructures on quasicrystalline Al-Pd-Mn. Surface science. 2004;569(1-3):163-75.

[201] Sharma H, Shimoda M, Tsai A. Quasicrystal surfaces: structure and growth of atomic overlayers. Advances in Physics. 2007;56(3):403-64.

[202] Fournée V, Ledieu J, Shimoda M, Krajčí M, Sharma HR, McGrath R. Thin film growth on quasicrystalline surfaces. Israel Journal of Chemistry. 2011;51(11-12):1314-25.

[203] Pussi K, Gierer M, Diehl R. The uniaxially aperiodic structure of a thin Cu film on fivefoldi-Al–Pd–Mn. Journal of Physics: Condensed Matter. 2009;21(47):474213.

[204] Smerdon J, Ledieu J, McGrath R, Noakes T, Bailey P, Draxler M, et al. Characterization of aperiodic and periodic thin Cu films formed on the five-fold surface of i-Al 70 Pd 21 Mn 9 using medium-energy ion scattering spectroscopy. Physical Review B—Condensed Matter and Materials Physics. 2006;74(3):035429.

[205] Ledieu J, Hoeft J, Reid D, Smerdon J, Diehl R, Ferralis N, et al. Copper adsorption on the fivefold Al 70 Pd 21 Mn 9 quasicrystal surface. Physical Review B—Condensed Matter and Materials Physics. 2005;72(3):035420.

[206] McGrath R, Ledieu J, Cox EJ, Diehl RD. Quasicrystal surfaces: structure and potential astemplates. Journal of Physics: Condensed Matter. 2002;14(4):R119.

[207] Smerdon JA, Wearing LH, Parle J, Leung L, Sharma HR, Ledieu J, et al. Ordering of adsorbed species on quasicrystal surfaces. Philosophical Magazine. 2008;88(13-15):2073-82.

[208] Sharma H, Coates S, Alofi A, McGrath R. Growth of pentacene molecules on Tsai-type quasicrystals and related crystal surfaces. Journal of Vacuum Science & Technology A. 2022;40(1).

[209] Fournée V, Ledieu J, Gaudry E, Sharma HR, McGrath R. Ultra-thin films on complex metallic alloy surfaces: A perspective. Recent Advances in Thin Films. 2020:13-34.

[210] Ledieu J, McGrath R. Nanostructured quasiperiodic surfaces: the origin of pentagonal hollows and their role inadsorption and nucleation processes. Journal of Physics: Condensed Matter. 2003;15(42):S3113.

[211] Cai T, Ledieu J, McGrath R, Fournée V, Lograsso T, Ross A, et al. Pseudomorphic starfish: nucleation of extrinsic metal atoms on a quasicrystalline substrate. Surface Science. 2003;526(1-2):115-20.

[212] Smerdon J, Parle J, Wearing L, Lograsso TA, Ross A, McGrath R. Nucleation and growth of a quasicrystalline monolayer: Bi adsorption on the fivefold surface of i-Al 70 Pd 21 Mn 9. Physical Review B—Condensed Matter and Materials Physics. 2008;78(7):075407.

[213] Ledieu J, Leung L, Wearing L, McGrath R, Lograsso TA, Wu D, et al. Self-assembly, structure, and electronic properties of a quasiperiodic lead monolayer. Physical Review B—Condensed Matter and Materials Physics. 2008;77(7):073409.

[214] Franke K, Sharma H, Theis W, Gille P, Ebert P, Rieder K. Quasicrystalline epitaxial single element monolayers on icosahedral Al-Pd-Mn and decagonal Al-Ni-Co quasicrystal surfaces. Physical review letters. 2002;89(15):156104.

[215] Smerdon J, Leung L, Parle J, Jenks C, McGrath R, Fournée V, et al. Formation of a quasicrystalline Pb monolayer on the 10-fold surface of the decagonal Al–Ni–Co quasicrystal. Surface science. 2008;602(14):2496-501.

[216] Sharma H, Shimoda M, Ross A, Lograsso TA, Tsai A. Real-space observation of quasicrystalline Sn monolayer formed on the fivefold surface of icosahedral Al 63 Cu 24 Fe 13 quasicrystal. Physical Review B—Condensed Matter and Materials Physics. 2005;72(4):045428.

[217] Sharma H, Nozawa K, Smerdon J, Nugent P, McLeod I, Dhanak V, et al. Templated three-dimensional growth of quasicrystalline lead. Nature communications. 2013;4(1):2715.

[218] Hars S, Sharma H, Smerdon J, Coates S, Nozawa K, Tsai A, et al. Growth of a bismuth thin film on the five-fold surface of the icosahedral Ag-In-Yb quasicrystal. Surface Science. 2018;678:222-7.

[219] Coates S, Thorn S, McGrath R, Sharma HR, Tsai AP. Unique growth mode observed in a Pb thin film on the threefold surface of an i-Ag-In-Yb quasicrystal. Physical Review Materials. 2020;4(2):026003.

[220] Hoeft J, Ledieu J, Haq S, Lograsso T, Ross A, Mcgrath R. Adsorption of benzene on the five-fold surface of the i-Al70Pd21Mn9 quasicrystal. Philosophical Magazine. 2006;86(6-8):869-74.

[221] Park JY, Ogletree D, Salmeron M, Ribeiro R, Canfield PC, Jenks C, et al. Elastic and inelastic deformations of ethylene-passivated tenfold decagonal Al-Ni-Co quasicrystal surfaces. Physical Review B—Condensed Matter and Materials Physics. 2005;71(14):144203.

[222] Fournée V, Gaudry É, Ledieu J, De Weerd MC, Wu D, Lograsso T. Self-organized molecular films with long-range quasiperiodic order. ACS nano. 2014;8(4):3646-53.

[223] Ledieu J, Muryn C, Thornton G, Diehl R, Lograsso T, Delaney D, et al. C60 adsorption on the quasicrystalline surface of Al70Pd21Mn9. Surface science. 2001;472(1-2):89-96.

[224] Kalashnyk N, Ledieu J, Gaudry É, Cui C, Tsai AP, Fournée V. Building 2D quasicrystals from 5-fold symmetric corannulene molecules. Nano Research. 2018;11:2129-38.

[225] Wasio NA, Quardokus RC, Forrest RP, Lent CS, Corcelli SA, Christie JA, et al. Self-assembly of hydrogen-bonded two-dimensional quasicrystals. Nature. 2014;507(7490):86-9.

[226] Maniraj M, Lyu L, Mousavion S, Becker S, Emmerich S, Jungkenn D, et al. Aperiodically ordered nano-graphene on the quasicrystalline substrate. New Journal of Physics. 2020;22(9):093056.

[227] O'Hanlon JF. A user's guide to vacuum technology. John Wiley & Sons; 2003.

[228] Umrath W. Fundamentals of Vacuum Technology. Leybold; 2016.

[229] Heidelberg-Instruments. Heidelberg Instruments website; 2022. `https://heidelberg-instruments.com/product/nanofrazor-scholar/`.

[230] Norrman K, Ghanbari-Siahkali A, Larsen N. 6 Studies of spin-coated polymer films. Annual Reports Section" C"(Physical Chemistry). 2005;101:174-201.

[231] Sahu N, Parija B, Panigrahi S. Fundamental understanding and modeling of spin coating process: A review. Indian Journal of Physics. 2009;83(4):493-502.

[232] Instruments H. NanoFrazor Recipe Book. Heidelberg Instruments; 2020.

[233] Materials KA. LOR and PMGI Resists for Bi-layer Lift-off Processing, Technical Data Sheet; 2021.

[234] AllResist. Thermally structurable positive resist AR-P 8100, Technical Data Sheet; 2022.

[235] Lassaline N. Generating smooth potential landscapes with thermal scanning-probe lithography. Journal of Physics: Materials. 2023;7(1):015008.

[236] Paul PC, Knoll AW, Holzner F, Despont M, Duerig U. Rapid turnaround scanning probe nanolithography. Nanotechnology. 2011;22(27):275306.

[237] Mamin H, Rugar D. Thermomechanical writing with an atomic force microscope tip. Applied Physics Letters. 1992;61(8):1003-5.

[238] Lee J, Beechem T, Wright TL, Nelson BA, Graham S, King WP. Electrical, thermal, and mechanical characterization of silicon microcantilever heaters. Journal of Microelectromechanical Systems. 2006;15(6):1644-55.

[239] Fletcher PC, Felts JR, Dai Z, Jacobs TD, Zeng H, Lee W, et al. Wear-resistant diamond nanoprobe tips with integrated silicon heater for tip-based nanomanufacturing. ACS nano. 2010;4(6):3338-44.

[240] Spieser M, Rawlings C, Lörtscher E, Duerig U, Knoll AW. Comprehensive modeling of Joule heated cantilever probes. Journal of applied physics. 2017;121(17).

[241] Knoll A, Rothuizen H, Gotsmann B, Duerig U. Wear-less floating contact imaging of polymer surfaces. Nanotechnology. 2010;21(18):185701.

[242] Wright AJ. Spin transport and associated background effects in all-metallic non-local spin valves. The University of Liverpool (United Kingdom); 2023.

[243] Wells OC. Scanning Electron Microscopy. In: Buschow KHJ, Cahn RW, Flemings MC, Ilschner B, Kramer EJ, Mahajan S, et al., editors. Encyclopedia of Materials: Science and Technology. Oxford: Elsevier; 2001. p. 8265-9. Available from: `https://www.sciencedirect.com/science/article/pii/B0080431526014790`.

[244] Achim C, Schmiedeberg M, Löwen H. Growth modes of quasicrystals. Physical Review Letters. 2014;112(25):255501.

[245] Tsai AP, Cui C. Crystal growth of quasicrystals. In: Handbook of crystal growth. Elsevier; 2015. p. 1113-56.

[246] Gille P, Bauer B, Hahne M, Smontara A, Dolinšek J. Single crystal growth of Al-based intermetallic phases being approximants to quasicrystals. Journal of crystal growth. 2011;318(1):1016-20.

[247] Cox EJ, Ledieu J, Mcgrath R, Diehl RD, Jenks CJ, Fisher I. The Ten-Fold Surface of The Decagonal Al 72 Ni 11 Co 17 Quasicrystal Studied by Leed, Spa-Leed, AES and STM. MRS Online Proceedings Library. 2000;643:1131-6.

[248] Mäder R, Widmer R, Bauer B, Gille P, Gröning P, Steurer W, et al. Revealing the atomic surface structure of the (100) Y-Al-Ni-Co approximant by low-energy electron diffraction and scanning tunneling microscopy. Physical Review B—Condensed Matter and Materials Physics. 2010;81(6):064201.

[249] Binnig G, Rohrer H. Scanning tunneling microscopy. Surface science. 1983;126(1-3):236-44.

[250] Horcas I, Fernández R, Gomez-Rodriguez J, Colchero J, Gómez-Herrero J, Baro AM. WSXM: A software for scanning probe microscopy and a tool for nanotechnology. Review of scientific instruments. 2007;78(1).

[251] Voigtländer B. Atomic Force Microscopy. Springer; 2019.

[252] Nečas D, Klapetek P. Gwyddion: an open-source software for SPM data analysis. Open Physics. 2012;10(1):181-8.

[253] Franco V, Dodrill B. Magnetic measurement techniques for materials characterization. Springer; 2021.

[254] Bowe S. Magnetisation dynamics in magnetostrictive nanostructures [Dissertation]. University of Nottingham; 2017.

[255] Source DL. I06 Beamline specifications; 2009. `https://www.diamond.ac.uk/Instruments/Magnetic-Materials/I06/Beamline-Guide/specs.html`.

[256] Stöhr J, Wu Y. X-ray magnetic circular dichroism: Basic concepts and theory for 3d transition metal atoms. New Directions in Research with Third-Generation Soft X-Ray Synchrotron Radiation Sources. 1994:221-50.

[257] Rivas M. X-ray magnetic circular dichroism (XMCD). University of British Columbia; 2021.

[258] Blundell S. Magnetism in condensed matter. OUP Oxford; 2001.

[259] Joos JJ, Bassirian P, Gypens P, Mulkers J, Litzius K, Van Waeyenberge B, et al. Tutorial: Simulating modern magnetic material systems in mumax3. Journal of Applied Physics. 2023;134(17).

[260] Leliaert J, Dvornik M, Mulkers J, De Clercq J, Milošević M, Van Waeyenberge B. Fast micromagnetic simulations on GPU—recent advances made with mumax 3. Journal of Physics D: Applied Physics. 2018;51(12):123002.

[261] Randall J, Lyding J, Schmucker S, Von Ehr J, Ballard J, Saini R, et al. Atomic precision lithography on Si. Journal of Vacuum Science & Technology B: Microelectronics and Nanometer Structures Processing, Measurement, and Phenomena. 2009;27(6):2764-8.

[262] Rothuizen H, Despont M, Drechsler U, Hagleitner C, Sebastian A, Wiesmann D. Design of power-optimized thermal cantilevers for scanning probe topography sensing. In: 2009 IEEE 22nd International Conference on Micro Electro Mechanical Systems. IEEE; 2009. p. 603-6.

[263] Ryu Cho YK, Rawlings CD, Wolf H, Spieser M, Bisig S, Reidt S, et al. Sub-10 nanometer feature size in silicon using thermal scanning probe lithography. ACS nano. 2017;11(12):11890-7.

[264] Pellegrini PE, Nista SV, Moshkalev S. Assembly and Bilayer Liftoff of Periodic Nanostructures with Sub-20 nm Resolution Using Thermal Scanning Probe Lithography. Nanomanufacturing. 2024;4(3):173-86.

[265] Albisetti E, Calò A, Zanut A, Zheng X, de Peppo GM, Riedo E. Thermal scanning probe lithography. Nature Reviews Methods Primers. 2022;2(1):32.

[266] Liu X, Zanut A, Sladkova-Faure M, Xie L, Weck M, Zheng X, et al. Cost and Time Effective Lithography of Reusable Millimeter Size Bone Tissue Replicas With Sub-15 nm Feature Size on A Biocompatible Polymer. Advanced Functional Materials. 2021;31(19):2008662.

[267] Synowicki RA, Hilfiker JN, Dammel RR, Henderson CL. Refractive-index measurements of photoresist and antireflective coatings with variable angle spectroscopic ellipsometry. In: Metrology, Inspection, and Process Control for Microlithography XII. vol. 3332. SPIE; 1998. p. 384-90.

[268] Nelson BA, King WP. Modeling and simulation of the interface temperature between a heated silicon tip and a substrate. Nanoscale and Microscale Thermophysical Engineering. 2008;12(1):98-115.

[269] Holzner F. Thermal scanning probe lithography using polyphthalaldehyde [Ph.D. thesis]. ETH Zurich; 2013.

[270] Gotsmann B, Lantz MA, Knoll A, Dürig U. Nanoscale thermal and mechanical interactions studies using heatable probes. Nanotechnology: Online. 2010:121-69.

[271] Yovanovich MM, Culham JR, Teertstra P. Analytical modeling of spreading resistance in flux tubes, half spaces, and compound disks. IEEE Transactions on Components, Packaging, and Manufacturing Technology: Part A. 1998;21(1):168-76.

[272] Inc EC. Properties of silicon and silicon wafers; Last accessed March 2025. https://www.el-cat.com/silicon-properties.htm.

[273] Cerrada ML. Introduction to the viscoelastic response in polymers. Instituto de Ciencia y Tecnología de Polímeros. 2005.

[274] Smith D, Myers JS, Kaplan CS, Goodman-Strauss C. An aperiodic monotile. arXiv preprint arXiv:230310798. 2023.

[275] Hu W, Zhang Z, Liao Y, Li Q, Shi Y, Zhang H, et al. Distinguishing artificial spin ice states using magnetoresistance effect for neuromorphic computing. Nature Communications. 2023;14(1):2562.

[276] Jeong HC, Steinhardt PJ. Cluster approach for quasicrystals. Physical review letters. 1994;73(14):1943.

[277] Gahler F, Jeong HC. Quasicrystalline ground states without matching rules. Journal of Physics A: Mathematical and General. 1995;28(7):1807.

[278] Farhan A, Derlet PM, Anghinolfi L, Kleibert A, Heyderman LJ. Magnetic charge and moment dynamics in artificial kagome spin ice. Physical Review B. 2017;96(6):064409.

[279] Zhang X, Duzgun A, Lao Y, Subzwari S, Bingham NS, Sklenar J, et al. String phase in an artificial spin ice. Nature communications. 2021;12(1):6514.

[280] Parakkat VM, Krishnan KM. Fabrication of hybrid artificial spin ice arrays with periodic site-specific local magnetic fields. Journal of Micromechanics and Microengineering. 2020;30(9):095002.

[281] Budrikis Z, Livesey K, Morgan J, Akerman J, Stein A, Langridge S, et al. Domain dynamics and fluctuations in artificial square ice at finite temperatures. New Journal of Physics. 2012;14(3):035014.

[282] John Greaves S, Muraoka H. Formation of thermally induced ground states in two-dimensional square spin ices. Journal of Applied Physics. 2012;112(4).

[283] Chern GW, Morrison MJ, Nisoli C. Degeneracy and criticality from emergent frustration in artificial spin ice. Physical review letters. 2013;111(17):177201.

[284] Schildknecht D, Heyderman LJ, Derlet PM. Phase diagram of dipolar-coupled XY moments on disordered square lattices. Physical Review B. 2018;98(6):064420.

[285] Macêdo R, Macauley G, Nascimento F, Stamps R. Apparent ferromagnetism in the pinwheel artificial spin ice. Physical Review B. 2018;98(1):014437.

[286] Yu L, Wang Y, Li J, Zhu F, Meng X, Cao J, et al. Monte Carlo simulation on a new artificial spin ice lattice consisting of hexagons and three-moment vertices. AIP Advances. 2017;7(8).

[287] Tong D. University of Cambridge Part III Mathematical Tripos. arXiv preprint arXiv:09080333. 2009.

[288] Barman A, Gubbiotti G, Ladak S, Adeyeye AO, Krawczyk M, Gräfe J, et al. The 2021 magnonics roadmap. Journal of Physics: Condensed Matter. 2021;33(41):413001.

[289] Drisko J, Marsh T, Cumings J. Topological frustration of artificial spin ice. Nature communications. 2017;8(1):14009.

[290] Materials A. Properties of SiN; Last accessed May 2025. website azom.com.

[291] Nakakura J, Ziherl P, Dotera T. Fourfold metallic-mean quasicrystals as aperiodic approximants of the square lattice. Physical Review B. 2024;110(1):014108.

[292] Finch GI, Quarrrell AG. Crystal structure and orientation in thin films. Nature. 1933;131(3320):877-7.

[293] Hu Z, Yang S. Endohedral metallofullerene molecular nanomagnets. Chemical Society Reviews. 2024.

[294] Marrows CH, Barker J, Moore TA, Moorsom T. Neuromorphic computing with spintronics. npj Spintronics. 2024;2(1):12.

[295] Im MY, Fischer P, Yamada K, Sato T, Kasai S, Nakatani Y, et al. Symmetry breaking in the formation of magnetic vortex states in a permalloy nanodisk. Nature communications. 2012;3(1):983.

[296] Yamada K, Kasai S, Nakatani Y, Kobayashi K, Kohno H, Thiaville A, et al. Electrical switching of the vortex core in a magnetic disk. Nature materials. 2007;6(4):270-3.

[297] Choe SB, Acremann Y, Scholl A, Bauer A, Doran A, Stohr J, et al. Vortex core-driven magnetization dynamics. Science. 2004;304(5669):420-2.

[298] Hellman F, Hoffmann A, Tserkovnyak Y, Beach GS, Fullerton EE, Leighton C, et al. Interface-induced phenomena in magnetism. Reviews of modern physics. 2017;89(2):025006.

[299] Thiel PA, McGrath R. Surfaces of quasicrystals and complex metallic alloys. Surface and Interface Science. 2013;3:349-82.

[300] Coates S, Burnie D, Sharma HR, McGrath R. Scanning Tunnelling Microscopy Studies of Tsai-Type Quasicrystal Approximants. Israel Journal of Chemistry. 2023:e202300116.

[301] Young K, Smerdon J, Sharma H, Lahti M, Pussi K, McGrath R. Acene adsorption on a Fibonacci-modulated Cu film. Physical Review B—Condensed Matter and Materials Physics. 2013;87(8):085407.

[302] Tsai AP, Inoue A, Masumoto T. New decagonal Al–Ni–Fe and Al–Ni–Co alloys prepared by liquid quenching. Materials transactions, JIM. 1989;30(2):150-4.

[303] Steurer W, Haibach T, Zhang B, Kek S, Lück R. The structure of decagonal Al70Ni15Co15. Acta Crystallographica Section B: Structural Science. 1993;49(4):661-75.

[304] Theis W, Rotenberg E, Franke KJ, Gille P, Horn K. Electronic valence bands in decagonal Al-Ni-Co. Physical Review B. 2003;68(10):104205.

[305] Janot C. Quasicrystals: A Primer. Second Edition. Oxford Science Publications; 1994.

[306] Trebin HR. Quasicrystals: structure and physical properties. John Wiley & Sons; 2003.

[307] Krätschmer W, Lamb LD, Fostiropoulos K, Huffman DR. Solid C60: a new form of carbon. Nature. 1990;347(6291):354-8.

[308] Moriarty PJ. Fullerene adsorption on semiconductor surfaces. Surface Science Reports. 2010;65(7):175-227.

[309] de Boer JL, van Smaalen S, Petricek V, DusekP M, Verheijen MA, Meijer G. Hexagonal close-packed C60. Chemical physics letters. 1994;219(5-6):469-72.

[310] Encyclopedia T. Square-triangle - Discovered by Schlottmann, Martin; 1998. https://tilings.math.uni-bielefeld.de/substitution/square-triangle/.

Appendix A

MuMax3 Simulation Code

A.1 Introduction

Provided in this chapter is an example script for calculating the E_{Total} of each configuration of the 3i vertex of the Ammann-Beenker tiling. The model code setup is explained in Section 4.7.4.

A.2 Example Script for 3i Total Energy

```
SetMesh(256, 256, 1, 4e-09, 4e-09, 4e-09, 0, 0, 0)
Msat = 8.6e+5
Aex = 1.3e-11
alpha = 0.5
lex := sqrt(1.3e-11/(0.5*mu0*pow(8.6e+5, 2)))
n := 4e-07
q := 2.56e-07
a := Ellipsoid(n, n/4, n/100).transl(q, 0, 0)
b := Ellipsoid(n, n/4, n/100).transl(q, 0, 0).rotz(-pi/4)
c := Ellipsoid(n, n/4, n/100).transl(q, 0, 0).rotz(-2*pi/4)
d := Ellipsoid(n, n/4, n/100).transl(q, 0, 0).rotz(-3*pi/4)
e := Ellipsoid(n, n/4, n/100).transl(q, 0, 0).rotz(-4*pi/4)
f := Ellipsoid(n, n/4, n/100).transl(q, 0, 0).rotz(-5*pi/4)
g := Ellipsoid(n, n/4, n/100).transl(q, 0, 0).rotz(-6*pi/4)
h := Ellipsoid(n, n/4, n/100).transl(q, 0, 0).rotz(-7*pi/4)
// type1:
setgeom( b.add(e).add(h))
//000
m.setinshape( b, uniform(1,-1,0) )
```

```
m.setinshape( e, uniform(-1,0,0) )
m.setinshape( h, uniform(1,1,0) )
save(m)
snapshot(m)
tableadd(E_total)
tablesave()
save(m)
//001
m.setinshape( b, uniform(1,-1,0) )
m.setinshape( e, uniform(-1,0,0) )
m.setinshape( h, uniform(-1,-1,0) )
save(m)
snapshot(m)
tablesave()
save(m)
//010
m.setinshape( b, uniform(1,-1,0) )
m.setinshape( e, uniform(1,0,0) )
m.setinshape( h, uniform(1,1,0) )
save(m)
snapshot(m)
tablesave()
save(m)
//011
m.setinshape( b, uniform(1,-1,0) )
m.setinshape( e, uniform(1,0,0) )
m.setinshape( h, uniform(-1,-1,0) )
save(m)
snapshot(m)
tablesave()
save(m)
//100
m.setinshape( b, uniform(-1,1,0) )
m.setinshape( e, uniform(-1,0,0) )
m.setinshape( h, uniform(1,1,0) )
save(m)
snapshot(m)
tablesave()
```

```
save(m)
//101
m.setinshape( b, uniform(-1,1,0) )
m.setinshape( e, uniform(-1,0,0) )
m.setinshape( h, uniform(-1,-1,0) )
save(m)
snapshot(m)
tablesave()
save(m)
//110
m.setinshape( b, uniform(-1,1,0) )
m.setinshape( e, uniform(1,0,0) )
m.setinshape( h, uniform(1,1,0) )
save(m)
snapshot(m)
tablesave()
save(m)
//111
m.setinshape( b, uniform(-1,1,0) )
m.setinshape( e, uniform(1,0,0) )
m.setinshape( h, uniform(-1,-1,0) )
save(m)
snapshot(m)
tablesave()
save(m)
```

Appendix B

Publications

Project Publications

- **L. Chandler**, O. Barker, A. Wright, L. O'Brien, S. Coates, R. McGrath, R. Lifshitz, and H. R. Sharma. Fabricating Quasiperiodic Tilings with Thermal-Scanning Probe Lithography. Israel Journal of Chemistry. 64, 10-11. 2023.

- **L. Chandler**, S. Coates, P.Gille, R. McGrath, and H. R. Sharma. Quasiperiodic arrays of finite-size C_{60} molecular chains induced by anisotropic growth. *In submission.*

- **L. Chandler**, S. Coates, O. Barker, T. James, C. Fields, A. Wright, R. Lifshitz, P. Moriarty, L. O'Brien, R. McGrath, and H. R. Sharma. Magnetic ordering and frustration in Ammann-Beenker artificial spin-ice. *In preparation.*

Oral Presentations

- *Fabricating Nanomagnetic Quasiperiodic Tilings.* Online European-CMetAC ASCI Workshop. 2023.

- *Magnetic properties of quasiperiodic artificial spin-ice tilings fabricated with nanolithography.* European-CMetAC Days, Slovenia. 2023.

- *Advances in nanomagnetic quasiperiodic tilings fabricated with nanolithography.* Online European-CMetAC ASCI Workshop. 2024.

Poster Presentations

- *Multiscale Quasiperiodic Architectures and Characterising Their Physical Properties.* Nanoscience Surfaces Summer School, Liverpool. **Thin Films Surfaces Group**

Poster Award. 2022.

- *Quasiperiodic Tilings Fabricated With Nanolithography and their Magnetic Properties.* European-CMetAC Days, Croatia. **ECMetAC Young Scientists Poster Presentation Award**. 2022.

- *Magnetic Ordering of Quasiperiodic Thin Film Tilings Fabricated with Nanolithography.* Surface Science Days 5, Chester. 2023.

- *Magnetic Ordering of the Octagonal Amman-Beenker Tiling Fabricated with Nanolithography.* 15th International Conference on Quasicrystals, Israel. **IUCr Award for Young Scientists**. 2023.